Nonlinear Buckling of Delaminated Panels

A thesis submitted to Imperial College London
for the degree of Doctor of Philosophy

by

Christina Völlmecke

Department of Civil and Environmental Engineering,
Imperial College of Science, Technology & Medicine,
London SW7 2AZ, United Kingdom

I hereby declare that this thesis and the work reported herein was composed and originated entirely by myself, unless appropriately referenced otherwise.

Wenn wir wüssten, was wir tun, würden wir es nicht Forschung nennen, oder?

[If we knew what it was we were doing, it would not be called research, would it?]

Albert Einstein (1879–1955)

Abstract

Laminated structures have increasingly gained popularity in engineering applications owing to their advantageous properties. Particularly in aerospace applications, laminated components, typically comprising fibre-reinforced composites, have a soaring demand owing to their high strength to weight ratio. However, owing to the complex nature of the material, several different failure mechanisms may occur; amongst them is delamination, *i.e.* the separation at the interface between two laminates. This defect is often difficult to detect, yet may significantly reduce a component's load carrying capacity and subsequently may severely affect its safe working conditions. It is therefore of utmost importance to assess the effects of delaminations on the structural elements carefully. Since components in aerospace applications often comprise laminated panels, a geometrically nonlinear plate delamination model is derived analytically by extending a previously developed two-layer strut model. This type of structural component is commonly analysed as an engineering simplification since flat plates are often used as an archetype to simplify more complex structural forms. Thus, an isotropic plate is currently considered, which reflects the simplest constitutive behaviour, and it can represent to some extent the behaviour of a laminated composite that has a uniform or symmetric lay-up sequence. A rectangular defect is located in the centre of this uniformly compressed, isotropic rectangular plated panel representing the delamination. Whilst trigonometric out-of-plane displacement functions are used in a Rayleigh–Ritz procedure yielding the governing equations that describe the mechanical behaviour of the plate, in-plane deformations are obtained via von Kármán's compatibility equation. An

indication of the residual capacity of the panel after critical buckling is obtained by investigating the nonlinear postbuckling range, where delamination propagation is incorporated by introducing a discrete cohesive zone model at the boundaries of the delaminated region. Different configurations are investigated in the neighbourhood of the previously evaluated *transitional depth* of delamination, which constitutes the boundary between local and global buckling. Initially, a uniformly spreading defect is investigated for various different defect sizes and depths. Subsequently, geometric parameters are linked to the response of the panel to generalize the outcomes with quantitative comparisons being undertaken against previous results and those obtained with the commercial finite element software ABAQUS. It is found that the model compares well and several criteria for the initial design of the damaged panels are proposed such that delamination growth may be accommodated safely and efficiently. Furthermore, uni-directional growth of the delamination is considered in a pilot study with suggestions being made regarding the growth direction tendency.

Acknowledgements

I would like to express my sincere gratitude to my principal supervisor Dr M. Ahmer Wadee for his support, expertise and encouragement throughout the entire time of this work. In particular, I would like to thank him for introducing me to elastic stability theory during the course of my studies at Imperial College. Thanks are also due to my second supervisor Dr Luke A. Louca for his interest in the project.

I would like to acknowledge the financial support for the last two years of this work provided by the Engineering and Physical Sciences Research Council. Furthermore, thanks are due to the Department of Civil and Environmental Engineering for funding me with a fees only award during the first year of my research.

I would also like to acknowledge the partial financial support provided by the Old Centralians' Trust to attend the Second International Conference on Buckling and Postbuckling Behaviour of Composite Laminated Shell Structures in Braunschweig, Germany, in September 2008, as well as the International Conference on Computational & Experimental Engineering and Sciences held in Phuket, Thailand, in April 2009. Additionally, thanks are due to the Royal Academy of Engineering for also partially funding my attendance at the latter conference.

I would like to express my appreciation for the expertise advice and encouragement I received from Dr Jenny E. Gladstone (née Wright), as well as Professors Chris J. Budd and Giles W. Hunt at the University of Bath.

My gratitude goes to all my colleagues at Imperial, especially to Stylianos Yiatros,

without whom my time at Imperial would have been far less enjoyable, Dr Katherine Cashell for her emotional support during the difficult times and Marios Theofanous for his expertise in finite element modelling. Furthermore, I would like to thank Dr Miguel Castro for his expert help dealing with IT questions.

I would like to express my sincere thanks to Professor Wolfgang H. Müller at the Lehrstuhl Kontinuumsmechanik und Materialtheorie (LKM), Institut für Mechanik, Fakultät V, Technische Universität Berlin, for providing me with the opportunity to develop further within academia as well as his patience during the final stages of the current work. Furthermore, I would like to thank everybody at LKM for giving me such a warm welcome in my new working environment.

I am deeply indebted to my family and friends for their support, encouragement and belief in me throughout this demanding time of my academic career. My heartfelt thanks goes out to each and every one of them.

Last but not least, I would like to express my deepest love and sincerest gratefulness to James S. B. Smart for being the greatest support in any sense anyone could ever wish for. Without him this work would have been very difficult to undertake and complete and my time in England would have been far less memorable. His exceptionally altruistic support, encouragement and love helped me persevere during this, at times, difficult period in my life and I will be eternally thankful for that.

Contents

List of Figures

Nomenclature

Lower case Roman letters

a	length of the delaminated patch in the x_i direction
b	width of the delaminated patch in the y_i direction
c	relative depth of delamination
c_t	transitional depth
i	variable corresponding to each part i of the panel ($i = 1, 2$ for upper or lower laminate, respectively, and $i = 3$ for the intact part of the panel)
i	fracture mode
j	variable corresponding to each buckling mode j of the panel
k	plate buckling coefficient accounting for the boundary conditions in equation (3.43)
l_cz	length of the cohesive zone
l_s	parameter defining the position of the spring in the cohesive zone model
q	transverse load
t	thickness of the panel
w_i	out-of-plane displacement functions per part i of the panel
x_i	$\equiv x$; longitudinal direction
y_i	$\equiv y$; transverse direction
z_i	$\equiv z$; out-of-plane direction

Upper case Roman letters

B	overall width of the panel in the y_i-direction
D_i	flexural rigidity per part i of the panel
E_i	$\equiv E_{x_i}$; Young's Modulus per part i of the panel
E_x, E_y, E_z	Young's Modulus in directions x, y, z respectively
$\mathcal{E}^{\mathrm{C}}$	end-shortening at the critical load of the undamaged panel
$\mathcal{E}_i$	end-shortening per part i of the panel
$\mathcal{E}$	total end-shortening
$\mathcal{E}_N$	normalized end-shortening
G_{iC}	critical strain energy release rate corresponding to fracture mode i
G_{IC}	critical strain energy release rate corresponding to fracture mode I
G	strain energy release rate
I_i	second moment of area $I_{yy,i}$ per part i of the panel
K	linear elastic spring stiffness in the cohesive zone model
L	overall length of the panel in the x_i-direction
N_x, N_y	uniformly distributed in-plane force in directions x, y respectively
N_{xy}	uniformly distributed in-plane force in the xy-direction
P	$\equiv P_x$
P^{C}	critical load of an undamaged panel
P_x, P_y	uniformly distributed load in directions x, y respectively
P^{C}	critical load
$Q_{i,m_i n_i}$	amplitude of the out-of-plane displacement w_i in the Fourier Series representation
Q_i	amplitude of the out-of-plane displacement w_i
Q_4	end-shortening of the panel in the x_i-direction
U_{b_i}	strain energy from bending per part i of the panel
U_b	total strain energy from bending
U_{m_i}	strain energy from membrane stretching per part i of the panel
U_m	total strain energy from membrane stretching

V	total potential energy
$\mathbf{V_{ij}}$	Hessian Matrix with entries V_{ij}

Lower case Greek letters

γ_{xy}	shear strain in the xy-plane
δ_{c}	critical separation of the laminates
$\delta_x(P)$	spring extension along $x = a/2 - l_s$
$\delta_y(P)$	spring extension along $y = b/2 - l_s$
$\delta_{\max}$	maximum separation of the laminates
ε_x, ε_y	direct strain in directions x, y respectively
θ	angle of rotation
λ	delamination slenderness
ν	Poisson's ratio
$\sigma_{\mathrm{c}}(P)$	maximum cohesive surface stress
$\sigma_{\max}$	$\equiv \sigma_{\mathrm{c}}(P)$
σ_{x_i}, σ_{y_i}	direct stress per part i of the panel
	in directions x, y respectively
τ_{xy}	shear stress in the xy-plane
ϕ_{delam}	delamination ratio $= ab/(BL)$
φ_i	Airy stress functions per part i of the panel
ψ	factor accounting for the shift in neutral axis

Upper case Greek letters

Γ	strain energy release rate
Λ	normalized load
Λ_j^{C}	normalized critical load
$\Lambda_j^{\mathrm{prop}}$	normalized load at which propagation begins

$\Lambda_j^{\min}$	minimum normalized load for a propagating delamination
$\Lambda_j^{\max}$	maximum normalized load for a propagating delamination
$\mathbf{\Phi}_j$	eigenvector comprising Q_i corresponding to buckling mode j

Notation for postbuckling graphs

PU	Postbuckling path of an undamaged panel
FE	Path of the finite element model containing a stationary delamination
S1	First physical postbuckling path of a damaged panel
S2	Second physical postbuckling path of a damaged panel
NS1	First non-physical postbuckling path of a damaged panel
NS2	Second non-physical postbuckling path of a damaged panel
P1	First postbuckling path of a damaged panel containing a uniformly propagating delamination
P2	Second postbuckling path of a damaged panel containing a uniformly propagating delamination
P1x	First postbuckling path of a damaged panel containing propagating delamination in the x_i-direction
P2x	Second postbuckling path of a damaged panel containing a uniformly propagating delamination in the x_i-direction
P1y	First postbuckling path of a damaged panel containing propagating delamination in the y_i-direction
P2y	Second postbuckling path of a damaged panel containing a uniformly propagating delamination in the y_i-direction

Supplementary notation for Appendix A

a, b, t	length, width and thickness of the plate in Figure A.1
$\mathbf{a}$	matrix comprising the membrane flexibility coefficients [equation (3) in Little (1987)]
E_x, E_y	Young's moduli in the x and y directions [equation (A.2)]
F	force or stress function [equation (25) in Little (1987)]
G	shear modulus [equation (A.2)]
I	integer coefficient of a term in γ_{ij}
I_m, I_n, I_{pq}, I_{xi}, I_{yi}	integers [equations (30), (32), (34) and (15) in Little (1987)]
m_i, n_i	integers which define the Fourier terms in the series for w [equation (15) and Table (2) in Little (1987)]
p, q	integers which define the Fourier terms in the series for γ_{ij} and F [equations (22), (25) and Table 3 in Little (1987)]
s_i	displacement function in the series for w [equations (12) and (15) in Little (1987)]
α	aspect ratio of the plate (= a/b)
γ_{ij}	trigonometrical part of a term in $\mathcal{N}()$ [equations (20) and (22) in Little (1987)]
η_{pq}	coefficients in the series of F [equations (25) and (26) in Little (1987)]
$\mathcal{N}()$	nonlinear differential operator [equation (A18) in Little (1987)]
ψ_{pq}	coefficient in series for $\mathcal{N}(w)$ [equation (23) in Little (1987)]

Chapter 1

Introduction

Owing to their high strength to weight ratio and subsequent weight saving (Cutler, 1999), fibre-reinforced composites are used in many engineering applications. "In the case of carbon fibre and similar advanced composites the prime market was in aeronautics" (The Design Council, 1989). However, applications can range from aeronautical, marine and space structures, via vehicle parts, applications in surgery, such as artificial joints etc., to sports equipment, *e.g.* skis, tennis racquets and so on (Berthelot, 1999).

Since there is such a broad spectrum of different structural components, geometries and applications that this class of material can be utilized for, a limitation for the current study is made. Hence, this work specifically investigates the behaviour of fibre-reinforced composite panels. The buckling and failure under buckling-driven delamination in fibre-reinforced composite panels are the topic of investigation currently. The buckling and postbuckling responses under uniaxial, in-plane compression as well as different delamination propagation scenarios are examined that are crucial for design considerations of such components in service.

In the first part of the current chapter, the principles of composite materials and specifically fibre-reinforced composites are introduced as well as potential applica-

tions of the materials and their failure modes, with particular emphasis being placed on delamination damage. In the second part of this chapter, the underlying theoretical background of elastic structural stability theory is presented with one of the approximation methods that can be employed to investigate the buckling and postbuckling of structures based on energy minimization being described in detail. Furthermore, some fundamental examples of stability phenomena are presented. Subsequently, the detailed aims and objectives of this work are outlined and the thesis structure is described.

1.1 Composite materials

The word "composite" is derived from the Latin word *compositus* and essentially means "made of two or more different parts" (Berthelot, 1999). A composite material generally combines one or more solid components in a continuous phase, with the solid constituent usually being of superior material properties to those of the compound. The solid, or discontinuous, phase is also called the *reinforcement* and the continuous phase is referred to as the *matrix*, see Figure 1.1; examples of those and their applications can be found in Table 1.1, which is classified by the nature of constituents not their form, *i.e.* fibres or particles.

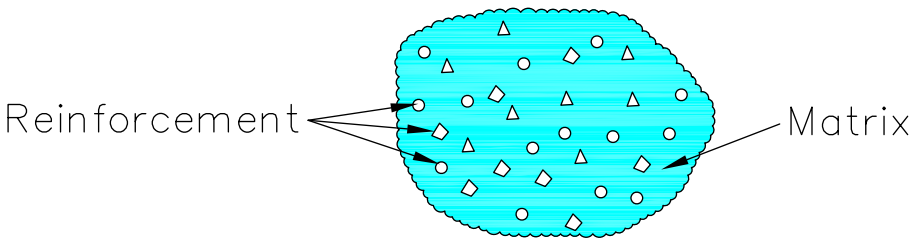

Figure 1.1: A generic composite material.

The advantages of using composite materials are apparent. Instead of using traditional materials, such as timber and steel etc., the designer is hereby empowered to "tailor" the material by changing the physical and mechanical behaviour to suit the

	Constituents	Areas of Application
1. *Organic Matrix Composites*		
Paper, cardboard	Resin/fillers/cellulose fibres	Printing, packaging
Particle panels	Resin/wood shavings	Woodwork
Fibre panels	Resin/wood fibres	Building
Coated canvas	Pliant resins/cloth	Sports/buildings
Impervious materials	Elastomers/bitumen/ textiles	Roofing, earthworks, etc.
Tyres	Rubber/canvas/steel	Automotive parts
Laminates	Resin/fillers/glass fibres carbon fibres, etc.	Multiple areas, *e.g.* aerospace, marine etc.
Reinforced plastics	Resins/microspheres	Multiple areas, *e.g.* aerospace, marine etc.
2. *Mineral Matrix Composites*		
Concrete	Cement/sand/gravel	Civil Engineering
Carbon-carbon composites	Carbon/carbon fibres	Aerospace, sports, biomedicine, etc.
Ceramic composites	Ceramic/ceramic fibres	Thermomechanical items
3. *Metallic Matrix Composites*		
	Aluminium/boron fibres	Aerospace
	Aluminium/carbon fibres	Aerospace
4. *Sandwiches*		
Skins	Metals, laminates, etc.	Multiple areas, *e.g.* aerospace, helicopters etc.
Cores	Foam, honeycombs, balsa reinforced plastics, etc.	Multiple areas, *e.g.* sports equipment, packaging etc.

Table 1.1: Examples of composite materials from Berthelot (1999).

performance requirement; a specific material for a specific purpose can then be created (Simitses *et al.*, 1985). This is particularly the case for fibre composites where the fibres can be arranged according to the loading scenario. In particle composites, *e.g.* concrete, the reinforcement (not to be confused with reinforced composite) does not have a distinct direction and may sometimes only be used to reduce the cost of the material by acting as a filler. However, it also improves certain material properties, *e.g.* temperature behaviour, shrinkage, etc.

A vast range of composites can be created depending on the application and design criteria. However, in the following sections, the discussion is limited to fibre-reinforced composites which by themselves have a broad range of potential uses, manufacturing techniques and designs that are only touched upon herein such that the general principles of these materials are introduced.

1.1.1 Fibre-reinforced composites

The material discussed in the subsequent sections is a composite that constitutes the matrix, which usually comprises resin, and fibres as the reinforcement, hence the name. The role of the matrix is to transmit the external loads to the fibres and protect them; their mechanical properties are usually modest. In contrast, the reinforcement is responsible for the gain in greater mechanical performance but the actual capability to develop its full strength in tension, bending and compression is derived from the resin (The Design Council, 1989).

The material is discussed principally on two levels: at the micro scale level, *i.e.* fibres and polymers, and at the meso scale level, *i.e.* different fibre arrangement architectures; the resulting macroscopic behaviour of the constituents provides the basis of the material properties employed in the following chapters (Rolfes *et al.*, 2009).

The polymer matrix can generally be grouped into two broad categories; *thermosetting resins*, which are essentially of low molecular weight that harden by an irre-

versible process of chemical crosslinking into very high molecular weight products, and *thermoplastics*, which are already strong solids with high molecular weight that can soften when heated and regain their properties when cooled (The Design Council, 1989). In the aerospace industries, *thermostable* resins have been specifically designed to meet the criteria of the constantly changing environments. However, the most widely used of all resins in the group of thermosetting resins is the unsaturated polyester resin. Its principal advantages include low production costs, good stiffness due to a high modulus of elasticity as well as good dimensional stability, *i.e.* its ability to maintain its original dimensions while being used for its intended purpose. However, its disadvantages include: sensitivity to cracking, considerable shrinkage and degradation in ultraviolet light. Epoxide resins are used most commonly after unsaturated polyester resins, but account for only about 5% of the composites market due to their high price (Berthelot, 1999), despite their good mechanical properties, low shrinkage during curing and other advantages. Different types of fillers and additives can be used to manipulate certain behavioural aspects of the resins or the costs.

In terms of the reinforcement, a broader choice is available. However the most commonly used are in forms of fibres and their derivatives that usually make up a volume fraction between 0.3 and 0.7 of the composite (Berthelot, 1999). Amongst the fibre types are glass fibres, carbon fibres, aramid fibres, ceramic fibres, thermostable synthetic fibres and other fibres, *e.g.* fibres of vegetable origin, mineral origin or metal fibres. Despite its brittle nature in bulk form, glass has good mechanical properties when made in thin fibres whilst being produced at low cost. It is for this reason that they are the most common reinforcement used in composites. Carbon fibres, however, also have a long history because of their good thermal and electrical conduction properties. The low specific stiffness of glass is its main disadvantage and the combination of very high theoretical strengths and stiffnesses whilst maintaining a low density make carbon fibres very appealing for various industrial applications; an abundance of developments have been made in different fabrication processes to obtain the best possible carbon fibre.

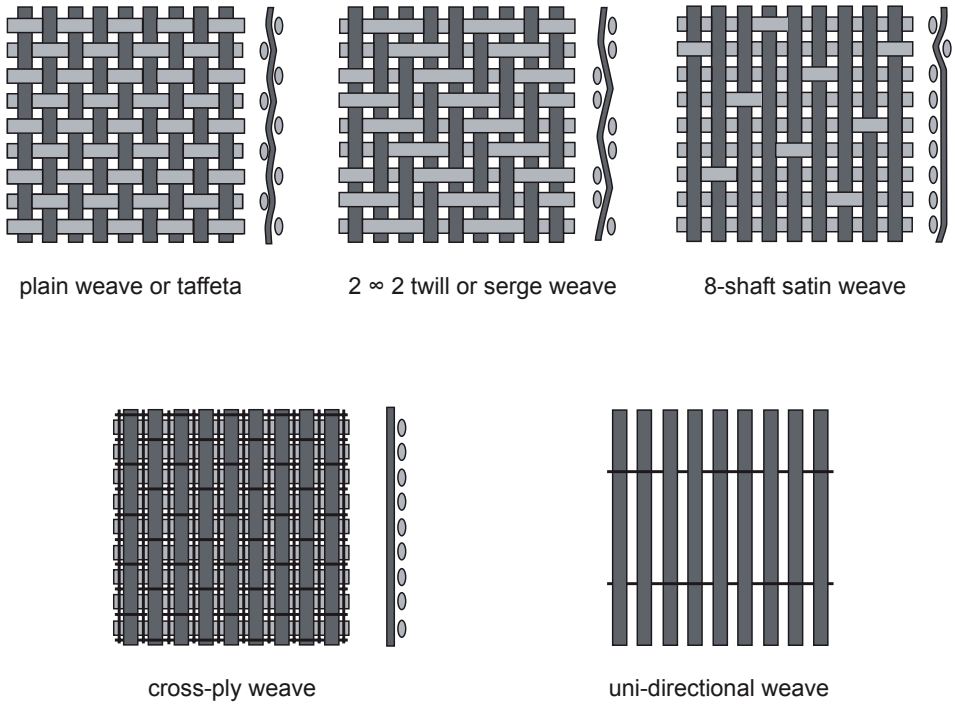

Figure 1.2: Different types of weaves taken from Berthelot (1999).

A single fibre, also referred to as a *monofilament*, can be gathered together into a bundle which is called a *strand* or *yarn*. Those in turn can then be used to produce surface tissues, such as mats, woven fabrics etc., or multidirectional woven structures. Whereas mats are essentially just sheets of continuous or discontinuous yarns arbitrarily distributed on a plane, cloths and woven fabrics are made by interlaced strands or yarns. Different types of weaves have been developed, ranging from plain weave, twill weave, satin weave, cross-ply weave to unidirectional weave (Figure 1.2). The mechanical properties clearly depend on the fibre and the type of weave, with unidirectional and high modulus weaves giving the best performance, followed by satin and twill weaves over plain weaves. Multidirectional woven structures are either achieved using preforms, interlacing the threads helically for cylinders for example, or multidirectional cloths. These are also called volume weavings where threads are arranged in multiple directions. The latter type of weave has increasingly become a topic of recent investigation because of its advantage of better strength properties and its capability of containing damage within a confined space. With advanced

numerical methods the behaviour can be simulated on the meso-mechanical level, considering different aspects of micromechanics, and the weave can be improved (Verpoest & Lomov, 2009).

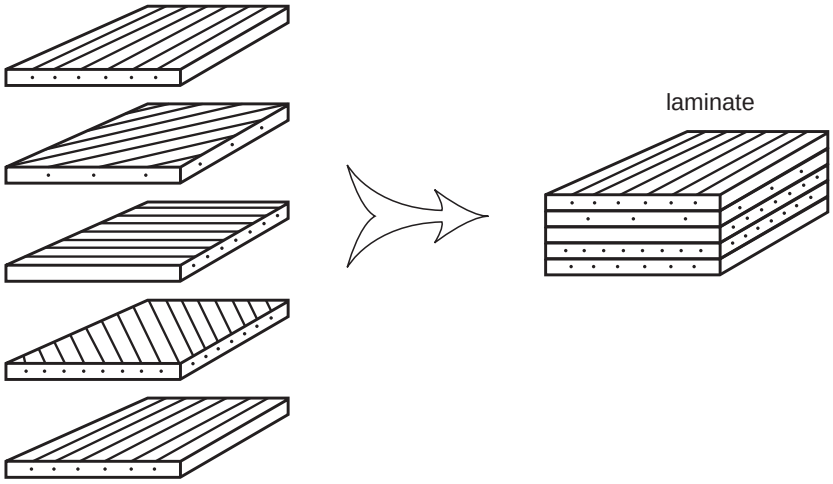

Figure 1.3: Constitution of a laminate taken from Berthelot (1999).

Fibre-reinforced composite materials can be manufactured using various different moulding techniques with the majority consisting of processes with successive layers comprising matrix and reinforcement, called *lamination*. Moulding processes include, amongst others, contact, vacuum, compression, continuous moulding etc. The simplest form, which is contact moulding, generally leads to one smooth surface depending on the surface of the mould whereas the quality of the product depends on the skill of the moulder. The process of curing can be accelerated by heating and compression, hence autoclaves are commonly used. With a view to the ease and advanced automation of manufacturing processes, so called *preprегs*[1] or *compounds* are used, which are manufactured using the same technique as moulding processes. However, fibres in desired arrangements are previously cured to such an extent that the preimpregnated forms can be cut, handled and then laminated (Berthelot, 1999). The principal advantage of those products is that high fibre to volume ratios can be achieved, thus high mechanical performance is ensured whilst improving the working conditions and automation of the procedure.

[1] *Prepreg* stems from *preimpregnates*.

Through these processes laminates, sometimes referred to as plies or layers, as illustrated in Figure 1.3, are manufactured and various types can be distinguished between. For example, there can be laminates with unidirectional strands or cloths, made up of laminates with positive and negative angles, symmetric laminates or sequences, or hybrid laminates, containing different types of fibre materials or weaves and strands, or even sandwich composites, where a core is coated and two sheet skins are attached. In unidirectional composites, every type of laminate can essentially be reduced to a unidirectional layer, which constitutes parallel fibres embedded in the resin, which is designated a number referring to the angle of orientation between the fibre direction and the x-reference axis (Berthelot, 1999). If successive layers have a different angle of orientation, a '/' separates them, otherwise a numerical subscript denotes their number as illustrated in Figure 1.4a. The layers are assigned from one face to the other; positive and negative angles can be assigned (Figure 1.4b) as well as symmetry conditions and repetitions. It is avoided here to go into further depth regarding the stacking sequence possibilities and notation since the aim is to provide a general introduction of the possibilities in building composites. The model in Chapter 3 is developed assuming isotropic material properties in accordance with the findings in Chapter 2, hence a more detailed review on the notation of composite lay-ups appears to be superfluous, since the main concern is the macro-mechanical behaviour once the laminates contain a defect.

1.1.2 Uses of fibre-reinforced composites

As mentioned in the opening of this chapter, fibre-reinforced composites are used in many engineering applications due to their advantage of being able to tailor the material to suit a particular loading scenario. In aeronautical applications, for example, it was "estimated that replacing 40% of an aluminium alloy structure by carbon fibre reinforced plastics would result in 12% saving of the total structural weight" (Megson, 1999). To that date, the use of composite materials in aircraft structures appeared to have had reached stagnation, in particular for the subsonic civil aircraft

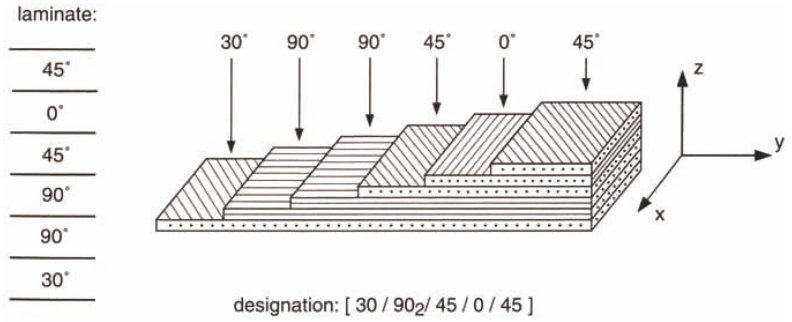

(a)

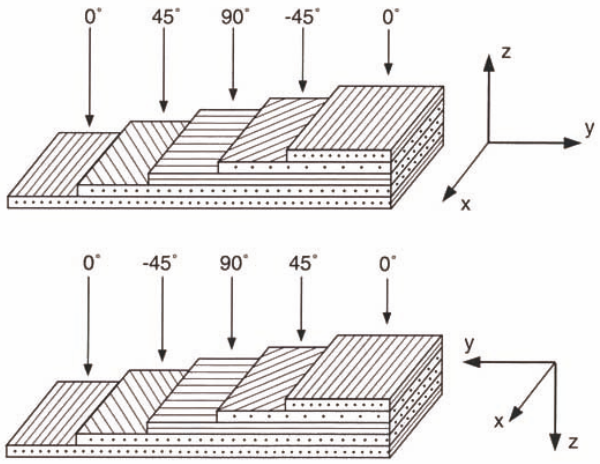

(b)

Figure 1.4: Stacking sequences of laminates. (a) Designation (here from bottom to top) and (b) sign convention, taken from Berthelot (1999).

sector where composites only composed approximately 15% of structural materials used.

Fibre-reinforced composites are commonly used in constructing unmanned aerial vehicles used in military applications. However, the pressure is now also on the commercial sector of the aeronautical industry to conceive innovative designs to reduce the impact on the environment by producing lighter and more efficient airliners. The two main competitors in this sector are Boeing and Airbus and their most recently conceived aircraft designs comprise 50% composites within the structure of the Boeing 787 Dreamliner (Bisagni & Walters, 2008), Figure 1.5a, and 52% of the airframe of the Airbus A350XWB, Figure 1.5b, is to be made of reinforced plastics (Marsh, 2007; Craven *et al.*, 2010). However, Boeing's maiden flight of the

(a) The Boeing 787 Dreamliner (picture taken from (Boeing, 2009))

(b) The Airbus A350 XWB (picture taken from (Marsh, 2007))

Figure 1.5: Different aeroplanes mainly made out of composites.

787 Dreamliner was postponed on several occasions (USA Today, 2009) but then flew for the first time on 15 December 2009 (BBC, 2009a). Though the company denied that it was due to the structure being largely manufactured with composites (BBC, 2009b). The change in the airframe construction method is said to reduce the amount of fuel required by 20% and subsequently the commensurate amount in emissions; airline operating costs could thereby be reduced as could potentially the prices for passengers. Furthermore, the advantages of using fibre-reinforced composites in this sector are that there is a vastly reduced risk of corrosion, thus the humidity in the cabin may be increased as could the travelling comfort for the passenger. In addition, different manufacturing techniques are employed using long panels that are designed to suit their specific loading scenario. They can be easily replaced in case of repair and fewer laps are required, again reducing the weight, emissions and travel time. All these factors are important in an industry that is estimated to increase in size of productivity by 5% annually within the next 20 years (Szodruch, 2008).

1.1.3 Failure of fibre-reinforced composites – Delamination

Owing to the complex nature of the material, various different failure mechanisms can occur, see Figure 1.6, such as fibre fracture, transverse and longitudinal matrix

fracture, and fracture of the fibre-matrix interface (Simitses *et al.*, 1985; Garg, 1988; Whitcomb, 1989; Berthelot, 1999). Since the material is increasingly being used in aircraft structures, and other structures, it is crucial to simulate and investigate these failure mechanisms (Linde, 2008) to predict the damage behaviour. The main focus of this review is on the so-called *delamination*, which essentially means the separation at the interface between laminates (Johnson, 1985).

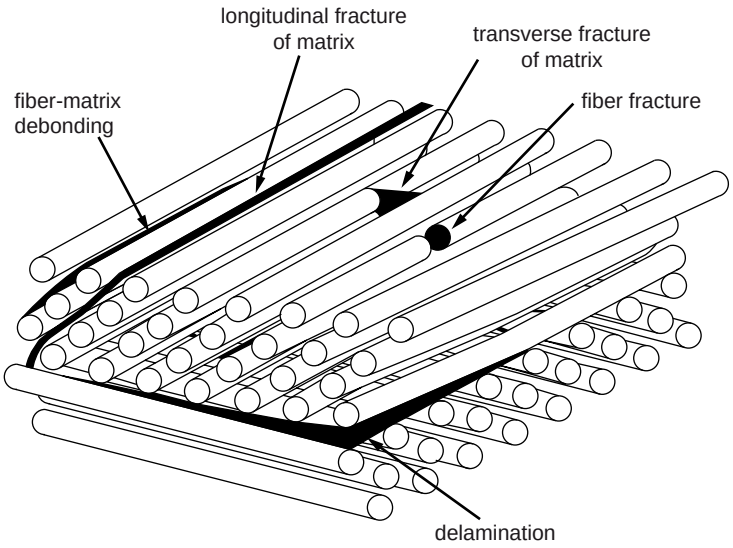

Figure 1.6: Defects observed in laminated materials taken from Berthelot (1999).

The causes of delamination are manifold and the separation can occur during manufacturing or in-service scenarios. During the lamination process, thermal and chemical shrinkage can lead to stresses that may result in delamination. Furthermore, accidental air pockets, adhesion failures or imperfections may also introduce delamination. During service or maintenance an impact, such as a bird strike, from runway debris or dropping a tool, could be reasons for a newly introduced delamination. In addition, matrix cracks could also lead to interface cracks as well as interlaminar stresses at free edges due to the mismatch of material properties (Bottega & Maewal, 1983; Shivakumar & Whitcomb, 1985; Garg, 1988; Kardomateas & Schmueser, 1988; Bolotin, 1996; Bolotin, 2001).

Delaminations can occur in different shapes. The latter cause in the previous paragraph may yield so-called *free-edge* delaminations, which may also be critical at holes and notches, whereas *embedded* delaminations usually occur from the other aforementioned causes. Embedded delaminations can occur in different shapes, usually circular or elliptical, and depths in the laminated material. Often, those delaminations resulting from a low-velocity impact are barely visible, also referred to as *barely visible impact damage* (BVID) (Garg, 1988; Kardomateas, 1993; Nilsson *et al.*, 1993; Melin & Schön, 2001; Butler *et al.*, 2007; Rhead *et al.*, 2008; Wimmer & Pettermann, 2008; Craven *et al.*, 2010). Non-destructive damage detection can be undertaken optically via microscopic observation, using radiography analysis (X-rays), acoustic emission analysis using transducers or ultrasonic C-scans, where a short pulse of ultrasonic energy is incident on a sample and measurement of the transmitted pulse indicates its attenuation, which is influenced by delaminations, voids, the condition of the fibre–matrix interface and so on.

Whilst fibre and matrix cracking may be more relevant in tension (Sekine *et al.*, 2000), delamination can considerably reduce the load carrying capacity of a component in compression[2] and BVIDs may even lead to a snap-back response (Wimmer & Pettermann, 2008). The significant strength and stiffness degradation can be crucial to the stability and integrity of the structural component and results can be catastrophic (Shivakumar & Whitcomb, 1985; Garg, 1988; Kardomateas & Schmueser, 1988; Short *et al.*, 2001). It is therefore important to investigate the behaviour of these structures carefully to ensure their safe application.

1.2 Theoretical background

Before introducing the main body of this thesis, some underlying theoretical principles are introduced. This section begins with the fundamentals of elastic stability

[2] A stiffness and strength reduction under compressive loading of up to 60 % resulting from delamination damage is quoted by Craven *et al.* (2010).

theory, describing the axioms that form the foundation of the procedures that follow later. Since fibre-reinforced composites are usually brittle, material plasticity is not a significant issue. Hence, material nonlinearities, *i.e.* material yielding, are not accounted for in the model developed in Chapter 3, and the following sections solely deal with elastic buckling theory incorporating geometric nonlinearities. In the course of the section, distinct buckling phenomena are described and subsequently the methodology of modelling the nonlinear postbuckling behaviour with the energy principles and Rayleigh–Ritz method is established.

1.2.1 Fundamentals of Elastic Stability Theory

Pioneering work in nonlinear bifurcation theory of continuous elastic systems was conducted by Koiter (1945), which represented the first general approach for modelling postbuckling behaviour. Over the subsequent decades, various other researchers (Roorda, 1965; Supple, 1967; Chilver, 1967; Sewell, 1970; Johns & Chilver, 1971) investigated in the area of elastic stability theory; Koiter's seminal work, based on the calculus of variations, was enhanced by introducing generalized coordinates, assuming that the postbuckling behaviour can be described by a series of modes (Hutchinson & Koiter, 1970; Croll & Walker, 1972; Thompson & Supple, 1973; Thompson & Hunt, 1973; Thompson & Hunt, 1984; Hunt, 1986; Hunt, 1989; Hunt, 2006). This type of approach is the basis for the energy approach utilized to investigate the model in this thesis and its characteristics are therefore discussed in detail.

The basis of this approach is that an n degree of freedom, conservative mechanical system can be described by the same number of spatial configurations, specified through the *generalized coordinates* Q_i, where i is an integer, running from 1 to n. Hence, a single-valued, continuous and "well-behaved" total potential energy function V (Thompson & Hunt, 1973), based on the concept that no energy dissipates, consisting of the internal (strain) energy U minus the work done by the loads $P\mathcal{E}$,

can be derived:

$$V(Q_i, P) = U(Q_i) - P\mathcal{E}(Q_i)\,, \tag{1.1}$$

where $\mathcal{E}$ is the distance that the load P moves in the load direction. In discrete mechanical systems, such as a spring and rigid-link model, equation (1.1) may be derived directly, whereas in continuous systems the buckling shapes may be described by employing modal discretization. This will be discussed in more detail when the Rayleigh–Ritz approach is introduced later in this chapter.

Two axioms are fundamental in the theory of elastic stability using total potential energy; the first defines the equilibrium of a system and the second describes its stability (Thompson & Hunt, 1973; Thompson & Hunt, 1984).

> Axiom I: *A stationary value of the total potential energy with respect to the generalized coordinates is necessary and sufficient for the equilibrium of the system.*

The first axiom can be summarized as follows:

$$V_i \equiv \frac{\partial V}{\partial Q_i} = 0 \quad (\text{for all } i)\,. \tag{1.2}$$

For the analysis of discrete conservative systems, the second axiom combined with Axiom I is essential, since the stability of the equilibrium is defined thus.

> Axiom II: *A complete relative minimum of the total potential energy with respect to the generalized coordinates is necessary and sufficient for the stability of an equilibrium state of the system.*

Whereas the first axiom can be used to derive Newton's laws of motion, there is no entirely general proof for the second axiom. The second axiom can be visualised by the *rolling ball analogy*, which depicts the stability of a system (Timoshenko & Gere, 1961; Croll & Walker, 1972; Thompson & Hunt, 1973; Thompson & Hunt, 1984). Consider Figure 1.7a, since work is required to displace the centre of gravity

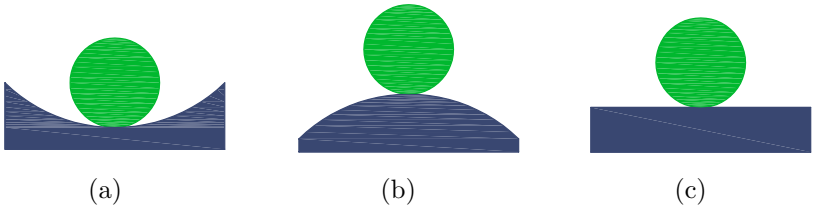

(a) (b) (c)

Figure 1.7: Rolling ball analogy. (a) Stable, (b) unstable and (c) neutral equilibrium.

of the ball on the concave surface, hence increasing the potential energy of such system, the equilibrium is called *stable*. Therefore, the energy of the system is at a minimum ($V_{\min} : \partial^2 V/\partial Q_i^2 > 0$). The second case in Figure 1.7b, the convex surface, any perturbation from the equilibrium state decreases the total potential energy hence this is referred to as *unstable* with the energy being at a maximum, ($V_{\max} : \partial^2 V/\partial Q_i^2 < 0$). The third and last case (Figure 1.7c) is where there is no change in energy during displacement, meaning that the equilibrium is indifferent or *neutral*, ($V_{\text{flat}} : \partial^n V/\partial Q_i^n = 0$). It should be noted, that for each system only the shape of the supporting surface is relevant for the stability, not the "weight" of the ball or the absolute magnitude of V (Timoshenko & Gere, 1961).

Having established the principles behind nonlinear buckling theory, a methodology that can be used to investigate the stability behaviour of different structural configurations is discussed in the following section.

1.2.2 Rayleigh–Ritz method

Since most nonlinear structural mechanics problems cannot be solved exactly or in closed form, the aid of approximate methods is necessary to analyse such problems. The Rayleigh–Ritz method is an approximate method that can be employed to investigate structural stability via the calculation of the total potential energy. This type of method has been covered in many textbooks (Timoshenko & Gere, 1961; Thompson & Hunt, 1973; Thompson & Hunt, 1984; Bažant & Cedolin, 1991) and has been successfully employed by many research workers for analysing more

complex types of structures that are similar to the type of problem this work is concerned about (see §2.5). Owing to its approach in approximating a structure's continuous displacement, it is the most convenient technique for a semi-analytical assessment of the problem and therefore the general concept of the procedure is discussed herein. It should be noted, however, that the finite element method also adopts the Rayleigh–Ritz approach but since its method of discretizing a continuous displacement via more arbitrary shape functions results in a large number of elements and degrees of freedom, this method can be regarded as purely numerical; for example see Zienkiewicz *et al.* (2005) for details.

To employ the Rayleigh–Ritz method, an approximate function $f_n(x, y)$ describing the structural displacement that satisfies the geometric boundary conditions of the two-dimensional structure, in this case, needs to be assumed as follows:

$$\begin{aligned} f_n(x,y) &= \sum_{i=1}^{n} Q_i h_i(x,y) \\ &= Q_1 h_1(x,y) + Q_2 h_2(x,y) + Q_3 h_3(x,y) + ... + Q_n h_n(x,y)\,, \end{aligned} \tag{1.3}$$

where Q_i $(i = 1 \ldots n)$ are the generalized coordinates defining the amplitudes of $h_i(x, y)$, the functions describing the units of postbuckling deflection of the structure. The underlying theorem states that when $n \longrightarrow \infty$ the exact solution $f(x, y)$ is obtained for continuous structures; for rigid link and spring models, however, the mode shapes can be described accurately via a finite number of generalized coordinates. The kinematically admissible functions $h_i(x, y)$ are usually of polynomial or sinusoidal form and are not required to satisfy the static boundary conditions of the system (Thompson & Hunt, 1973; Bažant & Cedolin, 1991) but the approximations are better if they do. The assumed function $f_n(x, y)$ can subsequently be used to obtain the strain energy U and the work done $P\mathcal{E}$ forming the total potential energy as given in equation (1.1).

To find the critical loads, *linear eigenvalue analysis* can be performed. Since only the second derivatives of V are examined, no information about the system's behaviour after buckling is supplied. For a multiple degree of freedom system, the *Hessian*

matrix $\mathbf{V_{ij}}$ therefore needs to be obtained. Critical equilibrium, the special case of $P = P^{\mathrm{C}}$, requires a matrix of the second derivatives of V with the following entries:

$$V_{ij} = \frac{\partial^2 V}{\partial Q_i \partial Q_j}\,; \tag{1.4}$$

this symmetric matrix, which includes cross derivatives, is singular at the critical states, *i.e.*:

$$\det(\mathbf{V_{ij}}) = 0\,, \tag{1.5}$$

and the critical loads are readily available after solving for P^{C}. The determinant is also referred to as the *stability determinant*, because its vanishing indicates a critical equilibrium state where the system begins to buckle. This holds for diagonalized as well as for non-diagonalized systems (Thompson & Hunt, 1973). Once the critical loads are obtained, the potential energy can be expanded about the critical state P^{C} to examine the behaviour of the system after buckling; this is also called the *perturbation method*. Hence, the first derivative of V with respect to each generalized coordinate Q_i is set to zero, equation (1.2), and a set of n simultaneous equations can be obtained that describe the equilibrium state; if large deflections are assumed in the formulation these equilibrium equations give the postbuckling paths, since they contain the relationship between the buckled deformations, *i.e.* $f_n(x, y)$, and the load P.

With the procedure outlined above a system is readily analysed by employing approximate analytical, continuous displacement functions $f_n(x, y)$. This is one of the major benefits of this procedure that by simply using integration, to obtain the energy expressions, and differentiation, to obtain the equilibrium equations, a relationship between load and deflection can be ascertained in a very straightforward procedure without having to resort purely to numerical methods. In addition, structures can be modelled without initial imperfections, such that the principal behaviour stemming from the perfect case can be established.

Despite the advantages the method offers, it has some drawbacks. Foremost it is evident, that employing approximate functions for the displacement $f_n(x, y)$ yields

inaccurate results. Depending on the magnitude of the approximation of the actual displacement field, the procedure potentially leads to an overestimation of the stiffness and buckling load that is remote from the real solution of the actual critical load due to an incorrect energy expression. This error can however be contained or minimized if a sufficient number of terms are used when describing the deflection $f_n(x, y)$. However, in some cases this may lead to a high number of degrees of freedom Q_i necessary to be employed which diminishes the convenient simplicity of the approach. In these cases, using a Rayleigh–Ritz procedure in the classical sense becomes impractical and numerical methods such as the commonly used finite element method, based on similar principles, may be preferable.

From the above discussion it should be noted that so long as the deflection of the structure only requires a reasonably small number of degrees of freedom in $f_n(x, y)$ to be modelled relatively accurately, the method offers the advantage of analytical, phenomenological and systematic investigation of the buckling and postbuckling behaviour. In the current work, the displacement and the resulting stresses can be approximated with sinusoidal functions (§3.4.1 and §3.4.2 respectively) which have been successfully used in the past to study the buckling and postbuckling behaviour of plates (Timoshenko & Woinowsky-Krieger, 1959; Timoshenko & Gere, 1961; Szilard, 1974; Williams & Aalami, 1979) and are therefore deemed as appropriate for the accuracy of the subsequent analyses.

Having introduced the approximate method that will be used to obtain the buckling and postbuckling behaviour of the structure investigated in this work, a selected number of buckling phenomena are discussed in the following section to introduce further terminology that is applicable for the interpretation of the results in Chapters 4–8.

1.2.3 Nonlinear buckling phenomena

Since the principles behind nonlinear buckling theory, namely the two axioms, as well as the approximate Rayleigh–Ritz method have been established in the previous sections, a selected number of buckling phenomena are subsequently discussed in a very brief review of various seminal publications (Chilver, 1967; Johns & Chilver, 1971; Croll & Walker, 1972; Hutchinson & Koiter, 1970; Thompson & Hunt, 1973; Thompson & Hunt, 1984; Hunt *et al.*, 1986; Hunt, 1989; Lord *et al.*, 1997; Hunt, 2006; Wadee, 2007). It should be noted that unstable equilibrium paths are indicated with dashed lines in the following graphs and stable paths with solid lines.

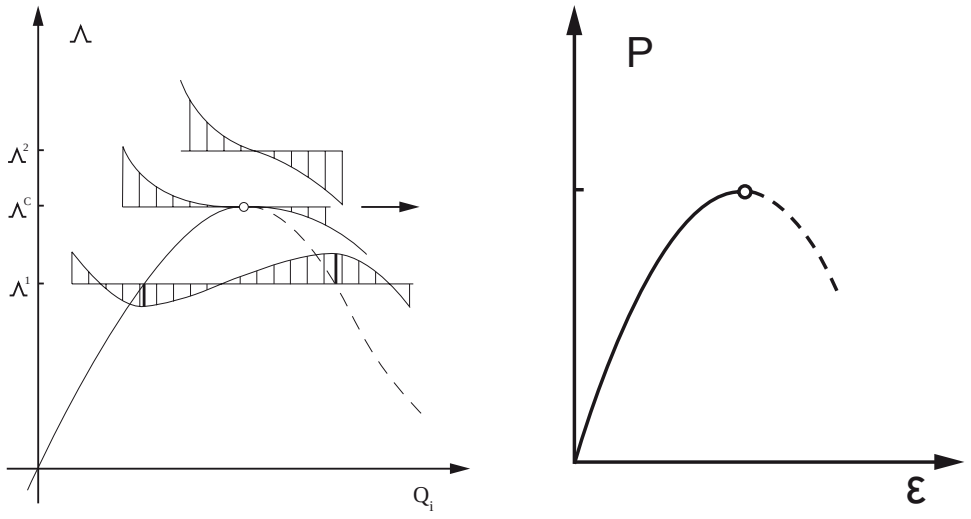

(a) (b)

Figure 1.8: Limit point, after Thompson & Hunt (1973). (a) Energy transformation at the limit point and (b) load versus end-shortening.

The first phenomenon discussed herein is the *limit point* or *fold catastrophe*, Figure 1.8, which as Thompson & Hunt (1984) describe "arises right across the spectrum of sciences, and is *the* typical mode of failure for a system under a single load control". An imperfect, or real, structure will always fail under load at such a point, where the initially stable equilibrium path from the origin after reaching a local maximum loses its stability. At the point of the local maximum of the load parameter, the horizontal point of inflection, Figure 1.8a, there are no local equilibrium states for higher

values of the load which implies that a physical system would snap dynamically under dead loading (or load control). In the load versus end-shortening graph, Figure 1.8b, this can be seen in the unstable, decreasing function after the limit point. This phenomenon occurs in shallow arches or domes in practical applications. Furthermore, this limiting point may be a smooth maximum or sometimes be seen as a sharp *cusp* depending on the viewpoint in three-dimensional space.

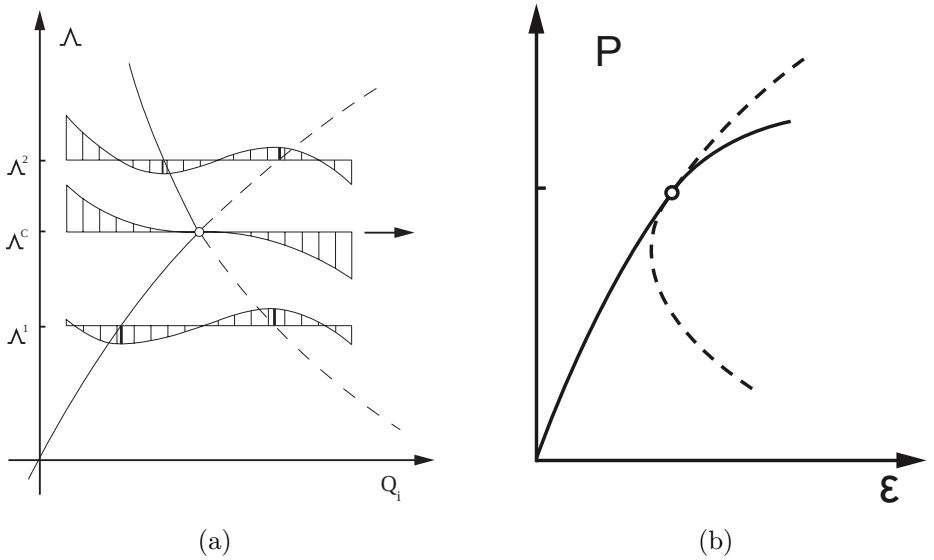

Figure 1.9: Asymmetric point of bifurcation, after Thompson & Hunt (1973). (a) Energy transformation at the point of bifurcation and (b) load versus end-shortening.

The second phenomenon in the current discussion is that of a *bifurcation point* or *branching point*. In this scenario, an initially stable *fundamental* equilibrium path is intersected at the *critical point* by distinct and continuous *postbuckling* paths. The fundamental, pre-buckling path may or may not be *trivial*, *i.e.* all degrees of freedom being equal to zero, until it reaches the critical point. At this point of inflection, which can be either stable or unstable depending on the system, the system branches to the postbuckling state. There are several different distinct cases for this type of buckling, *e.g.* an asymmetric type of bifurcation (Figure 1.9) or a symmetric bifurcation which can display either a supercritical, *i.e.* stable (Figure 1.10), or subcritical, *i.e.* unstable behaviour (Figure 1.11). In the former, the system is either stable or unstable depending on the direction of the generalized coordinate Q_i (Figure 1.9a);

if it is unstable, the system would snap dynamically from the critical equilibrium state if it is under load control. These types of structures are highly imperfection sensitive and it is well known that unstable asymmetric bifurcations have higher imperfection sensitivity than unstable symmetric ones (Bažant & Cedolin, 1991).

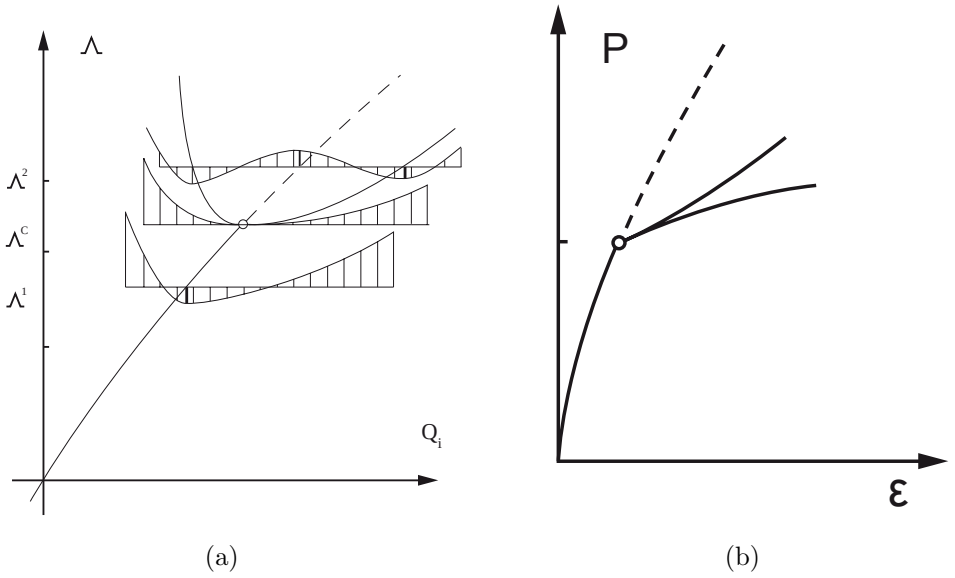

Figure 1.10: Stable-symmetric point of bifurcation, after Thompson & Hunt (1973). (a) Energy transformation at the point of bifurcation and (b) load versus end-shortening.

In the case of a *stable-symmetric bifurcation*, Figure 1.10, which in practice can be observed in the postbuckling behaviour of plates, the load parameter can be increased along the fundamental path until it reaches the branching point. At this point, a smooth and stably rising postbuckling path intersects the fundamental path at the point of zero slope. This point is not unstable, thus no dynamical snap would occur for a physical structure under slowly increasing loading (Thompson & Hunt, 1984) and the load can be steadily increased resulting in a positive postbuckling stiffness or reserve capacity, which is usually limited ultimately by the material.

The last configuration examined here is the *unstable-symmetric bifurcation*, Figure 1.11, which can typically be observed in shells. A subcritical, unstable postbuckling path intersects the fundamental path here. At the point of intersection, the critical

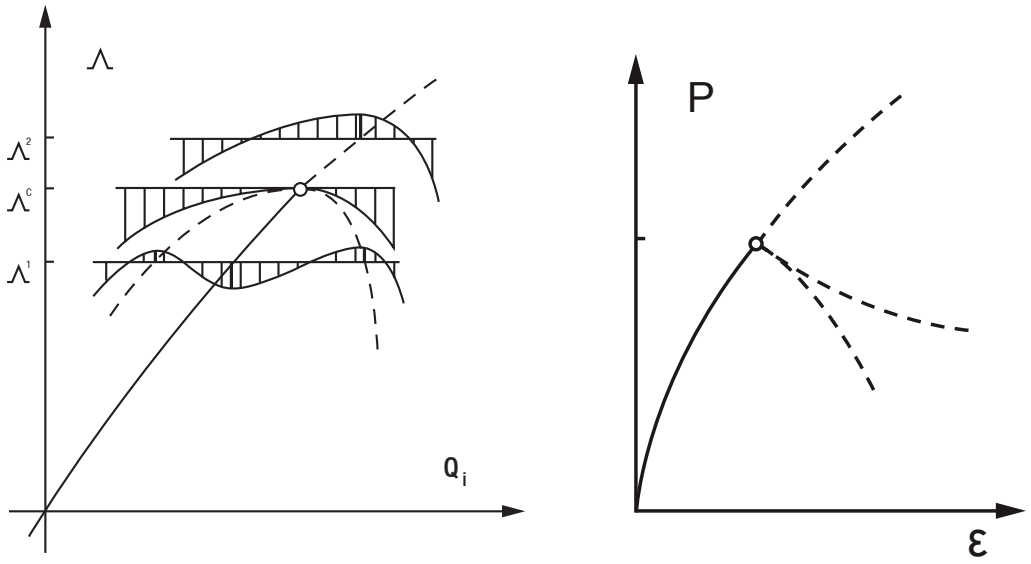

(a) (b)

Figure 1.11: Unstable-symmetric point of bifurcation, after Thompson & Hunt (1973). (a) Energy transformation at the point of bifurcation and (b) load versus end-shortening.

point, the equilibrium is seen to be unstable which means that the load parameter cannot be increased further along the fundamental path. Thus, a dynamical snap would occur under dead loading conditions at the critical point in the direction of the small perturbation.

1.3 Thesis outline

The motivation for this work comes from the serious effects delaminations can have on the safe working conditions of composites as outlined in §1.1.3. A model containing an embedded delamination is therefore developed in an analytical form and is investigated via minimum energy principles employing a Rayleigh–Ritz procedure. To enable the designer to exploit the full potential of these panels, it is crucial initially to obtain the loads at which buckling occurs since they may be lower than for an undamaged panel. Moreover, it is of utmost importance to incorporate delamina-

tion propagation in the postbuckling stages since this can lead to further structural instability as the delamination grows. Hence, not only does the load at which growth occurs have to be determined, but also the growth behaviour of different delamination configurations to establish threshold values for different parameters for the design of such panels.

Now that the fundamentals of fibre-reinforced composites and the underlying theoretical background have been introduced, a brief outline of this thesis is presented.

1.3.1 Buckling and postbuckling of laminated structures

In Chapter 2 a literature review is undertaken that discusses various publications on modelling the buckling and postbuckling behaviour of delaminated panels and struts. It begins with different geometric configurations that have been investigated in the past, in particular plates or struts, which may contain different types of delamination geometries. Various loading scenarios are discussed as well as modelling techniques and approaches that have been successfully employed by previous investigators. The chapter concludes by summarizing the essential findings from this review.

1.3.2 The delaminated panel model

Having established previous results and investigations in Chapter 2 the delaminated plate model is established in Chapter 3 building on earlier work by, amongst others, Bottega (1983), Chai & Babcock (1985), Shivakumar & Whitcomb (1985), Peck & Springer (1991), Hunt *et al.* (2004). Initially, the structural geometry of the model is described followed by the assumptions and simplifications used to derive the displacement and stress functions employed in the Rayleigh–Ritz formulations. Furthermore, the expressions for the strain energy in bending and membrane stretching as well as the work done terms are derived to obtain the total potential energy of the system. Finally, the finite element model that is developed to validate the

results in the subsequent chapters is described.

1.3.3 Initial buckling of the delaminated panel

With the model developed in Chapter 3 the delaminated plate is initially investigated for critical buckling using only linearized analysis in Chapter 4. The procedure with which this is undertaken was described in the current chapter and results for the critical loads for a square and rectangular delamination are parametrically investigated and conclusions are drawn. Some of these results are furthermore validated with existing results in the literature as well as the finite element model that is described and presented in Chapter 3. In addition, the eigenvectors of the corresponding critical loads are identified, namely the *closing*, *opening* and *transverse opening* modes.

1.3.4 Postbuckling regime of a stationary delamination

Chapter 5 deals with the postbuckling regime of a stationary delamination, *i.e.* no delamination propagation is allowed for in the configurations discussed. The numerical code AUTO (Doedel, 2007), employed to solve for the postbuckling solutions is discussed and the equilibrium paths for different delamination configurations are presented and validated. The problem of physical and non-physical postbuckling solutions that may appear in the bifurcation graphs is addressed. Furthermore, the influence of certain parametric configurations on the magnitude of the outward deflection of the laminates are discussed, *i.e.* local, mixed or global buckling, and the topic of modal contamination is addressed. In addition, a finite element comparison is conducted followed by an investigation of mode interaction.

1.3.5 Delamination propagation modelling

A review of different modelling techniques for delamination propagation is given in Chapter 6 outlining the principles behind selected approaches, namely basic fracture mechanics, the virtual crack closure technique and cohesive zone modelling. The discrete cohesive zone model, which is employed in the current study, is subsequently described in detail as well as the underlying assumptions and formulation. Finally, the algorithm that is used in AUTO to incorporate the discrete cohesive zone model into the formulation from the preceding chapters is described.

1.3.6 Postbuckling regime of a uniformly propagating delamination

In Chapter 7, delamination propagation is included into the model and results originating from a square delamination are presented and discussed for different parametric configurations, mainly around the transitional depth that constitutes the boundary between local and global buckling. Four different delamination sizes are investigated and their equilibrium paths are shown and examined in detail. Furthermore, validation of the results is undertaken against results in the literature as well as finite element results. The chapter concludes with suggestions for design criteria for the panel to exploit the material beyond the buckling range obtained with linear analysis.

1.3.7 Postbuckling regime of a unidirectionally propagating delamination

In this part of the current work a pilot study is conducted on unidirectional delamination propagation. Initially, the growth is assumed to originate from a square delamination but further cases are studied with propagation from a wide or long

rectangular defect. This topic is also part of the further work section of the final chapter since it has the potential to be investigated in much greater detail.

1.3.8 Conclusions and further work

The work concludes by summarizing the findings as well as their implications. Possible extensions to the current research are then presented.

Chapter 2

Buckling and postbuckling of laminated structures

2.1 Introduction

Over the past three decades, the modelling of structures with delaminations has become increasingly a popular topic of investigation by researchers because of the advantages of using composite materials in various industries, as discussed in the previous chapter. To obtain a chronological overview, one may start in the 1980s where pioneering work had been undertaken by Chai & Babcock (1981) with a simple one-dimensional model of a delaminated strut. Later, Bottega & Maewal (1983) published their research on delamination modelling of an embedded delamination in a circular plate. These works were followed by Shivakumar & Whitcomb (1985), Simitses *et al.* (1985) and Chai & Babcock (1985) and a book by Johnson *et al.* (1985). Later, towards the end of that decade, Garg (1988), Kachanov (1988), Kardomateas & Schmueser (1988) and Whitcomb (1989) all published work on that subject. Shortly after that at the beginning of the next decade, Davidson (1991), Peck & Springer (1991) and Yin & Jane (1992a; 1992b) published their investigations and findings using various approaches on the topic of delamination

modelling. Over the course of the 1990s, fundamental research was conducted by Nilsson & Stårakers (1992), Nilsson (1993), Kardomateas (1993), Kardomateas & Pelegri (1994), Davidson (1995) as well as Bolotin (1996), who reviewed the state of the art at the time, and Kim & Kedward (1999). After the turn of the century, Kouchakzadeh & Sekine (2000), Sekine *et al.* (2000), Bolotin (2001), Hwang & Liu (2001), Melin (2001), Nilsson (2001a; 2001b) and Short *et al.* (2001; 2002) underpinned and extended previous findings. More recently, Hunt *et al.* (2004), Hwang & Huang (2005), Wright (2006a), Rhead *et al.* (2008) and Wimmer & Petermann (2008) investigated the behaviour of delaminated structures.

Furthermore, it should be mentioned that extensive investigations have also been undertaken and are currently being made by various authors to study the buckling and postbuckling behaviour of sandwich panels suffering from delamination (Somers *et al.*, 1991; Frostig, 1992; Wadee & Blackmore, 2001; Wadee, 2002; Østergaard, 2008). In sandwich panels, the debond usually occurs between the core material, *e.g.* honeycomb core, and the face plate, *e.g.* aluminium, essentially due to similar or the same reasons as in laminated composite structures (§1.1.3). However, since the focus is on laminated composite materials, the papers on delamination in sandwich panels are mentioned in passing for completeness but are not reviewed in detail.

Within this chapter, most of the above and some additional articles will be reviewed, with the most relevant papers in significant depth. The chapter is divided into several sections within which different structural configurations are discussed, however the primary investigation currently focuses on research into plates or two-dimensional structural elements. These structural members containing various delamination geometries, focusing on pre-existing embedded delaminations, are subjected to various different loading scenarios. Furthermore, modelling techniques and approaches ranging from analytical modelling, numerical modelling and experimental approaches are discussed. Subsequently, models containing a non-stationary defect are studied, but it should be noted that a more detailed discussion on modelling delamination propagation in terms of the local growth in the delamination

is undertaken in Chapter 6. Concluding the current chapter, the key findings are stated that are important for the following chapters.

2.2 Structural configurations

As mentioned before, different structural configurations containing a delamination defect have been investigated by researchers over past decades, such as delaminated struts (Chai *et al.*, 1981; Simitses *et al.*, 1985; Kardomateas & Schmueser, 1988; Hunt *et al.*, 2004; Wright, 2006a), flat circular plates (Bottega & Maewal, 1983), flat rectangular plates (Chai & Babcock, 1985; Shivakumar & Whitcomb, 1985; Whitcomb, 1989; Peck & Springer, 1991; Yin & Jane, 1992a; Yin & Jane, 1992b; Kardomateas, 1993; Nilsson *et al.*, 1993; Gaudenzi, 1997; Kim & Kedward, 1999; Sekine *et al.*, 2000; Rhead *et al.*, 2008), curved plates (Short *et al.*, 2002) and cylindrical shells (Bolotin, 2001). Furthermore, the debonding of stringers in stiffened panels have been investigated (Orifici *et al.*, 2007; Orifici *et al.*, 2008) as well as delamination occurring in stiffeners of curved panels (Wimmer & Pettermann, 2008). Since the main aim of the current work is to develop an analytical model of a delaminated flat plate, the latter two cases are mentioned for completeness but will not be discussed further since they comprise an entirely different subdomain of delamination modelling.

2.2.1 Struts

For the works on struts, three different articles are herein reviewed in detail namely, Chai & Babcock (1981), Simitses *et al.* (1985) and Hunt *et al.* (2004). The one-dimensional model Chai & Babcock developed in their groundbreaking work was essentially a homogeneous, isotropic and linearly elastic beam-column approach with a pre-existing delamination under axial compression. The single delamination split the beam into two parts and was located in the centre of the strut. Furthermore,

it was assumed that the dimension of the damage length was small compared to the strut size but large compared to the laminate thickness. First a "thin-film" case was discussed followed by the development of the general case model. Growth of the damaged region was incorporated via a fracture mechanics approach and the conditions for this were derived by examining the change in stored fracture energy of the system as the delamination propagates. Furthermore, a distinction was made between: (a) the case where the delamination existed prior to loading the strut or (b) the case where the strut was loaded first and the defect occurs in the loaded structure. For case (a), it was established that the growth of the delamination may be stable, unstable or restabilizing depending on the parameters and thus "could form the base for an experimental study of the applicability" of their proposed analytical model. For case (b), the model was deemed to be unable to withstand the process of growth or a dynamic snap, since an excess of energy was released when the structure goes from the unbuckled to the buckled configuration. However, the magnitude of the excess energy released could be captured, which resulted in a lower load for the initiation of growth. The findings were consistent with previous experimental evidence despite the fact that "quantitative comparison (...) with impact experiments" was deemed as not meaningful because the complex nature of the dynamic delamination process was beyond the capabilities of the model according to the authors.

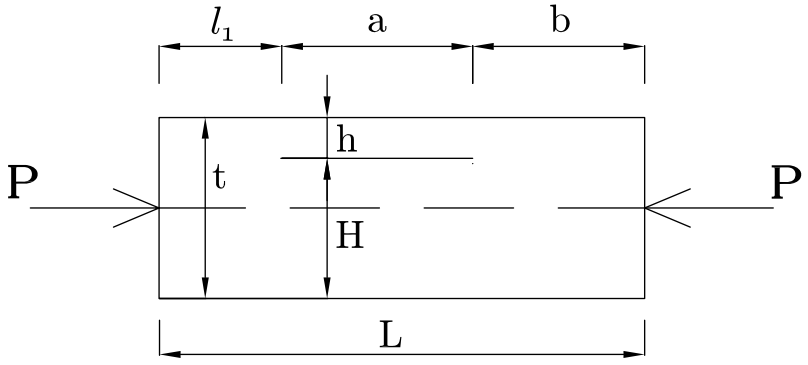

Figure 2.1: The delaminated strut model as investigated by Simitses *et al.* (1985).

Simitses *et al.* (1985) developed their simple model, Figure 2.1, based on the same as-

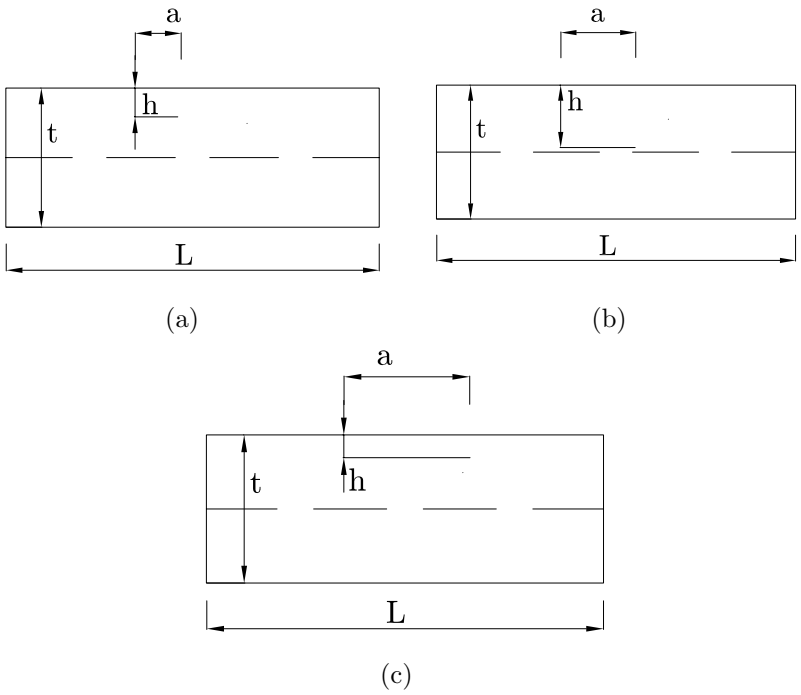

Figure 2.2: Different cases of the delaminated plate model investigated by Simitses *et al.* (1985); threshold for clamped end conditions: (a) $\bar{a} \leqslant \bar{h}$ for $\bar{h} \leqslant 0.2$, (b) $\bar{a} \leqslant \bar{h}$ for $\bar{h} > 0.2$ and (c) $\bar{a} \geqslant \bar{h}$.

sumptions to investigate the effect of size, location and thickness of the delamination on the buckling load. In their case it was assumed, moreover, that the delamination existed prior to loading, rather than allowing both scenarios as above, and the overall strut was investigated with either clamped or simply supported edges. The buckling equations were investigated using a perturbation approach which fundamentally stated that an adjacent equilibrium position exists at a bifurcation point or limit point; as outlined in §1.2. During their studies they concluded that for clamped conditions of the strut, provided that the delamination thickness itself was relatively small ($\bar{h} \leqslant 0.2$), where $\bar{a} = a/L$ and $\bar{h} = h/t$, the effect of the delamination on the buckling load was not significant as long as the length of the delamination was smaller than or equal to the depth of the delamination ($\bar{a} \leqslant \bar{h}$), Figure 2.2a. However, under the same condition that $\bar{a} \leqslant \bar{h}$, the buckling load was increasingly affected once the delamination moved deeper into the panel and approached mid-depth (*i.e.* for cases $0.2 < \bar{h} \leqslant 0.5$), Figure 2.2b. Furthermore, the buckling load

decreased significantly for thinner delaminations, where the delamination thickness was smaller than the length of the delamination, *i.e.* ($\bar{a} \geq \bar{h}$), Figure 2.2c. It was also understood that this scenario may potentially lead to delamination growth if the load was further increased, since thin-film buckling occurred where only the upper laminate experienced buckling while the rest of the structure remained basically undeflected. For simply supported conditions the same trends could be observed, but the described threshold shifted to $\bar{a} \leqslant 2\bar{h}$. In other words, thin film behaviour occurred later. In addition, they investigated the effect of a delamination that was located unsymmetrically with respect to the midpoint of the strut, *i.e.* $l_1 \neq b$. In both support cases, simply supported or clamped, it was concluded that the symmetrical delamination was the most critical case.

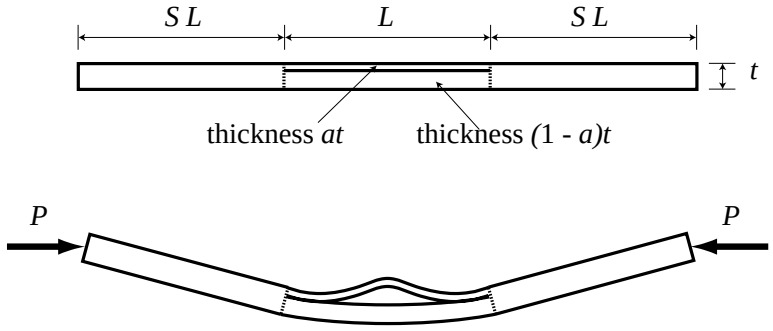

Figure 2.3: The delaminated strut model as investigated by Hunt *et al.* (2004).

The final paper within this detailed review dealing with delaminated struts is the nonlinear four degree of freedom Rayleigh–Ritz model developed by Hunt *et al.* (2004), Figure 2.3. This model was the original inspiration for the current work and is, amongst others, one of the principal bases for the model developed in Chapter 3. Again, a pre-existing delamination was assumed within this approach, but no delamination propagation was considered. The model geometry is reminiscent of the ones described above, though owing to the Rayleigh–Ritz procedure pursued, the formulations were different, *i.e.* trigonometric displacement functions were assumed to model the behaviour of the intact and delaminated parts, yielding the basis for the energy formulation. Strain energy stored in bending, stretching and

the work done were derived and accumulated to evaluate the total potential energy. A linear eigenvalue analysis was performed to obtain critical loads and associated mode shapes that could be compared to finite element results for validation purposes. With the energy approach, several distinct critical loads were obtained via parametric investigations. In the course of the studies it was found that the critical loads changed with the depth of the delamination and the corresponding mode shapes were referred to as closing, Figure 2.4a, and opening modes, Figure 2.4b, for the first and second critical load, respectively. The postbuckling analysis was per-

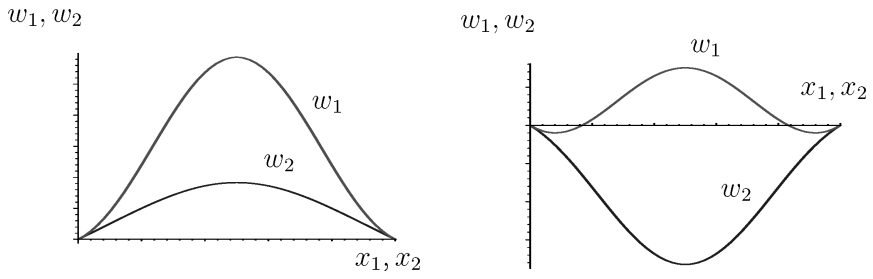

Figure 2.4: Mode shapes identified by Hunt *et al.* (2004); (a) closing mode and (b) opening mode. Note that w_i refers to the out-of-plane displacement of laminate i.

formed via an optimization scheme to find minimum energy solutions and distinct equilibrium solutions were found. Physical and non-physical postbuckling solutions were detected, as well as stable and unstable postbuckling equilibrium solutions depending on the parametric configuration. Non-physical solutions were essentially when the laminates intersected; please refer to §5.2.1 for further discussion of this topic. Furthermore, either "thin-film", or local, buckling, mixed mode or global buckling could be observed. The local case was identified to be stable or plate-like over the initial postbuckling range whereas the mixed mode case was understood to be unstable or shell-like (as seen in §1.2.3). The advantage of this approach was that due to the nature of the formulations, based on the total potential energy concept, the stability behaviour could be readily classified.

2.2.2 Plates

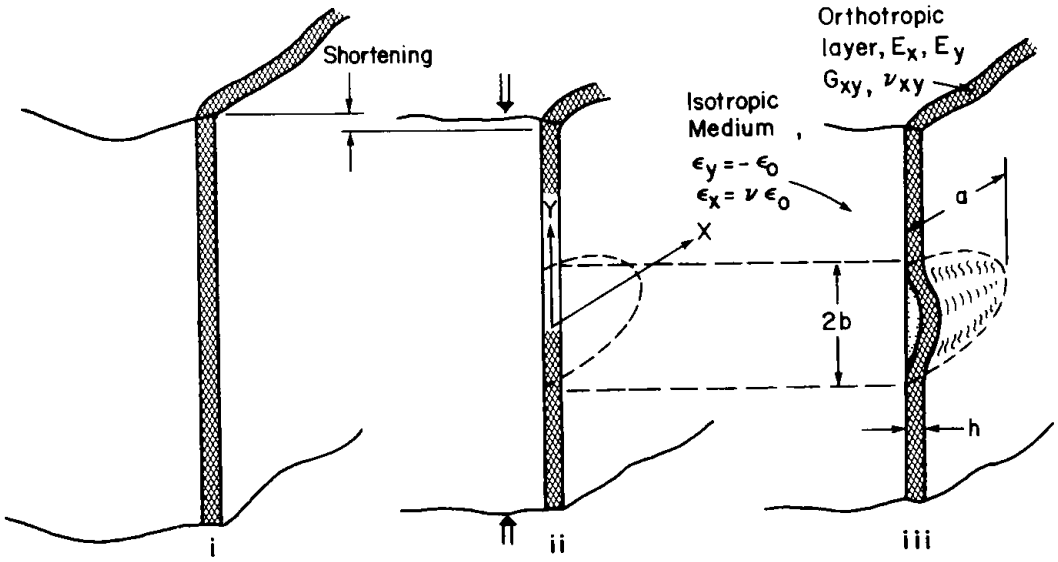

Figure 2.5: The delaminated plate model after Chai & Babcock (1985). Stages of the delamination; (i) unstressed state, (ii) uniformly axially compressed state and (iii) buckled configuration.

Some years after their pioneering one-dimensional model, Chai & Babcock (1985) published their investigations on their two-dimensional, analytical model. The model contained a single, near-surface delamination that was elliptic in shape which separated a thin orthotropic layer from a thick isotropic plate. The Rayleigh–Ritz method was employed to find the postbuckling solutions and a fracture mechanics based energy criterion determined the self-similar propagation behaviour under quasi-static growth conditions. Again, a distinction was made between a structure that was loaded prior to the delamination occurring and a pre-existing delamination before loading begins. Three stages were considered, the first one being an unstressed state, Figure 2.5(i), followed by a uniaxially compressed state with an elliptical delamination, Figure 2.5(ii). The final state differs from the previous state only in the buckled configuration of the delamination, Figure 2.5(iii), where the stresses in the parent medium remained unchanged.

Polynomial displacement functions were assumed to describe the out-of-plane be-

haviour of the delamination. The buckling loads were determined with the Rayleigh–Ritz procedure, and the postbuckling response was obtained numerically using the Newton–Raphson method. The delamination then grew in the postbuckling range when the strain energy release rate of the structure reached the value required to create a new unit of interlaminar surface. With emphasis placed on initially circular defects, a distinction was made between cases where the delamination grew in the load direction or transverse to it either in an isotropic or orthotropic case. In the former configuration, it was found that for very thick or small delaminations, *i.e.* where the radius of the delamination was approximately the same or less than the depth of the delamination, propagation followed immediately after buckling. As in the one-dimensional case, a "snap out" behaviour was observed from the unbuckled to the buckled configuration when the delamination was introduced into a pre-loaded structure. This means that the system buckled locally at the applied load level and part of the energy released in this transition could transfer into the propagation of the delamination, *i.e.* increasing the radius, and subsequently lowering the applied load. Furthermore, a tendency to grow unstably in the perpendicular direction to the load was found for an initially circular delamination until the aspect ratio of the delamination becomes sufficiently large, then growth in the loading direction was also observed.

For the elliptical delamination, investigations were made regarding the aspect ratio of the delamination. Here, a distinction was made between stable and unstable growth. In the orthotropic case, the fibre alignments parallel and perpendicular to the loading direction were investigated. In the former case, the buckling load was found to decrease the propagation strain with growth being observed primarily in the loading axis, except for large defects where the radius was more than twice the depth of the delamination. In cases where the fibres were orientated normal to the load, the buckling load and delamination growth initiation strain could be increased. The growth behaviour was predominantly perpendicular to the loading direction and a circular delamination was observed not to buckle or grow in most applications.

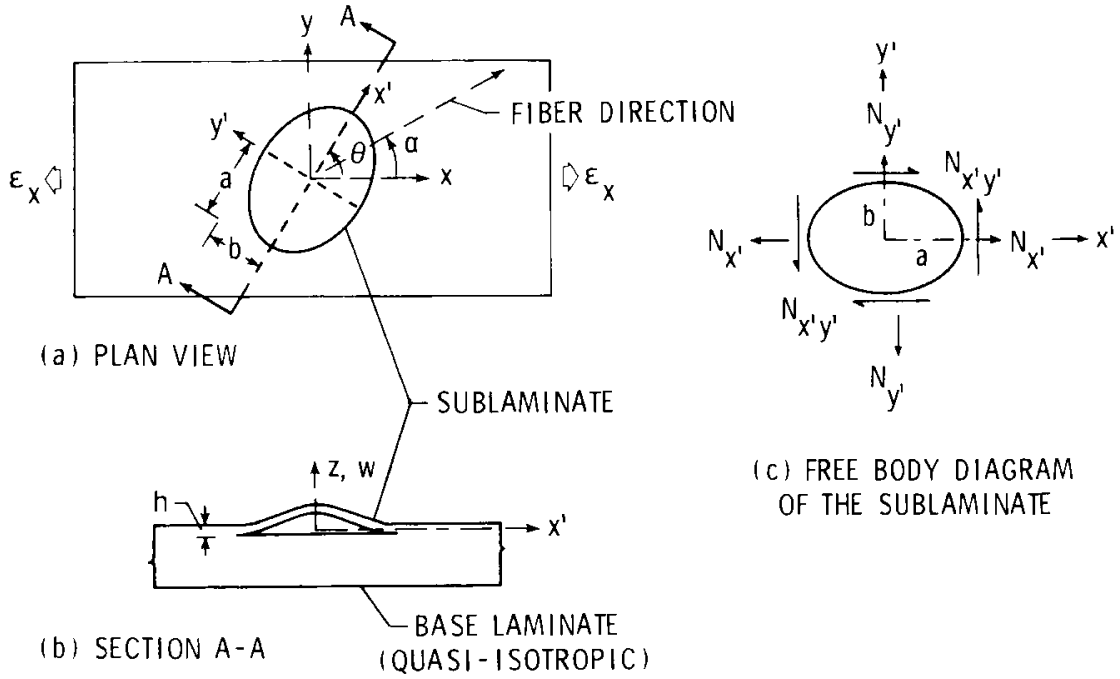

Figure 2.6: The delaminated plate model by Shivakumar & Whitcomb (1985). (a) Plan view, (b) section through the buckled panel and (c) free body diagram of the laminate.

In the same year as Chai & Babcock's paper, Shivakumar & Whitcomb (1985) published their work on the buckling of a quasi-isotropic composite plate containing a single embedded near-surface delamination, Figure 2.6. Again, Rayleigh–Ritz formulations were employed forming the basis of the energy method used for the parametric investigation. Polynomial displacement functions were used to obtain the total potential energy for the studies considering the effect of the shape and material orientation on the buckling behaviour. In addition, a finite element formulation was employed based on the same model. Inward buckling was neglected as it would result in a nonlinear contact problem and it was also pointed out that the sublaminate may buckle when the base or parent medium was in tension due to the mismatch of Poisson's ratio. In all cases, good agreement was found between the Rayleigh–Ritz method and the finite element approach. Concluding, they found that despite the base plate being in a state of uniaxial compression, the sublaminate was generally under biaxial loading. In unidirectional lay-ups, this stress state might result in

what the authors refer to as "tensile buckling" of the sublaminate. This occurs when the fibres were almost perpendicular to the load direction and the delamination was elongated in the loading direction leading to buckling of the delamination due to Poisson's ratio. Furthermore, it was found that the compressive buckling load increased with increasing angle between the load and fibre direction and the direction of the elongation of the sublaminate; the lowest buckling strain correlated with the initial growth direction of a circular delamination.

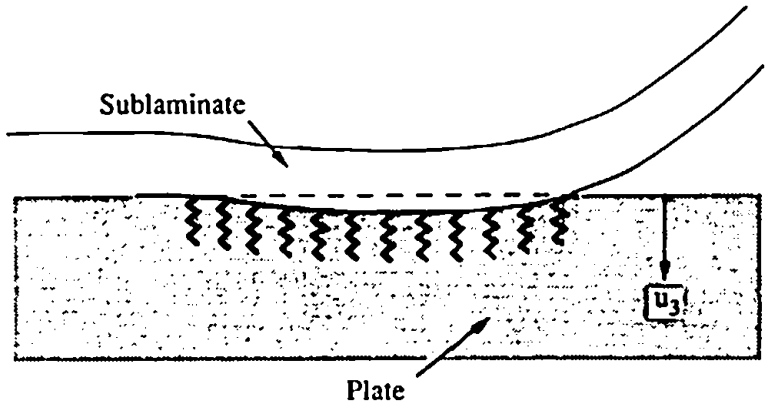

Figure 2.7: Model of the contact force between the sublaminate and the plate after Peck & Springer (1991).

At the beginning of the 1990s, Peck & Springer (1991) published their analytical results, again employing a Rayleigh–Ritz procedure and experimental investigations of the plate model containing an embedded, elliptical delamination subject to in-plane, shear and thermal loads. The authors specifically built upon the work of the two plate models previously described, their geometry and assumptions, and extended them by incorporating transverse shear deformations, postbuckling deformations, contact effects, thermal loads and unsymmetrical sublaminates. Furthermore with their experimental investigations, they obtained extensive data in particular by measuring the entire load–strain history of the sublaminate far into the postbuckling regime. With the Rayleigh–Ritz formulations, allowing for higher order shear deformations and the contact problem described essentially as a plate on an elastic foundation, critical loads and loads at which growth initiated were derived through minimization of the total potential energy. A fracture energy approach

was employed for the investigations on the delamination propagation. In the experiments, thin teflon discs were inserted between selected plies before curing in the autoclave to simulate the delaminations. Their analytical and measured results generally agreed reasonably for the buckling loads, whereas for growth only fairly poor agreement was observed. They found that it was important to include the higher order polynomial terms when describing the in-plane behaviour of the sublaminates since their omission made the sublaminate too stiff. Furthermore, inclusion of the contact problem, Figure 2.7, was important because otherwise the analyses at times would predict physically unfeasible deflections. Also, residual thermal stresses affected the predicted buckling load depending on the degree of mismatch between the plate and laminate lay-up sequence.

2.3 Delamination geometries

As discussed in §1.1.3, delaminations can occur in different ways depending on the reason, *i.e.* open or closed delaminations. In this section, only closed, or embedded, delaminations are reviewed with regards to the model that is developed in Chapter 3. Embedded delaminations have been investigated in different geometric configurations; elliptical or circular in shape (Bottega & Maewal, 1983; Chai & Babcock, 1985; Shivakumar & Whitcomb, 1985; Whitcomb, 1989; Davidson, 1991; Peck & Springer, 1991; Kim & Kedward, 1999; Sekine *et al.*, 2000; Butler *et al.*, 2007), rectangular (Short *et al.*, 2001; Short *et al.*, 2002; Li *et al.*, 2005), through-the-width configurations (Kardomateas & Schmueser, 1988; Hunt *et al.*, 2004) and multiple delaminations (Kim & Kedward, 1999; Hwang & Liu, 2001; Hwang & Huang, 2005; Cappello & Tumino, 2006).

The buckling and growth of a pre-existing concentric circular delamination was the subject of investigation by Bottega & Maewal (1983) who developed a two-layer circular plate model with clamped edges subject to a uniform compressive force. Owing to the circumferential symmetry, the system was treated as a one-dimensional

problem. The delamination was assumed to be large enough for buckling, and subsequent propagation resulting from the displacement, to occur prior to overall buckling and the growth being governed by the aforementioned fracture mechanics approach. In their assessment, they described the response under force-controlled loading, in which case the delamination grew until the layers were completely separated. For a smaller delamination, and displacement controlled loading, it initially grew in an unstable fashion until it restabilized. For a larger delamination, both loading scenarios yielded stable growth. In addition, the influence of imperfections on the delamination growth was investigated, but it was concluded that they only have a minor effect on the behaviour.

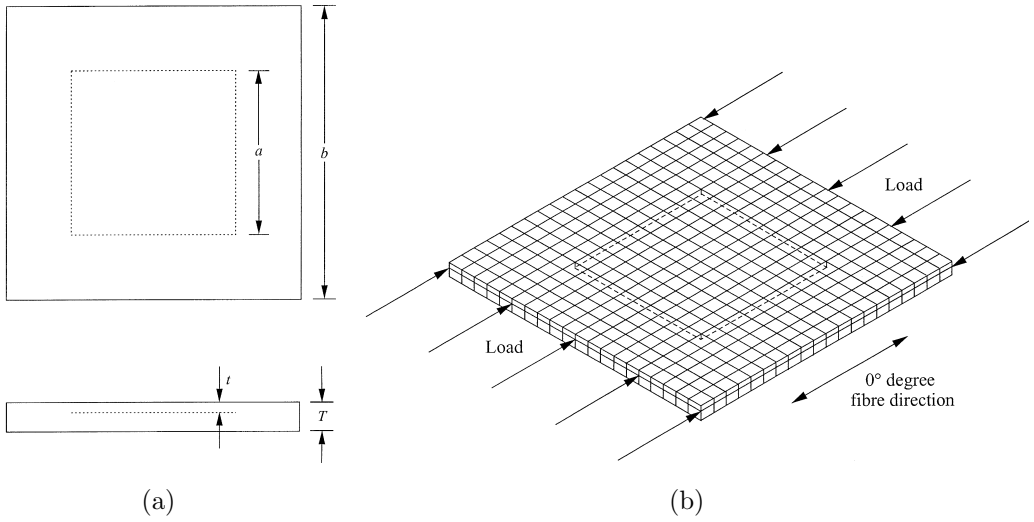

Figure 2.8: The delaminated plate model by Short *et al.* (2001). Geometry of the (a) isotropic models and (b) of the finite element model.

An embedded rectangular delamination was investigated by Short *et al.* (2001) with finite element models (Figure 2.8) and experiments on plates containing artificial delaminations implemented by inlaying teflon films during the lay-up. Parametric studies were undertaken to investigate the impact of size and through thickness position of the delamination. No growth occurred in the specimens they tested and failure was preceded by overall buckling of the panel. A local or global buckling mode depending on the geometry was observed. The former implying that only the sublaminate buckled, whereas in the second case both sublaminates buckled. With

this in mind, a buckling mode map was developed that predicted the buckling mode, whether it was local or global, for delaminated plates of different delamination size and through thickness location.

A through-the-width delamination was considered by Kardomateas & Schmueser (1988) in their one-dimensional plate model consisting of an upper and lower part and base plate, which was investigated using the perturbation technique. Three instability modes were observed; global, mixed and local, or thin-film, buckling. It was concluded that for short delaminations, global buckling dominated, whereas for larger lengths, local buckling of the delaminated layer occurred first. Furthermore, material parameters did not seem to affect the range of instability modes and the range of mixed mode buckling was smaller the closer the delamination was located to the surface. The model was additionally enhanced by including transverse shear effects which appeared to cause a reduction in the critical loads. Growth was incorporated via a fracture mechanics approach and the transverse shear effects seemed to increase the strain energy release rate. Also, if the fracture energy was relatively small, the delamination propagation under a constant applied force was typically a catastrophic process, *i.e.* the load corresponding to a constant fracture energy decreased with delamination propagation and hence unstable growth was observed. However, for larger values of the critical strain energy the load could be increased substantially beyond its critical value before the defect started to increase in size.

The final article reviewed in this section is by Hwang & Liu (2001) on the buckling of plates under uniaxial compression containing multiple delaminations. The nonlinear analysis was undertaken by employing the finite element method and contact elements were utilized to prevent the laminates from passing through each other. Different multiple delamination scenarios were considered, all containing four delaminations arranged evenly from the middle to the top interface; one delamination being longer than the others and was highlighted. In the first type, also referred to by the authors as "Type I", the longest delamination was above the shorter ones (Figure 2.9) whereas in the second case, "Type II", the position of the longest de-

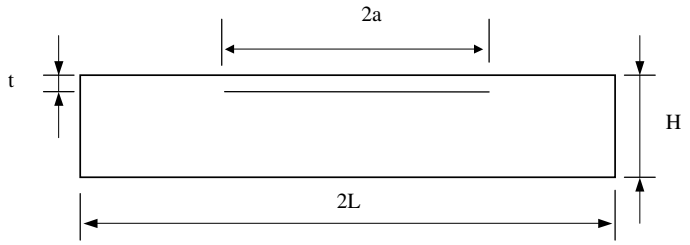

(a) Type IA delamination

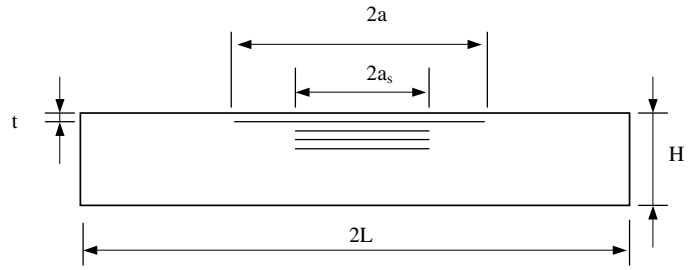

(b) Type IB delamination

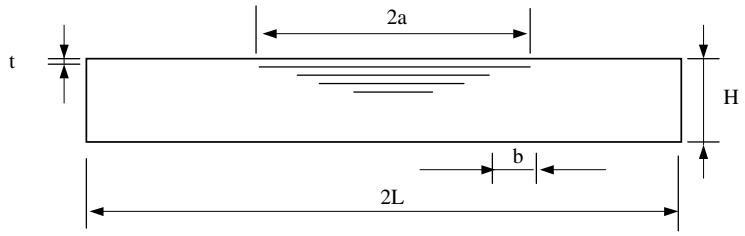

(c) Type IC delamination

Figure 2.9: Multiple delamination configuration investigated by Hwang & Liu (2001); Type I delaminations.

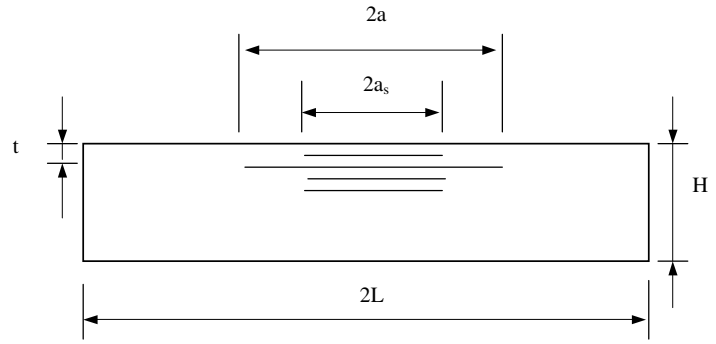

(a) Type IIA delamination

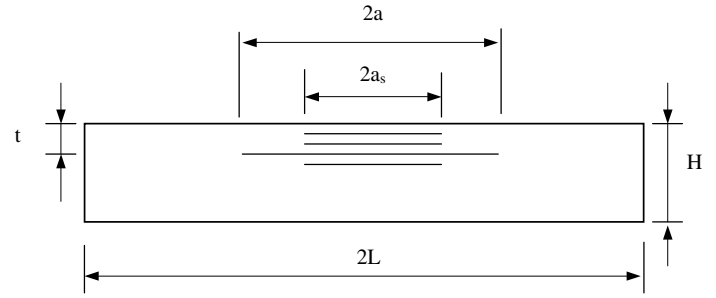

(b) Type IIB delamination

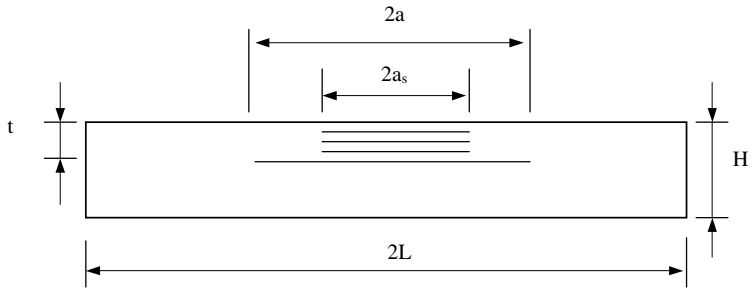

(c) Type IIC delamination

Figure 2.10: Multiple delamination configuration investigated by Hwang & Liu (2001); Type II delaminations.

lamination could be between or beneath the other delaminations (Figure 2.10). It was concluded that for the first configuration, Type I delaminations, the buckling behaviour was very much similar to a single delamination with the delaminations beneath imposing no significant effect on the buckling loads. For Type II delaminations, it was found that since the longer delamination was closer to the surface the effect of the shorter delamination reduced. This was not the case, however, when the long delamination was close to the midplane and the buckling behaviour changed from global to mixed to local buckling when increasing the length ratio between the laminates.

2.4 Loading scenarios

Different loading scenarios have been considered by various researchers ranging from cyclic loading or fatigue loads (Melin & Schön, 2001; Butler *et al.*, 2007) to static or quasi-static loading conditions (Chai *et al.*, 1981; Bottega & Maewal, 1983; Chai & Babcock, 1985; Simitses *et al.*, 1985; Whitcomb, 1989; Peck & Springer, 1991; Hunt *et al.*, 2004). The former is more relevant with respect to delamination propagation which will be discussed as part of the further work in §9.2. The latter scenario is relevant with regards to the development of the plate model in Chapter 3. The loading conditions found in the literature comprise transversely loaded plates (Whitcomb, 1989), plates under shear and thermal loads (Peck & Springer, 1991), and axial compression (Chai *et al.*, 1981; Bottega & Maewal, 1983; Chai & Babcock, 1985; Shivakumar & Whitcomb, 1985; Simitses *et al.*, 1985; Yin & Jane, 1992a; Sekine *et al.*, 2000; Hwang & Liu, 2001; Short *et al.*, 2001; Hunt *et al.*, 2004; Rhead *et al.*, 2008). Furthermore, Bottega & Maewal (1983) distinguished between force-controlled and displacement-controlled loading as discussed in the previous section.

The work reviewed in the current section is by Davidson (1991) who developed a single, elliptically shaped, delaminated plate model that was investigated under

uniaxial and biaxial compression by utilizing the Rayleigh–Ritz method with higher order polynomial functions. The results were compared to experiments and seven different cases were considered depending on the relative angle of orientation of the lay-up sequence of the sublaminate to the base plate. Again, teflon inlays were inserted during the manufacturing of the specimens to allow for the defects. The analysis was used to predict the onset of delamination buckling and for moderately sized delaminations the accuracy of the theory was deemed as "quite good". Both assessments showed that sublaminate buckling, when the overall buckling stress is higher than that of the delaminate, may lead to "subregion" buckling for large delaminations, with buckling only occurring over a certain region of the defect since the desired mode shapes were prevented from developing by contact constraints. For "moderately" sized delaminations, the assumed mode shape occurred, and the transition to the aforementioned phenomena was deemed to be influenced not only by the size of the delamination, but also by the material properties and the magnitude of global plate bending. Thus it was concluded, that what defines the size of the delamination, *i.e.* "large" or "moderately" sized, depends on the problem considered but their predictions were deemed as conservative by the authors. However, it was concluded, that a more refined analysis might be necessary in cases with large delaminations to capture the true behaviour, as the critical buckling stress was predicted to be "significantly below the design stress".

2.5 Modelling techniques and approaches

Modelling techniques are manifold when assessing the buckling and postbuckling behaviour of delaminated structures. Analytical methods have been successfully employed by various authors by minimization of the total potential energy; either utilizing the calculus of variations (Bottega & Maewal, 1983), a perturbation technique (Simitses *et al.*, 1985; Kardomateas & Schmueser, 1988; Kardomateas, 1993), a Rayleigh–Ritz procedure (Chai *et al.*, 1981; Chai & Babcock, 1985; Shivakumar &

Whitcomb, 1985; Davidson, 1991; Peck & Springer, 1991; Yin & Jane, 1992a; Kim & Kedward, 1999; Hunt *et al.*, 2004) or a Newton–Raphson procedure (Whitcomb, 1989). Some of these authors solved the resulting equations from the Rayleigh–Ritz procedure with the aid of computer software, *e.g.* bespoke routines in FORTRAN (Nyhoff & Leestma, 1997), or their own developed or commercial finite element codes (Shivakumar & Whitcomb, 1985; Whitcomb, 1989; Nilsson *et al.*, 1993; Sekine *et al.*, 2000; Hwang & Liu, 2001; Short *et al.*, 2001; Short *et al.*, 2002; Hwang & Huang, 2005; Cappello & Tumino, 2006; Wimmer & Pettermann, 2008; Craven *et al.*, 2010). These results were obtained to validate the analytically obtained results (Hunt *et al.*, 2004) or to compare against experimental data. Experimental investigations into the buckling behaviour had been conducted by Peck & Schmueser (1991), Yin & Jane (1992b), Nilsson *et al.* (1993), Short *et al.* (2001; 2002), Melin *et al.* (2002) and others.

The first paper reviewed in this section is by Whitcomb (1989) who developed the geometrically nonlinear three-dimensional finite element program NONLIN3D based on minimum energy principles employing a Newton–Raphson procedure. Substructuring into linear and nonlinear regions was facilitated to reduce the amount of iterations required for the solution procedure. The linear parts were also referred to as the "superelement" with a reduced stiffness matrix. Once this part was developed, the nonlinear substructure could be obtained which was relevant only in the postbuckled regions. The virtual crack closure technique was employed for the delamination propagation analysis, where by finding the displacements at certain nodes, the relative displacement could be obtained[1]. The laminates were described via homogeneous quasi-isotropic material properties to correlate with the objective of the investigations "to consider only the effect of geometric parameters" for the strain energy release rates. Results from a previously developed nonlinear closed form analytical solution and their finite element code for a transversely loaded plate were discussed and compared for a small, thin circular defect. The closed form was stated to be exact for linear deflections yet "approximate for large deflections of

[1]Different approaches of delamination growth modelling will be discussed in Chapter 6.

plates according to Kirchhoff–Love plate theory". A discrepancy in the highest load level was indicated only, which was established for results from the aforementioned inaccuracy of the closed form solution in this range. Systematic convergency studies were performed, subdividing the coarse two-dimensional mesh into a refined mesh and with the values of the strain energy release rates used as a measurement for adequacy. In all cases, the fracture Mode III was negligible and even a crude model appeared sufficient for the other modes[2]. It was concluded that the fracture problem was a mixed-mode problem that if only Mode I was considered perpendicular growth to the loading direction would be expected. On the other hand, if only Mode II was considered, the delamination would grow parallel to the load. In addition, it was noted that parts of the delamination would overlap and contact elements would be required to account for this effect.

Kim & Kedward (1999) developed an analytical model based on the Rayleigh–Ritz method employing polynomial functions describing the out-of-plane displacement behaviour of the sublaminates whilst trigonometric functions were used for the overall plate. In-plane deformations were assumed to behave linearly prior to buckling. The method was used to formulate the eigenvalue problem to predict the initial critical loads and eigenvectors via matrix manipulation; postbuckling and delamination growth being beyond the scope of the article. Global and local buckling analysis was performed, with an assumed stiffness reduction for the delaminated zone in the former and the presupposition that only the near-surface laminate would deform in the local mode. Initially, a discretization study was undertaken with up to nine terms in the Fourier series of the displacement to investigate the convergency rate of the formulations with respect to the shape of the delamination (Figure 2.11a). The results were compared to those obtained via finite element solutions and it was concluded that a single rectangular representation of the circular delamination can be deemed as appropriate for the global analysis, so far as the delamination areas matched (Figure 2.11b). In the local analysis, this type of representation did not appear to be a good choice, therefore local buckling analysis was performed separately

[2]Please refer to Figure 6.2 in §6.2 for fracture mode types and further discussion on that topic.

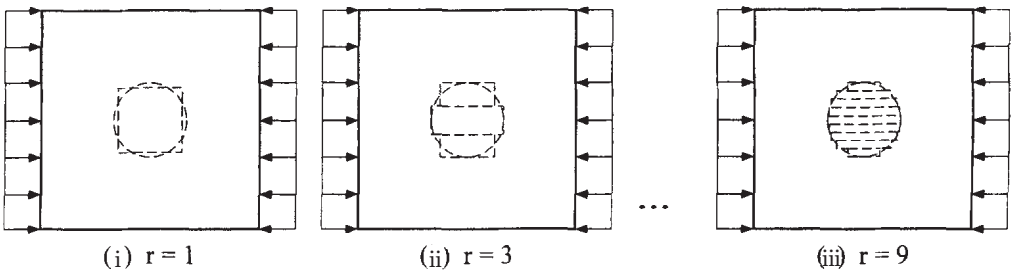

(a)

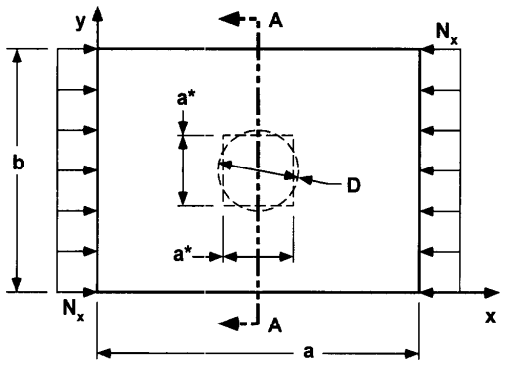

(b)

Figure 2.11: The delaminated plate model by Kim & Kedward (1999); (a) Discretization study (with 'r' indicating the number of rectangles used to discretize) and (b) case study problem.

using a circular plate, and all results were compared to the finite element model. Different aspect ratios of plates and delaminations were investigated, demonstrating that the method is applicable to non-square plates. Furthermore, the effect of the location of the delamination with respect to the plate thickness was studied and the mode behaviour, *i.e.* local, mixed or global, was captured.

The final paper reviewed within this section is the work by Nilsson *et al.* (1993) who presented numerical and experimental investigations into the buckling and growth behaviour of initially circular, embedded delaminations under uniaxial compression. The contact behaviour resulting from the local buckling of the sublaminate was evaluated using a predictor–corrector numerical scheme that was formulated as an optimization problem, which assessed nodes of interpenetration and subsequently imposing constraints. Once the applied load was sufficiently high, delamination

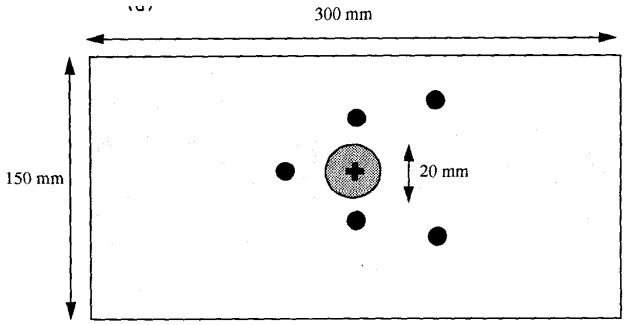

(a)

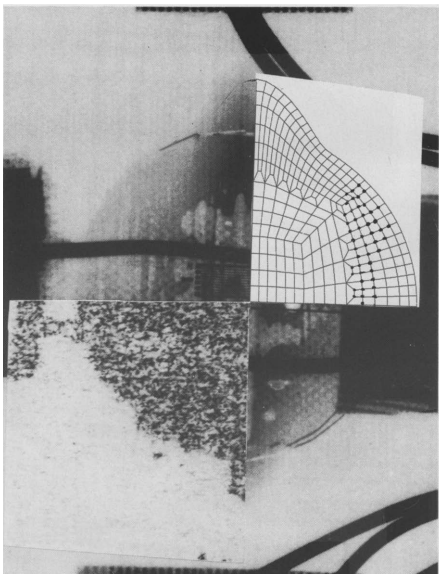

(b)

Figure 2.12: The delaminated plate model by Nilsson *et al.* (1993). (a) Specimen geometry for plates and strain gauge layout (solid circles) used in the experiments and (b) the resulting X-ray radiograph together with ultrasonic C-scan photo (lower left) and the corresponding finite element mesh with nodes in contact shown.

growth would occur under the assumption that the delamination front was smooth at all times. A fracture energy approach was utilized, computing the growth parameters discretely along the delamination front until the governing criteria was reached and an algorithm was employed to incorporate this method into the numerical investigations with an automatic mesh generator. Experimental studies were undertaken on large cross-ply specimens where 0.025 mm thick, circular teflon films were placed, periodically spaced, under one sublaminate to simulate the embedded debond. The panel was then sectioned into discrete specimens such that the "defect was centrally located in the panel of each specimen" (Figure 2.12a). An anti-buckling frame, which essentially preserved the global stability of the plates, was placed leaving a square area exposed. Six strain gauges and transducers were used to measure the strain field within the frame and additionally, acoustic emissions were measured via another transducer to capture the initiation of each increment in delamination evolution. With the aid of ultrasonic C-scans, where a short pulse of ultrasonic energy is imposed on a sample with the measurement of the transmitted pulse indicating the sample's attenuation of the incident pulse, and X-rays, the size and shape of the internally growing delamination was measured with high precision (Figure 2.12b). Three different plates were tested with several load cases, initially up to the first buckling case and then subsequent loadings for the growth cases. In a microscopic examination it was observed that a small initial imperfection was introduced by the teflon films used for the simulation of the defect. It was concluded that the theoretical and numerical method simulated the growth determined experimentally very well and the authors were confident in their approach to simulate interface cracks.

2.6 Summary of known results

A review of various pertinent groundbreaking and seminal publications has been presented. A summary of the essential findings with respect to the buckling loads and modes from the review is presented in the bullet points below.

- The critical buckling loads decrease with the increasing size of the delamination (Simitses *et al.*, 1985; Kim & Kedward, 1999).

- The critical loads change with the depth of the delamination (Kim & Kedward, 1999; Hunt *et al.*, 2004).

- Different buckling modes, *i.e.* closing or opening, can be identified depending on the parametric configuration (Kim & Kedward, 1999; Short *et al.*, 2001; Hunt *et al.*, 2004).

- Different modal magnitudes, *i.e.* giving local, mixed or global responses, are observed depending on the parametric configuration (Simitses *et al.*, 1985; Kim & Kedward, 1999; Hunt *et al.*, 2004).

- Material parameters do not seem to affect the range of instability modes and the likelihood of mixed mode buckling occurring is smaller the closer the delamination is located to the surface (Kardomateas & Schmueser, 1988).

- Non-physical buckling modes may result from the analysis (Whitcomb, 1989; Davidson, 1991; Peck & Springer, 1991; Hunt *et al.*, 2004) and the introduction of constraint criteria may be necessary to capture the true behaviour.

- Thin-film buckling is observed as stable buckling (plate-like) and mixed mode buckling is observed as unstable buckling (shell-like) for the strut model investigated by Hunt *et al.* (2004).

- After initial buckling, the laminates may reverse direction (Hunt *et al.*, 2004).

- Buckling under tension may occur in the sublaminate due to the mismatch of Possion's ratio (Shivakumar & Whitcomb, 1985).

- For multiple delaminations, see Figure 2.9, where the longest delamination is closer to the surface than the shorter delamination, the buckling behaviour is similar to a single delamination with the delaminations beneath imposing no significant effect on the buckling loads (Hwang & Liu, 2001).

- For multiple delaminations, see Figure 2.10, where the long delamination is located towards the midplane and shorter delaminations are present above the longer one, the buckling behaviour becomes increasingly influenced by the presence of the shorter delaminations. The buckling behaviour subsequently changes from global to mixed to local buckling when increasing the length ratio between the laminates (Hwang & Liu, 2001).

Finally, for investigations into the propagation behaviour of the delaminations, the following summary points are as follows.

- Thin-film buckling is understood to lead to delamination growth (Chai *et al.*, 1981; Simitses *et al.*, 1985; Kim & Kedward, 1999; Hunt *et al.*, 2004).
- For isotropic plates, it was found that for very deep or small delaminations, *i.e.* the radius of the delamination being approximately the same or less than the depth of the delamination, propagation followed immediately after buckling (Chai & Babcock, 1985).
- The growth direction is predominantly in the direction normal to the load (Chai & Babcock, 1985).
- Force-controlled, or so-called dead, loading may lead to catastrophic debonding of the laminates (Bottega & Maewal, 1983).
- In displacement controlled, or rigid, loading the system may restabilize after an initially unstable growth behaviour; however, for a larger delamination, both loading scenarios may yield stable growth. (Bottega & Maewal, 1983).
- The influence of imperfections on the delamination growth is only of minor significance (Bottega & Maewal, 1983).
- For orthotropic cases: placing the fibres in the direction of the load decreases the buckling strength and growth initiation load; growth is parallel to the loading axis except for large delaminations. For fibres aligned perpendicular

to the loading direction an increase in both buckling load and growth initiation load is observed and propagation occurs normal to loading direction, *i.e.* in the fibre direction, and for most cases a circular delamination does not buckle or grow (Chai & Babcock, 1985).

- Residual thermal stresses affect the predicted buckling load depending on the degree of mismatch between the plate and layup sequence of the delaminated region (Peck & Springer, 1991).

- If the magnitude of the fracture energy, defined as the energy required to produce a new unit of delamination, is relatively small, the delamination propagation under a constant applied force is typically a catastrophic process; a decreasing load corresponds to a constant fracture energy during the growth process, *i.e.* unstable growth occurs (Kardomateas & Schmueser, 1988).

- The fracture Mode III is in all cases almost negligible (Whitcomb, 1989; Nilsson *et al.*, 1993)

- Even a crudely discretized formulation appears sufficient for the growth criteria to be modelled accurately (Whitcomb, 1989).

- In the early stages of local buckling, when overall buckling of the panel does not dominate the behaviour, a pure fracture Mode I dominates the growth behaviour (Chai & Babcock, 1985; Melin & Schön, 2001).

- The fracture problem is a mixed-mode problem in that if only Mode I was considered, growth perpendicular to the loading direction would be expected. On the other hand, if only Mode II was considered, the delamination would grow parallel to the load (Whitcomb, 1989).

Chapter 3

The delaminated panel model

3.1 Introduction

As extensively discussed in the previous chapter many researchers have investigated and are currently working on the topic of delamination modelling through various different methodologies and approaches, incorporating various configurations and conditions. Since many applications in structures, particularly in aircraft structures, contain thin rectangular plated panels which are subjected to in-plane stresses (Bisagni & Walters, 2008) a model for a composite plate is developed herein.

The chapter opens by introducing the elements of the analytical delaminated plate model and concerns itself primarily with the plate geometry, stating the assumptions and simplifications applied to the structure; these affect the choice of displacement functions w_i that are subsequently used to obtain expressions for the Airy stress functions φ_i needed to develop the total potential energy. Thereafter the governing expressions for a uniaxially compressed plate are formulated in conjunction with the Rayleigh–Ritz method to obtain the total potential energy of the system which comprises strain energy in bending, membrane or stretching energy and the work done by the compressive loads. The total potential energy is subsequently used to find

the buckling and postbuckling solutions in Chapters 4–8 using the procedure outlined in §1.2.2. Finally, the finite element model used for validation and comparison purposes is described.

3.2 Structural geometry

The geometrically nonlinear analytical delaminated plate model is developed in the style of the two-layer strut model presented by Hunt *et al.* (2004) and Wright (2006a; 2006b) which had some features reminiscent of the strut models derived by Chai & Babcock (1981), Simitses *et al.* (1985) and Kardomateas & Schmueser (1988). By extending the one-dimensional model, a rectangular plate is developed that is reminiscent of the plate models shown by previous authors, that include: Bottega (1983), Chai & Babcock (1985), Shivakumar & Whitcomb (1985), Peck & Springer (1991). However, instead of incorporating an embedded elliptical or circular delamination, a rectangular delaminated patch is introduced (Short *et al.*, 2001; Short *et al.*, 2002; Li *et al.*, 2005), as illustrated in Figure 3.1a. The overall dimensions of the plate are L and B in the x- and y-directions respectively and the plate has a uniform thickness t. The pre-existing defect of dimensions a and b is centrally located to capture the case with the most severe stress concentrations (Simitses *et al.*, 1985; Nilsson *et al.*, 1993; Short *et al.*, 2002) and is surrounded by the intact parts of the plate. The delaminated patch contains two distinct laminates, referred to as upper and lower (Kardomateas & Schmueser, 1988; Sekine *et al.*, 2000) or top and bottom laminate (Short *et al.*, 2001), which are also modelled as plates. The depth of the delamination is described with the ratio c, as depicted in Figure 3.1b; laminate thicknesses are therefore ct for the upper laminate and $(1-c)t$ for the lower laminate. The panel is under quasi-static uniaxial uniformly distributed in-plane compression P (Rhead *et al.*, 2008).

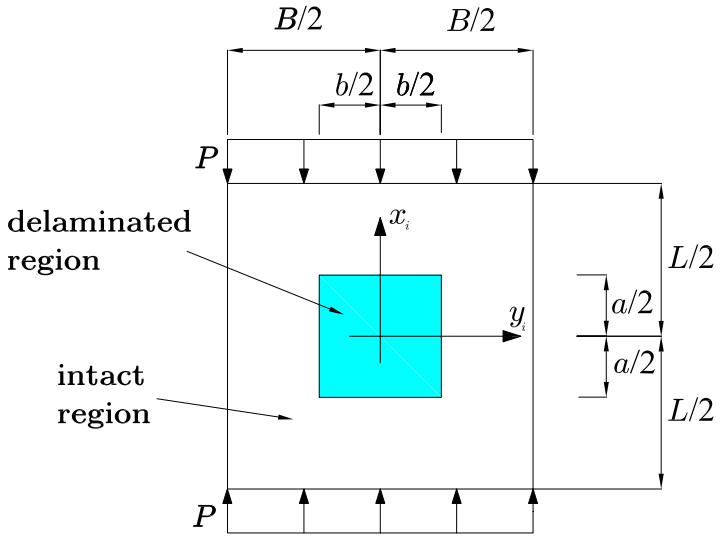

(a) Panel plan view

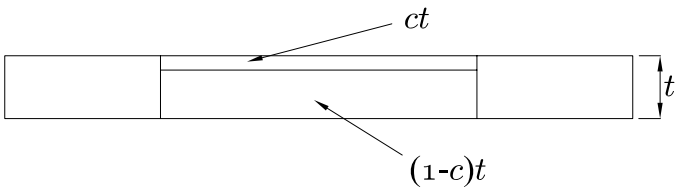

(b) Panel cross-section

Figure 3.1: Geometry of the delaminated panel model.

3.3 Assumptions and simplifications

The plate and sublaminates are assumed to be homogeneous and isotropic throughout the whole specimen and no stacking sequence effects or variations on material properties are taken into account for the sake of simplicity (Bottega & Maewal, 1983; Shivakumar & Whitcomb, 1985; Whitcomb, 1989; Yin & Jane, 1992a). The intact parts and the delaminated patch are assumed to behave linearly elastically (Chai *et al.*, 1981; Simitses *et al.*, 1985; Peck & Springer, 1991; Kardomateas, 1993) which is true if the plate is assumed to be sufficiently thin relative to its span (Bažant & Cedolin, 1991). This, in addition, means that buckling occurs, rather than compressive failure and that through-thickness shear deformation may be neglected. In accordance with Peck & Springer (1991) the delamination is assumed to occur be-

tween two adjacent plies and perfect bonding exists between the adjacent layers. Furthermore the deformation of the sublaminate does not influence the strains and stresses of the intact panel. However, as will be seen in §3.4.2, the influence of the intact panel on the delaminated patch is taken into account. In addition, transverse normal stresses are assumed to be zero in all parts of the plate, *i.e.* plane stress, which results in the requirement for an alternative approach when incorporating delamination growth, as will be discussed in Chapter 6. The intact plate is modelled as simply supported on all four edges (Short *et al.*, 2001) and is restrained from in-plane movement along the edges $y = \pm B/2$, *i.e.* no pull-in is allowed along those edges. However, the panel can move freely in the x-direction with the edges $x = \pm L/2$ remaining straight in-plane after deformation (Timoshenko & Woinowsky-Krieger, 1959). The edges of the delaminated patch are assumed to be clamped locally due to the constraint of the intact panel (Nilsson *et al.*, 1993; Hunt *et al.*, 2004; Wright, 2006b) with edge rotations occurring only from the overall panel. Two modelling constraints therefore apply at the intersection between the intact and delaminated layers:

1. The rotations and displacements of the intact and delaminated parts must be the same.

2. No relative shearing movement must occur between the laminates at the interface.

In the strut model presented by Hunt *et al.* (2004), these restrictions are enforced by introducing a single degree of freedom (DOF) at the interface and introducing a further DOF to link the amount of axial stretching. However, applying this approach in the current model is much more difficult due to the extra dimension of the current system. Instead, the transverse displacement functions in §3.4.1 are chosen such that they comply with the constraints above; the displacement (Peck & Springer, 1991) and the slope at the interface are therefore equal (Shivakumar & Whitcomb, 1985; Simitses *et al.*, 1985; Nilsson *et al.*, 1993).

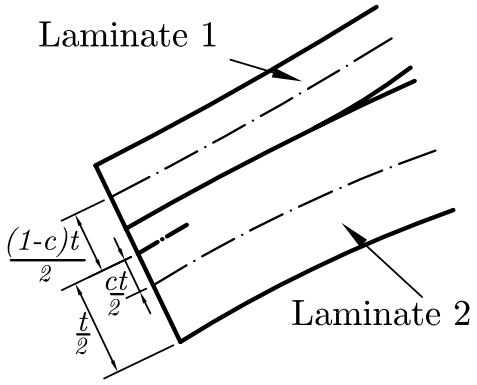

Figure 3.2: The geometry at the ends of the delaminated region.

3.4 Geometrically nonlinear Rayleigh–Ritz formulation

Since plates possess a postcritical reserve capacity, meaning that they are capable of resisting loads higher than the critical loads, nonlinear theory has to be applied to exploit their full potential. In this work, nonlinear theory for moderately large deflections is incorporated, where linearized expressions for the curvature are still valid (Bažant & Cedolin, 1991), *e.g.* see equations (3.20) and (A.1), since rotations tend to be small, *c.f.* Wadee (1998) pages 56–57. However, the redistribution of the in-plane forces due to the deflections are taken into account using Airy's stress function, which are developed in §3.4.2. The two governing equations after Föppl and von Kármán (Timoshenko & Woinowsky-Krieger, 1959; Bažant & Cedolin, 1991) are the compatibility equation:

$$\nabla^4\varphi = E\left[\left(\frac{\partial^2 w}{\partial x\partial y}\right)^2 - \frac{\partial^2 w}{\partial x^2}\frac{\partial^2 w}{\partial y^2}\right], \tag{3.1}$$

and the equilibrium equation:

$$\nabla^4 w = \frac{t}{D}\left(\frac{q}{t} + \frac{\partial^2\varphi}{\partial y^2}\frac{\partial^2 w}{\partial x^2} + \frac{\partial^2\varphi}{\partial x^2}\frac{\partial^2 w}{\partial y^2} - 2\frac{\partial^2\varphi}{\partial x\partial y}\frac{\partial^2 w}{\partial x\partial y}\right), \tag{3.2}$$

where the biharmonic operator ∇^4 is defined as

$$\nabla^4 = \frac{\partial^4}{\partial x^4} + 2\frac{\partial^4}{\partial x^2\partial y^2} + \frac{\partial^4}{\partial y^4}. \tag{3.3}$$

Equations (3.1) and (3.2) form a system of two coupled nonlinear fourth order partial differential equations, where w is the out-of-plane deflection, φ is the Airy stress function, q is the transverse load, D is the plate flexural rigidity and t is the plate thickness. Those equations are rather complicated to solve analytically, however, approximate solutions are discussed in the literature, *e.g.* Timoshenko & Woinowsky-Krieger (1959). The equations above form the basis for deriving w and φ.

3.4.1 Out-of-plane displacement functions

In the present section, the selection of the kinematically admissible transverse displacement functions is described. These are required to satisfy the geometric boundary conditions of the problem, namely the simply supported or clamped edge constraints for the intact or delaminated parts respectively, whereas satisfaction of the static boundary conditions is not essential when utilizing a Rayleigh–Ritz procedure (Thompson & Hunt, 1973). The governing equation for a plate in bending under transverse and in-plane loading dates back to St Venant in 1883 (Timoshenko & Woinowsky-Krieger, 1959; Timoshenko & Gere, 1961; Szilard, 1974; Williams & Aalami, 1979). Reducing the governing differential equation (3.2) according to the assumptions in §3.3, by eliminating q, the transverse load, as well as $\partial^2\varphi/\partial x^2$ and $\partial^2\varphi/(\partial y\partial x)$, the in-plane stress in the y-direction and shear stress respectively, and substituting P for $t\partial^2\varphi/\partial y^2$, the uniformly distributed compression force[1], the following equation is obtained:

$$\nabla^4 w = \frac{P}{D}\Big(\frac{\partial^2 w}{\partial x^2}\Big)\,. \tag{3.4}$$

The classical methods available for solving equation (3.4) include: (a) Navier's method, applicable only to simply supported rectangular plates which reduces the equation to the solution of algebraic equations by employing double Fourier series for both deflection and loading or (b) Levy–Nádai's technique (Timoshenko &

[1]The effects of the out-of-plane deflection on the stresses in the panel are incorporated utilizing the stress functions derived in §3.4.2.

Woinowsky-Krieger, 1959). The latter technique only requires two opposite edges to be simply supported while the remaining two edges admit arbitrary boundary conditions. Solutions are obtained by means of single trigonometric series and superimposing the particular and homogeneous solution of equation (3.4). However, the desire is to employ a conventional Rayleigh–Ritz procedure, as outlined in §1.2.2, which has been successfully employed in previous investigations on the behaviour of delaminated structures (Chapter 2), and the aim is to keep the model simple and straightforward. The Fourier series is therefore truncated later when describing the displacements. However, it is understood that this subsequently leads to an approximation of the actual behaviour, since it restricts the behaviour of the plate to either positive or negative single sine waves, particularly if only one DOF is chosen for the displacement. Various authors have employed polynomial functions to describe the out-of-plane behaviour of the panels due to buckling (Chai & Babcock, 1985; Shivakumar & Whitcomb, 1985; Peck & Springer, 1991; Yin & Jane, 1992a; Kim & Kedward, 1999). However these functions usually require more terms in the series and subsequently more DOFs to describe the deflection accurately. Hence, trigonometric displacement functions are utilized currently and a sinusoidal clamped-end mode (Figure 3.3a) is employed to describe the buckling displacement of each of the delaminated plates; this introduces DOFs accounting for the amplitude of the upper and lower lamina, Q_{1,m_in_i} and Q_{2,m_in_i}, respectively. Moreover, the second term is added to comply with the overall buckling mode and the requirement to obtain matching slopes at the interface between the delaminated area and the intact panel as discussed above, *i.e.* the local displacement is superimposed on the overall displacement. With x_i and y_i being measured along the centre-line of each laminate i, the lateral displacement of each of the laminates (Figure 3.3), may be expressed as follows:

$$\begin{aligned} w_i &= \sum_{m_i}\sum_{n_i} Q_{i,m_in_i} \cos^2\frac{m_i\pi x_i}{a} \cos^2\frac{n_i\pi y_i}{b} \\ &\quad + \sum_{m_3}\sum_{n_3} Q_{3,m_3n_3} \cos\frac{m_3\pi x_3}{L} \cos\frac{n_3\pi y_3}{B} \end{aligned} \tag{3.5}$$

where $i = 1$ or 2 for the top or bottom laminate respectively. The summation notation indicates that further terms in the series can be used. However, in §4.3.1 it will be shown that employing the first term in each series is sufficient when modelling the buckling behaviour (Shivakumar & Whitcomb, 1985). This minimizes the number of DOFs within the model.

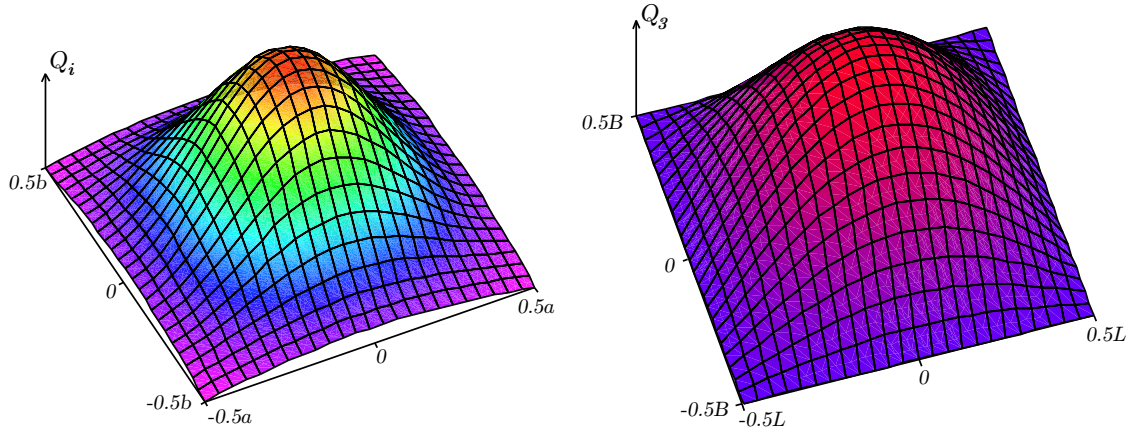

(a) (b)

Figure 3.3: Out-of-plane displacement functions; (a) delaminated patch, w_i, and (b) intact panel w_3.

Since the plate edges of the intact panel are pinned, the lateral displacement of this part, w_3, shown in Figure 3.3b, can be expressed with the commonly used double Fourier series (Timoshenko & Woinowsky-Krieger, 1959):

$$w_3 = \sum_{m_3} \sum_{n_3} Q_{3,m_3 n_3} \cos \frac{m_3 \pi x_3}{L} \cos \frac{n_3 \pi y_3}{B}, \tag{3.6}$$

where the DOFs describing the amplitude of the overall mode, $Q_{3,m_3 n_3}$ are defined with x_3 and x_3 originating from the centre of the panel. This shape function satisfies both static and kinematic boundary conditions for the simple supports on the four edges of the panel.

As mentioned above, the condition of equal slopes at the intersection between the delaminated and intact parts has to be satisfied. With the above displacement

functions this is achieved, since:

$$\left.\frac{\partial w_i}{\partial x_i}\right|_{x_i=\pm a/2} = \left.\frac{\partial w_3}{\partial x_3}\right|_{x_i=\pm a/2} \tag{3.7}$$

and

$$\left.\frac{\partial w_i}{\partial y_i}\right|_{y_i=\pm b/2} = \left.\frac{\partial w_3}{\partial y_3}\right|_{y_i=\pm b/2}. \tag{3.8}$$

3.4.2 Stress functions

It is understood that the middle surface of a plate undergoes stretching when the plate is bent into a nondevelopable surface, (Timoshenko & Woinowsky-Krieger, 1959). Hence, assuming a state of bending without membrane action is not accurate beyond critical buckling, because significant membrane strains are developed in the middle surface which influence the subsequent postbuckling stiffness and therefore cannot be neglected (Yin & Jane, 1992a). To account for these effects, Airy stress functions φ_i (Timoshenko & Woinowsky-Krieger, 1959; Everall & Hunt, 1999) for the delaminated and intact parts have been derived. This has been achieved by substituting the expressions for w_i into the von Kármán compatibility equation (3.1) and integrating directly to obtain φ_i. The coefficient comprising the Young's modulus E acting on the right-hand side expression of equation (3.1) has been deliberately dropped when deriving the stress functions, such that the procedure is in accordance with Everall (1999). However, it is included later for each laminate when the stresses, equation (3.10)–(3.12), are substituted into the strain energy—the detailed derivation being described in §3.5.2.

Moreover, this approach is employed since it prevents further freedoms from being introduced into the model when describing the in-plane stretching behaviour of the plates. The stress function for the undelaminated plate with simple supports can be subsequently expressed as follows:

$$\varphi_3 = \frac{1}{2}\frac{Q_4}{L}y_3^2 - \frac{Q_3^2}{32L^2B^2}\left(L^4\cos\frac{2\pi x_3}{L} + B^4\cos\frac{2\pi y_3}{B}\right), \tag{3.9}$$

where the first term in the expression is added to allow for uniform compression before buckling occurs, whereby Q_4 is introduced as the generalized coordinate for overall end-shortening, see Figure 3.4a. With the usual definition of the stresses being related to the second partial derivative of φ_i (Timoshenko & Woinowsky-Krieger, 1959):

$$\sigma_{x_i} = E_i \frac{\partial^2 \varphi_i}{\partial y_i^2}, \tag{3.10}$$

$$\sigma_{y_i} = E_i \frac{\partial^2 \varphi_i}{\partial x_i^2}, \tag{3.11}$$

$$\tau_{x_i y_i} = G_i \frac{\partial^2 \varphi_i}{\partial x_i \partial y_i}, \tag{3.12}$$

the derived stress functions can be verified, see Figures 3.4b and 3.5 for σ_{y_3} and σ_{y_i} for the intact or delaminated parts respectively[2]. The stress functions show tension in the centre of the panel and compression on the edges as expected from the qualitative postbuckling behaviour of plates and are hence adopted.

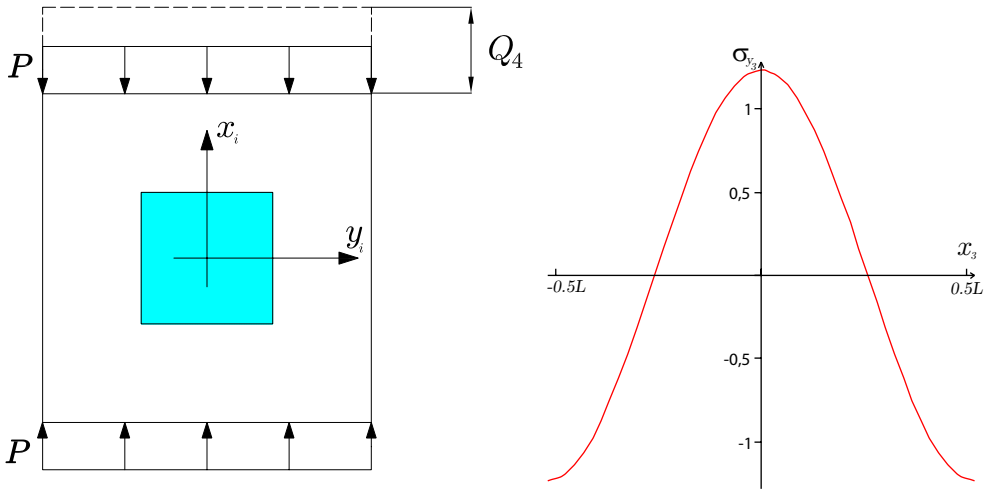

(a) (b)

Figure 3.4: (a) Pure compressive degree of freedom Q_4. (b) Transverse stress σ_{y_3} from global buckling in the whole panel over the length of the intact panel.

However, for the delaminated part of the plate the process of solving the fourth order partial differential equation (3.1) for the stress function is cumbersome owing to the

[2]The stress functions are symmetric, hence only components of σ_{y_i} are shown for illustrative purposes.

nature of the out-of-plane displacement function given in equation (3.5). Hence, an approximation is introduced, which is derived as follows. Initially, the right hand side of equation (3.1) is evaluated with the known expressions for the displacement functions, equation (3.5), using the local term only, *i.e.* the first term with Q_1 or Q_2. Then the evaluated parts are split into three, each part belonging to the corresponding terms on the left hand side of the compatibility equation (3.1). Those parts associated with x_i are integrated four times with respect to x_i, those associated with y_i are integrated four times with respect to y_i and the mixed term twice with respect to x_i and then twice with respect to y_i. With this procedure, the effects of the local out-of-plane deflection on the stress function for the delaminated parts are derived. However, the expressions are lengthy and are subsequently reduced to a more compact form resulting in those terms that can be seen as the parts associated with Q_i^2 in equations (3.16) and (3.17). These shortened expressions are verified by applying the conditions for straight-edged, clamped plates as given by Everall (1999), where the first condition is given by symmetry:

$$\frac{\partial^2 \varphi_i}{\partial x_i^2}\Big|_{x_i=a/2} - \frac{\partial^2 \varphi_i}{\partial x_i^2}\Big|_{x_i=-a/2} = 0, \tag{3.13}$$

the second condition is that the buckling pattern for two plates placed end-to-end is antisymmetric and hence the corresponding stress distribution must be symmetric:

$$\frac{\partial \sigma_{y_i}}{\partial x_i} = 0 \Rightarrow \frac{\partial^3 \varphi_i}{\partial x_i^3} = 0 \quad \text{at} \quad x_i = \pm a/2, \tag{3.14}$$

finally, the third condition is that φ accounts for the change from the uniformly applied load, thus:

$$\int_{-b/2}^{b/2} \sigma_{x_i} \mathrm{d}y_i = \int_{-b/2}^{b/2} E_i \frac{\partial^2 \varphi_i}{\partial y_i^2} \mathrm{d}y_i = 0 \quad \text{at} \quad x_i = \pm a/2. \tag{3.15}$$

Moreover, mixed terms $Q_i Q_3$, containing the local and global out-of-plane generalized coordinates—Q_1 and Q_2 being local and Q_3 being global—are added in equations (3.16) and (3.17) to allow for mixed mode effects resulting from the simultaneous buckling of the delaminated patch and the overall panel. These terms are derived using a procedure developed by Little (1987) taking into consideration the different boundary conditions of the clamped edges of the delaminated patch and

simply-supported edges of the overall panel. The method is applied twice, once for clamped edges in the x_i direction with length a and simply-supported edges in the y_i direction with length B and vice versa. The resulting expressions are added together and then halved such that the effects are not included twice; a more detailed description on this derivation can be found in Appendix A. The last term in equations (3.16) and (3.17) are added to allow for the effects of the overall plate buckling on the local patch and hence the expression for φ_3 in equation (3.9) is superimposed.

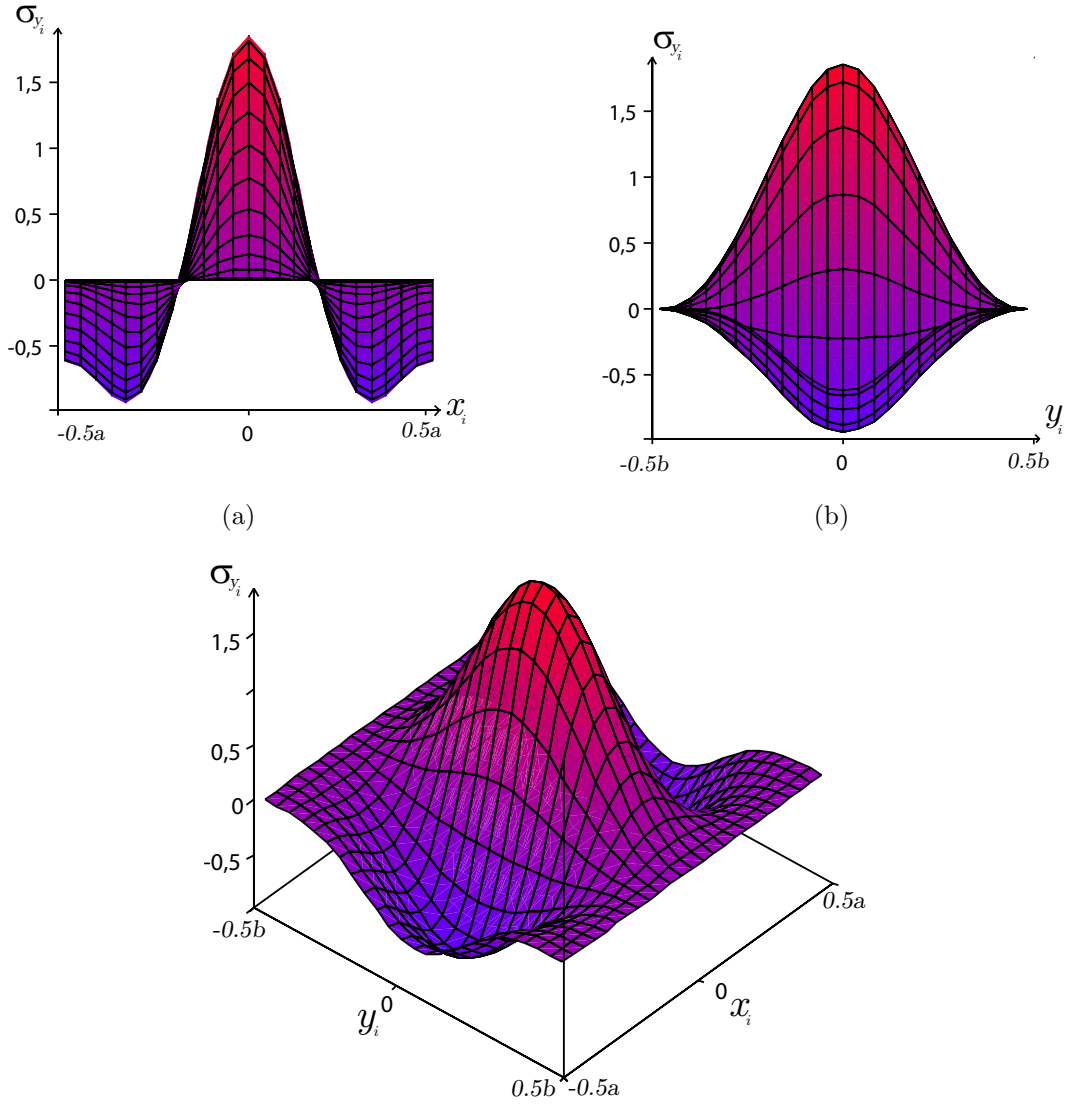

Figure 3.5: Stress σ_{y_i} from local buckling over the length of the delaminated patch; (a) along the x_i-axis, (b) along the y_i-axis and (c) 3-dimensional view.

The expressions for the stress functions for the delaminated patch can be derived:

$$\begin{aligned}\varphi_1 = {} & \frac{1}{2}\frac{Q_4}{L}y_1^2 + \frac{B^2}{a\pi^2}\left[(1-c)t - 2\psi\right]\left.\frac{\partial w_1}{\partial x_1}\right|_{x_1=-a/2} + \frac{L^2}{b\pi^2}\left[(1-c)t - 2\psi\right]\left.\frac{\partial w_1}{\partial y_1}\right|_{y_1=-b/2} \\ & - \frac{Q_1^2}{32a^2b^2}\left(a^4\cos^4\frac{\pi x_1}{a}\cos^2\frac{\pi y_1}{b} + b^4\cos^2\frac{\pi x_1}{a}\cos^4\frac{\pi y_1}{b}\right) \\ & + \frac{1}{2}\frac{Q_1Q_3}{128}\left(\frac{a^2}{2B^2}\cos\frac{4\pi x_1}{a} + \frac{8B^2}{a^2}\cos\frac{2\pi y_1}{B}\right. \\ & + \frac{8}{(B/a+a/B)^2}\cos\frac{2\pi x_1}{a}\cos\frac{2\pi y_1}{B} + \frac{8a^2}{B^2}\cos\frac{2\pi x_1}{a} + \frac{b^2}{2L^2}\cos\frac{4\pi y_1}{b} \\ & \left. + \frac{8L^2}{b^2}\cos\frac{2\pi x_1}{L} + \frac{8}{(L/b+b/L)^2}\cos\frac{2\pi x_1}{L}\cos\frac{2\pi y_1}{b} + \frac{8b^2}{L^2}\cos\frac{2\pi y_1}{b}\right) \\ & - \frac{Q_3^2}{32L^2B^2}\left(L^4\cos\frac{2\pi x_1}{L} + B^4\cos\frac{2\pi y_1}{B}\right)\end{aligned} \tag{3.16}$$

and

$$\begin{aligned}\varphi_2 = {} & \frac{1}{2}\frac{Q_4}{L}y_2^2 - \frac{B^2}{a\pi^2}(ct+2\psi)\left.\frac{\partial w_2}{\partial x_2}\right|_{x_2=-a/2} - \frac{L^2}{b\pi^2}(ct+2\psi)\left.\frac{\partial w_2}{\partial y_2}\right|_{y_2=-b/2} \\ & - \frac{Q_2^2}{32a^2b^2}\left(a^4\cos^4\frac{\pi x_2}{a}\cos^2\frac{\pi y_2}{b} + b^4\cos^2\frac{\pi x_2}{a}\cos^4\frac{\pi y_2}{b}\right) \\ & + \frac{1}{2}\frac{Q_2Q_3}{128}\left(\frac{a^2}{2B^2}\cos\frac{4\pi x_2}{a} + \frac{8B^2}{a^2}\cos\frac{2\pi y_2}{B}\right. \\ & + \frac{8}{(B/a+a/B)^2}\cos\frac{2\pi x_2}{a}\cos\frac{2\pi y_2}{B} + \frac{8a^2}{B^2}\cos\frac{2\pi x_2}{a} + \frac{b^2}{2L^2}\cos\frac{4\pi y_2}{b} \\ & \left. + \frac{8L^2}{b^2}\cos\frac{2\pi x_2}{L} + \frac{8}{(L/b+b/L)^2}\cos\frac{2\pi x_2}{L}\cos\frac{2\pi y_2}{b} + \frac{8b^2}{L^2}\cos\frac{2\pi y_2}{b}\right) \\ & - \frac{Q_3^2}{32L^2B^2}\left(L^4\cos\frac{2\pi x_2}{L} + B^4\cos\frac{2\pi y_2}{B}\right),\end{aligned} \tag{3.17}$$

with

$$\psi = \frac{c(1-c)(E_1-E_2)t}{2[E_1c + E_2(1-c)]}, \tag{3.18}$$

where the quantity ψ accounts for the shift in the neutral axis when using different material properties (Hunt *et al.*, 2004; Wright, 2006a; Wright, 2006b) (see Figure 3.2); again with $i = 1, 2$ for the top and bottom laminate respectively. In equations (3.16) and (3.17) the first term again accounts for the in-plane compression before buckling, while the second and third terms are included to account for either the biaxial compressive (Shivakumar & Whitcomb, 1985) or the tensile effects from

overall buckling in the laminates (Hunt *et al.*, 2004; Wright, 2006a). The subsequent terms incorporate the membrane stretching according to large deflection plate theory (Williams & Aalami, 1979).

3.5 Governing equations

The thin elastic plates in the structure develop their strength by transferring loads with a combination of bending and membrane actions (Williams & Aalami, 1979), both of which are derived below. Furthermore, to apply the procedure of minimizing the total potential energy, to evaluate the buckling and postbuckling behaviour of the structure, the work done by the external load needs to be evaluated.

3.5.1 Strain energy from bending

To account for the effects of bending on the strain energy, the plate is regarded as being deflected by distributed bending moments only such that the mid-plane undergoes out-of-plane deformations (w_i in the z_i-direction only). Hence, the strain energy stored due to flexural actions alone can be calculated (Williams & Aalami, 1979). The incremental contribution of strain energy stored by the moments can be obtained by taking half the product of the moment and the angle between corresponding sides after bending $\mathrm{d}\theta$ (Timoshenko & Woinowsky-Krieger, 1959). This can also basically be described by a series of rotational springs, where the incremental strain energy can be formulated as:

$$\mathrm{d}U = \frac{1}{2} M \mathrm{d}\theta \,, \tag{3.19}$$

where $M = M_x \,\mathrm{d}y$ and $\mathrm{d}\theta$ can be related to the curvature as follows

$$\mathrm{d}\theta = -\frac{\partial^2 w}{\partial x^2} \mathrm{d}x \,. \tag{3.20}$$

This can also be done accordingly for M_y and the twisting moments M_{xy} and M_{yx}; substituting equation (3.20) into equation (3.19) and adding all the contributions

together, the strain energy in bending U_{b_i} can be derived thus (Timoshenko & Woinowsky-Krieger, 1959):

$$U_{b_i} = \frac{D_i}{2} \int\int \left\{ \left(\frac{\partial^2 w_i}{\partial x_i^2} + \frac{\partial^2 w_i}{\partial y_i^2} \right)^2 - 2(1-\nu) \left[\frac{\partial^2 w_i}{\partial x_i^2} \frac{\partial^2 w_i}{\partial y_i^2} - \left(\frac{\partial^2 w_i}{\partial x_i \partial y_i} \right)^2 \right] \right\} \mathrm{d}y_i \, \mathrm{d}x_i, \quad (3.21)$$

with the plate flexural rigidity D_i being:

$$D_i = \frac{(EI)_i}{1-\nu^2}, \quad (3.22)$$

where:

$$(EI)_1 = E_1 \frac{(ct)^3}{12}, \qquad (EI)_2 = E_2 \frac{[(1-c)t]^3}{12},$$
$$(EI)_3 = E_1 \left\{ \frac{(ct)^3}{12} + ct \left[\frac{(1-c)t}{2} - \psi \right]^2 \right\} + E_2 \left\{ \frac{(1-c)^3 t^3}{12} + (1-c)t \left[\frac{ct}{2} + \psi \right]^2 \right\}. \quad (3.23)$$

Also, if C_i is defined thus:

$$C_i = \left(\frac{\partial^2 w_i}{\partial x_i^2} + \frac{\partial^2 w_i}{\partial y_i^2} \right)^2 - 2(1-\nu) \left[\frac{\partial^2 w_i}{\partial x_i^2} \frac{\partial^2 w_i}{\partial y_i^2} - \left(\frac{\partial^2 w_i}{\partial x_i \partial y_i} \right)^2 \right] \quad (3.24)$$

then the components for the delaminated parts would be:

$$U_{b_i} = \frac{D_i}{2} \int_{-a/2}^{a/2} \int_{-b/2}^{b/2} C_i \, \mathrm{d}y_i \, \mathrm{d}x_i, \quad (3.25)$$

where $i = 1$ or 2; for the undelaminated part:

$$U_{b_3} = \frac{D_3}{2} \left[\int_{-B/2}^{B/2} \int_{-L/2}^{L/2} C_3 \, \mathrm{d}y_3 \, \mathrm{d}x_3 - \int_{-b/2}^{b/2} \int_{-a/2}^{a/2} C_3 \, \mathrm{d}y_3 \, \mathrm{d}x_3 \right]. \quad (3.26)$$

Thus the total strain energy in bending is:

$$U_b = \sum_{i=1}^{3} U_{b_i}. \quad (3.27)$$

3.5.2 Strain energy from membrane action

Having established the strain energy accumulated by flexure, the strain energy from membrane behaviour needs to be derived to allow for the effects in the plane of the

plates; owing to moderately large deflections, this can be several times the plate thickness (Williams & Aalami, 1979). In the previous subsection, it was assumed that the plate is bent by moments only. In addition, there are forces acting on the middle planes of the plates, assuming plane stress conditions as established in §3.3, a two dimensional elasticity problem is obtained (Timoshenko & Gere, 1961). To solve this, the uniformly distributed in-plane forces $N_{x_i} = t_i\sigma_{x_i}$, $N_{y_i} = t_i\sigma_{y_i}$ and $N_{x_iy_i} = t_i\tau_{x_iy_i}$ need to be determined as well as the components of strain ε_{x_i}, ε_{y_i} and $\gamma_{x_iy_i}$, where the latter can be obtained from Hooke's law, thus:

$$\varepsilon_{x_i} = \frac{1}{E_i t_i}(N_{x_i} - \nu N_{y_i}) \tag{3.28}$$

$$\varepsilon_{y_i} = \frac{1}{E_i t_i}(N_{y_i} - \nu N_{x_i}) \tag{3.29}$$

$$\gamma_{xy_i} = \frac{N_{xy_i}}{G_i t_i}\,. \tag{3.30}$$

Since the membrane energy stored in a plate is defined as:

$$U_m = \frac{1}{2}\int\int \Big(N_x\varepsilon_x + N_y\varepsilon_y + N_{xy}\gamma_{xy}\Big)\mathrm{d}x\,\mathrm{d}y\,, \tag{3.31}$$

and it is known that the stresses are related to Airy's stress function via equations (3.10)–(3.12), substituting these expressions into equations (3.28)–(3.30) and the resulting expressions into (3.31), the strain energy stored within the plate "membranes" U_{m_i}, is developed. First, defining S_i, where:

$$S_i = (\nabla^2\varphi_i)^2 - 2(1+\nu)\left[\frac{\partial^2\varphi_i}{\partial x_i^2}\frac{\partial^2\varphi_i}{\partial y_i^2} - \Big(\frac{\partial^2\varphi_i}{\partial x_i \partial y_i}\Big)^2\right], \tag{3.32}$$

the expression for the individual laminates is:

$$U_{m_i} = \frac{E_i t\left[(i-1) - (-1)^i c\right]}{2(1-\nu^2)}\int_{-b/2}^{b/2}\int_{-a/2}^{a/2} S_i\,\mathrm{d}y_i\,\mathrm{d}x_i, \tag{3.33}$$

where $i = 1$ and 2 and $E_i t\left[(i-1) - (-1)^i c\right]/(1-\nu^2)$ is the in-plane stiffness of the sublaminates. The overall panel membrane energy U_{m_3} is:

$$U_{m_3} = \frac{\left[E_1 c + E_2(1-c)\right]t}{2(1-\nu^2)}\left[\int_{-B/2}^{B/2}\int_{-L/2}^{L/2} S_3\,\mathrm{d}y_3\,\mathrm{d}x_3 - \int_{-b/2}^{b/2}\int_{-a/2}^{a/2} S_3\,\mathrm{d}y_3\,\mathrm{d}x_3\right], \tag{3.34}$$

with the total strain energy from membrane action being:

$$U_m = \sum_{i=1}^{3} U_{m_i}. \tag{3.35}$$

3.5.3 Work done

To complete the required total potential energy components, the work done by the external loads needs to be obtained. To derive the work done by the load for a plate under uniaxial compression, the end-shortening of the plate needs to be obtained (Thompson & Hunt, 1984). This can be done similarly to the Euler strut regarding the plate as inextensional but double integration is required when accounting for the end-shortening $\mathcal{E}$ due to the out-of-plane displacements w_i, thus:

$$\mathcal{E} = \frac{1}{2}\int\int\left(\frac{\partial w_i}{\partial x_i}\right)^2 \mathrm{d}y_i\,\mathrm{d}x_i\,. \tag{3.36}$$

The general expression for the work done by the uniformly distributed load is subsequently $P\mathcal{E}$ where $P = P_x = \sigma_x t_i$, with c or $(1-c)$ in the work done expressions for each laminate of the delaminated part. Therefore, for the undelaminated part:

$$(P\mathcal{E})_3 = \frac{1}{2}P\left[\int_{-B/2}^{B/2}\int_{-L/2}^{L/2}\left(\frac{\partial w_3}{\partial x_3}\right)^2 \mathrm{d}y_3\,\mathrm{d}x_3 - \int_{-b/2}^{b/2}\int_{-a/2}^{a/2}\left(\frac{\partial w_3}{\partial x_3}\right)^2 \mathrm{d}y_3\,\mathrm{d}x_3\right], \tag{3.37}$$

with the delaminated parts being:

$$(P\mathcal{E})_1 = \frac{1}{2}Pc\int_{-b/2}^{b/2}\int_{-a/2}^{a/2}\left(\frac{\partial w_1}{\partial x_1}\right)^2 \mathrm{d}y_1\,\mathrm{d}x_1, \tag{3.38}$$

and

$$(P\mathcal{E})_2 = \frac{1}{2}P(1-c)\int_{-b/2}^{b/2}\int_{-a/2}^{a/2}\left(\frac{\partial w_2}{\partial x_2}\right)^2 \mathrm{d}y_2\,\mathrm{d}x_2. \tag{3.39}$$

Including the term from pure squashing, described by Q_4, the expression for the total work done by load becomes:

$$P\mathcal{E} = P\left[\sum_{i=1}^{3}\mathcal{E}_i + BQ_4\right]. \tag{3.40}$$

3.5.4 Total potential energy

Having established the strain energy terms from bending and membrane action as well as the work done by the external load, the total potential energy V of the

plate system can be formulated, with the evaluation of the displacement and stress functions w_i and φ_i respectively, thus:

$$V = U_b + U_m - P\mathcal{E}, \tag{3.41}$$

where the full expressions for the individual components are given in the preceding sections.

3.5.5 Normalization

In the following chapters all equilibrium loads presented in the tables and graphs are normalized with respect to the critical load P^{C} for an undamaged panel (Timoshenko & Woinowsky-Krieger, 1959), where:

$$P^{\mathrm{C}} = \frac{k\pi^2(EI)_3}{(1-\nu^2)B^2} \tag{3.42}$$

and

$$k = \left(\frac{n_3 B}{m_3 L} + \frac{m_3 L}{n_3 B}\right)^2 \tag{3.43}$$

where m_3 and n_3 are odd numbers describing the wave lengths in the displacement of the overall panel w_3 in equation (3.6) resulting in $k = 4$ for a simply-supported plate of square dimensions. The normalized load Λ can subsequently be defined thus:

$$\Lambda = P/P^{\mathrm{C}}. \tag{3.44}$$

The total end-shortening $\mathcal{E}$, given from equation (3.40) after dividing by the load P, is also normalized with respect to the end-shortening of an undamaged panel $\mathcal{E}^{\mathrm{C}}$ when $P = P^{\mathrm{C}}$ (Hunt *et al.*, 2004), where:

$$\mathcal{E}^{\mathrm{C}} = \frac{P^{\mathrm{C}} L}{E_3 t}. \tag{3.45}$$

Hence, the normalized end-shortening $\mathcal{E}_N$ is defined thus:

$$\mathcal{E}_N = \mathcal{E}/\mathcal{E}^{\mathrm{C}}. \tag{3.46}$$

3.6 Finite element model

The finite element analysis of delaminated isotropic plates was conducted to verify the validity of the proposed analytical formulation, using the commercial finite element analysis package ABAQUS (2006). The model was developed under my supervision by my colleague Marios Theofanous by adhering to the previously discussed assumptions in §3.3 that were involved in the derivation of the analytical model. Hence, a linear elastic isotropic material response is assumed and a single delamination located at various depths of the plate is considered. Owing to the large span to thickness ratio, the 4-noded doubly curved reduced integration shell element S4R was employed to discretize the structure. To maintain consistency with the analytical model, shear deformations were suppressed by specifying high stiffness values for out-of-plane shear deformations and zero stiffness for in-plane shear deformations. In accordance with the analytical model described in §3.2, the rectangular delamination area was centrally positioned.

Mesh convergence studies were carried out to specify an adequate mesh density. Hence, the critical load corresponding to the first mode shape of the intact plate, obtained numerically for various mesh densities, was compared to the analytical solution and it was concluded that a global element size equal to the shell thickness was adequate for the purpose of this study. A finer mesh, equal to the thickness of the thinnest sublaminate was employed in the delaminated region to capture more accurately the local plate modes.

Symmetry of the panels was exploited by analysing half the panel and applying suitable boundary conditions along the mid-surface of the shell elements. Modelling a quarter of the panel was another alternative, but since higher modes, which are not accounted for by the analytical model later on during the studies, may be of potential interest, suppressing them by additional symmetry boundary conditions was not enforced. It should be noted that either symmetric or antisymmetric modes can be extracted by modelling a symmetric structure depending on whether symmetric or

antisymmetric boundary conditions are applied along the axis of symmetry; mixed buckling modes, including coupled symmetric and antisymmetric buckling modes on the local and global level can also be captured. This would necessitate four different analyses to be run for each quarter panel model to extract all combinations of either the symmetric or antisymmetric boundary conditions along the axis of symmetry for each of the two sublaminates.

The edges of the panels were simply supported and kinematic coupling was applied to the loaded edges which forced them to remain straight. The delaminated region was modelled by simulating two separate plates that were tied along their edges to the intact plate using the TIE constraint (Craven *et al.*, 2010). The modelled reference surface of all shell elements coincided with their mid-surfaces; hence no eccentricities were present in the model. Owing to the adopted modelling approach, *i.e.* modelling two separate plates in the delaminated region, there is a possibility of the laminates passing through each other. However, it was decided to forego the complicated definition of contact between the laminate layers and check the validity and physical possibility of the derived mode shapes by inspection, in order not to compromise the simplicity and computational efficiency of the numerical model.

The basic panel model was square with a width and length of 100 mm and had an overall thickness of $t = 2$ mm, see Figure 3.6. Eigenvalue buckling analysis was carried out, using subspace iteration as the eigenvalue extraction method and the derived eigenvalues were compared to the analytical predictions for the cases considered in due course. Various delamination sizes and depths were modelled as will be seen when validating the results in the following chapters.

After the validation of the analytical model with respect to critical loads and mode shapes using linear eigenvalue analysis, as will be shown in Chapter 4, geometric nonlinearity was subsequently incorporated in the finite element models to capture the postbuckling response of a plate with a stationary delamination, as presented in Chapter 5. The focus was on the postbuckling response corresponding to the first, or lowest, buckling mode shape. It is well known that the introduction of a

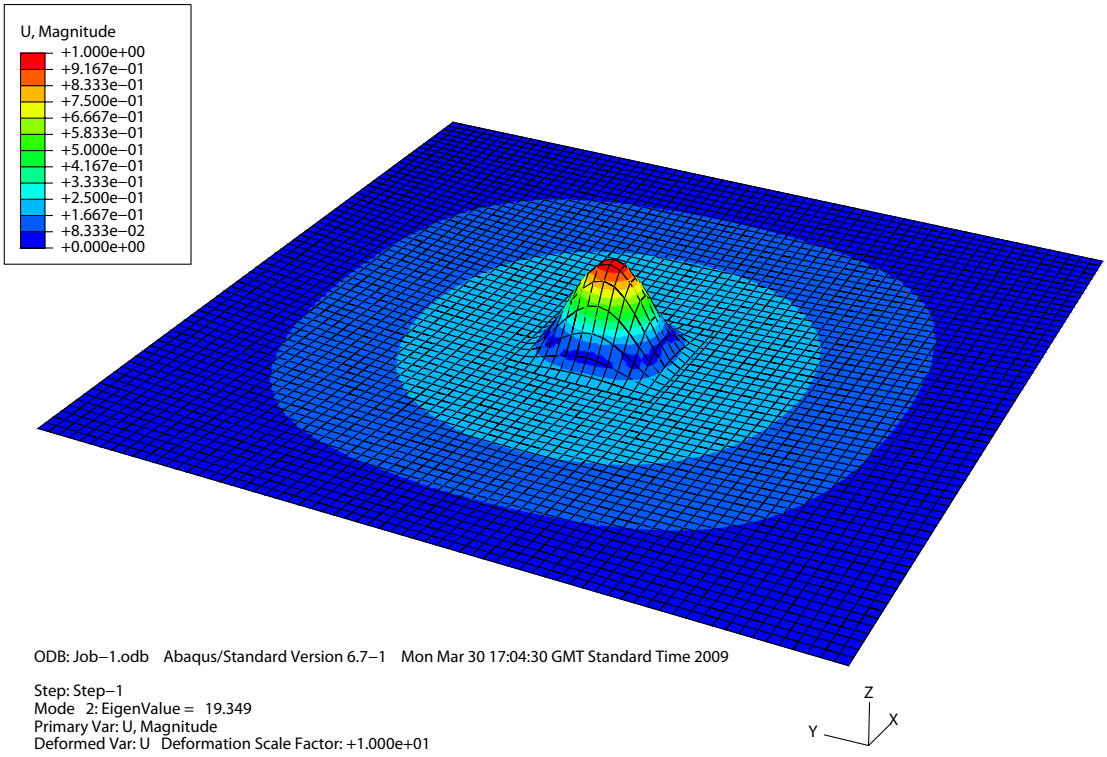

Figure 3.6: The finite element model of the delaminated plate.

small perturbation is necessary for postbuckling analysis with a finite element code (Belytschko *et al.*, 2000). Therefore a geometric imperfection in the form of the relevant buckling mode shape was introduced with an imperfection amplitude equal to $L/10000$. This imperfection amplitude was sufficient to trigger the instability but was deemed small enough to give results sufficiently close to the perfect case. A general static analysis including geometric nonlinearity was adopted for the imperfect system and the postbuckling response was then traced up to a load level equal to twice the critical buckling load of the intact plate.

Chapter 4

Initial buckling of the delaminated panel

4.1 Introduction

In this chapter, the methodology for predicting the critical buckling load using linear analysis is presented. The Rayleigh–Ritz method, as described in §1.2.2, is implemented in conjunction with the analytical formulation derived in the previous chapter. This type of approach has been successfully employed in previous studies (Yin & Jane, 1992a; Kim & Kedward, 1999; Hunt *et al.*, 2004).

The critical loads are obtained for different delamination geometries, namely square or rectangular, and related to the size and depth of the delamination. Furthermore, the corresponding eigenvectors are determined that correspond to the critical loads. Conclusions are drawn regarding dimensional constraints and the results are compared with data from the literature, as well as results obtained with the finite element model developed in the previous chapter.

4.2 Linear Analysis

To determine the critical loads, a *linear eigenvalue analysis* is performed by examining the second derivatives of the total potential energy V in the fundamental state with respect to the generalized coordinates (Thompson & Hunt, 1984), as discussed in §1.2.2. However, this type of analysis provides no information about the system's behaviour after initial buckling. Postbuckling behaviour is controlled by higher order terms of V about the critical state, which is covered in later chapters.

Substituting the admissible transverse displacement functions from §3.4.1 into the expressions for bending energy U_b, membrane energy U_m and work done $P\mathcal{E}$, as described in §3.5, produces the following four degree of freedom total potential energy function $V(Q_1, Q_2, Q_3, Q_4, P)$, equation (4.1), which is for simplicity, presented as a power series in general theory form as defined by Thompson and Hunt (1973; 1984):

$$\begin{aligned} V(Q_i, P) \;=\; & \tfrac{1}{2}V_{11}Q_1^2 + \tfrac{1}{2}V_{22}Q_2^2 + \tfrac{1}{2}V_{33}Q_3^2 + \tfrac{1}{2}V_{44}Q_4^2 \\ & + V_{13}Q_1Q_3 + V_{23}Q_2Q_3 \\ & + V_{134}Q_1Q_3Q_4 + V_{234}Q_2Q_3Q_4 \\ & + \tfrac{1}{2}V_{113}Q_1^2Q_3 + \tfrac{1}{2}V_{114}Q_1^2Q_4 + \tfrac{1}{2}V_{133}Q_1Q_3^2 \\ & + \tfrac{1}{2}V_{223}Q_2^2Q_3 + \tfrac{1}{2}V_{224}Q_2^2Q_4 + \tfrac{1}{2}V_{233}Q_2Q_3^2 \\ & + \tfrac{1}{2}V_{334}Q_3^2Q_4 \\ & + \tfrac{1}{24}V_{1111}Q_1^4 + \tfrac{1}{24}V_{2222}Q_2^4 + \tfrac{1}{24}V_{3333}Q_3^4 \\ & + \tfrac{1}{4}V_{1133}Q_1^2Q_3^2 + V_{2233}Q_2^2Q_3^2 \\ & + \tfrac{1}{6}V_{1113}Q_1^3Q_3 + \tfrac{1}{6}V_{1333}Q_1Q_3^3 \\ & + \tfrac{1}{6}V_{2223}Q_2^3Q_3 + \tfrac{1}{6}V_{2333}Q_2Q_3^3 \\ & - P\left(V_4'Q_4 + \tfrac{1}{2}V_{11}'Q_1^2 + \tfrac{1}{2}V_{22}'Q_2^2 + \tfrac{1}{2}V_{33}'Q_3^2\right. \\ & \qquad \left. + V_{13}Q_1Q_3 + V_{23}Q_2Q_3\right) \end{aligned} \tag{4.1}$$

where the subscript i $(= 1 \ldots 4)$ represents a partial derivative with respect to Q_i and the prime denotes a partial derivative with respect to P.

It turns out that V can be reduced through elimination of the generalized coordinate Q_4 (Hunt *et al.*, 2004). This reduction is carried out by solving the equilibrium equation with respect to Q_4:

$$\frac{\partial V}{\partial Q_4} = 0\,, \tag{4.2}$$

and substituting the resulting expression for Q_4 back into V, equation (4.1). This results in a three degree of freedom form for the total potential energy which is presented below again in general theory form, with P^2 terms being dropped since they vanish on differentiation with respect to Q_i:

$$\begin{aligned} V(Q_1,Q_2,Q_3,P) \;=\; & \frac{1}{2}V_{11}Q_1^2+\frac{1}{2}V_{22}Q_2^2+\frac{1}{2}V_{33}Q_3^2 \\ & +V_{13}Q_1Q_3+V_{23}Q_2Q_3 \\ & +\frac{1}{2}V_{113}Q_1^2Q_3+\frac{1}{2}V_{133}Q_1Q_3^2 \\ & +\frac{1}{2}V_{223}Q_2^2Q_3+\frac{1}{2}V_{233}Q_2Q_3^2 \\ & +\frac{1}{24}V_{1111}Q_1^4+\frac{1}{24}V_{2222}Q_2^4+\frac{1}{24}V_{3333}Q_3^4 \\ & +\frac{1}{4}V_{1122}Q_1^2Q_2^2+\frac{1}{4}V_{1133}Q_1^2Q_3^2+\frac{1}{4}V_{2233}Q_2^2Q_3^2 \\ & +\frac{1}{6}V_{1113}Q_1^3Q_3+\frac{1}{6}V_{1333}Q_1Q_3^3 \\ & +\frac{1}{6}V_{2223}Q_2^3Q_3+\frac{1}{6}V_{2333}Q_2Q_3^3 \\ & +\frac{1}{2}V_{1123}Q_1^2Q_2Q_3+\frac{1}{2}V_{1223}Q_1Q_2^2Q_3+\frac{1}{2}V_{1233}Q_1Q_2Q_3^2 \\ & -P\big(\frac{1}{2}V'_{11}Q_1^2+\frac{1}{2}V'_{22}Q_2^2+\frac{1}{2}V'_{33}Q_3^2 \\ & \quad +V'_{13}Q_1Q_3+V'_{23}Q_2Q_3\big)\,. \end{aligned} \tag{4.3}$$

Since the quadratic cross-terms Q_iQ_j are present the system is termed as *non-diagonalized*. The requirement for critical equilibrium therefore becomes a singular matrix of the second derivatives for multiple degrees of freedom systems. This is termed the *Hessian matrix*, $\mathbf{V_{ij}}$, with the following entries:

$$V_{ij} = \frac{\partial^2 V}{\partial Q_i \partial Q_j}, \tag{4.4}$$

which also includes cross derivatives where $i \neq j$ and is symmetric, (Croll & Walker,

1972; Thompson & Hunt, 1973; Thompson & Hunt, 1984). Since the generalized coordinate Q_4 is eliminated, an easily solvable 3×3 matrix is derived:

$$\mathbf{V_{ij}} = \begin{pmatrix} V_{11} & V_{12} & V_{13} \\ V_{21} & V_{22} & V_{23} \\ V_{31} & V_{32} & V_{33} \end{pmatrix} .$$

Along the trivial fundamental path, denoted by the superscript F, all Q_i-terms are zero, since the panel is flat before the point of buckling (Shivakumar & Whitcomb, 1985). Hence, for linear analysis, the higher derivatives are zero and the elements of the matrix can be determined:

$$V_{11}^{\mathrm{F}} = \frac{\partial^2 V}{\partial Q_1^2} = V_{11} - P^{\mathrm{F}} V'_{11} \tag{4.5}$$

$$V_{22}^{\mathrm{F}} = \frac{\partial^2 V}{\partial Q_2^2} = V_{22} - P^{\mathrm{F}} V'_{22} \tag{4.6}$$

$$V_{33}^{\mathrm{F}} = \frac{\partial^2 V}{\partial Q_3^2} = V_{33} - P^{\mathrm{F}} V'_{33} \tag{4.7}$$

$$V_{12}^{\mathrm{F}} = \frac{\partial^2 V}{\partial Q_1 \partial Q_2} = 0 \tag{4.8}$$

$$V_{13}^{\mathrm{F}} = \frac{\partial^2 V}{\partial Q_1 \partial Q_3} = V_{13} - P^{\mathrm{F}} V'_{13} \tag{4.9}$$

$$V_{23}^{\mathrm{F}} = \frac{\partial^2 V}{\partial Q_2 \partial Q_3} = V_{23} - P^{\mathrm{F}} V'_{23} \, . \tag{4.10}$$

Having determined the matrix of second derivatives, the following method is used to find the critical buckling loads of the system. The determinant of the matrix is non-zero everywhere along the fundamental path and is often referred to as the *stability determinant*. The matrix becomes singular at the critical states which holds for diagonalized as well as non-diagonalized systems (Thompson & Hunt, 1973).

Since along the trivial fundamental path all generalized coordinates Q_1, Q_2 and Q_3 are zero, *i.e.* no deformation, the determinant of the Hessian matrix at the critical point coincides with the determinant of the Hessian matrix along the fundamental path, $V_{ij}^{\mathrm{C}} = V_{ij}^{\mathrm{F}}$. Consequently, the determinant can be determined as follows:

$$\det(\mathbf{V_{ij}^{C}}) = V_{11}^{\mathrm{C}} V_{22}^{\mathrm{C}} V_{33}^{\mathrm{C}} - [\, (V_{13}^{\mathrm{C}})^2 V_{22}^{\mathrm{C}} + (V_{23}^{\mathrm{C}})^2 V_{11}^{\mathrm{C}} \,] \, . \tag{4.11}$$

Setting the determinant to zero yields the three critical loads, P_1^{C}, P_2^{C} and P_3^{C}:

$$\det(\mathbf{V}_{\mathbf{ij}}^{\mathrm{C}}) = 0\,. \tag{4.12}$$

The resulting critical loads depend on dimensional parameters such as the delamination depth, area, aspect ratios and material properties. An analytical result is too lengthy to present here, but in §4.3 results for different parameters, *i.e.* delamination depth c, length a and area ab, are presented for a fixed set of material parameters shown in Table 4.1.

Furthermore, it is worth reiterating that results obtained with this energy method are always approximate since the transverse displacement modes w_i are assumed (for more detail see §1.2.2). Hence, this can always be regarded as an upper bound since the actual minima of the potential energy for the "true" solution will be less than, or in the best case, equal to the case when employing trial functions.

4.2.1 Eigenvectors

Having determined the critical loads in the previous section, the relative mode shape amplitudes corresponding to these eigenvalues from the linearized analysis can be established, namely the relationship between Q_1, Q_2 and Q_3 at the critical loads. To establish the eigenvectors $\mathbf{\Phi}_j$ corresponding to the eigenvalues, the critical loads $P_1^{\mathrm{C}}, P_2^{\mathrm{C}}$ and P_3^{C} are substituted into the Hessian matrix $\mathbf{V}_{\mathbf{ij}}^{\mathrm{C}}$. Subsequently, the following set of linear equations need to be solved:

$$\mathbf{V}_{\mathbf{ij}}^{\mathrm{C}}\,\mathbf{\Phi}_j = 0\,, \tag{4.13}$$

or with $\mathbf{\Phi}_j$ containing Q_i

$$\begin{pmatrix} V_{11}^{\mathrm{C}} & 0 & V_{13}^{\mathrm{C}} \\ 0 & V_{22}^{C} & V_{23}^{C} \\ V_{13}^{C} & V_{23}^{C} & V_{33}^{C} \end{pmatrix} \begin{bmatrix} Q_1 \\ Q_2 \\ Q_3 \end{bmatrix} = \begin{bmatrix} 0 \\ 0 \\ 0 \end{bmatrix}.$$

From this, the following set of eigenvectors are obtained:

$$\frac{Q_1}{Q_3} = -\frac{V_{13}^{\mathrm{C}}}{V_{11}^{\mathrm{C}}} \tag{4.14}$$

and

$$\frac{Q_2}{Q_3} = -\frac{V_{23}^{\mathrm{C}}}{V_{22}^{\mathrm{C}}}\,. \tag{4.15}$$

Three distinct sets of eigenvectors corresponding to each critical load P_j^{C} can be subsequently obtained and are discussed in §4.3.2.

4.3 Results and validation

With the linear eigenvalue analysis outlined above, parametric investigations are undertaken regarding the influence of geometric parameters on the critical buckling loads. Furthermore, the corresponding eigenvectors are obtained and the results are discussed in the following sections.

The panels investigated are square of overall dimensions $L = B = 100$ mm (Chen & Sun, 1999; Melin & Schön, 2001; Melin *et al.*, 2002), and thickness $t = 2$ mm with the delamination size and depth being stated in each example. The material properties are taken from Kim & Kedward (1999) for an eight ply plate $[0/45/90/-45]_{\mathbf{s}}$ quasi-isotropic carbon-fibre-reinforced composite[1], as given in Table 4.1. However,

E_x (kN/mm^2)	E_y (kN/mm^2)	ν	Ply thickness (mm)
71.7	69.5	0.04	0.304

Table 4.1: Lamina properties of AS4/8552 eight harness satin fabric, taken from Kim & Kedward (1999), used to obtain the smeared isotropic material properties.

smeared material properties are used for the analysis and the results are normalized with the critical load for an undamaged panel as described in §3.5.5; hence the

[1]For lay-up designation and definitions please refer to Chapter 1, §1.1.1, Figure 1.4.

dimensions of the panel, the thickness as well as the Young's modulus are only stated for completeness here. Furthermore, it should be noted that the values in the table are smeared properties and the model established in the previous chapter uses E_x only, since isotropic material behaviour is incorporated only in the current study. All manipulation in the linear buckling range was carried out using the symbolic computation package Maple (Heck, 1996).

4.3.1 Critical buckling loads

Several different parametric studies using linearized analysis have been conducted to assess the panel behaviour with changing parameters and to validate the model. Results for $c = 0.25$ are presented herein; results for $c = 0.125$ can be found in Appendix B.1. The results are compared to existing findings in the literature as well as results obtained with the finite element model described in §3.6.

Initially, convergency studies were undertaken to reduce the number of degrees of freedom used in the analysis and to make the model computationally more efficient. The results obtained using more degrees of freedom in the trigonometric expressions for the displacements yielded no significant deviation. Hence, equations (3.5) and (3.6) with Q_{1,m_in_i}, Q_{2,m_in_i} and Q_{3,m_3n_3} respectively were reduced to only one degree of freedom per series; only $Q_{1,11}$, $Q_{2,11}$ and $Q_{3,11}$ are used and are referred henceforth as Q_1, Q_2 and Q_3 for simplicity. The reduced displacement functions can be derived thus:

$$w_i = Q_i \cos^2 \frac{\pi x_i}{a} \cos^2 \frac{\pi y_i}{b} + Q_3 \cos \frac{\pi x_3}{L} \cos \frac{\pi y_3}{B} \,, \tag{4.16}$$

for the two laminates, with $i = 1, 2$ for the upper and lower laminate respectively, and for the overall panel:

$$w_3 = Q_3 \cos \frac{\pi x_3}{L} \cos \frac{\pi y_3}{B} \,. \tag{4.17}$$

The linear eigenvalue analysis outlined in §4.3 clearly also holds for more degrees of freedom. However, the matrix transformations obviously change and may not be

as straightforward as for a 3×3 matrix, but the system is nevertheless solvable. Nonetheless, it is possible to reduce the system to a three degree of freedom system, as discussed at the beginning of this chapter, and thus the linear analysis is described using the reduced system.

4.3.1.1 Square delamination

The first investigations undertaken regard the influence of the size of the delamination on the first critical load (Simitses *et al.*, 1985; Kim & Kedward, 1999; Tsutsui *et al.*, 2004) for a square delamination. With the developed model, the decrease of the first critical load with the size of the delamination can be shown (Gaudenzi, 1997; Chen & Sun, 1999; Sekine *et al.*, 2000; Gaudenzi *et al.*, 2001; Short *et al.*, 2001; Cappello & Tumino, 2006; Craven *et al.*, 2010) and is here compared to the results by Kim and Kedward (1999) for their analysis of a circular delamination as discussed in §2.5. The comparison is graphically illustrated in Figure 4.1 for a delamination located at one-quarter of the depth, *i.e.* $c = 0.25$.

In Figure 4.1, the thickest line, denoted as "Analytical Model 1 Term RR", illustrates the behaviour of the model developed within the current work using only one term per series as outlined above. The critical loads are compared to values obtained by Kim & Kedward (1999) for their one term ("1 Term RR") and also their four term ("4 Term RR") Rayleigh–Ritz discretization. Additionally, their results for purely local buckling ("sublaminate") and from their finite element model ("FEM") are included in the graph. In all cases the length ratio a/L was adjusted, such that is corresponds to the same delaminated area, since Kim & Kedward use a circular delamination. It can be seen that the analytical model developed within this work yields a very good comparison with the findings of Kim & Kedward particularly for small delaminations up to the size of $a = 0.4L$ and $b = 0.4B$ for the case of $c = 0.25$. In fact, the current analytical model compares even better with their finite element model and their four term Rayleigh–Ritz model rather than their analytical model and always resides below their values, thus delivers safe results, assuming that the

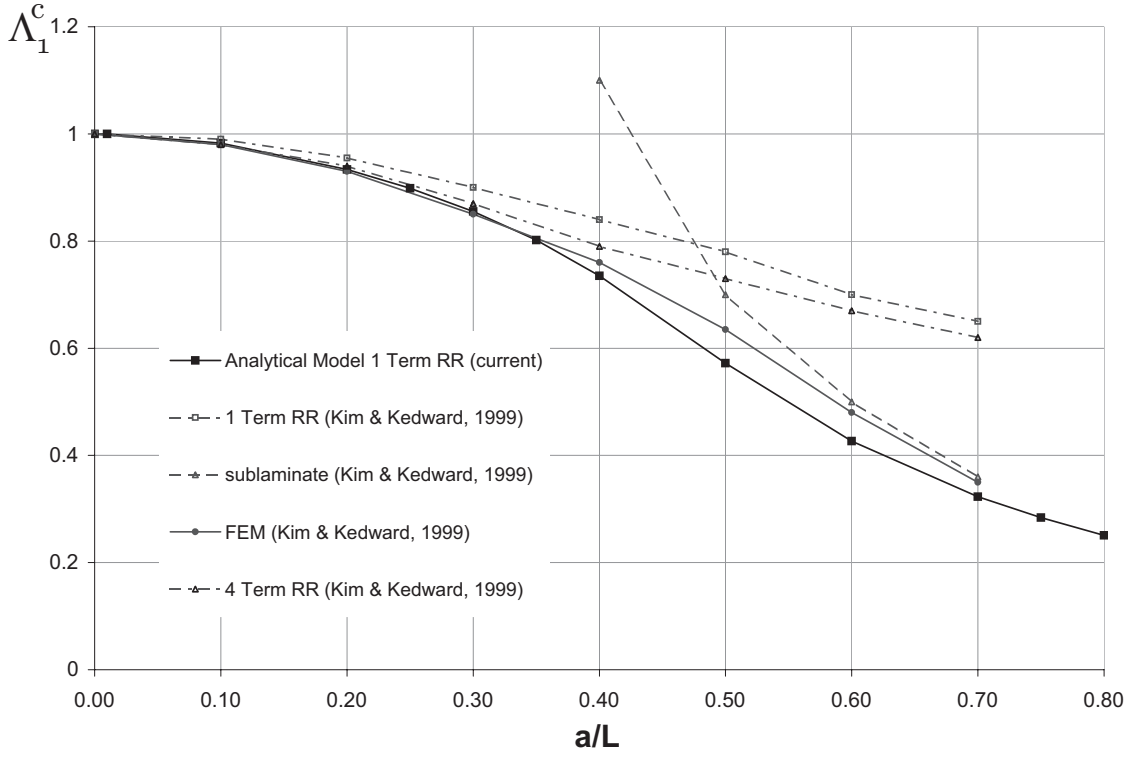

Figure 4.1: Normalized critical load Λ_1^{C} versus delamination size for $c = 0.25$.

finite element results are taken as the benchmark. Once the delamination becomes larger and sublaminate buckling becomes dominant, the discrepancy between the results grows. However, the results obtained with the analytical model developed within this study remain below the results from the literature and can therefore also be deemed as safe for the same reasons as above as well as the fact that the Rayleigh–Ritz method applied yields an upper bound when compared to the "true" solution of the structure as previously discussed. When identifying the eigenvector corresponding to the first critical load, it can be seen that local buckling initiates slightly earlier in the present model. This explains the deviation in the results, Figure 4.2, where local buckling becomes dominant since the current model displays lower load levels for this buckling case. With a view to buckling driven delamination growth, this can again be deemed as safe since the model therefore initiates growth at slightly lower load levels.

In Figure 4.2, the analytical results are compared to the values obtained with the

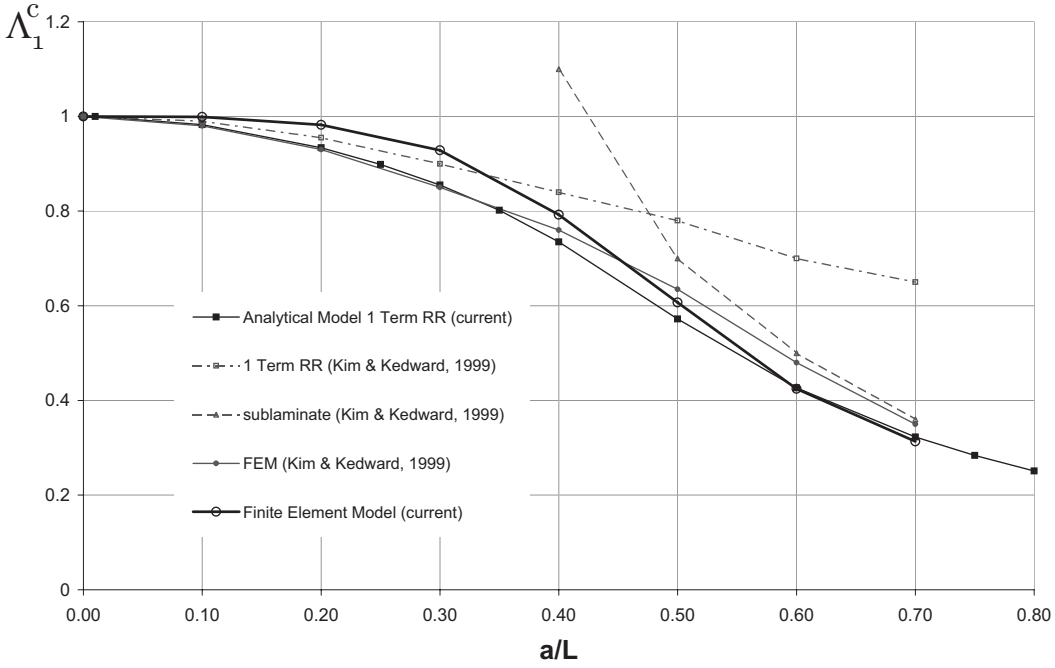

Figure 4.2: Normalized critical load Λ_1^C versus delamination size for $c = 0.25$ compared to results obtained with the finite element model from §3.6 and results from the literature (Kim & Kedward, 1999).

finite element model described in the previous chapter. Additionally, the results by Kim & Kedward are still shown in the graph. It can be seen that the finite element model compares very well with the analytical solution for very small delaminations up to a size of $a = 0.1L$ and $b = 0.1B$. Thereafter, the finite element results are slightly higher than the analytical results and the results from the literature, thus the analytical model can still be regarded as safe, as outlined before. This can also be observed for a delamination at relative depth $c = 0.125$ which is presented in Appendix B in Figure B.1.

Moreover, in Figure 4.3, it can be seen that the critical loads vary with the relative depth of the delamination c, where the first two critical loads are plotted for a fixed delamination size of $a = 0.4L$ and $b = 0.4B$; this compares directly with the findings in Hunt *et al.* (2004) and Wright (2006a) for the two-layer delaminated strut. This behaviour is commonly observed for different delamination sizes, where a plateau is observed for the first critical load when the delamination is located deeper within

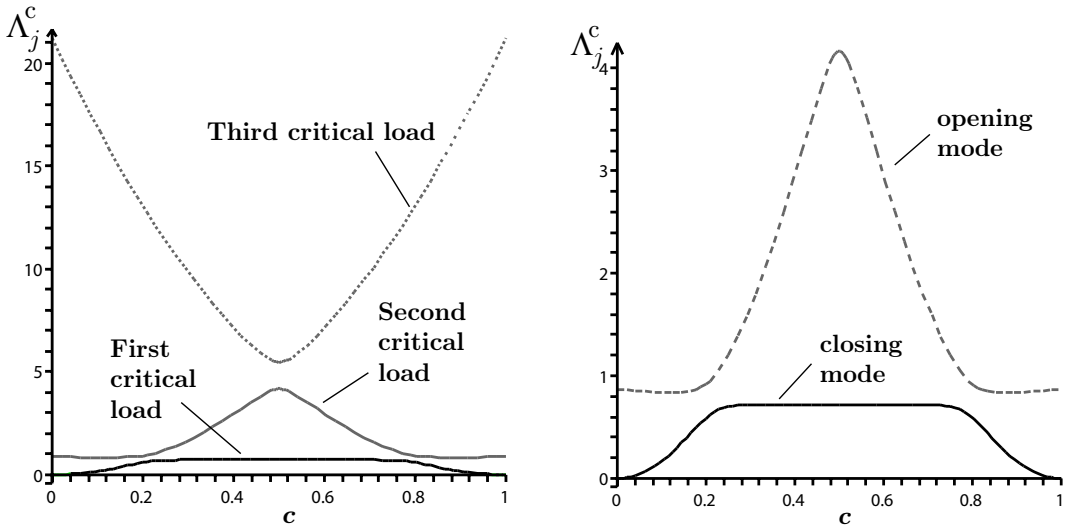

Figure 4.3: Normalized critical loads Λ_j^{C} versus relative delamination depth c for (a) all three normalized critical loads and (b) lowest two normalized critical loads.

the panel. For a delamination closer to the surface, the first and second critical loads drop considerably, which emphasizes the importance of investigating so-called *thin-film buckling* (Yu, 2003; Hunt *et al.*, 2004; Mei *et al.*, 2007) that can promote delamination propagation depending on the relative opening between the laminates as will be discussed further in later chapters. It should also be noted in Figure 4.3a that the second and third critical load are very close when the delamination is at half depth, *i.e.* $c = 0.5$. The potential of coincident branching points (Chilver, 1967; Johns & Chilver, 1971) may be found here. H

4.3.1.2 Rectangular delamination

In addition to the investigations into the influence of geometric parameters for square delaminations, rectangular delaminations are also studied. Rectangular delaminations with an aspect ratio $a/b \neq 1$ can be either long, *i.e.* $a/b > 1$, Figure 4.4a, or wide, *i.e.* $a/b < 1$, Figure 4.4b. In the course of the investigations, four different configurations are studied in addition to the square delaminations; two long delaminations with $a/b = 1.5$ and 2 as well as two wide delaminations with $b/a = 1.5$ and

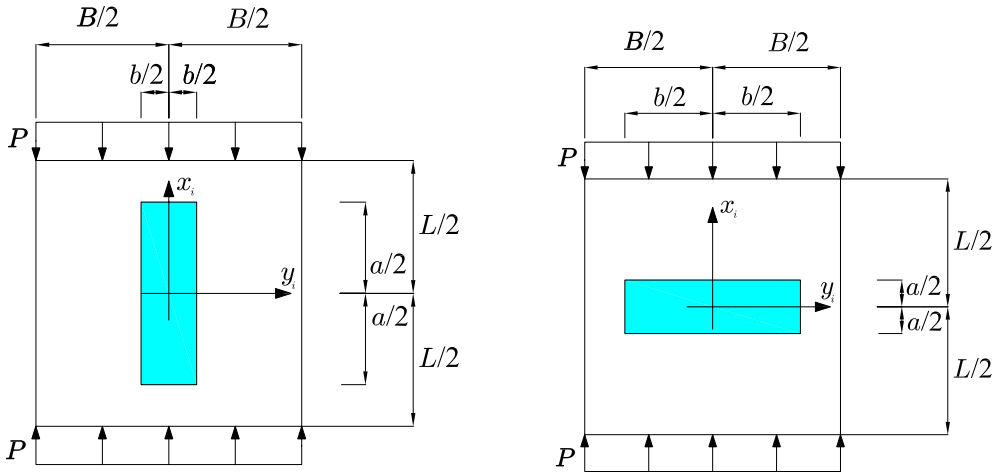

Figure 4.4: Rectangular delamination geometry: (a) long and (b) wide delamination.

2 (or $a/b = 2/3$ and $1/2$ respectively). The results again for $c = 0.25$ are presented in Figure 4.5; the load decrease with increasing delamination size can again be observed. It should be noted that the graphs show the normalized critical load Λ_1^{C} versus the delamination ratio $\phi_{\mathrm{delam}} = ab/(BL)$ since otherwise a comparison in a single graph would not give meaningful results. Further to the decrease in load value it should be noted that for a long delamination the load reduction is not as pronounced. This again ties in with findings for long delaminations by Kim & Kedward (1999). Sekine *et al.* (2000) and Tafreshi & Oswald (2003) also studied the effects of the delamination patch shape and found that enlarging the delamination in the loading direction has a very small effect on the buckling loads whereas increasing the delamination size in the other direction has a greater effect; note also that the authors studied an elliptical delamination and additionally considered the effect of fibre orientation in their investigation.

Moreover, from Figure 4.5 it can be seen that the results for a wide delamination are closer to the critical load for a square delamination. In addition, it is emphasized currently that for a long delamination of aspect ratio $a/b = 2$, the model may yield a critical load that is too high because of the limitation of the shape function. This is because with a four degree of freedom model only the first plate mode for the

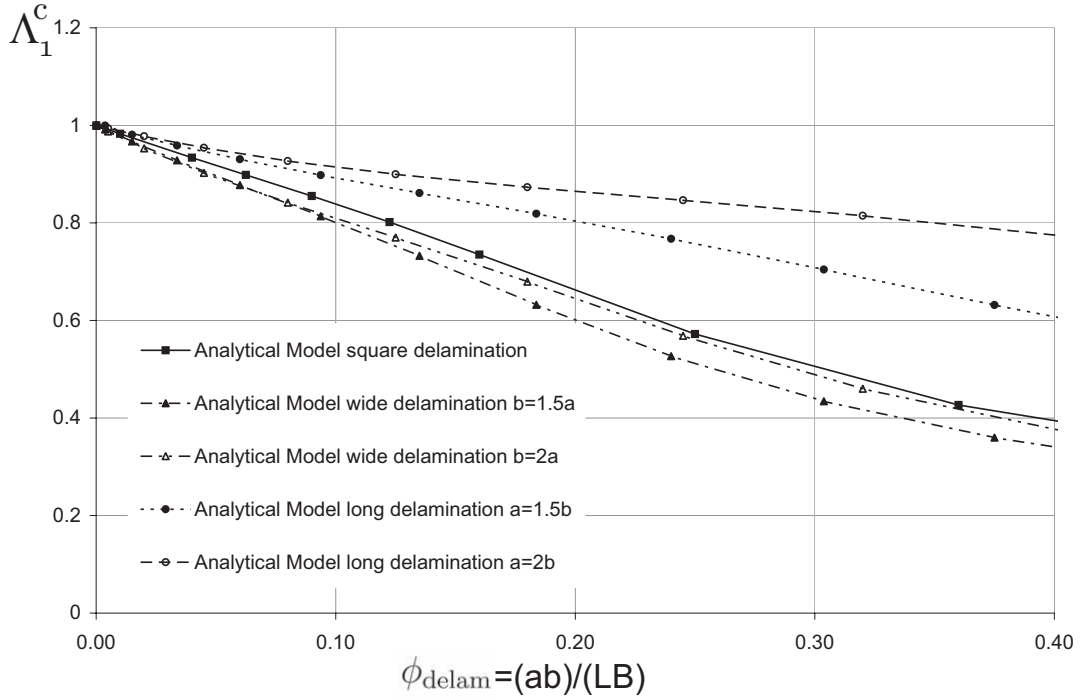

Figure 4.5: Normalized critical load Λ_1^{C} versus delamination ratio ϕ_{delam} for $c = 0.25$ for rectangular delaminations.

laminates is captured and hence may be the reason why the critical loads for the long delaminations show a larger discrepancy.

4.3.2 Eigenvectors

As outlined in §4.2.1, the eigenvectors or mode shapes corresponding to the critical loads can be identified. Three mode shapes can be obtained when out of plane displacements are truncated to equations (4.16) and (4.17) for the first, second and third critical load.

A *closing* mode is always observed for the first critical load, which means that both laminates deflect in the same direction, (Figure 4.6a). This kind of behaviour was also previously observed by Hunt *et al.* (2004). Moreover, for the second critical load, an *opening* mode, can be detected where the laminates split open and displace in opposite directions (Figure 4.6b). The latter case is potentially more dangerous when

it comes to delamination propagation, which will be discussed in the subsequent chapters, since the peeling stresses are generally greater. However, whether and at what load level propagation occurs depends on the extent of the deflection, since the growth criteria is governed by the relative opening of the laminates, which will be described in detail in §6.3. Moreover, it can be detected that the magnitude of the deflection of each laminate changes with the relative delamination depth c, which will be presented in §5.2.2. The third mode, corresponding to the third critical load, is denoted as the *reverse* mode; here, both laminates essentially buckle in the opposite direction to the overall panel. However, since the third critical load is triggered at such high load levels, this mode is unlikely to occur in a natural loading sequence and is not pursued further.

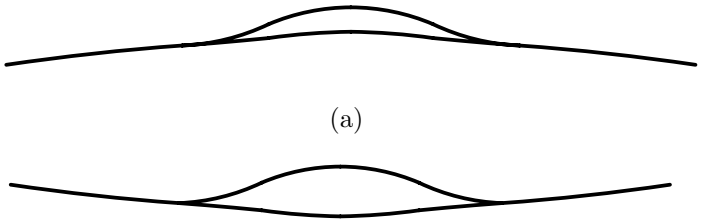

(a)

(b)

Figure 4.6: Critical modes of buckling: (a) closing mode—First critical load; (b) opening mode—Second critical load.

Comparing the eigenvectors to the results obtained with the finite element model described in §3.6 yields a very good comparison. For example, for a delamination of dimensions $a = 0.5L$ and $b = 0.5B$, a local closing mode is observed using the finite element model, see Figure 4.7. Comparing this with the eigenvectors obtained via linearized analysis where $Q_1 = 4.12$, $Q_2 = 0.04$ and $Q_3 = 1$, a local closing mode can also be observed. However, the magnitudes of the displacements will be discussed in greater detail in the following chapter when the postbuckling behaviour is investigated for a stationary delamination.

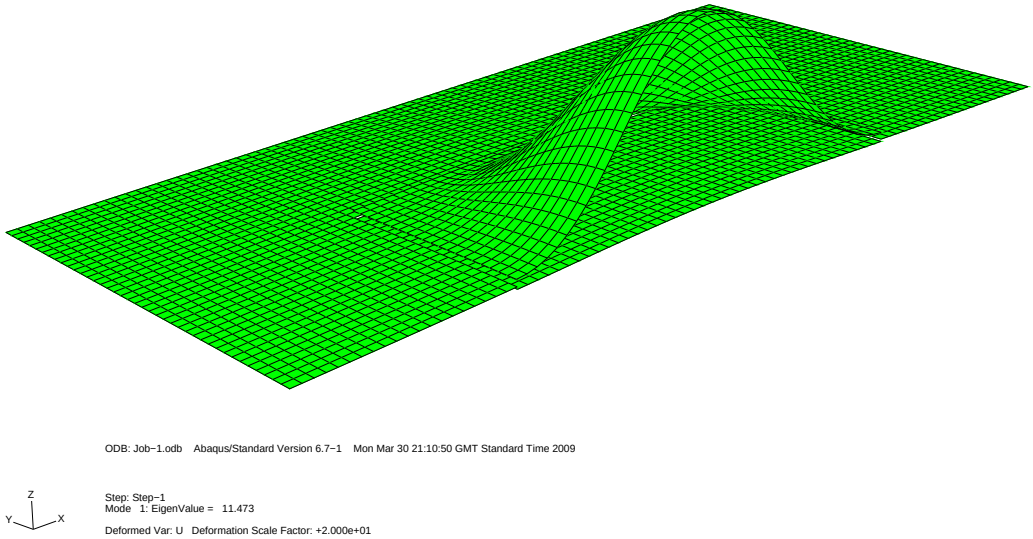

Figure 4.7: Local closing mode at intial buckling for $a = 0.5L$ and $b = 0.5B$ as evaluated using finite element analysis within ABAQUS (2006).

4.4 Concluding remarks

From the discussions and results in this chapter it can be seen that the model developed in Chapter 3 yields a good comparison using linearized analysis with existing results in the literature as well as the finite element model. It can also be seen that smaller delaminations have little or no influence on the buckling load when only linearized analysis is employed.

It can be concluded that the critical loads decrease with the size of the delamination as expected. A long rectangular delamination is not as critical as a square delamination, but a wide delamination yields slightly lower critical loads than a square delamination with the difference being to a lesser extent than for the long delamination. Furthermore, the critical loads vary with the depth of the delamination c, where a plateau can be observed for the first critical load for delaminations at mid-depth. However, once the delamination is located closer to the surface of the panel, a rapid decline in load level can be observed for both the first and second critical load. This will be discussed in further detail when the postbuckling regime is examined in detail in Chapter 5.

Three distinct mode shapes can also be identified corresponding to the critical loads. For the first critical load, a *closing* mode is seen where both laminates as well as the intact parts of the panel deflect in the same direction. An *opening* mode corresponds to the second critical load, where the upper laminate deflects in the opposite direction to the lower laminate and the intact panel. This may potentially be the most dangerous case with respect to delamination growth due to the nature of the eigenvector, which will be discussed in detail in Chapter 6. Since the third critical load would be triggered at such a high load level, the eigenvector is deemed to be of limited interest. However, for completeness it is identified as a *reverse* mode where both upper and lower laminates deflect in the opposite direction to the overall panel.

In the next chapter, the postbuckling regime for a stationary delamination will be discussed where the relative mode intensity for different delamination configurations will be investigated. This study will form the basis of the delamination propagation model in Chapter 6.

Chapter 5

Postbuckling regime of a stationary delamination

5.1 Introduction

In the current chapter, the postbuckling behaviour of the analytical panel with a stationary delamination is investigated. Since the system is non-diagonalized a closed form analytical solution could not be obtained. Hence, a numerical study is conducted using the powerful continuation software AUTO (Doedel, 2007) to solve the equilibrium equations simultaneously. The software also allows path following and detection of branching points and subsequent equilibrium paths. The procedure for solving the system of equilibrium equations is outlined, various studies are conducted and discussed in detail.

Initially, the issue of physical and non-physical solutions yielding from this type of analysis are addressed; different delamination configurations, *i.e.* depths and sizes, are then investigated via a parametric study in the postbuckling range, focusing on panels with so-called barely visible impact damage (BVID). Furthermore, a comparison with the finite element model is presented with the buckling mechanism and

mode interaction being described in detail.

5.1.1 Numerical experimentation

As mentioned in the previous chapter, the total potential energy function V is complicated due to the nature of the model. Thus, there is little hope of solving the system in closed form in the postbuckling range and numerical methods are necessary. To employ such approaches, the total potential energy function V, equation (4.1), has to be differentiated with respect to the generalized coordinates to obtain the four equilibrium equations, *i.e.* utilizing Axiom I, §1.2.1, thus:

$$V_i = \frac{\partial V}{\partial Q_i} = 0\,. \tag{5.1}$$

These equations describe the equilibrium surface of the system and have to be solved simultaneously for such a multiple degree of freedom system. To perform this, AUTO (Doedel, 2007) is employed, because of its capability of following paths as outlined below. However, before the software can be implemented, the equations first had to be converted into a FORTRAN compatible format (Nyhoff & Leestma, 1997) since AUTO requires such input files. The code generation is undertaken in MAPLE (Heck, 1996) employing the in-built `codegen` package, using the command $\mathsf{Fortran}(V_i)$ for each equilibrium equation above. Hence, a set of nonlinear algebraic equations is obtained that is inserted into the FORTRAN file required by AUTO based on the example `"ab"`—refer to the AUTO manual for details (Doedel, 2007). All four equilibrium equations depend on the following parameters: Young's Moduli E_i for each part of the panel (where $i = 1, 2$ for top or bottom part and $i = 3$ for the intact part), thickness t_i, length and width of the panel (L and B respectively), size of the delaminations (a and b), relative depth of the delamination c. Furthermore, all equations contain the entire set of generalized coordinates Q_i ($i = 1...4$) as well as the load P.

5.1.1.1 Numerical code AUTO

The numerical code AUTO is a very powerful piece of software capable of detecting various different types of bifurcation points outlined in §1.2.3 as well as performing numerical continuation whilst varying model parameters in the equations (Seydel, 1994). In the code, the principal algorithms are aimed at the continuation of solutions of systems of equations, be they algebraic of differential equations, subject to boundary conditions and integral constraints of the form:

$$u'(t) = f(u(t), p), \quad f(\cdot, \cdot), u(\cdot) \in \mathbb{R}^n \,, \tag{5.2}$$

where p denotes one or more free parameters. Furthermore, AUTO can undertake a limited bifurcation analysis of algebraic systems of the form:

$$f(u, p) = 0, \quad f(\cdot, \cdot) \in \mathbb{R}^n \,. \tag{5.3}$$

For the type of problem discussed in the current work, the latter is the case and rewriting equation (5.3) in a vectorial form yields:

$$\mathbf{f}(\mathbf{u}, p) = 0 \,, \tag{5.4}$$

where $\mathbf{f}$ and $\mathbf{u}$ denote n-dimensional vectors. The free parameter remains p, which is varied to observe how an initial solution of $\mathbf{f}$ evolves (Wadee, 1998).

Since AUTO is a well established and tested code (Doedel, 1984; Seydel, 1994; Doedel, 1997; Seydel, 1997), an outline of the solution procedure is described because the software was employed as a tool to solve the system of equations developed currently.

Essentially, the code uses the method of orthogonal collocation (de Boor & Schwartz, 1973) to discretize the problem whilst automatically adapting its mesh to distribute evenly the error from local discretization (Russell & Christiansen, 1978). Then *predictor–corrector* methods such as the Newton–Raphson method (Bažant & Cedolin, 1991) are employed in the continuation routines, with which, as the name

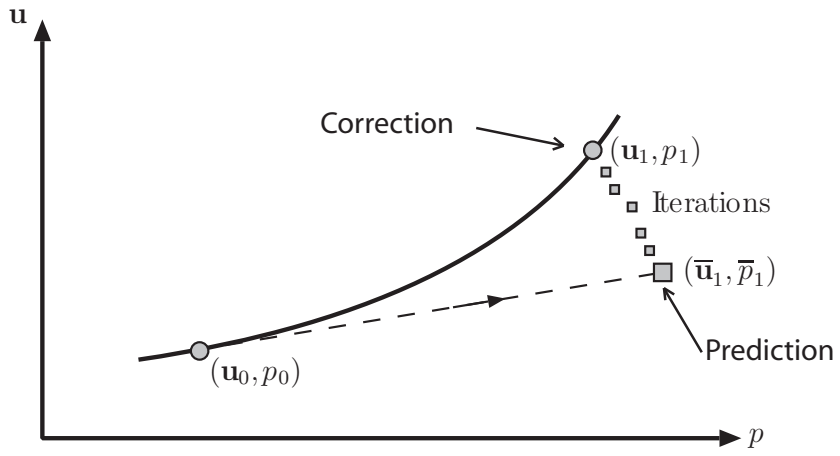

Figure 5.1: Principles of the predictor–corrector methods.

indicates, the problem is solved in two parts. Initially a solution $\mathbf{f}(\bar{\mathbf{u}}_\mathbf{1}, \bar{p}_1)$ originating from the starting values $\mathbf{f}(\mathbf{u_0}, p_0)$ is "predicted" with an increment of the free parameter p. The solution is then "corrected" using iteration from the initial guess, see Figure 5.1, to the actual solution $\mathbf{f}(\mathbf{u_1}, p_1)$. Since this method becomes unstable at limit points or folds, this procedure is combined with pseudo-arclength continuation (Riks, 1972); even when folds are detected on the solution path computations can be continued. Further details can be found in the review by Doedel (1997) on the advantages and limitations of the numerical bifurcation analysis.

For the purpose of the numerical investigations in this thesis, AUTO is employed to detect folds and bifurcations, since it can detect various different types of critical points using the Jacobian and Hessian matrices of the system of equations (Wadee, 1998) whilst varying model parameters. In the current chapter, only one model parameter is varied, namely the load P; however, in Chapter 6 when delamination growth is incorporated, further parameters need to be varied which will be explained with the discussion of the algorithm in §6.3.1.

5.2 Results and validation

In the following sections results obtained with the numerical continuation package AUTO, as described in the preceding section, are discussed. All panels investigated are square with overall dimensions $L = B = 100$ mm (Chen & Sun, 1999; Melin & Schön, 2001; Melin *et al.*, 2002) and thickness $t = 2$ mm. Since the critical loads are again normalized as outlined before, the thickness of the panel is of less relevance as long as the panel is thin compared to its span (Shivakumar & Whitcomb, 1985; Nilsson *et al.*, 1993), which is the case with the slenderness being $L/t = 50$ as in Bottega (1983). The material properties are taken from Turon *et al.* (2007) for a carbon-fibre-reinforced epoxy laminate T300/977-2, as given in Table 5.1.

E_x (kN/mm^2)	$E_y = E_z$ (kN/mm^2)	G_{IC} (N/mm)	ν	σ_{max} (N/mm^2)
140.0	11.0	0.352	0.25	60

Table 5.1: Material and interface properties of panel T300/977-2 from Turon *et al.* (2007). Note that E_x, E_y and E_z are the respective Young's moduli for the axial (x), transverse (y) and out-of-plane (z) directions. Moreover, since the current model deals with isotropic plates, the relevant values taken for the numerical study are only E_x, ν and G_{IC}, with E_z only being used to evaluate the length of the cohesive zone l_{cz} in the following chapter.

Since the problem of barely visible impact damage (BVID) is a major concern in composite construction, the postbuckling investigation focuses on this type of defect. Hence, a delamination size of $a = 0.15L$ and $b = 0.15B$ is chosen in accordance with previous studies (Whitcomb, 1989; Melin & Schön, 2001; Mitrevski *et al.*, 2006). As shown with linearized analysis in Chapter 4 the critical loads compare well with the literature as well as the finite element model for these small delamination sizes. Table 5.2 summarizes the cases presented for a stationary delamination where the delamination depth is varied to examine the change in behaviour for different values of c. The value of c being 0.05 is chosen to be the smallest value since it corresponds

to a sublaminate thickness of $t_1 = 0.1$ mm which approximately corresponds to values found in the literature for laminate thicknesses (The Design Council, 1989; Nilsson *et al.*, 1993; Melin *et al.*, 2002).

Case	a	b	% delaminated area	c	Λ_1^C	Λ_2^C
STAT-A	$0.15L$	$0.15B$	2.25	0.050	0.295	0.979
STAT-B	$0.15L$	$0.15B$	2.25	0.085	0.801	1.045
STAT-C	$0.15L$	$0.15B$	2.25	0.120	0.939	1.783
STAT-D	$0.15L$	$0.15B$	2.25	0.500	0.950	29.629
STAT-E	$0.40L$	$0.40B$	16.00	0.500	0.749	4.166

Table 5.2: Example cases for the postbuckling investigation with a stationary delamination.

For the cases in Table 5.2, the general postbuckling behaviour and subsequent implications when incorporating delamination propagation (Chapter 6) are discussed. Furthermore, a validation of the analytical postbuckling model with the finite element model described in §3.6 is carried out.

The abbreviations presented in Table 5.3 will be applied to the notation in all subsequent graphs in the current chapter; a label will denote each case depicted where more than one case is plotted.

Label	Description
PU	Postbuckling path of an undamaged panel
S1	First physical postbuckling path of a damaged panel
S2	Second physical postbuckling path of a damaged panel
NS1	First non-physical postbuckling path of a damaged panel
NS2	Second non-physical postbuckling path of a damaged panel
FE	Path of the finite element model containing a stationary delamination

Table 5.3: Abbreviations for the graph labels describing the postbuckling behaviour of a panel containing a stationary delamination.

The first two normalized critical buckling loads are denoted as Λ_1^C and Λ_2^C respectively and the behaviour after initial buckling is investigated herein. Chai & Babcock (1985) identified that the first or second critical load and mode can be triggered by changing the loading sequence, whether the panel contains a delamination that is then loaded, or whether a delamination occurs during loading of the panel as outlined in Chapter 2; this is a key point because it highlights the importance of investigating the postbuckling equilibrium paths originating from both the first and second critical loads.

5.2.1 Physical and non-physical solutions

In the current section the equilibrium paths of case STAT-A are presented purely to address the topic of non-physical postbuckling solutions (Figure 5.2); their postbuckling implications are discussed later. The graphs in Figure 5.3 present the buckling behaviour of the laminates, *i.e.* Λ versus Q_i, and the absolute values of Q_i are non-dimensionalized with the total panel thickness t.

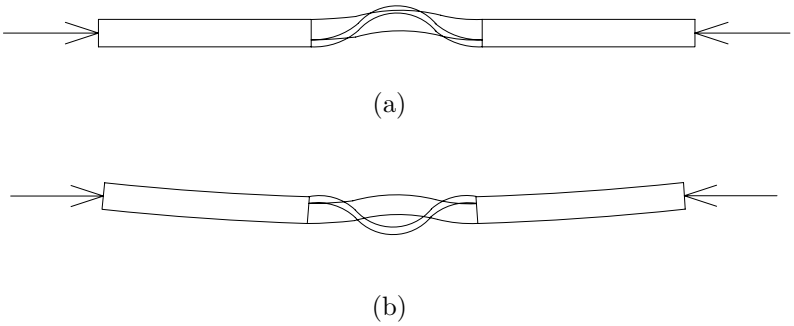

(a)

(b)

Figure 5.2: Non-physical eigenvectors; (a) non-physical *closing* and (b) non-physical *opening* mode.

It should be noted that the postbuckling analysis yields physical and non-physical equilibrium branches (Sekine *et al.*, 2000; Hunt *et al.*, 2004). Non-physical branches are those that essentially show two laminates deflecting such that they would penetrate. This can occur at both the first and second critical loads, see Figure 5.2.

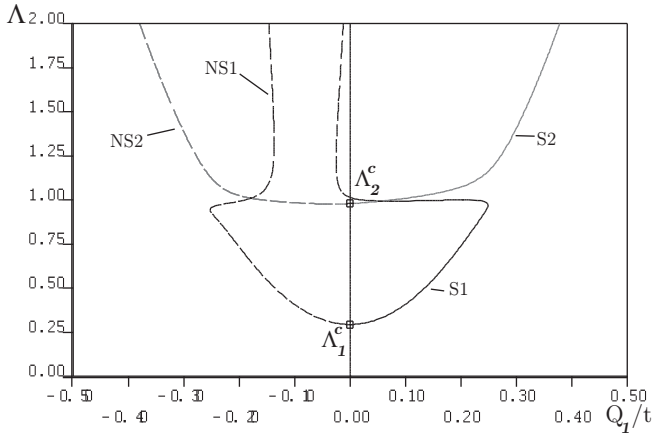

(a)

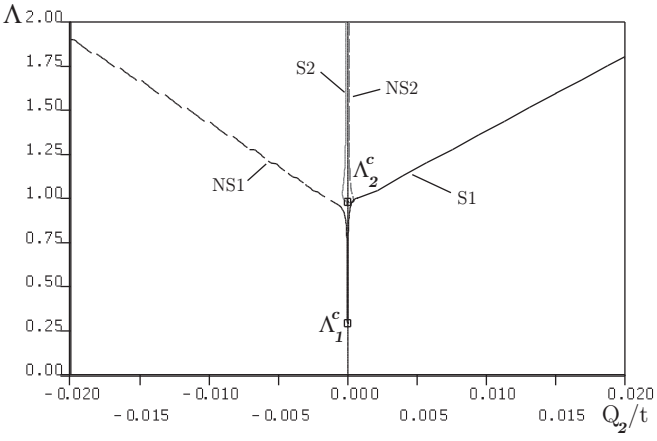

(b)

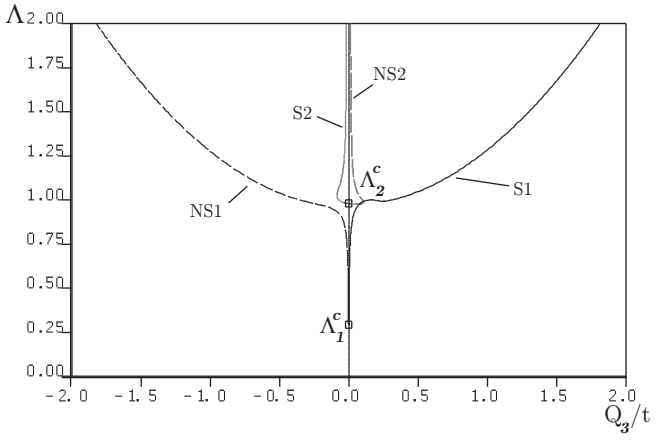

(c)

Figure 5.3: Postbuckling equilibrium paths for the local mode, case STAT-A. Graphs show the normalized axial load Λ versus (a) Q_1/t (upper laminate), (b) Q_2/t (lower laminate) and (c) Q_3/t (intact part).

This theoretical phenomenon, stemming from the analysis procedure, has also been observed by Hunt *et al.* (2004) in their delaminated strut model. Since they cannot exist in practice, the non-physical branches are discarded in later analysis (Nilsson *et al.*, 1993). However, it is worth noting that this behaviour could, in principle, be prevented by introducing a penalty function for the contact problem that naturally arises from such eigenvectors (Nilsson, 2001b). The non-physical branches are presented with dashed lines in Figure 5.3, with paths NS1 and NS2 for the first and second equilibrium paths, respectively. A general asymmetry in the branches can furthermore be observed. This asymmetry yields from the second and third part of the stress functions for the delaminated parts—equations (3.16) and (3.17)—which account for the effect of the overall panel on the undelaminated parts, *i.e.* either biaxial, uniform compression or tension which is imposed on the delaminated layers due to the displacement of the overall panel. However, once Q_3 becomes larger, Figure 5.3c, the overall panel buckle dominates and the local branches of Q_1 and Q_2 diminish for the closing mode, as shown in the curving back of the paths in Figure 5.3a and 5.3b respectively. This phenomenon will be explained in further detail in §5.2.4.

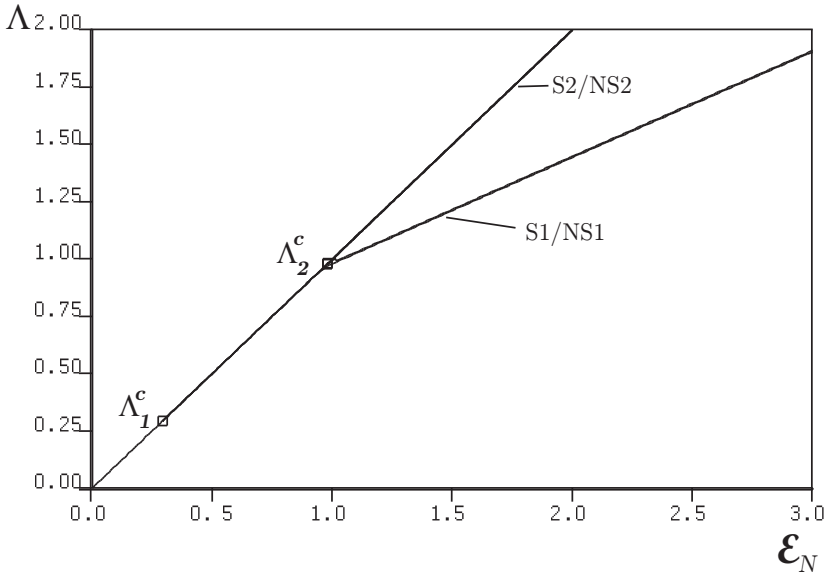

Figure 5.4: Normalized axial load Λ versus normalized end-shortening $\mathcal{E}_N$, case STAT-A.

In Figure 5.4, the normalized load Λ versus normalized end-shortening $\mathcal{E}_N$ is presented. For physical and non-physical branches the results are almost identical. It should also be noted that the stiffness decrease is more pronounced at the first critical load, *i.e.* paths S1 and NS1. However, this reduction in residual capacity is only present once the overall degree of freedom Q_3 dominates the behaviour. The stiffness decrease at the second critical load is negligible at a delamination of such small dimensions, *i.e.* for paths S2 and NS2.

5.2.2 Equilibrium solutions and mode behaviour

In this section, the postbuckling equilibrium solutions are discussed for various different delamination depths as denoted in Table 5.2. The first three cases, STAT-A, -B and -C, all of dimensions $a = 0.15L$ and $b = 0.15B$, are in the neighbourhood of the *transitional* delamination depth c_t where the modal behaviour essentially changes from local to mixed to global. This depth is observed to be situated in the range of 10–20% of the overall depth by Melin and Schön (2001) for their investigations on small delaminations; a finding that will also be demonstrated. In Figure 5.5 this region of the parameter space is magnified and c_t for the present configuration can be observed to be at around one-tenth of the depth from the surface of the panel, as will be demonstrated in the subsequent discussion.

It is noted that the postbuckling behaviour differs regarding the order of magnitude of the buckles; *i.e. local*, *mixed* or *global* modes can be identified, see Figures 5.6–5.8 (Kardomateas, 1993; Kim & Hong, 1997; Sekine *et al.*, 2000; Tafreshi, 2003). A sharp transition from global to local buckling usually takes place (Yin & Jane, 1992a).

For the first and second critical loads, *local* mode behaviour is observed when the delamination is located very close to the surface of the panel, *i.e.* case STAT-A and -B, which is also known as *thin-film buckling* (Chai *et al.*, 1981; Simitses *et al.*, 1985; Yu, 2003; Hunt *et al.*, 2004; Mei *et al.*, 2007). This means that the upper laminate

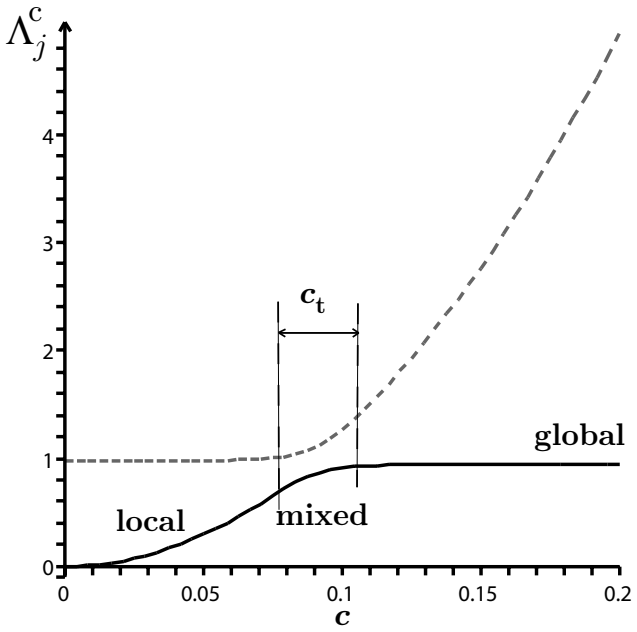

Figure 5.5: Transitional depth c_t: defined where the local mode transforms into the global mode through the mixed mode.

deflects in a more exaggerated fashion than the lower laminate, *i.e.* $Q_1 \gg Q_2$, see Figures 5.6 and 5.7. Even though it is the *closing* mode in the case of the first critical load, paths S1, where both laminates essentially deflect in the same direction (§4.3.2), the magnitude of the deflection of the thinner laminate completely dominates the behaviour which is particularly relevant for cases with small or barely visible delaminations that are often difficult to detect (Melin & Schön, 2001).

When the delamination is at a certain depth, the mode behaviour immediately after the first critical load changes from the *local* mode (case STAT-A) via a *mixed* mode (case STAT-B), *i.e.* $Q_1 \approx Q_3$, to effectively *global* buckling (case STAT-C and -D) mode where $Q_3 \gg Q_1, Q_2$, implying that overall buckling of the panel governs the behaviour once the critical load is triggered, see paths S1 in Figures 5.6–5.8.

The postbuckling equilibrium paths are shown subsequently where all cases are combined in one plot to show the difference in magnitude of the deflections, which is particularly visible for Q_1.

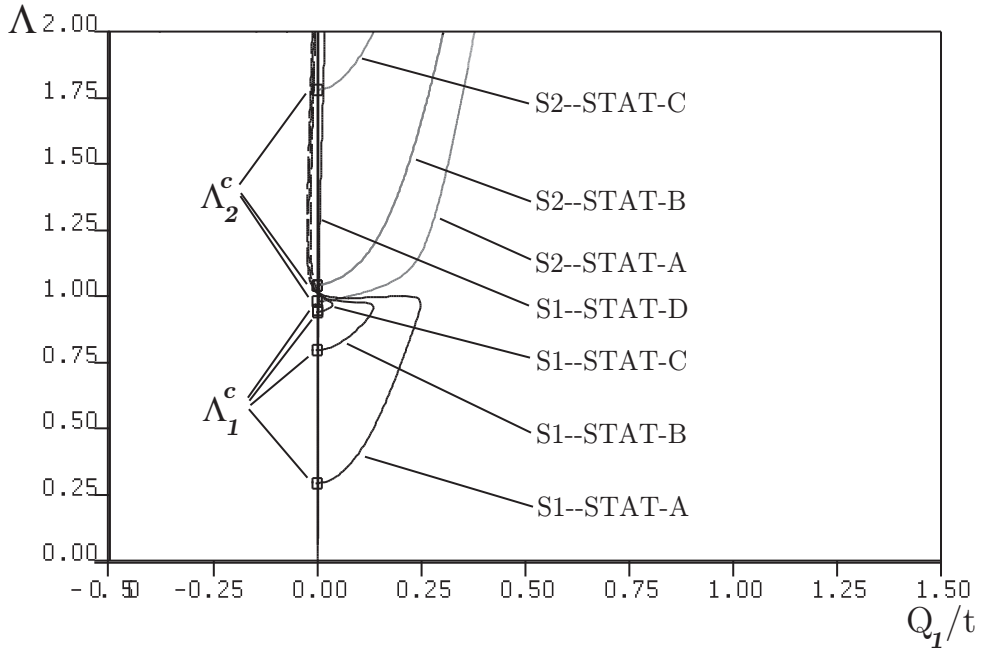

Figure 5.6: Postbuckling equilibrium paths for cases STAT-A, -B, -C and -D. Normalized axial load Λ versus Q_1/t.

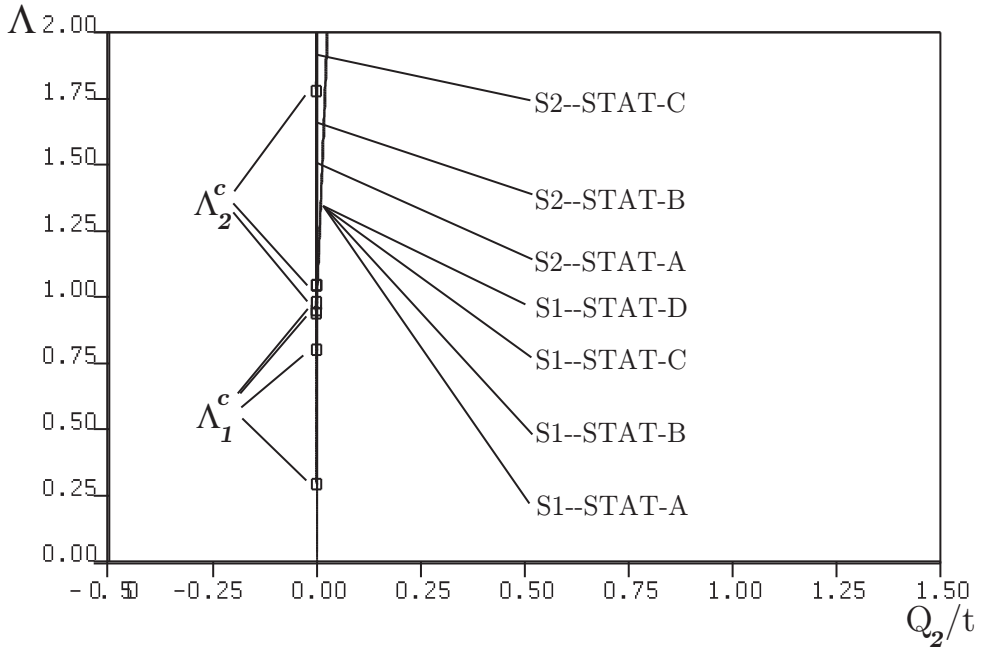

Figure 5.7: Postbuckling equilibrium paths for cases STAT-A, -B, -C and -D. Normalized axial load Λ versus Q_2/t.

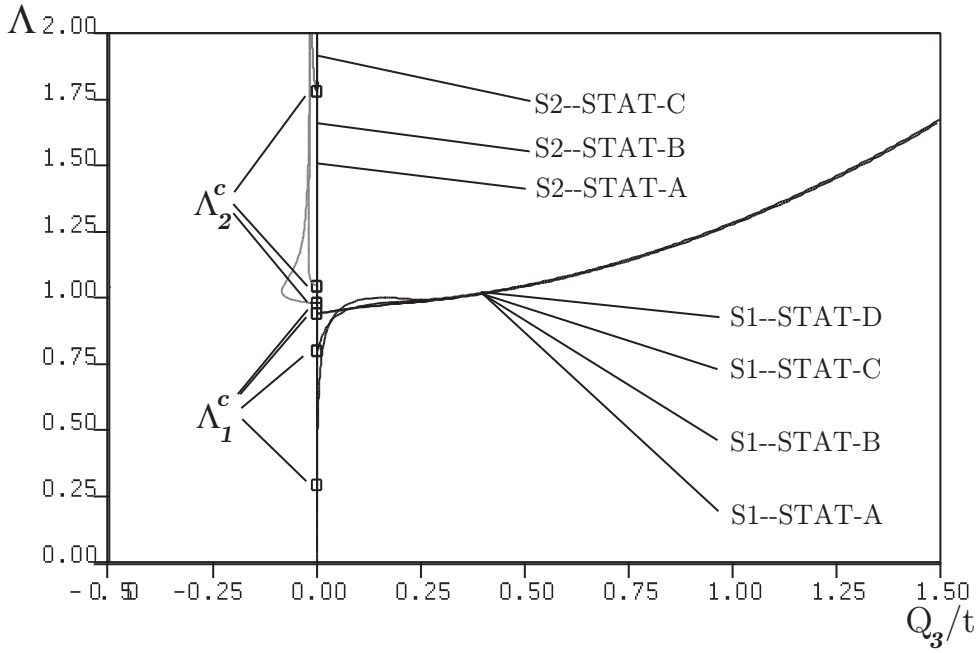

Figure 5.8: Postbuckling equilibrium paths for cases STAT-A, -B, -C and -D. Normalized axial load Λ versus Q_3/t.

As outlined above, the upper laminate displacement measure Q_1 is much larger than that of the lower laminate Q_2 for the *thin-film buckle*. This behaviour, however, does not persist for very long as the displacement measure for the overall panel Q_3 also begins to grow significantly. As shown in Figure 5.9 and also observed by Hunt *et al.* (2004) the decrease in stiffness is more dramatic after the first critical load, *i.e.* path S1, than after the second critical load, path S2, after an initially higher stiffness. This implies that a high reserve of stiffness is still present within the panel when only a local buckle occurs, but this instability soon influences the overall degree of freedom (Sekine *et al.*, 2000) which, in turn, causes a loss in stiffness once Q_3 dominates the behaviour. At the second critical load, the reduction in residual capacity is less pronounced. Bearing in mind that delamination propagation is not yet included, the expectation may be that the stiffness reduction would be more severe when this is incorporated, particularly when it is known to be the opening mode.

The second example case STAT-B presented is a *mixed* mode; typical *mixed* mode

behaviour is observed where $Q_1 > Q_2$, but Q_3 is large immediately after buckling occurs at the first critical load. Furthermore, the first and second critical buckling loads are relatively close together (Chilver, 1967; Johns & Chilver, 1971) for a delamination roughly at the transitional depth c_t which confirms the findings using linearized analysis shown in Figure 5.5. The decrease in stiffness is again more pronounced at the first critical load; this time, however, without the initially stiffer part (Figure 5.9) as in the earlier case. The relative difference between Q_1 and Q_2 is however still present, see both Figures 5.6 and 5.7, and could potentially promote delamination propagation if such a criterion depends on the relative opening between the laminates.

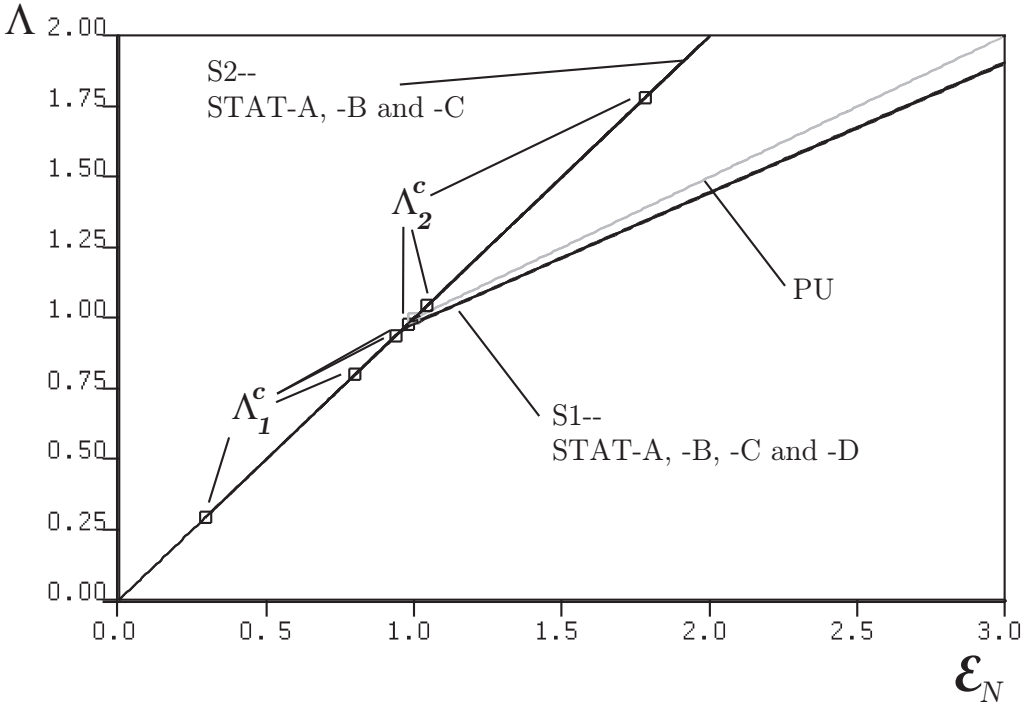

Figure 5.9: Normalized axial load Λ versus normalized end-shortening $\mathcal{E}_N$, cases STAT-A, -B, -C, and -D.

The third and fourth examples, cases STAT-C and -D, presented are global modes. Comparing case STAT-C with STAT-A and -B in Figures 5.6–5.8, it can clearly be noted that now the degree of freedom Q_3 governs the behaviour. However, the stiffness decrease remains the same, as can be seen in Figure 5.9.

In case STAT-D where $c = 0.5$, *i.e.* a delamination located at half-depth, it should be noted that the two laminates (degrees of freedom: Q_1 and Q_2) buckle with the same intensity in the same direction at the first critical load, which is the expected response (Short *et al.*, 2001). The overall buckle, however, dominates the behaviour immediately at the first critical load and in the postbuckling path S1, as seen in Figure 5.8. The decrease in stiffness being ultimately the same as in the other cases, just initiating from a higher critical load, as seen in Figure 5.9. However, with $Q_1 \approx Q_2$ and assuming only Mode I fracture occurs, there is no cause for undue concern of further stiffness reductions caused by delamination propagation in the case of the first critical load because of the *closing* mode behaviour, particularly if the growth criteria is governed by the relative opening between the laminates[1].

Finally, it should be noted that although various delamination sizes and depths are investigated, all panels exhibit stable postbuckling behaviour within the elastic range. Furthermore, the load versus end-shortening graph yields the same results in terms of the ultimate loss of stiffness for the same delamination size regardless of the initial depth of the delamination; the only difference is the reduction in the initial critical load when the delamination is located closer to the surface (see Table 5.2). It can be seen that the end-shortening for thinner delaminations is asymptotic to the end-shortening curve of the delamination at half-depth; hence the value of the critical load and the end-shortening can be deemed as a useful and quick estimate for a particular delamination size.

This can also be seen in Figure 5.10, where case STAT-E is included which has a larger delamination at mid-depth (see Table 5.2). As in the case of STAT-D, where c is also 0.5, the loss in stiffness occurs immediately after the critical load is triggered. However, the critical load is now already lower than that for a smaller delamination (cases STAT-A–D), as previously established in Chapter 4. The total reserve capacity is subsequently less than that for a smaller delamination and the postbuckling

[1]However, once Mode II fracture may be considered, growth may also occur in this scenario; this will be discussed in the further works section of the last chapter.

path for half-depth delaminations appears to be a reasonable benchmark for the residual capacity for a stationary delamination. Thus, the size of the delamination is of crucial importance and needs to be contained to guarantee a certain reserve capacity of the panel, since a larger delamination would lead to a lower initial critical load and subsequently lower reserve capacity in the postbuckling range when compared to an undamaged panel. The result is that in all cases the reserve capacity is less than one-half of the stiffness, which is the case for an undamaged simply supported panel with restrained edges (Bulson, 1969).

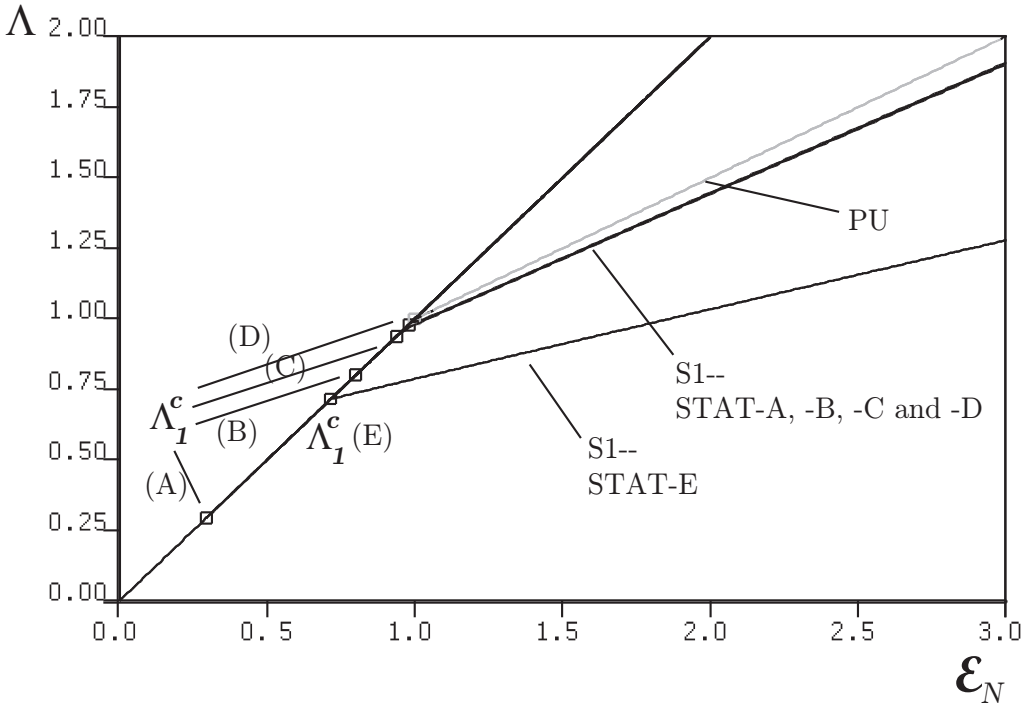

Figure 5.10: Normalized axial load Λ versus normalized end-shortening $\mathcal{E}_N$, cases STAT-A, -B, -C, -D and -E.

However, the mode behaviour in the postbuckling range changes with the depth and becomes a local mode with smaller values of c, which is understood to be crucial when considering delamination propagation (Hunt *et al.*, 2004) if the relative opening of the laminates is used for the growth criterion. Despite the fact that the load can still be increased, as seen in Figures 5.9 and 5.10, it is therefore essential to incorporate a growth criterion to establish a safe design scenario; this will be covered in Chapters

6–8.

Finally, the stiffness decrease for the second critical load, paths S2, is less than for the first critical load. This can be explained by the nature of the modes, *i.e.* closing or opening. In the former case, where buckling is triggered at the first critical load, the panel loses stability due to the defect since both laminates buckle in the same direction (recall Figure 4.6a). In the second case, the opening mode, the laminates deflect in opposite directions and therefore essentially "re-stabilize" the system, Figure 5.11, and hence a global instability is not triggered. Furthermore, the net second moment of area is slightly higher. This restabilization effect is reduced when propagation is considered.

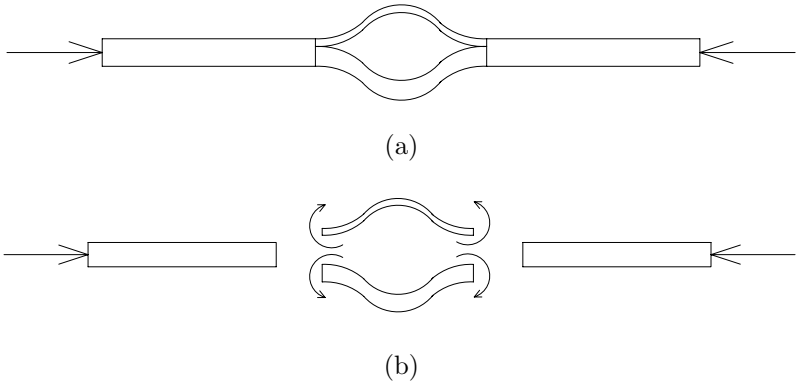

(a)

(b)

Figure 5.11: *Opening* mode; (a) configuration and (b) schematic of moment balance.

5.2.3 Finite element comparison

To validate the model, cases STAT-A, STAT-B and STAT-C were also investigated using the finite element model. The critical loads obtained with the analytical model are compared with the finite element model and the results are presented in Table 5.4. Furthermore, the model is validated in the postbuckling range for those three cases as shown in Figure 5.13.

It should be noted that the finite element model slightly underestimates the first critical load and overestimates the second critical load for $c = 0.05$ and $c = 0.085$,

Case	Λ_1^{C}	Λ_1^{FE}	error (%)	Λ_2^{C}	Λ_2^{FE}	Error (%)
STAT-A	0.295	0.292	-1.01	0.979	0.998	1.90
STAT-B	0.801	0.818	2.07	1.045	1.076	2.88
STAT-C	0.939	0.998	5.91	1.783	1.710	-4.27
Average error			2.99			3.01

Table 5.4: Normalized critical buckling loads comparison with finite element results.

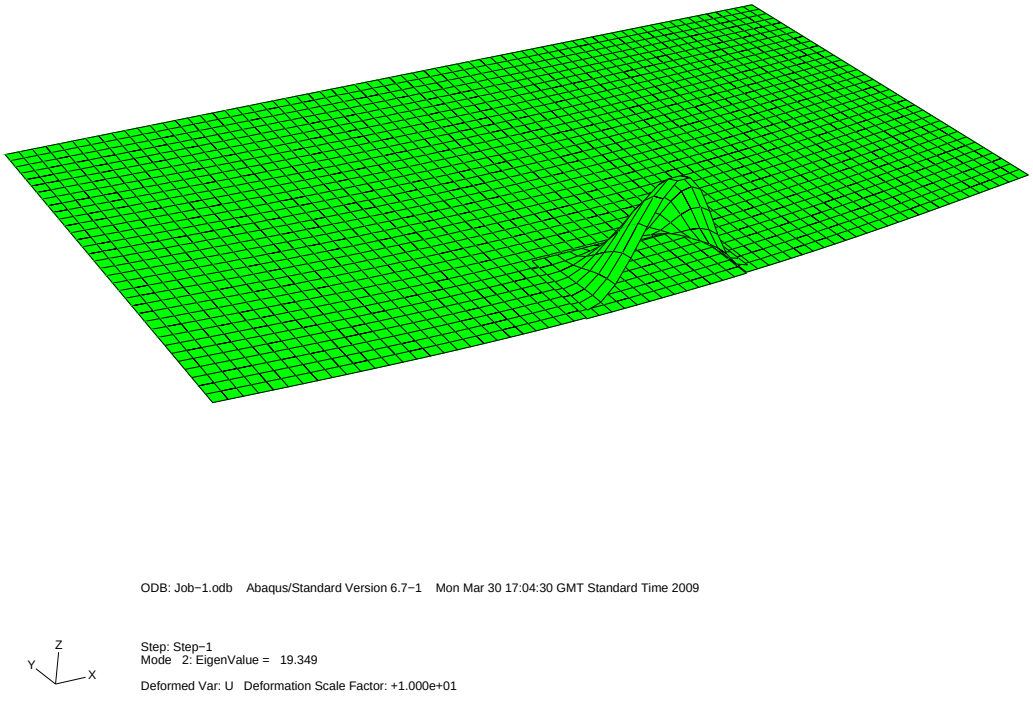

Figure 5.12: Finite element model: local *opening* mode.

cases STAT-A and -B, respectively. However, the error is very small in both instances. Once the delamination is located slightly deeper into the panel and mixed mode buckling is initiated, the error increases and now the first critical load is also overestimated. However, the average error is approximately 3% with the critical loads from the analytical model being almost matching or lower than the finite element solution and hence the results from the analytical model are deemed as satisfactory. It should also be noted, however, that the finite element model outputs an additional critical load between the first and second critical load from the analytical model as mentioned before in §3.6. This is partly due to the limitation in the available mode shapes since the analytical model is formulated with only the first terms in the series describing the out-of-plane displacement functions in equations (4.16) and (4.17). The simplicity of the model outweighs the fact that the mode in between is not picked up since the critical loads and modes are those that are relevant in the subsequent analysis when considering delamination propagation (Chapters 6–8). This will be explained in greater detail in following sections. Furthermore, the mode is only initially feasible since, with increasing load, the laminates penetrate and hence a contact problem would need to be formulated in the finite element procedure (Nilsson *et al.*, 1993), which would in itself stiffen the response.

The modal behaviour, *i.e.* closing and opening modes as well as local and global modes, was also identified with the finite element model and agrees with the analytical model. In Figure 5.12, the local opening mode for a small and thin delamination is shown which corresponds to the second critical load. The upper laminate deflects in the opposite direction to the lower laminate and the overall panel is only deflected marginally downwards, since this is a local mode. Hence, the deflection of the upper laminate dominates, as can be seen in the figure, and only a small overall panel deflection is be observed, as expected for such a small delamination.

In the postbuckling range, it can be established that the finite element model closely matches the analytical solutions for a stationary delamination, see Figure 5.13. The finite element solution, denoted by “FE” in the figure, is however higher than the

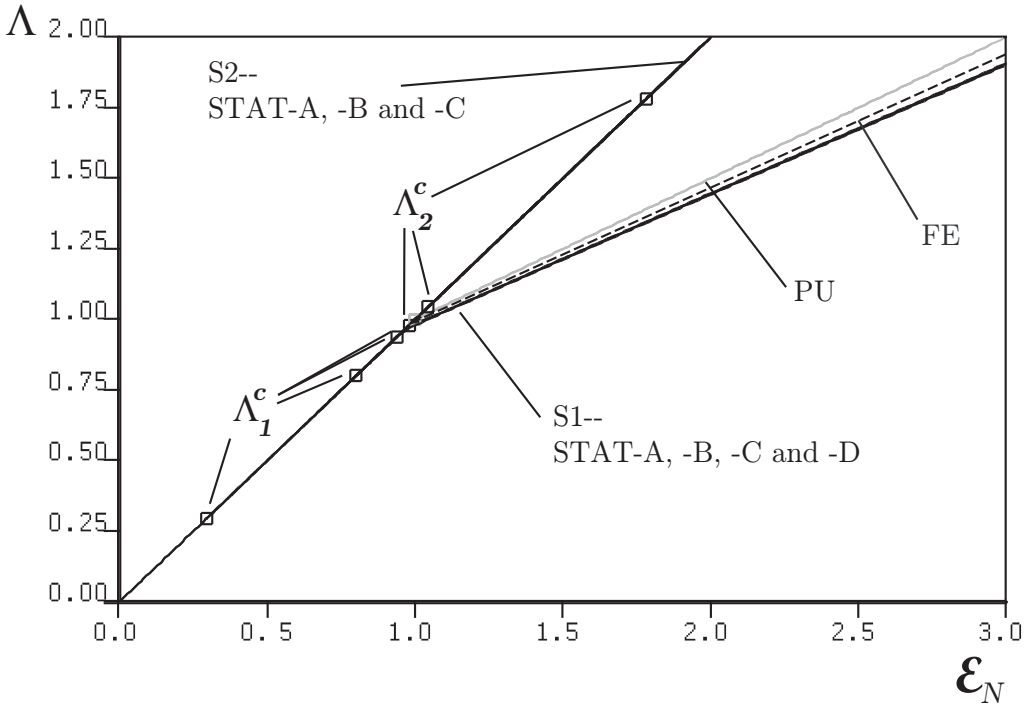

Figure 5.13: Normalized axial load Λ versus normalized end-shortening $\mathcal{E}_N$, cases STAT-A, -B, -C and -D; finite element comparison.

results obtained by the current model for all cases and therefore the analytical model can be deemed as safe.

5.2.4 Mode interaction

An investigation has been undertaken to determine potential mode jumping in the panels (Everall, 1999; Everall, 2000; Chen & Yu, 2006). Recalling Figure 5.6 one can clearly see that the equilibrium paths for the upper laminate from the first and second critical loads cross. This may indicate that mode jumping occurs, *i.e.* the closing mode would become an opening mode or vice versa when the load is increased. This had been observed previously by various other authors, in particular in the delaminated strut model developed by Wright (2006b). However, currently this type of mode jumping behaviour appears to not have been picked up by the model since the paths for the other degrees of freedoms in Figure 5.7 and 5.8 do

not coincide. This can also be seen in Figure 5.14 where essentially the equilibrium diagrams for the generalized coordinates Q_i are viewed from "above" with the Λ axis coming out of the plane. It appears that each postbuckling path has its distinct branch such that mode jumping occurs. Potentially, it may occur if higher modes are allowed in the formulations of the out-of-plane displacements, which is not the case in the present model. Furthermore, it should be noted that the paths are in fact very close such that AUTO may have not detected the jump but with a sufficient perturbation the mode jump could potentially occur which remains to be investigated.

Nonetheless, modal contamination or mode interaction (Chilver, 1967; Croll & Walker, 1972; Thompson & Hunt, 1973; Thompson & Hunt, 1984; Hunt *et al.*, 1986; Hunt, 1989; Falzon & Aliabadi, 2008) can be observed. This type of phenomena is found in compressed stringer stiffened panels (Koiter & Pignataro, 1976a; Koiter & Pignataro, 1976b), sandwich struts (Hunt *et al.*, 1988; Hunt & Wadee, 1998; Wadee *et al.*, 2010), built-up or reticulated columns (Thompson & Hunt, 1973) and prestressed stayed columns (Saito & Wadee, 2009) where an interaction between modes of local and global buckling may occur. In the present case, the mode interaction results in the loss in stiffness and is explained below. Furthermore, the physical behaviour of the panels in the *closing* mode is clarified; the example used is case STAT-B, a *mixed* mode type of buckling as described in §5.2.2.

The detected buckling mechanism, illustrated in Figure 5.16, has also been previously identified in a similar fashion by Gaudenzi *et al.* (2001). Figures 5.16a–5.16d can be described as follows corresponding to the notation in Figures 5.15, showing the bifurcation diagrams of the upper laminate (Figure 5.15a) and the intact panel (Figure 5.15b).

(i) The delaminated panel is loaded and initially straight (Figure 5.16a).

(ii) The first bifurcation point is triggered and the right-hand, thinner, laminate buckles only (Q_1) (Figure 5.16b).

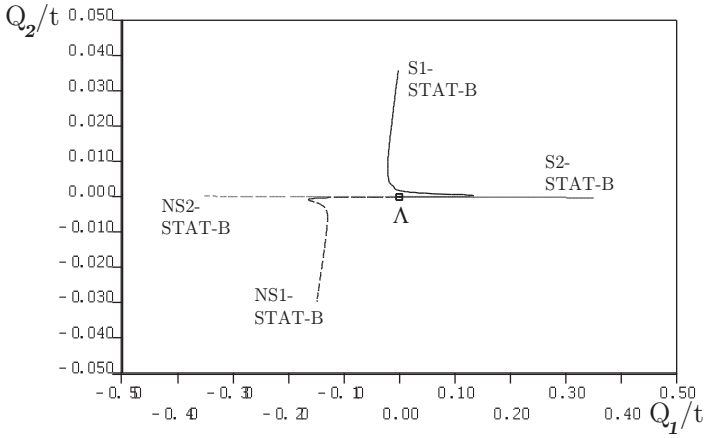

(a)

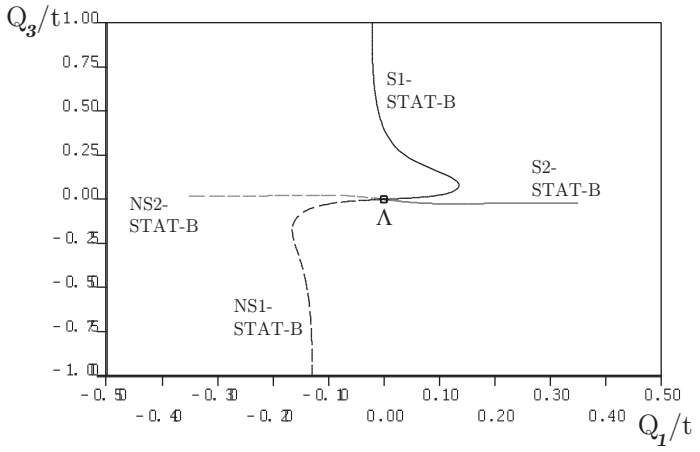

(b)

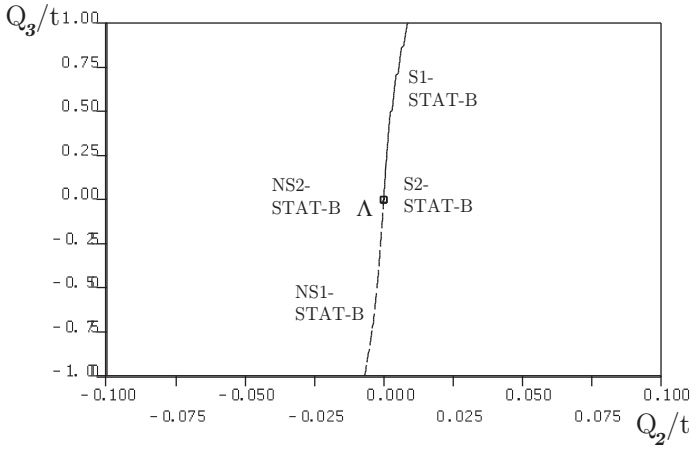

(c)

Figure 5.14: Postbuckling equilibrium paths for the mixed mode, case STAT-B. Graphs show the normalized degree of freedom of the upper laminate Q_1/t versus (a) Q_2/t (lower laminate), (b) Q_3/t (intact part); and (c) Q_2/t versus Q_3/t.

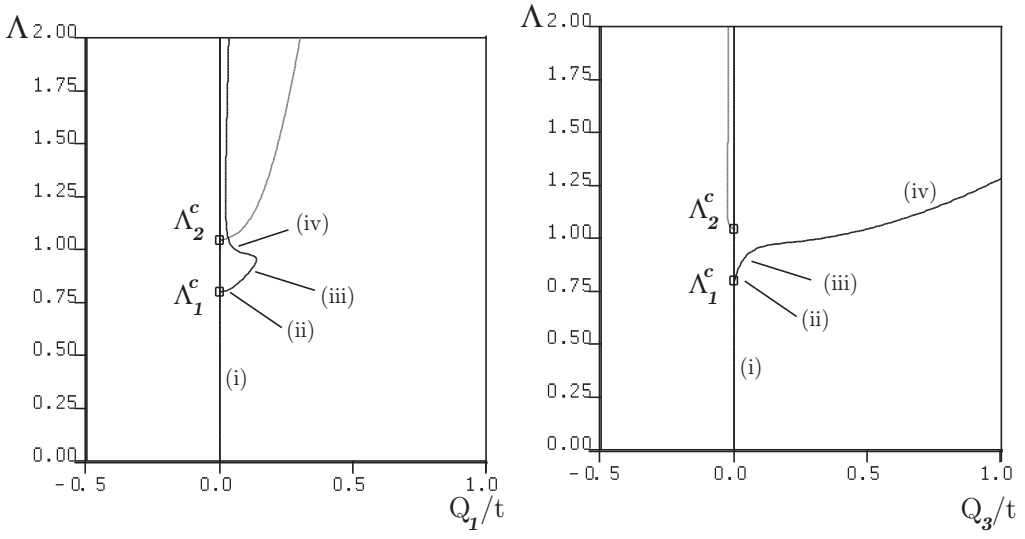

Figure 5.15: Postbuckling equilibrium paths for buckling mechanism—*closing* mode. Graphs show the normalized axial load Λ versus (a) Q_1/t (upper laminate) and (b) Q_3/t (intact panel).

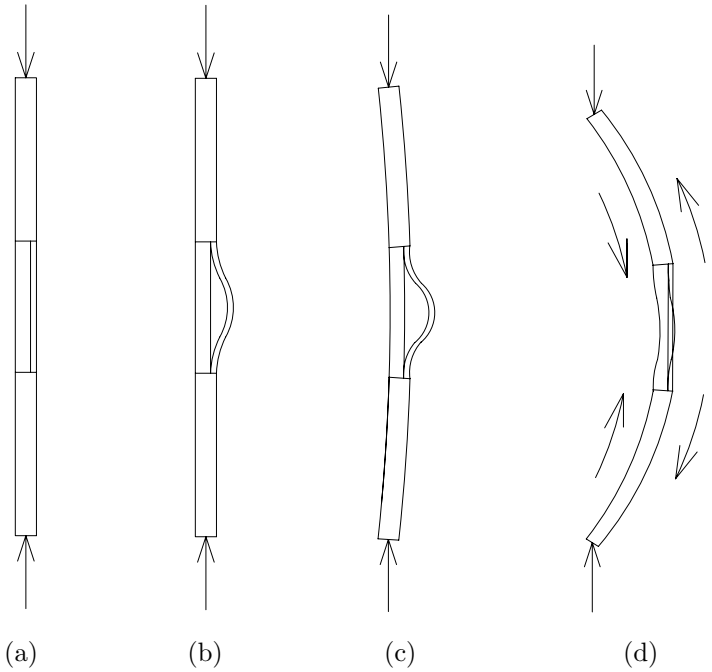

Figure 5.16: Buckling mechanism: *closing* mode; (a) initial configuration, (b) initial buckle of the upper laminate, (c) overall buckle initiates and (d) loss of stiffness due to overall buckling induced by local instability.

(iii) With increasing load, the local buckle also increases and the panel starts to buckle in the overall mode (Q_3) (Figure 5.16c).

(iv) Finally, the overall panel buckles severely (Figure 5.16d), which is induced by the local instability of the laminates and the stiffness decreases (see Figure 5.9); hence global buckling occurs. Once Q_3 is large, the local buckling restabilizes and the right-hand laminate buckle reduces due to the stretching effect on the outer fibres caused by the curvature of the overall panel. However, the left-hand laminate (Q_2) buckles marginally more due to the increase in compression in the inner fibres arising from the overall buckle. If the load is increased further, the deflection of the upper laminate becomes negative from the excessive curvature of the overall panel and a non-physical mode theoretically occurs. In practice, the thinner laminate would touch the thicker laminate and possibly slightly restabilize the buckle of the thicker laminate. Wadee and Blackmore (2001) modelled such behaviour for the one-dimensional problem of a sandwich strut undergoing face–core delamination. For the two-dimensional problem, however, this needs to be the subject of a separate investigation which is beyond the scope of the current study.

5.3 Concluding remarks

From the postbuckling analysis presented in this chapter for a stationary delamination, the following conclusions can be drawn. As already noted in the previous chapter, the critical load reduces with increasing delamination size, which can also be shown with the postbuckling analysis. However, the postbuckling analysis gives rise to the physical buckling behaviour after the critical load and must not be ignored if the panels are to be designed efficiently. In this chapter, the topic of physical and non-physical branches in the postbuckling equilibrium paths has been addressed first only for a qualitative discussion without allowing for any contact formulations; the non-physical branches are subsequently discarded.

Furthermore, the critical load reduces when the delamination is located closer to the surface of the panel. A transitional depth c_t can be determined, which is located at approximately 10%–20% of the thickness of this particular panel for smaller delaminations, where the modal behaviour changes from a local buckle, for thinner delaminations, via a mixed mode buckle to a global buckle of the overall panel.

It can also be seen that despite the fact that for small and thin delaminations, the critical load is very low, the postbuckling stiffness has a high reserve capacity until the overall panel starts to buckle. The stiffness reduction is then more pronounced and can be related directly to the instability introduced by the defect. For delaminations of the same dimensions but located closer to the mid-thickness of the panel, the overall buckling commences almost immediately after the critical load. Furthermore, it can be observed that the postbuckling paths of the thinner delaminations ultimately follow the path almost asymptotically. It is suggested, therefore, if the reserve capacity of a panel with a given defect is to be estimated, the postbuckling path of a delamination located at mid-depth may give a reasonable benchmark. However, delamination propagation is not yet incorporated into the model and it is identified that a dominant local buckle occurs in the cases where delaminations are relatively close to the surface (thin-films). The dominant local buckle of the sublaminate could potentially lead to the growth of the delamination which has to be investigated in depth.

Even for small delaminations, a stiffness reduction compared to an undamaged panel can be observed and the panels investigated never attain the residual capacity of one-half of the pre-buckling stiffness, as is the case for a simply supported panel without any defect. This clearly is a very important aspect when designing these types of structural elements, because the residual strength is reduced. Combining this finding with the potential of delamination spreading in cases of thin-film buckling, it is apparent that growth criteria need to be incorporated to make a safe estimate of the postbuckling capacity of the panels in-service.

A finite element comparison was undertaken as part of these investigations and

the numerical model yields an error of approximately 3%. The analytical model however, yields either approximately identical, for very thin delaminations, or lower loads compared to the finite element results and thus can be regarded as safe for the assumptions used so far. Furthermore, the mode behaviour corresponding to the matching critical loads is identical and hence the analytical model is shown to be valid. However, the finite element model may also lead to higher order local plate modes that are not captured by the analytical model due to the nature of the assumed out-of-plane displacement functions. Nevertheless, this turns out to be of less concern since these modes would rapidly lead to non-physical modes as discussed earlier. Furthermore, it can be established in the postbuckling range, that the finite element model's postbuckling stiffness closely matches the analytical solutions for a stationary delamination. The residual capacity is also marginally higher than the results obtained by the analytical model for all cases and subsequently can be deemed as basically giving a safe estimate for strength in the nonlinear range.

Chapter 6

Delamination propagation modelling

6.1 Introduction

Having established the elastic buckling and postbuckling behaviour of the delaminated plate model in Chapters 4 and 5 respectively, the irreversible damage mechanism of delamination propagation is now incorporated into the model. This mechanism can lead to significant structural weakening, particularly in compression (Orifici *et al.*, 2008). Internal delamination, see Figure 6.1, is the only mechanism in the inelastic range that is incorporated; no matrix cracks, fibre fracture or plasticity effects are considered. However, plasticity or fibre fracture from the effects of buckling could potentially be checked at the outermost fibres by evaluating the local strains, as will be discussed in §9.2.

From the previous chapter it is understood that, in particular, thinner delaminations may lead to delamination growth due to the dominant sublaminate buckling. The spread of the defect may lead to a structural instability (Shivakumar & Whitcomb, 1985) and may potentially reduce the residual capacity of the panel significantly

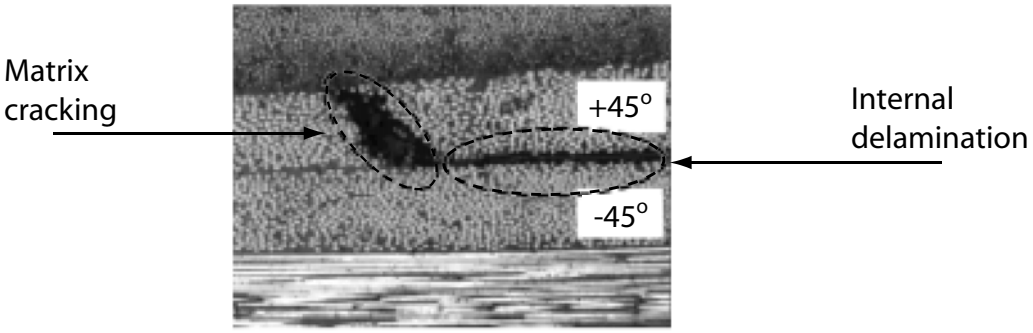

Figure 6.1: Internal delamination. This photograph from Camanho *et al.* (2001) shows an interaction between intralaminar and interlaminar damage.

and this subsequently has to be investigated carefully to predict safely the residual strength of the panels.

The problem of modelling delamination growth and introducing different growth criteria and models is a vast research field on its own (Pinho, 2005). Since the original aim of this work was to develop a relatively simple model to investigate the effects of different delaminations on the panel's capacity, rather than developing a sophisticated propagation model anew, it was decided purely to incorporate and apply such a model to allow the defect to spread. It is beyond the scope of this work to pursue the different approaches in every meticulous detail. However, a short review of delamination propagation modelling is presented currently, followed by a more detailed description of the discrete cohesive zone model that is adopted in the current work. The algorithm used to incorporate the growth criteria in AUTO (Doedel, 2007) is presented and numerical results for uniform delamination propagation will be discussed in the following chapters. Furthermore, this part of the current work has potential to be advanced in the future, as will be discussed in §9.2.

6.2 Delamination propagation modelling

Various different publications have addressed the topic of delamination propagation using different kinds or combinations of approaches, such as fracture mechanics

approaches (Griffith, 1921; Chai *et al.*, 1981; Wilkins *et al.*, 1982; Chai & Babcock, 1985; Kardomateas & Pelegri, 1994; Sheinman *et al.*, 1998), finite element modelling (Nilsson & Stårakers, 1992; Davidson, 1995; Alfano & Crisfield, 2001; Jensen & Sheinman, 2002; Camanho *et al.*, 2003; Østergaard, 2008), cohesive zone modelling or interface elements (Allix *et al.*, 1998; Mi *et al.*, 1998; Alfano & Crisfield, 2001; Elices *et al.*, 2002; Xie & Biggers, 2006; Xie *et al.*, 2006; Xie & Waas, 2006; Turon *et al.*, 2007), and experimental investigations (Davidson, 1995; Allix *et al.*, 1998; Wilkins *et al.*, 1982; Elices *et al.*, 2002). Different loading conditions have moreover been considered, ranging from dynamic or cyclic loading (Wilkins *et al.*, 1982; Allix *et al.*, 1998) to quasi-static or monotonic loading (Kardomateas & Pelegri, 1994; Bolotin, 1996; Jensen & Sheinman, 2002; Camanho *et al.*, 2003).

Possibly one of the earliest investigations on the growth of embedded delaminations close to the surface was undertaken by Chai and Babcock (1981; 1985). However, the closed form fracture mechanics approach utilized in those works, which is based on Griffith's (1921) groundbreaking findings, is only indirectly applied in the type of model presented later in §6.3 (Alfano & Crisfield, 2001).

In basic fracture mechanics, or linear elastic fracture mechanics—LEFM (Griffith, 1921; Bažant & Cedolin, 1991), the threshold maximum value of the interlaminar fracture toughness G_{iC} is compared to the strain energy G required to produce a new unit of interlaminar surface (Chai & Babcock, 1985). Once the strain energy released reaches the threshold value, the crack propagates. One method of calculating G per unit length $a*$ of crack width uses the total potential energy Π of the system thus:

$$tG = -\left[\frac{\partial \Pi}{\partial a*}\right]_u , \tag{6.1}$$

with t being the thickness of the structure, u being the displacement, and $\Pi(a*, u)$ being the total potential energy of the system, (Bažant & Cedolin, 1991). Other ways of determining G include, for example, stress intensity factors, J-integral or compliance changes and others, see Bažant & Cedolin (1991) for details.

The strain energy which is released G, sometimes denoted in the literature as Γ,

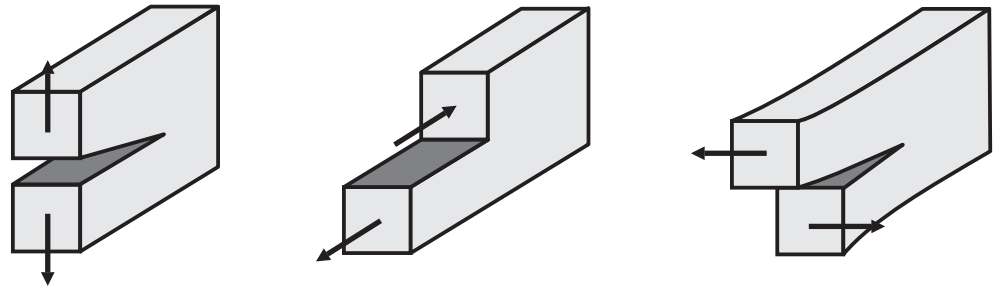

(a) (b) (c)

Figure 6.2: Crack growth modes taken from Orifici *et al.* (2007); (a) Mode I—opening, (b) Mode II—sliding and (c) Mode III—scissoring.

is, according to the separate mechanisms of crack growth, typically split into three components: namely Mode I—opening, Mode II—sliding or forward-shearing, and Mode III—scissoring or parallel-shearing, as shown in Figures 6.2a, 6.2b and 6.2c respectively, (Wilkins *et al.*, 1982; Bažant & Cedolin, 1991; Davidson, 1995; Allix *et al.*, 1998; Camanho *et al.*, 2003). However, as will be discussed later, a pure Mode I peeling mode is assumed in the current model.

The critical fracture toughness, G_{iC} corresponding to each crack growth mode i, can be determined for materials via specific tests; *e.g.* for Mode I, the opening mode, a double cantilever beam (DCB) test can be performed, Figure 6.3a, and for Mode II an end-notched flexure test can be performed, Figure 6.3b (Allix *et al.*, 1998). Similar tests can be conducted for mixed mode and Mode III fracture (Pinho, 2005).

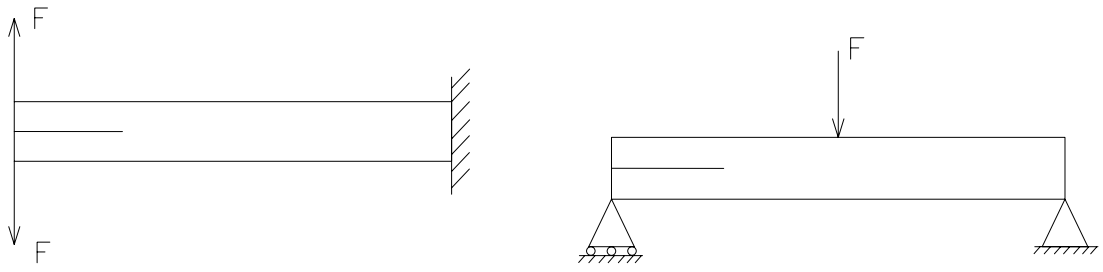

(a) (b)

Figure 6.3: Principles of fracture mechanics tests; (a) DCB test – pure Mode I and (b) ENF test – pure Mode II.

Another common approach to modelling crack propagation is the virtual crack closure technique—VCCT (Rybicki & Kanninen, 1977; Shivakumar *et al.*, 1988), where the components of the strain energy release rate are determined along the crack front based on two assumptions. Firstly, Irwin's assumption that the work necessary to close the crack to its original length is equal to the energy released in crack growth, and secondly that the crack growth does not significantly change the state of the crack tip (Camanho *et al.*, 2001; Orifici *et al.*, 2007). The nodal forces and displacements are used to compute the energy release rate and can be formulated in a simple form. Hence, this technique is often employed in finite element analysis due to its numerical advantage of capturing the crack development from a discrete approach.

The last approach reviewed forms the basis of the growth criteria incorporated in the current model and is based on cohesive elements, often employed in finite element models as an alternative approach to the approaches outlined above (Allix *et al.*, 1998; Mi *et al.*, 1998; Chen *et al.*, 1999; Alfano & Crisfield, 2001; Xie *et al.*, 2006; Turon *et al.*, 2007). These elements control the stresses and displacements at the delamination interface and have the advantage of allowing the determination of initiation as well as propagation of the defect; whereas the former is governed by a stress-based criteria, the latter is governed by fracture mechanics. However, it should be noted, that in the model discussed currently, a delamination already pre-exists, hence an initiation from an originally undamaged structure is not incorporated. Owing to the nature of the model, with the current plane stress assumption, see §3.3, stresses σ_z are not present and subsequently cannot be evaluated to employ a damage initiation criterion. However, the fracture mechanics type of damage modelling can be allowed for and will be subject of the following section.

6.3 The discrete cohesive zone model

The cohesive zone model or the interlaminar interface model in the spirit of finite elements is employed for the growth criteria to be incorporated into the formulation

developed in Chapter 3. This type of model has been successfully utilized by various authors to account for damage propagation (Allix *et al.*, 1998; Mi *et al.*, 1998; Alfano & Crisfield, 2001; Elices *et al.*, 2002; Xie *et al.*, 2006; Xie & Waas, 2006; Turon *et al.*, 2007; Benzerga *et al.*, 2008; Østergaard, 2008). Decohesion models can be divided into two principal categories: point or discrete cohesive elements or continuous decohesion elements (Xie *et al.*, 2006); the focus will be on the former since this is the approach implemented in the current model.

The current cohesive zone model type is based on the Dugdale–Barenblatt approach (Bažant & Cedolin, 1991; Camanho *et al.*, 2001) assuming that a fictitious crack extends to the beginning of the inelastic zone. One of the fundamentals of the approach is that the critical strain energy release rates G_{iC} corresponding to each fracture mode i, Figure 6.2, are inherent properties of the material interface and are independent of the load and geometry (Alfano & Crisfield, 2001). It is necessary to emphasize currently that, despite the capability of the approach to model mixed mode fracture processes, a pure Mode I type of fracture is assumed and incorporated into the model primarily for simplicity (Butler *et al.*, 2007; Rhead & Butler, 2009). However, because the growth is also conjectured to be critical in the thin-film closing buckling mode or opening mode delaminations, as demonstrated in the previous chapter, *i.e.* for small delaminations, the peeling mode dominates (Chai & Babcock, 1985; Melin & Schön, 2001). Mode II fracture is therefore insignificant due to the displacements at the interface of the defect to the intact panel (recall Figure 3.2), because overall buckling of the panel does not dominate the behaviour for the defect dimensions investigated. In addition, it has been shown by Rhead & Butler (2009) that assuming pure Mode I fracture gives a relatively safe lower bound despite the fact that in reality the propagation process would be of a mixed nature. Furthermore, the fracture Mode III is in all cases almost negligible (Whitcomb, 1989; Nilsson *et al.*, 1993). Hence, the following discussion will focus on a pure Mode I type of discrete cohesive zone model.

Before describing the method in detail, a few assumptions are made and discussed.

As mentioned before, the delamination is assumed to be pre-existing and growth occurs along a plane parallel to the reference plane (Chai *et al.*, 1981; Simitses *et al.*, 1985). The propagation occurs at the interfaces since their fracture toughness is lower than that of the plies (Wimmer & Pettermann, 2008) with a unidirectional lay-up yielding the worst case, *i.e.* the lowest, critical strain energy (Allix *et al.*, 1998). Furthermore, the propagation of delamination is considered to be buckling driven (Shivakumar & Whitcomb, 1985; Peck & Springer, 1991; Hutchinson *et al.*, 2000; Jensen & Sheinman, 2002) utilizing the steady-state nature of the buckle where deflections of the laminates provide the relevant criteria to determine the growth, since no interlaminar stresses occur until the delaminated region buckles (Shivakumar & Whitcomb, 1985). Propagation under quasi-static loading conditions is allowed for only (Bottega & Maewal, 1983; Bolotin, 1996; Kardomateas & Pelegri, 1994; Jensen & Sheinman, 2002; Camanho *et al.*, 2003), although it is understood that the discrete cohesive zone model is capable of capturing growth for cyclic loading conditions (Camanho *et al.*, 2001; Balzani & Wagner, 2008). Furthermore, for simplicity, the growth is assumed to be self-similar (Chai & Babcock, 1985; Peck & Springer, 1991) and rectilinear (Allix *et al.*, 1998) in both directions x and y in this chapter. Chapter 8 will address the topic of non-uniform delamination propagation.

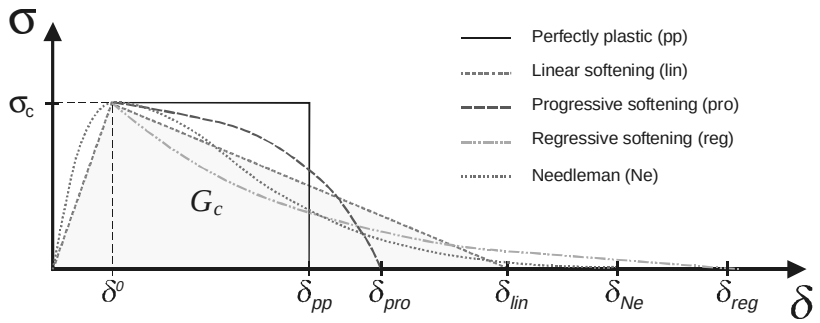

Figure 6.4: Constitutive strain softening relationships within the cohesive zone, taken from Camanho *et al.* (2001); with σ_c being the cohesive surface stress, δ the relative opening of the laminates and $G_\mathrm{C} \equiv G_\mathrm{iC}$ the critical strain energy release rate.

In cohesive zone modelling, the cohesive surface stress σ_c is related to the relative

opening of the laminates δ at the interface (Alfano & Crisfield, 2001; Camanho *et al.*, 2001; Elices *et al.*, 2002; Turon *et al.*, 2007) using a local energy balance, essentially based on the Griffith criteria (Griffith, 1921). Both σ_c and δ depend on the external load P and the interface is modelled with discrete springs of a certain stiffness K with both damage and fracture mechanics defining the response.

Different constitutive models can easily be adopted for this type of approach, as shown in Figure 6.4. However, for brittle materials, the bilinear cohesive zone material model is most commonly implemented, Figure 6.5 (Camanho *et al.*, 2001; Elices *et al.*, 2002; Camanho *et al.*, 2003; Xie *et al.*, 2006; Turon *et al.*, 2007), and will be utilized herein.

The relationship is characterized by the high initial stiffness K, holding the upper and lower laminates together in the linear elastic range until the stress reaches the tensile strength σ_c, sometimes also denoted as $\sigma_{\max}$. Subsequently, softening occurs

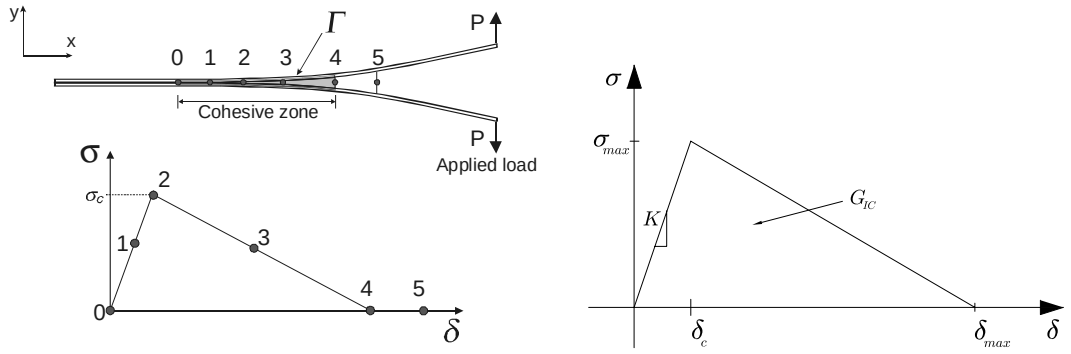

(a) (b)

Figure 6.5: Constitutive relationship used in the cohesive zone model. (a) Cohesive zone ahead of delamination tip from Camanho *et al.* (2001); (b) piecewise linear constitutive relationship with the area under the graph equating to G_{IC}, the critical strain energy release rate.

(Elices *et al.*, 2002) until the area under the curve reaches the critical strain energy release rate G_{IC} and the crack propagates. Thus, a complete debond of the interface occurs (Point 5 in Figure 6.5a) and the zone needs to be moved along usually by the

use of an algorithm (Whitcomb, 1989; Xie *et al.*, 2006). The work of separation per unit area can be calculated as the area under the curve with the following expression of Γ, (Alfano & Crisfield, 2001; Camanho *et al.*, 2001; Turon *et al.*, 2007):

$$\Gamma = \int_0^{\delta_{\max}} \sigma(P)\,\mathrm{d}\delta\,, \tag{6.2}$$

which for the bilinear constitutive relationship is given as:

$$\Gamma = \frac{1}{2}\sigma_{\max}\,\delta_{\max} = G_{\mathrm{IC}}\,. \tag{6.3}$$

Hence, once Γ equals G_{IC}, the critical strain energy release rate is reached; since G_{IC} and $\sigma_{\max}$ are taken as known material properties of the interface, the maximum separation $\delta_{\max}$ can be readily obtained by simple rearrangement of equation (6.3) (Alfano & Crisfield, 2001):

$$\delta_{\max} = \frac{2\,G_{\mathrm{IC}}}{\sigma_{\max}}\,. \tag{6.4}$$

The advantage of using this approach is that the delamination initiation, at the critical opening δ_{c}, as well as the damage growth—once the critical strain energy release rate at $\delta_{\max}$ is reached—can be predicted and analysed.

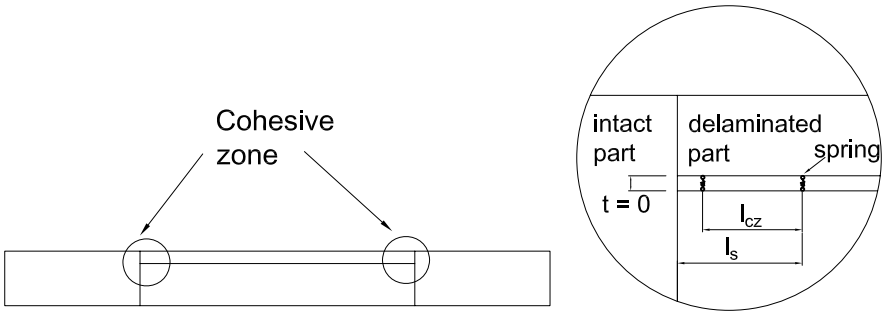

Figure 6.6: Discrete cohesive zone model; location of (a) model and (b) spring.

To incorporate this type of model an interface layer of zero thickness consisting of springs is positioned between the two layers of the delamination at the transition of the delaminated patch to the intact area, see Figure 6.6a.

The spring that contributes to the gain in the energy release rate is positioned in the delaminated part, at a distance $l_s = a/10$ or $l_s = b/10$ away from the intact

part, see Figure 6.6b. The length l_s is chosen because it is always conveniently located approximately in the middle of the outward bending moment region that would cause crack opening. It is furthermore understood that the positioning of the spring needs to be linked to the mode shapes and subsequently the overall dimensions of the delamination, rather than having a fixed value. This is because the displacements w_i of the laminates describe the clamped behaviour of the defect and hence the crack. The distance l_s is chosen at the point where the displacement of the laminate is approximately 10% of the overall amplitude of the laminas. Beyond this point, *i.e.* for $l_s > a/10$ or $l_s > b/10$, the displacements w_i increase dramatically, as shown for both closing and opening mode configurations in Figure 6.7. Hence, up to this point, $\delta(P)$ is small and reflects the virtual crack, resulting from the clamped conditions of the out-of-plane displacement functions. Furthermore, as will be observed in Chapter 7, the positioning of the spring at this location yields good comparison with existing growth predictions in the literature.

Since the postbuckling solutions of the panels are determined, the growth criteria can be calculated, (Kardomateas & Pelegri, 1994), via the extension of the spring, δ_x or δ_y, thus:

$$\delta_x(P) = \frac{1}{b}\left[\int_{-b/2}^{b/2} w_1\left(x_1 = a/2 - l_s, y_1\right) \mathrm{d}y_1 - \int_{-b/2}^{b/2} w_2\left(x_2 = a/2 - l_s, y_2\right) \mathrm{d}y_2\right] \quad (6.5)$$

and similarly for δ_y

$$\delta_y(P) = \frac{1}{a}\left[\int_{-a/2}^{a/2} w_1\left(y_1 = b/2 - l_s, x_1\right) \mathrm{d}x_1 - \int_{-a/2}^{a/2} w_2\left(y_2 = b/2 - l_s, x_2\right) \mathrm{d}x_2\right]. \quad (6.6)$$

The value is the same in both x and y directions due to the averaging over the width, thus $\delta(P)$ is subsequently used for simplicity. The values arising from the integration are averaged to model the cohesive zone as a unit width when evaluating the energy (Turon *et al.*, 2007).

The length of the cohesive zone, l_{cz}, *i.e.* the size of the step the springs are moved once the total debond occurs, is determined as a material property according to Hillerborg's model (Bažant & Cedolin, 1991; Elices *et al.*, 2002; Sun & Jin, 2006;

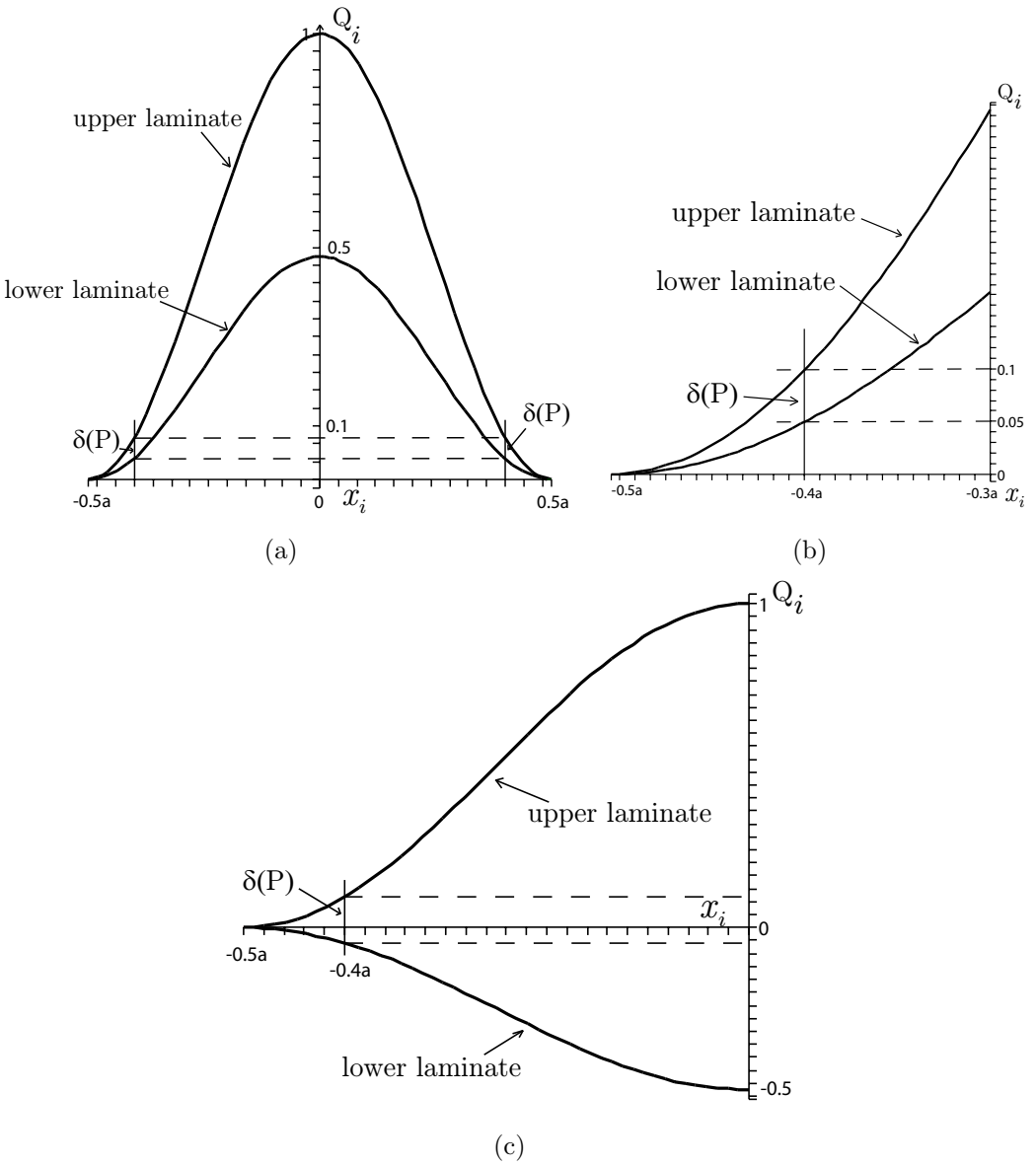

Figure 6.7: Schematic spring displacement $\delta(P)$ at spring location l_s; (a) closing mode, (b) closing mode enlarged and (c) opening mode.

Turon *et al.*, 2007) with:

$$l_{\text{cz}} = \frac{E_z G_{\text{IC}}}{\sigma_{\text{max}}^2}, \tag{6.7}$$

where E_z is the Young's modulus in the out-of-plane direction and σ_{max} is the maximum cohesive strength of the interface. Note that $l_{\text{cz}} \neq l_s$ (Figure 6.6b), since l_{cz} is the largest step, the springs can be moved once the first spring is fully delaminated and l_s is the parameter determining the position of that particular spring. This, however, requires a fine mesh (Orifici *et al.*, 2008) and usually a minimum of three finite elements are used in the cohesive zone (Turon *et al.*, 2007). To find a smooth solution that converges, the step size is adjusted during the procedure to find the postbuckling solution for a propagating delamination that is described below.

6.3.1 Algorithm for delamination propagation

The algorithm developed and incorporated into AUTO (Doedel, 2007) to allow for delamination growth is as follows:

1. The analysis in AUTO is started as usual and the critical loads are obtained, Point 1, Figure 6.8.

2. The equilibrium paths are traced and analysis is halted when δ is equal to δ_{max}, Point 2, Figure 6.8. At this point, the critical strain energy release rate G_{IC} is reached—equation (6.4)—and the cohesive zone has completely delaminated. The stress at which $\delta = \delta_c$, *i.e.* delamination propagation initiates, is of little interest in this static propagation model and therefore not included in the discussion.

3. The lengths a and b are increased by the amount of the cohesive length l_{cz} or by a smaller step size, if a smooth solution cannot be obtained by using l_{cz}, and the new equilibrium solution for this set of parameters is determined, Point 3, Figure 6.8. However, δ could be now larger or smaller than δ_{max}.

4. In the case that the $\delta > \delta_{\max}$, Point 4, Figure 6.8a, the load needs to be reduced to find the new equilibrium position corresponding to the maximum opening of the laminates, *i.e.* the solution releasing the maximum strain energy. In the other case, where $\delta < \delta_{\max}$, the load can be increased and new equilibrium position for the new set of parameters is found, Point 4, Figure 6.8b.

5. This procedure is continued until the propagation stops or sufficient propagation has occurred such that the algorithm is halted and the results are processed.

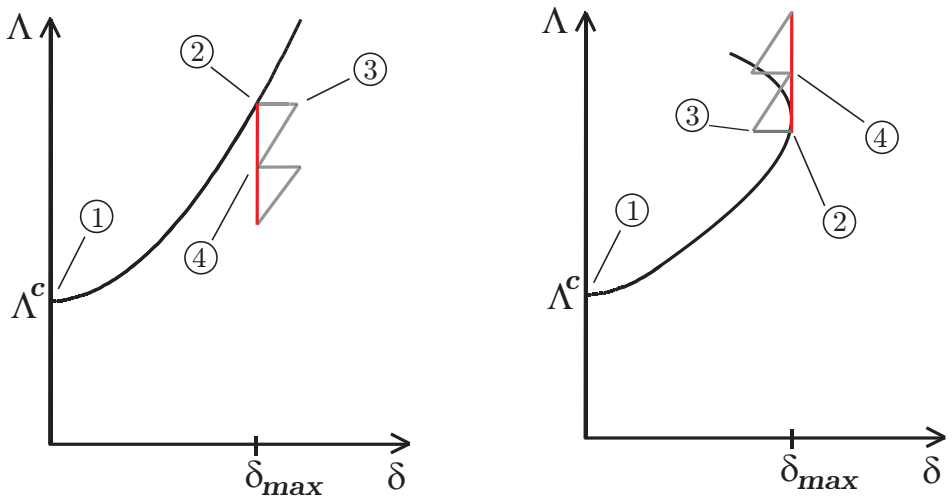

Figure 6.8: Delamination propagation in AUTO; adjustment for δ where the load needs to be (a) reduced or (b) increased.

The algorithm is presented in a further schematic in Figure 6.9 where the adjustment of the position of the cohesive zone is shown in detail. The incorporation of the irreversible damage mechanism has been established within this chapter and the following chapters will present the results obtained with the developed model. Initially, uniform damage growth will be incorporated for different defects of barely visible impact dimensions in the following chapter whereas Chapter 8 will discuss non-uniform delamination propagation as a pilot study.

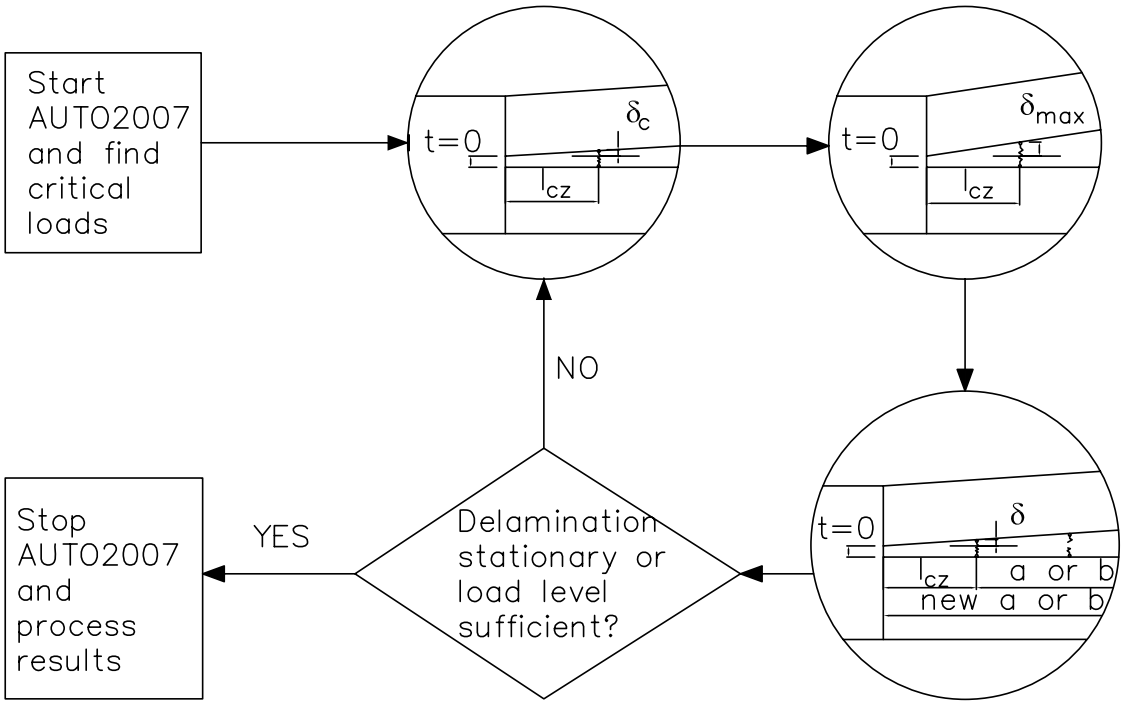

Figure 6.9: Delamination algorithm schematic.

Chapter 7

Postbuckling regime of a uniformly propagating delamination

Having described and outlined the algorithm employed when delamination propagation is incorporated using a discrete cohesive zone model in the previous chapter, numerical results for delaminated panels are presented. In the current chapter, results including uniform delamination propagation are presented and discussed. Various cases in the barely visible impact damage range have been extensively investigated and are presented herein.

Initially, the results for the different cases are described individually with a summary for each case. The results are then compared and related to parameters and conclusions are drawn regarding the damage behaviour and its importance.

7.1 Numerical experimentation and results

The investigations incorporate the delamination algorithm for uniform growth in both dimensions, *i.e.* x_i and y_i, see Figure 7.1; for different initial delamination sizes, see Table 7.1 and for the depths of delamination in each case, see Table 7.2.

However, the model has the potential of incorporating non-uniform delamination propagation as will be discussed Chapter 8 and further as part of the future work in §9.2.

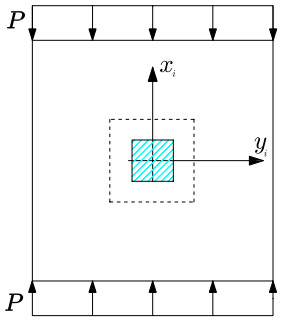

Figure 7.1: Uniform delamination propagation.

Material properties are again as summarized in Table 5.1 in §5.2. Uniform delamination is investigated for panels containing four different cases of a small or barely visible pre-existing delamination of dimensions as presented in Table 7.1; similar to values found in the literature (Whitcomb, 1989; Nilsson *et al.*, 1993; Short *et al.*, 2001; Craven *et al.*, 2010), and in accordance with the cases in Chapter 5. These types of delaminations are of primary concern owing to the difficulty in detecting this type of damage (Melin & Schön, 2001) whilst drastically reducing the strength of the panels. It was seen in §4.3.1.1 that the analytical model yields a good comparison with the finite element model around the transitional depth c_t where the critical buckling mode behaviour changes from local via mixed mode to global buckling. Subsequently, a range of depths is investigated for each case in the neighbourhood of the transitional depth c_t, where the parameters are chosen such that sublaminate buckling precedes overall buckling since otherwise the delamination cannot spread (Bottega & Maewal, 1983). This local buckling can promote the growth of the delamination away from its original location (Rhead & Butler, 2009) as will be seen in the subsequent examples. As in these articles, the critical delamination is assumed to lie within 20% of the plies closest to the surface, hence only these depths are investigated, as summarized in Table 7.2.

Case	a	b	% delaminated area
0	$0.12L$	$0.12B$	1.44
1	$0.15L$	$0.15B$	2.25
2	$0.20L$	$0.20B$	4.00
3	$0.25L$	$0.25B$	6.25

Table 7.1: Examples of postbuckling with uniform delamination propagation. The overall plate has dimensions $L = B = 100$ mm.

The convention for the abbreviations in the graphs are as described in Table 5.3, however cases now include uniform delamination propagation, see Table 7.3, these are denoted as paths "P1" and "P2". Again, the postbuckling equilibrium paths are compared to the perfect behaviour of the undamaged panel. It is worth emphasizing that non-physical branches are neglected for reasons outlined in Chapter 5.

As before, the first two normalized buckling paths are discussed (Chai & Babcock, 1985) and the postbuckling and growth characteristics are investigated herein. Furthermore, these characteristics are distinguished between force-controlled and displacement-controlled loading and their impact on the growth stability (Wimmer & Pettermann, 2008).

Case	(A)	(B)	(C)	(D)	(E)
0	**0.05**	*0.065*	0.075	0.10	–
1	**0.03**	**0.05**	*0.085*	0.12	0.20
2	**0.05**	*0.085*	0.11	0.15	–
3	**0.05**	*0.11*	0.15	0.20	–

Table 7.2: Values of delamination depth parameter c for postbuckling cases investigated with uniform delamination propagation. Thin-film buckling cases are indicated in **bold**, mixed mode cases in *italics* and global buckling in Roman font.

Label	Description
PU	Postbuckling path of an undamaged panel
S1	First physical postbuckling path of a damaged panel containing a stationary delamination
S2	Second physical postbuckling path of a damaged panel containing a stationary delamination
P1	First postbuckling path of a damaged panel containing a uniformly propagating delamination
P2	Second postbuckling path of a damaged panel containing a uniformly propagating delamination
FE	Path of the finite element model containing a stationary delamination

Table 7.3: Abbreviations for the graph labels describing the postbuckling behaviour of a panel containing a uniformly propagating delamination.

7.1.1 Results and discussion: Case 0

Initially, the model was compared with the literature in case 0, *i.e.* $a = b = 12$ mm. The results for this case are presented only in tabulated form and the focus is on the other three cases in this chapter.

The critical loads Λ_j^{C}, the loads at which propagation commences $\Lambda_j^{\mathrm{prop}}$ and the minimum loads reached during propagation Λ_j^{min} for each buckling mode j are presented in Tables 7.4–7.7; the notation that is used is shown schematically in Figure 7.2. Furthermore, it is stated for each case whether the growth is stationary when the algorithm, discussed in the previous chapter, is halted at Λ_j^{max} and to what extent the delamination has grown.

Melin and Schön (2001) stated in their literature review, Reference [17], that for a BVID, growth was observed to occur from 11 mm to 19 mm. Despite the different modelling approaches, this compares well quantitatively with the values found with the current model for case 0, Table 7.4, where the delamination grows from

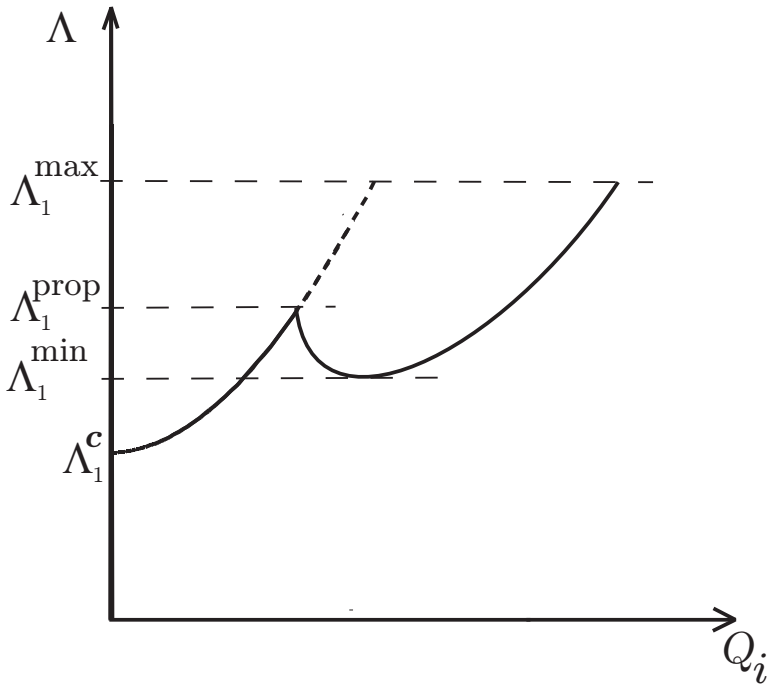

Figure 7.2: Schematic of notation in Tables 7.4–7.7.

12 mm to either 22 mm or 20 mm in case 0 (A) or (B) respectively. Thereafter the propagation is stationary and no further growth occurs since overall buckling governs the behaviour. This occurs at values $\Lambda_1^{\max} = 0.884$ and $\Lambda_2^{\max} = 0.901$ which is marginally lower than the value of $\Lambda^{\mathrm{C}}_{1,c=0.5} = 0.967$ for a delamination of this size at half depth, *i.e.* $c = 0.5$ (Table 7.8). This benchmark value had been established in §5.2.2 for the quick estimation of a panel's capacity. However, it can already be seen that even for small delaminations, a reduction in capacity due to the growth occurs. Moreover, the delamination growth rate reduces with the depth of the delamination (Melin *et al.*, 2002) for the first critical load, which will be discussed in greater detail in the subsequent examples.

Only in case 0 (B), the mixed mode case, a load drop is initially observed for the first critical load, before the system restabilizes. This unstable, shell-like behaviour was also previously identified by Hunt *et al.* (2004) for the mixed mode buckling case of the strut. However, the maximum load, if growth is permitted, before the system experiences an overall loss of stability, can be determined to be around 88%

Case 0	(A)	(B)	(C)	(D)
Λ_1^{C}	0.459	0.755	0.905	0.959
$\Lambda_1^{\mathrm{prop}}$	0.722	0.953	–	–
Λ_1^{min}	–	0.862	–	–
a and b at Λ_1^{min} (mm)	–	16.5	–	–
Λ_1^{max}	0.884	0.901	–	–
a and b at Λ_1^{max} (mm)	22	20	–	–
growth stationary at Λ_1^{max}?	yes	yes	–	–
Λ_2^{C}	0.994	1.024	1.139	1.915
$\Lambda_2^{\mathrm{prop}}$	1.046	1.237	1.384	2.1938
Λ_2^{min}	1.044	1.111	1.196	1.513
a and b at Λ_2^{min} (mm)	12.5	15.5	17	20
Λ_2^{max}	3.195	2.535	2.461	2.610
a and b at Λ_2^{max} (mm)	41	36	35	35
growth stationary at Λ_2^{max}?	no	no	no	no

Table 7.4: Results summary: Case 0.

of an undamaged panel's capacity, see Λ_1^{max} case 0 (A). In cases (C) and (D) no growth is observed for the first critical load. This is because overall buckling of the panel governs the behaviour.

In all cases, unstable growth was observed for the second critical load. However, there was no load drop below $\Lambda = 1$ observed in any of the cases. Hence, assuming a panel is not designed to withstand loads higher than the critical load for an undamaged panel, *i.e.* the panel is not designed using the postbuckling capacity, then a reduction due to the defect is of no concern and can be disregarded.

The following sections will, however, discuss this in more detail for the other cases investigated. Case 0 is the smallest of the BVIDs examined and was deemed not to be of critical nature since the growth is not significant and the load carrying capacity is not significantly affected. Hence, the focus in this chapter is on the other cases

with slightly larger delamination sizes.

7.1.2 Results and discussion: Case 1

In this section, a selection of the results varying relative delamination depths c for case 1, $a = b = 15$ mm, as summarized in Table 7.2, are presented and discussed. Currently, a value of $c = 0.03$, case 1 (A), is also included to investigate the impact when the delamination is even thinner than $c = 0.05$, which was studied in §5.2. In addition, a value of $c = 0.20$—case 1 (E)—is examined to allow for slightly deeper delaminations, beyond the transitional depth c_{t} established in Chapter 5, Figure 5.5, established in Chapter 5.

7.1.2.1 Case 1 (A)

The critical loads for case 1 (A) are triggered at $\Lambda_1^{\mathrm{C}} = 0.107$ and $\Lambda_2^{\mathrm{C}} = 0.975$. As shown in Figure 7.3, local upper laminate buckling occurs, with Q_1 dominating the behaviour in both equilibrium paths, at least initially. As established before, in the closing mode configuration, a global instability is soon triggered where Q_3 governs the buckling behaviour.

For the first critical load, delamination propagation occurs at a value of $\Lambda_1^{\mathrm{prop}} = 0.281$, *i.e.* the load can be increased by approximately 18% of the overall capacity of the undamaged panel until propagation occurs. The growth is stable under load-control in the spirit of the discussion by other authors (Bottega & Maewal, 1983; Kardomateas & Pelegri, 1994; Wimmer & Pettermann, 2008), Figure 7.4, which can furthermore be seen for the present case in Figure 7.5, where the load is plotted versus the growth. The delamination grows up to a size of $a = b = 39$ mm until the growth is arrested at $\Lambda_1^{\mathrm{max}} = 0.874$, which is lower than the value $\Lambda_{1,c=0.5}^{\mathrm{C}} = 0.950$ for a delamination at half depth, Table 7.8. It can be seen, comparing to case 0 that even a marginally larger delamination already leads to significantly higher growth

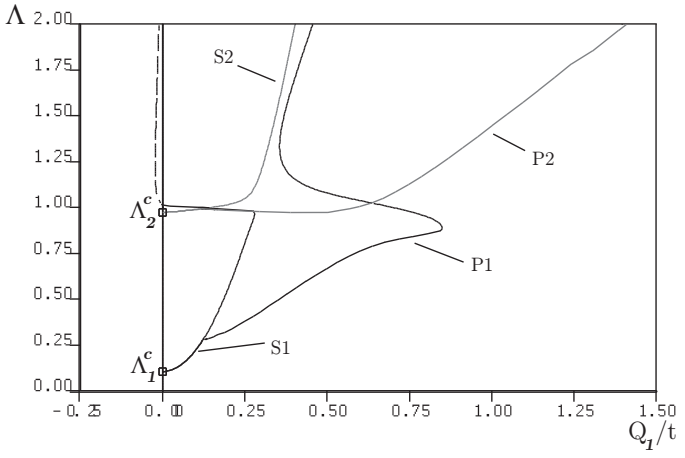

(a)

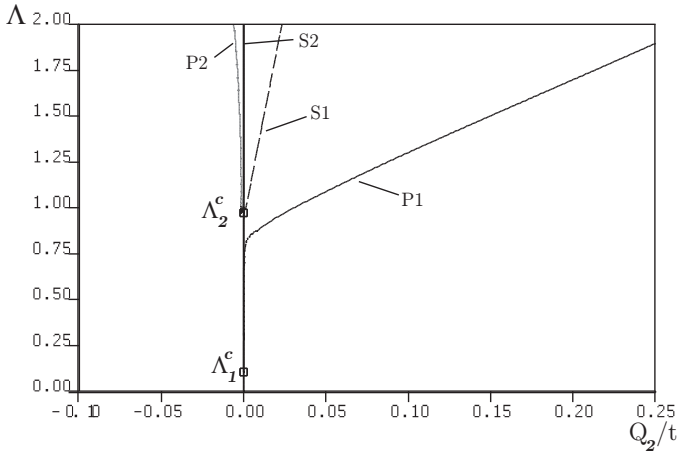

(b)

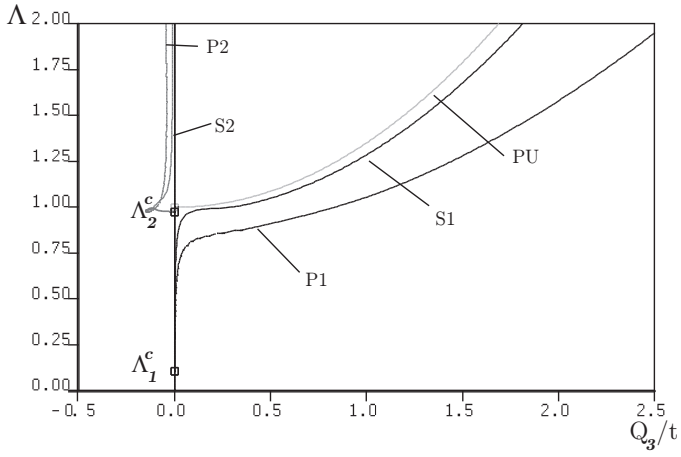

(c)

Figure 7.3: Postbuckling equilibrium paths for local mode: Case 1 (A). Graphs show the normalized axial load Λ versus (a) Q_1/t (upper laminate), (b) Q_2/t (lower laminate) and (c) Q_3/t (intact part).

and a further load reduction. However, this will be discussed in detail in the final part of this chapter.

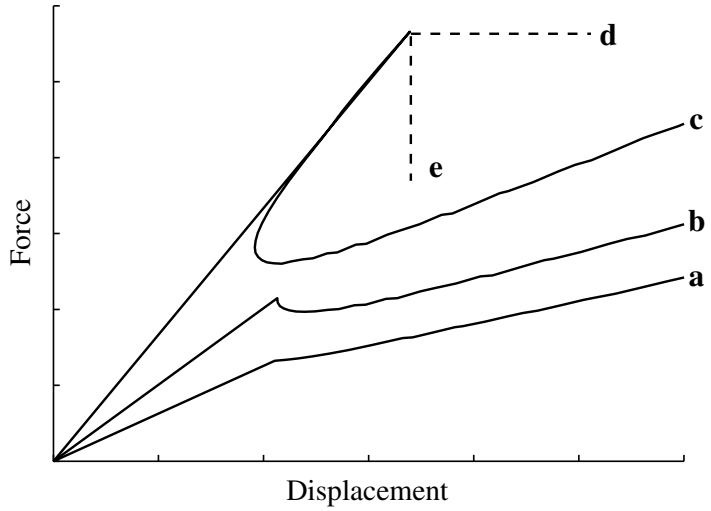

(a)

Figure 7.4: Generic examples for force–displacement behaviour caused by delamination growth after Wimmer & Pettermann (2008); (a) stable growth under force-controlled loading; (b) stable and (c) unstable growth under displacement controlled loading; (d) and (e) unstable growth under monotonic loading.

For the second postbuckling solution incorporating delamination propagation, path "P2", initiating from the second critical load, the increase in load until delamination propagation occurs is small after which the load drops, again insignificantly, to almost the original value of Λ_2^{C} indicated by the dashed horizontal line. At this point however, the delamination has grown to $a = b = 27.5$ mm, Figure 7.5b, thus a fast, but only marginally unstable, growth behaviour can be observed. After this, the propagation restabilizes and the load can be increased with growing delamination and the algorithm is halted once the load level exceeds $\Lambda = 2.0$.

Figure 7.5a shows the load versus end-shortening for case 1 (A) and it can be seen that for the first postbuckling path P1 the residual capacity reduces further when incorporating delamination propagation, compared to the stationary case. This is due to the fact that the local defect increases and thereby promotes the overall

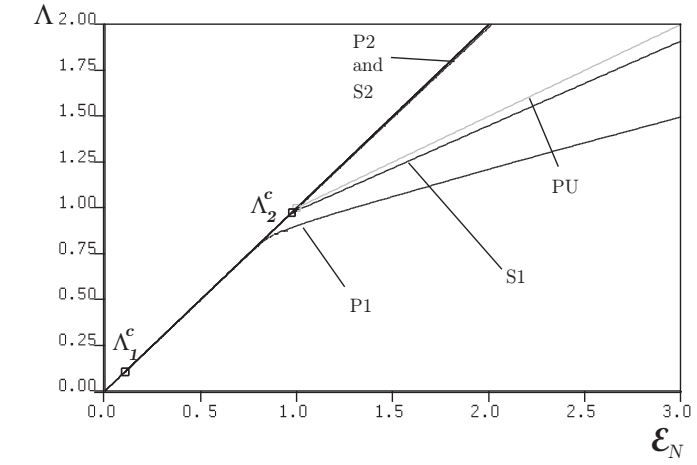

(a)

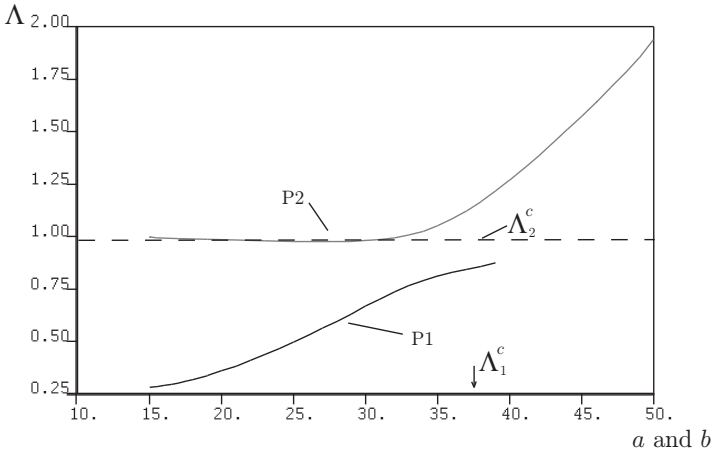

(b)

Figure 7.5: Delamination growth rate: Case 1 (A). Normalized axial load Λ versus (a) normalized end-shortening $\mathcal{E}_N$ and (b) delaminated patch dimensions a and b.

instability to occur at a lower load level. This is of importance since the system would then snap at a load level higher than the reduced critical load of 87.4% of the undamaged panel, thus if it were designed without accounting for the defect to spread, it could potentially have catastrophic consequences. That is, if the panel was located between two stringers, the instability of the panel may lead to stringer instability and so on. It is already apparent that it is of crucial importance to account for delamination propagation.

Furthermore, it should be noted, that even the reduced residual capacity in the postbuckling range of the damaged panel without delamination growth, path "S1", is no longer achievable since the reserve strength of the panels is significantly reduced by the presence of a propagating delamination, Figure 7.5a. For the opening mode configuration, no significant stiffness reduction can be observed, regardless of whether the defect grows or is stationary.

7.1.2.2 Case 1 (B)

The investigations for case 1 (B), *i.e.* $c = 0.05$, yielded no significant difference in terms of the mode behaviour compared to the previous case since the scenario is still in the thin-film buckling range. Thus, the postbuckling paths for the laminates and the overall panel are omitted here, but can be reviewed in the appendix §B.2.1, Figure B.2.

The critical loads are higher than for the previous case, again as expected, and are determined as $\Lambda_1^{\mathrm{C}} = 0.295$ and $\Lambda_2^{\mathrm{C}} = 0.979$; those values are indicated in the plots by dashed horizontal lines. Increasing the load after the first critical load monotonically, the delamination propagation is initiated at a load level of $\Lambda_1^{\mathrm{prop}} = 0.467$; a value that could also be confirmed with the finite element model. The ratio between $\Lambda_1^{\mathrm{prop}}$ and Λ_1^{C} is subsequently 1.58. Once the delamination propagates, a slight load drop is observed of approximately 2% of the undamaged panel's strength, where the delamination has propagated to a size of $a = b = 18$ mm; however, the overall

behaviour can still be regarded as plate-like or stable (Hunt *et al.*, 2004). Beyond this point, the load can be increased again until $\Lambda_1^{\max}$ reaches a value of 87.0% of the undamaged panel's capacity and $a = b = 39$ mm, Figure 7.6b, similar to case 1 (A), when the overall panel becomes unstable and henceforth Q_3 dominates the behaviour.

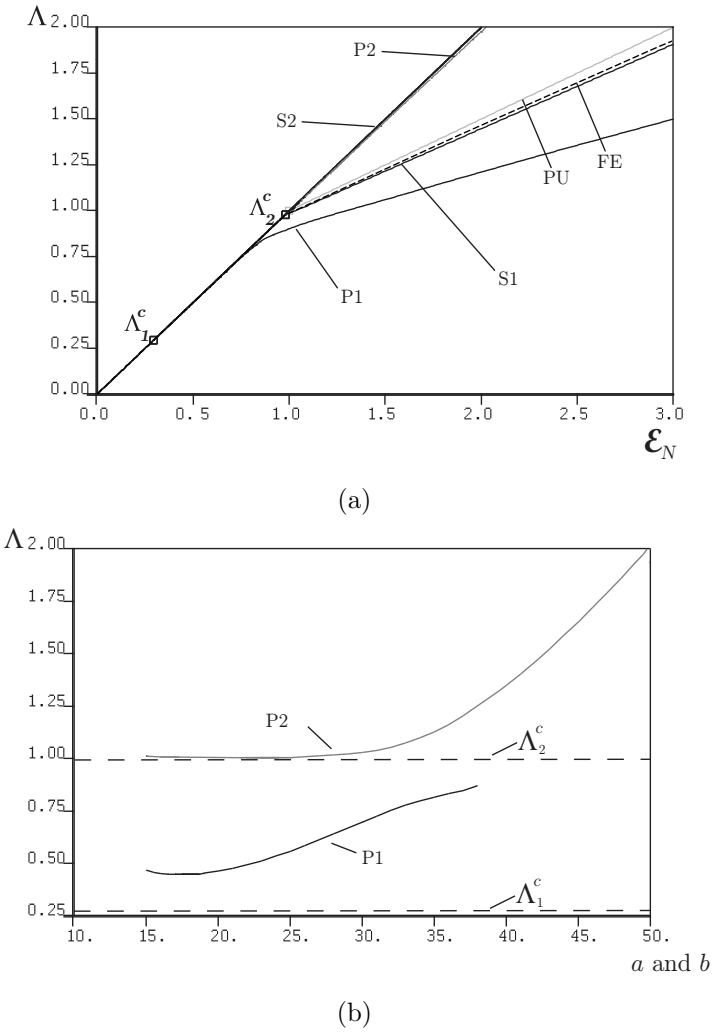

Figure 7.6: Delamination growth rate: Case 1 (B). Normalized axial load Λ versus (a) normalized end-shortening $\mathcal{E}_N$ and (b) delaminated patch dimensions a and b.

In Figure 7.6a, it should be noted that the residual capacity of a stationary delamination of the original size cannot be obtained when delamination growth is incorporated; the postbuckling response initially follows path "S1" until the relative displacement between the laminates becomes too great, *i.e.* $\delta(P) = \delta_{\max}$, at which

point it passes to path "P1". Moreover, it was found by Nilsson *et al.* (1993), who studied a pre-existing delamination at depth $c = 0.05$, that for a similar starting size of delamination the ratio of the load at which propagation commences Λ_1^{prop} to the buckling load Λ_1^{C} for the closing mode ranged from 1.55, from their numerical study, to 1.60 from their experimental study. This compares extremely favourably to the same ratio in the current study which is determined to be 1.58.

The reduction in stiffness at the first postbuckling solution including delamination propagation, path "P1", is as observed in case 1 (A), thus the residual capacity of a stationary delamination of the same original size cannot be obtained, as shown in Figure 7.6a.

For the second postbuckling solution, path "P2", a fast, marginally unstable growth occurs again at a load level around 100% of an undamaged panel's capacity, Figure 7.6b, and the system restabilizes at a slightly smaller delamination size than in the previous case, at $a = b = 22.5$ mm. The load can then be increased again with growing delamination size. However, owing to the nature of the opening mode, an overall instability is again not triggered and the residual capacity remains virtually unaffected, as shown in Figure 7.6a.

7.1.2.3 Case 1 (C)

The third case with a delamination of dimensions $a = b = 15$ mm, case 1 (C), contains a delamination located at $c = 0.085$, hence mixed mode buckling occurs according to Chapter 5, and Q_1 is now significantly smaller, as seen in Figure 7.7.

The first and second critical loads are triggered at $\Lambda_1^{\text{C}} = 0.801$ and $\Lambda_2^{\text{C}} = 1.045$, respectively, hence the second critical load is now triggered above the critical load of the undamaged case. The load can be increased from the first critical point up to a value of $\Lambda = 0.915$ until the delamination starts to grow. The growth occurs initially in an unstable manner, *i.e.* a load drop is observed down to a value of 0.721 of the undamaged capacity, to a delamination size of $a = b = 23.5$ mm, Figure

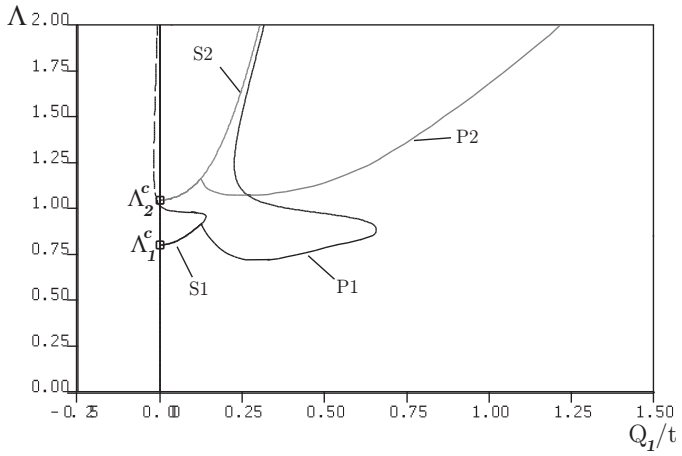

(a)

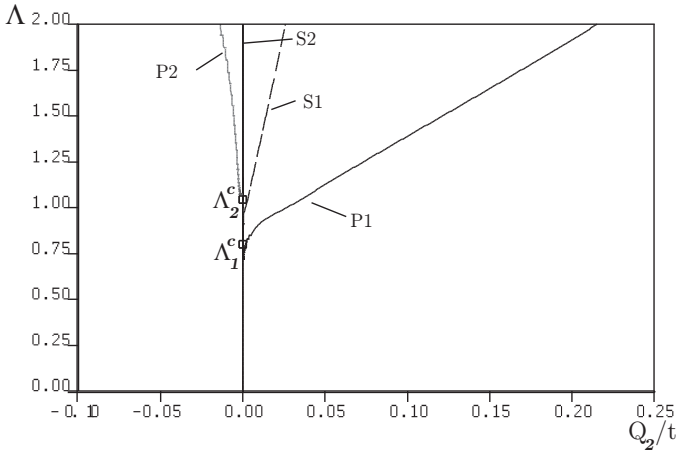

(b)

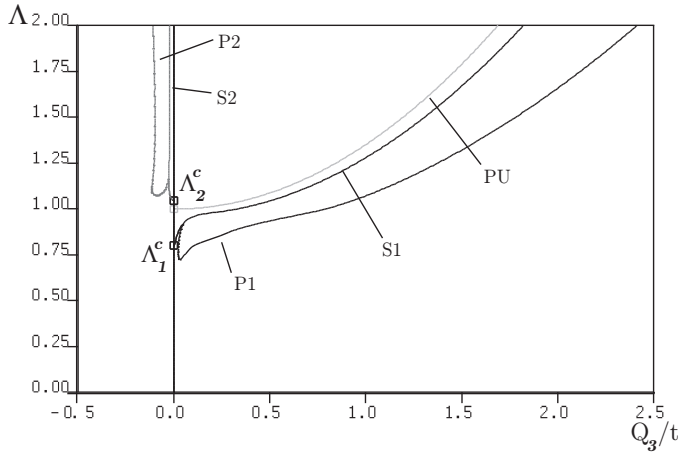

(c)

Figure 7.7: Postbuckling equilibrium paths for mixed mode: Case 1 (C). Graphs show the normalized axial load Λ versus (a) Q_1/t (upper laminate), (b) Q_2/t (lower laminate) and (c) Q_3/t (intact part).

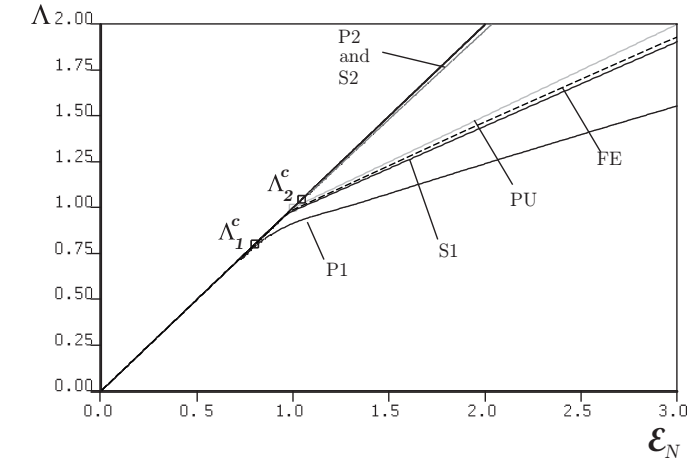

(a)

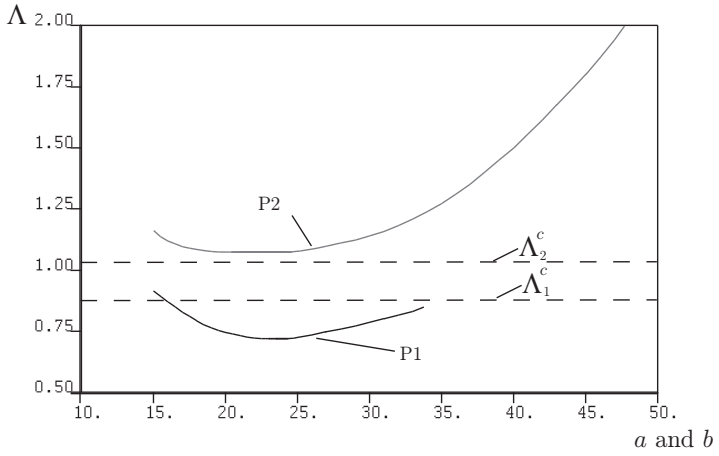

(b)

Figure 7.8: Delamination growth rate: Case 1 (C). Normalized axial load Λ versus (a) normalized end-shortening $\mathcal{E}_N$ and (b) delaminated patch dimensions a and b.

7.8b. Beyond this point, the system restabilizes and the load can be increased again up to a load of 0.849 of the undamaged capacity when the overall panel becomes unstable. It should be noted that the drop in load is below the initial critical buckling load, hence if the system is loaded by force-controlled loading a snap would occur and the delamination would grow dynamically from the initial $a = b = 15$ mm to $a = b = 39$ mm. Furthermore, the load at which global instability occurs is now approximately 2% lower than for the previous two cases (A) and (B).

At the second critical load, the system can be subjected to further load until the delamination starts to propagate at 116.2% of the undamaged capacity in an unstable manner. The growth stabilizes, as before, at a load level around 100% and the delamination grows to an extent of $a = b = 21.5$ mm, Figure 7.8b. This, again, is slightly less than in the previous two cases, but again the delamination growth rate decreases with increasing delamination size (Bottega & Maewal, 1983).

It can again be observed that the reserve capacity of the panel containing a stationary defect cannot be attained and the end-shortening curve is as in the previous two cases. Furthermore, the propagation has a minor effect on the residual capacity when the opening mode is triggered, paths "P1" and "P2" in Figure 7.8a respectively.

7.1.2.4 Case 1 (D)

Case 1 (D) considers a delamination that is located at depth $c = 0.12$, and global buckling governs the behaviour according to §5.2.2. This can be seen in the post-buckling equilibrium paths in Figure 7.9. It is evident that because of overall buckling dominating the behaviour of the panel, no delamination propagation occurs at the first critical load, path "S1". This is because in the closing mode configuration, no relative opening occurs between the laminate to promote delamination growth. Thus, clearly no further reduction in residual capacity occurs when growth is allowed for, Figure 7.10a, and the reduction in stiffness is as shown in Chapter 5 for a delamination of these parameters.

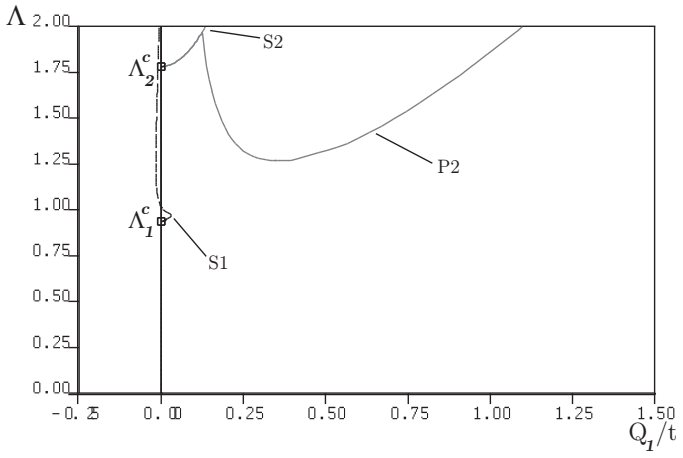

(a)

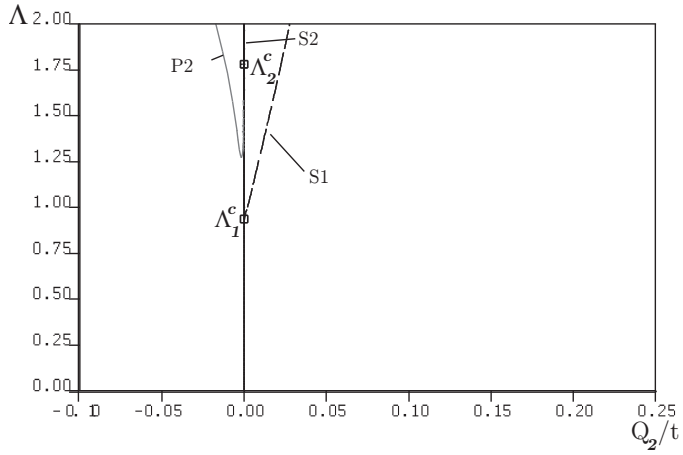

(b)

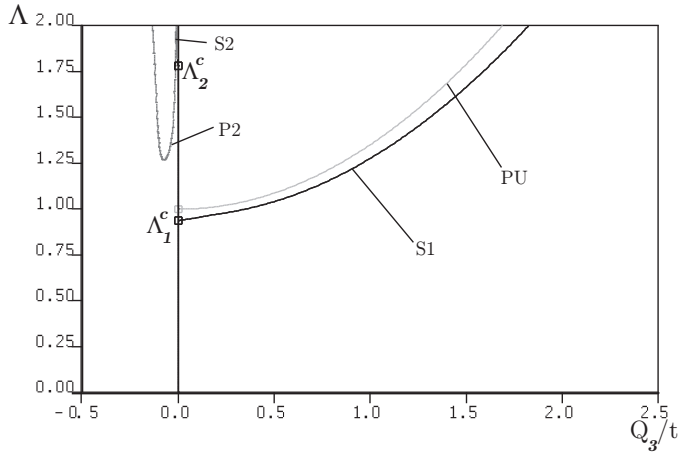

(c)

Figure 7.9: Postbuckling equilibrium paths for global mode: Case 1 (D). Graphs show the normalized axial load Λ versus (a) Q_1/t (upper laminate), (b) Q_2/t (lower laminate) and (c) Q_3/t (intact part). Note the lack of path "P1".

The second critical load is triggered at a load level of $\Lambda_2^{\mathrm{C}} = 1.783$ with the propagation initiating at $\Lambda_2^{\mathrm{prop}} = 1.965$. The growth characteristic is highly unstable, as can be seen in Figure 7.10b, and the delamination grows to a size of $a = b = 25.5$ mm at 127.1% capacity of an undamaged panel. Then the system restabilizes again and the load can be increased with increasing delamination size. Despite the unstable nature of the growth and the enlargement of the defect, the overall residual stability remains unchanged, Figure 7.10a, as in the previous cases, which can be explained by the opening configuration of this mode. Additionally, the load drop is never below 100% of a panel's capacity, thus the second postbuckling mode can be regarded as not critical.

7.1.2.5 Case 1 (E)

The last case considered with a delamination of dimensions $a = b = 15$ mm contains a delamination at depth $c = 0.20$. This case was investigated to eliminate out potential instabilities arising from the opening mode at higher load levels. The postbuckling equilibrium paths do not significantly differ from the previous case and hence are not shown herein.

As in the previous case, no growth occurs after the first critical load is triggered since sublaminate buckling does not govern the behaviour, path "S1". However, at the second critical load, $\Lambda_2^{\mathrm{C}} = 4.941$, after initial increase to $\Lambda_2^{\mathrm{prop}} = 5.128$, a highly unstable load drop with increasing delamination occurs. Nonetheless, the load never drops below $\Lambda = 2.0$ and can therefore be deemed as uncritical since this panel would not be designed to withstand such high load levels. Hence, under the condition that a panel would not be designed to withstand loads higher than 100% of the undamaged panel, growth would not occur.

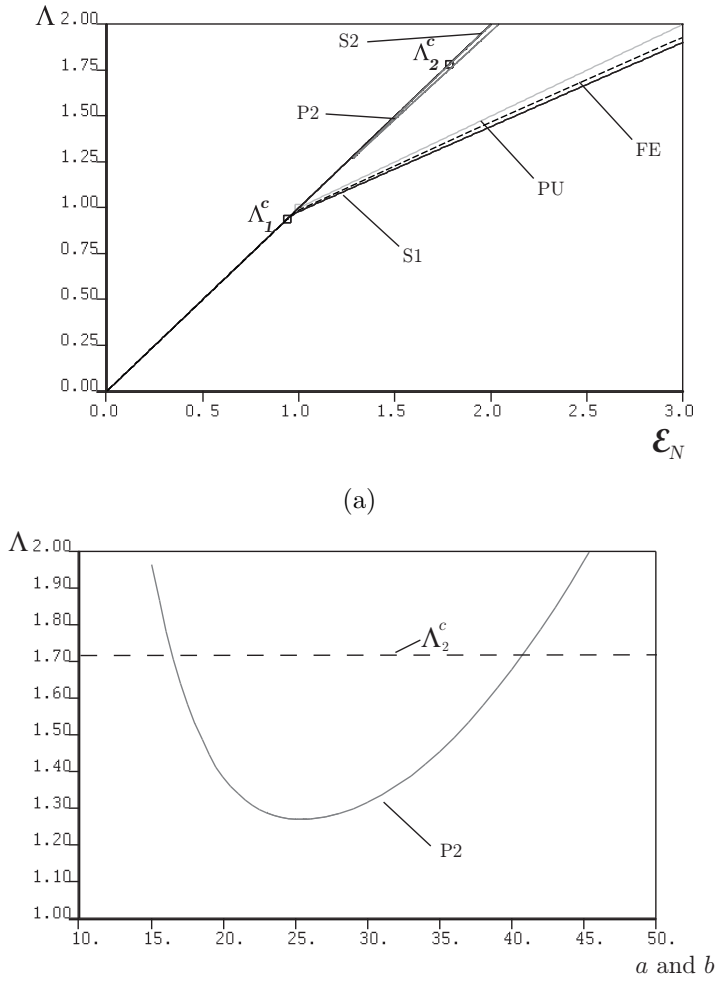

Figure 7.10: Delamination growth rate: Case 1 (D). Normalized axial load Λ versus (a) normalized end-shortening $\mathcal{E}_N$ and (b) delaminated patch dimensions a and b.

Case 1	(A)	(B)	(C)	(D)	(E)
Λ_1^{C}	0.107	0.295	0.801	0.939	0.949
$\Lambda_1^{\mathrm{prop}}$	0.281	0.467	0.915	–	–
Λ_1^{min}	–	0.447	0.721	–	–
a and b at Λ_1^{min} (mm)	–	18	23.5	–	–
Λ_1^{max}	0.874	0.870	0.849	–	–
a and b at Λ_1^{max} (mm)	39	39	35	–	–
growth stationary at Λ_1^{max}?	yes	yes	yes	–	–
Λ_2^{C}	0.975	0.979	1.045	1.783	4.941
$\Lambda_2^{\mathrm{prop}}$	0.995	1.012	1.162	1.965	5.128
Λ_2^{min}	0.976	1.005	1.073	1.271	2.039
a and b at Λ_2^{min} (mm)	27.5	22.5	21.5	25.5	33
Λ_2^{max}	2.08	2.366	2.515	2.660	3.0976
a and b at Λ_2^{max} (mm)	52	54.5	54.5	54.5	64
growth stationary at Λ_2^{max}?	no	no	no	no	no

Table 7.5: Results summary: Case 1.

7.1.2.6 Summary: Case 1

The findings for case 1 illustrated in the graphs in the preceding sections are summarized in Table 7.5. Concluding, it should be noted that for the case of a delamination of dimensions $a = b = 15$ mm, delamination growth occurs when the defect is nearer the surface or precisely at the transitional depth c_{t}.

For the first critical load, in the thin-film case, case (A), the growth is stable. This is also almost true for case (B), another thin-film configuration, where only a very slight load-drop is observed with small growth. The ratio between the load at which propagation occurs and the critical load in this configuration compares quantitatively and phenomenologically with values in the literature (Nilsson *et al.*, 1993). Furthermore, finite element analysis for this case gave the same results in

terms of the propagation load level. However, finite element modelling incorporating growth criteria is immensely time-consuming[1] and was therefore ceased after the propagation load level due to time constraints. For the mixed mode buckling case, *i.e.* case (B), the growth is unstable and a load drop below the initial buckling load is observed. This means that if the load was applied monotonically, a snap instability would occur. For case (C) and (D) no growth was observed at the first postbuckling path. The FE model confirms that the choice in generalized coordinates and the approximation for the stress functions was indeed appropriate since the comparisons with the static delamination model are excellent, as had been established in Chapter 5.

Only in case 1 (A) does the load drop below 100% of the undamaged panel for the second postbuckling path "P2" and a fast and unstable growth is observed. In case (B), similar behaviour is observed, where the delamination grows unstably at an almost constant load level of 100%, *i.e.* in both cases a snap would occur until the panel and growth restabilizes again.

7.1.3 Results and discussion: Case 2

In this section, a selection of the results is presented and discussed while varying relative delamination depths c for case 2, where $a = b = 20$ mm, as summarized in Table 7.2. Postbuckling paths are plotted for each case and then summarized in §7.1.3.5.

Four different delamination depths are investigated currently, again in the neighbourhood of the transitional depth c_t, where case (A) triggers thin-film buckling, (B) and (C) both trigger mixed mode buckling and (D) triggers global buckling.

[1] Pinho (2005) required approximately 5 hours for the simulation of growth of a simple double cantilever model for fracture Mode I, Figure 6.3a.

7.1.3.1 Case 2 (A)

In case 2 (A), the delamination is again located at $c = 0.05$ and the postbuckling equilibrium paths for the upper, lower and intact parts are shown in Figure 7.11. As in cases 1 (A) and (B), the buckling of the upper laminate dominates the behaviour in both the first and second postbuckling paths. In Figure 7.11a, it can clearly be seen that the buckling of the upper laminate, *i.e.* defined by Q_1, is the dominating mode and the order of magnitude of the buckle is far more pronounced than in case 1 (A), Figure 7.3a. In addition, the lower laminate buckling displacement also increases significantly for this initially larger, propagating delamination when compared to the previous case, as can be seen if Figures 7.3b and 7.11b are compared. Furthermore, it should be noted that since the system fully delaminates, as will be discussed subsequently, the overall panel never dominates the buckling behaviour, as seen in Figure 7.11.

After the first critical load, $\Lambda_1^{\mathrm{C}} = 0.166$, the load can be increased until delamination propagation is initiated at $\Lambda_1^{\mathrm{prop}} = 0.265$. An insignificant load drop occurs with a slight uniform growth of approximately 3 mm of the delamination, path "P1", but the system quickly recovers and the load can be monotonically increased with a growing delamination. Thus, as observed before, a largely stable growth behaviour, *i.e.* the defect only grows with increasing load, can be identified for the local buckling mode. The maximum load that can be achieved is at 86.9% of the undamaged panel's capacity. However, it should be noted that the system is now fully delaminated, *i.e.* $a = b = 100$ mm and hence the postbuckling stiffness as seen in Figure 7.12a may be overestimated. This is because the clamped edge conditions which governed the boundary conditions for the out-of-plane displacement functions would not be present any more. This, in turn, results in the probable invalidity of the displacement functions and subsequently the energy formulation using the Rayleigh–Ritz procedure. Nonetheless, a fully delaminated panel cannot be desired in any design scenario due to various other implications this would have on the integrity of the structural element, and hence must be avoided.

This delamination configuration compares well quantitatively as well as phenomenologically with investigations on buckling induced delamination growth by Nilsson *et al.* (1993). That particular article was part of the review in Chapter 2 and the comparison for this case is presented herewith. In their experimental investigations on an artificially introduced delamination of diameter 20 mm in a depth translating to approximately $c = 0.05$ it was also seen that delamination growth initiated at a load level 1.6 times higher than the initial buckling load. This is also the case in the present model, where $\Lambda_1^{\text{prop}}/\Lambda_1^{\text{C}} = 0.265/0.166 = 1.596 \approx 1.6$. Therefore, the current model yields an excellent comparison with their findings. Furthermore, the authors validated their findings with a finite element investigation where they found a ratio of 1.55 between the strain initiating delamination and the critical buckling strain, again in the same range as their experimental investigations and the findings with the current model employed in this study.

For the second critical load, which is triggered below that for an undamaged panel, where $\Lambda_2^{\text{C}} = 0.955$ the load can only be increased slightly until delamination propagation is initiated at $\Lambda_2^{\text{prop}} = 0.979$, *i.e.* as in the above thin-film configuration in case 1 at a load level below 100% of the undamaged panel's capacity. The load then drops to a value of 92.5% with delamination growth occurring up to lengths $a = b = 41.5$ mm, see Figure 7.12b path "P2". This is quite a substantial growth at a relatively small load drop and the propagation can therefore be regarded as fast and unstably propagating in the opening mode configuration. The system eventually restabilizes and the load can be increased again. The stiffness decrease is slightly more pronounced than in case 1, *c.f.* Figures 7.6a and Figure 7.12a, however it can still be deemed as insignificant compared to the stiffness decrease at the first critical load.

7.1.3.2 Case 2 (B)

Case 2 (B) has a delamination located at depth $c = 0.085$ and mixed mode buckling is triggered. The postbuckling equilibrium paths for the upper, lower and intact

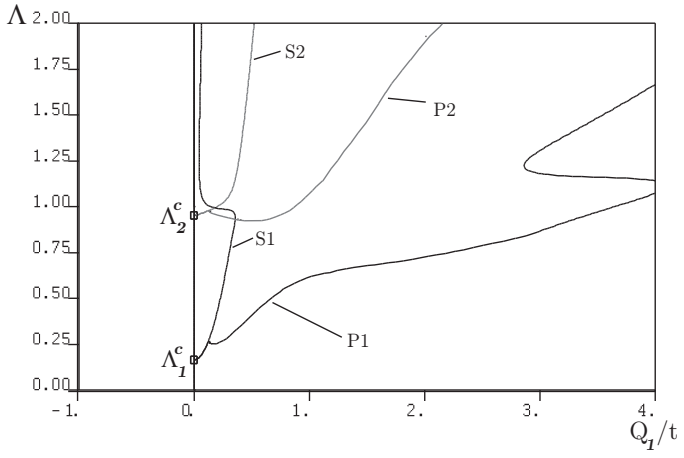

(a)

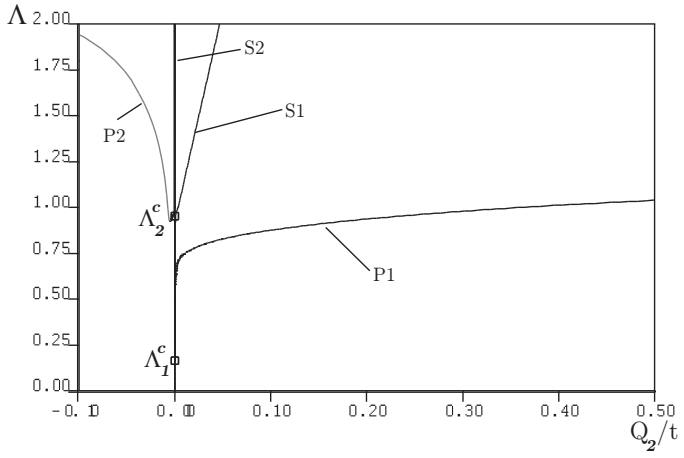

(b)

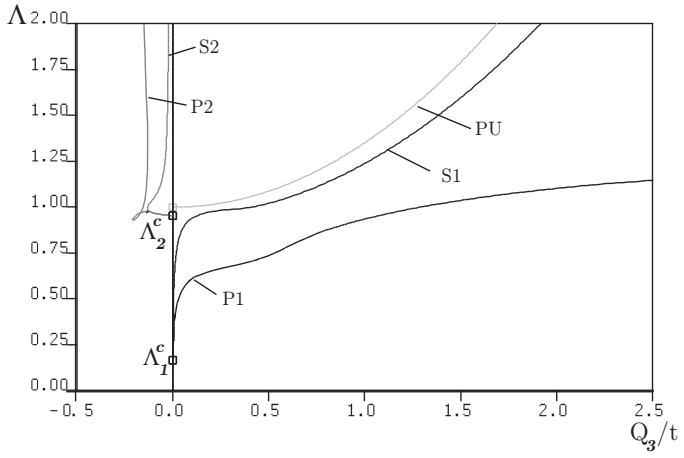

(c)

Figure 7.11: Postbuckling equilibrium paths for local mode: Case 2 (A). Graphs show the normalized axial load Λ versus (a) Q_1/t (upper laminate), (b) Q_2/t (lower laminate) and (c) Q_3/t (intact part).

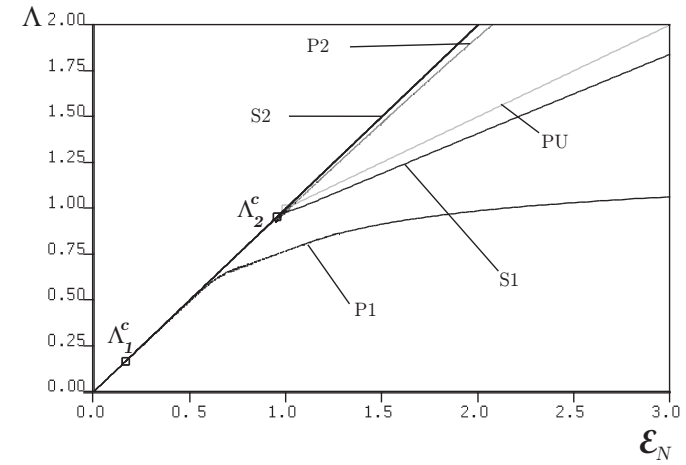

(a)

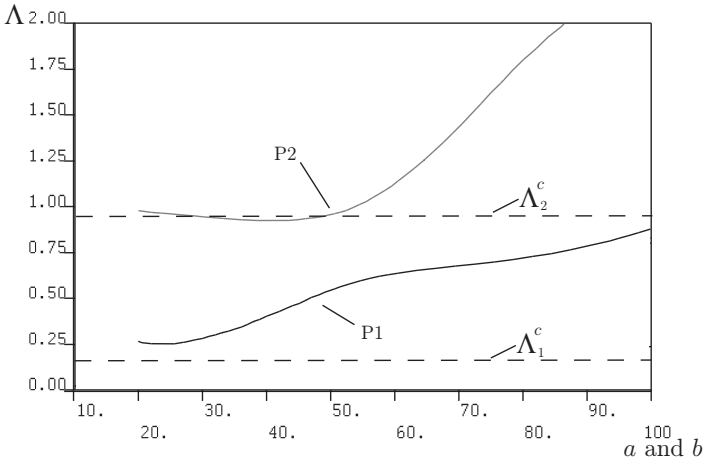

(b)

Figure 7.12: Delamination growth rate: Case 2 (A). Normalized axial load Λ versus (a) normalized end-shortening $\mathcal{E}_N$ and (b) delaminated patch dimensions a and b.

parts of the panel are shown in Figure 7.13, whereas the load versus end-shortening and growth rate graphs are shown in Figure 7.14.

The first critical load is triggered at $\Lambda_1^{\mathrm{C}} = 0.475$ and can be increased up to $\Lambda = 0.567$ when propagation occurs. However, as in the earlier mixed mode buckling example in case 1 (C), the load then drops below the initial critical load, in this configuration to a value of $\Lambda_1^{\min} = 0.417$, and the associated delamination size is $a = b = 36.5$ mm in the case of non-monotonic loading. The system then restabilizes and the load can be increased to $\Lambda_1^{\max} = 0.818$. However, again the panel is then fully delaminated, *i.e.* $a = b = 100$ mm, and the reserve stiffness in Figure 7.14a may be misleading due to the incorrect displacement functions employed, as explained previously. It should furthermore be noted that if monotonic loading, either displacement or force-controlled, is employed a dynamic snap would occur. Furthermore, since full delamination occurs, Q_3, *i.e.* the buckling of the intact part, never dominates the behaviour as could be seen in smaller delaminations discussed previously.

The second critical load is again triggered marginally below 100% at $\Lambda_2^{\mathrm{C}} = 0.968$ and can be increased up to $\Lambda = 1.007$ until the delamination starts to spread. With a fast increasing delamination, a small load drop is again observed to a value slightly smaller than the initial critical load to $\Lambda_2^{\min} = 0.965$ corresponding to $a = b = 36.5$ mm. The system then restabilizes and the load can be increased with increasing delamination, see path "P2" in Figure 7.14. It should again be noted that despite the large delamination, the stiffness decrease in the load versus end-shortening graph, Figure 7.14a, is not as pronounced for the opening mode as for the closing mode.

7.1.3.3 Case 2 (C)

The third case for a delamination of dimensions $a = b = 20$ mm contains a delamination at depth $c = 0.11$; this is a mixed mode case bordering on global buckling, *i.e.* little opening of the laminates. It should be noted that compared to case 2 (B),

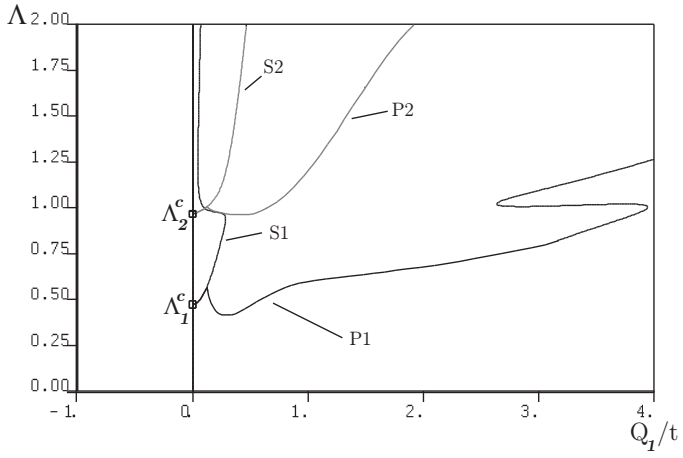

(a)

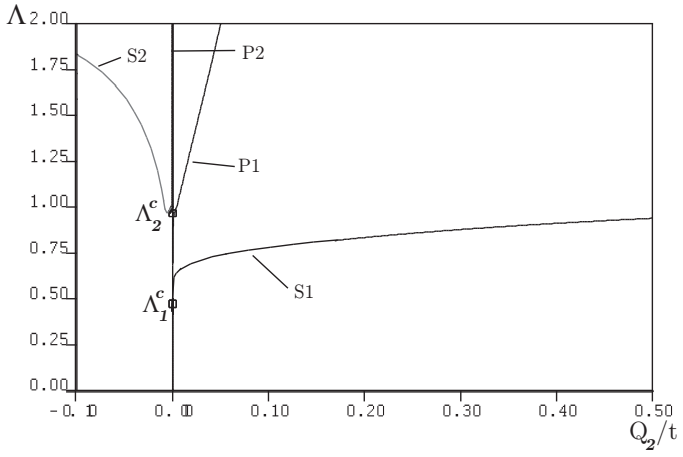

(b)

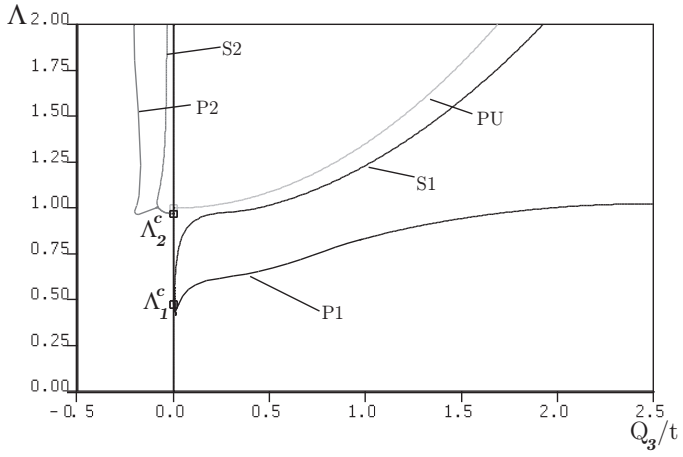

(c)

Figure 7.13: Postbuckling equilibrium paths for mixed mode: Case 2 (B). Graphs show the normalized axial load Λ versus (a) Q_1/t (upper laminate), (b) Q_2/t (lower laminate) and (c) Q_3/t (intact part).

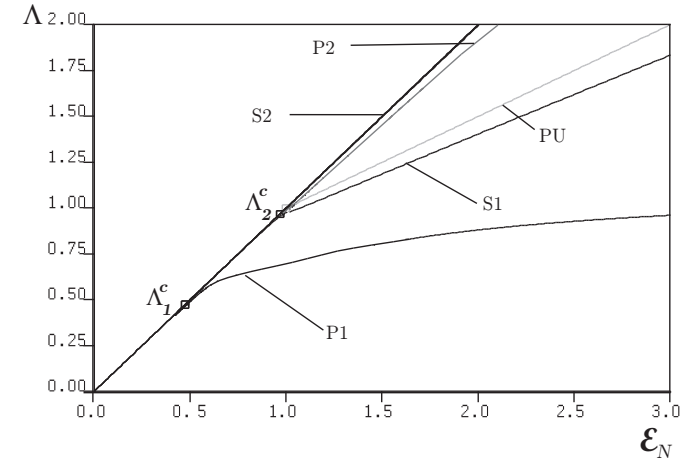

(a)

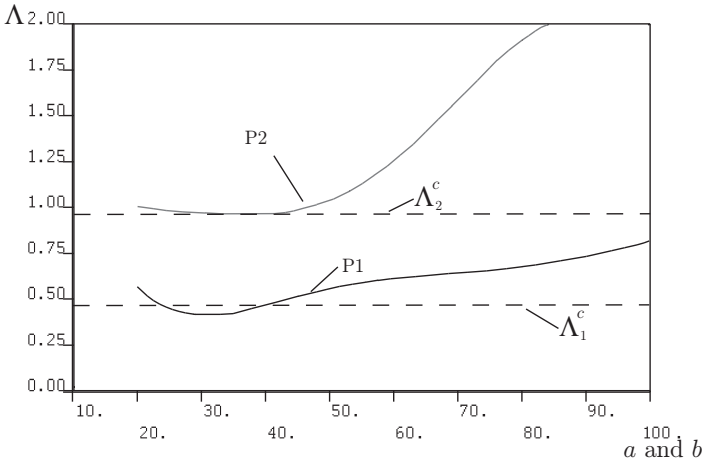

(b)

Figure 7.14: Delamination growth rate: Case 2 (B). Normalized axial load Λ versus (a) normalized end-shortening $\mathcal{E}_N$ and (b) delaminated patch dimensions a and b.

the deflection of the upper laminate Q_1 still dominates the behaviour, but it is not as pronounced as before, as can be seen by comparing Figure 7.15 with Figure 7.13.

The first critical load is triggered at $\Lambda_1^{\mathrm{C}} = 0.750$ and propagation starts at 82% of the undamaged panel's capacity. A significant load drop occurs to a load level of $\Lambda_1^{\min} = 0.520$, again below the initial critical load, path "P1" Figure 7.15a, where the delamination has grown to dimensions $a = b = 36.5$ mm, Figure 7.16b. With monotonic loading conditions the load can be increased with growing delamination up to a value of 79.1%, however, again, this load level corresponds to a fully delaminated panel, see Figure 7.16b. Hence the load level at which delamination propagation initiates can never be attained again which means that catastrophic failure would occur if force-controlled loading was employed.

The second critical load is just above 100% at $\Lambda_2^{\mathrm{C}} = 1.026$ and delamination propagation starts at $\Lambda_2^{\mathrm{prop}} = 1.098$, hence only a marginal increase in load is possible. The delamination is again fast growing and the system slowly restabilizes after the load reaches $\Lambda_2^{\min} = 0.997$ with $a = b = 34.5$ mm via non-monotonic loading conditions, see path "P2" in Figure 7.16b. Otherwise a dynamic snap would occur for monotonic loading conditions, as described before. The load can then be increased with increasing delamination size, however, the stiffness decrease is again not as pronounced as for the closing mode condition, Figure 7.16a.

7.1.3.4 Case 2 (D)

Case 2 (D) is the global buckling mode case for a delamination of dimensions $a = b = 20$ mm and $c = 0.15$ where the equilibrium graphs are shown in Figures 7.17 and 7.18. The postbuckling graphs are quite similar to the global buckling case for a delamination with $a = b = 15$ mm, as given in case 1 (D), §7.1.2.4.

As found in the cases for smaller delaminations, no growth occurs in the closing mode, *i.e.* the buckling mode corresponding to the first critical load. This is due to the minimal opening of the two sublaminates, Figures 7.17a and 7.17b, an insufficient

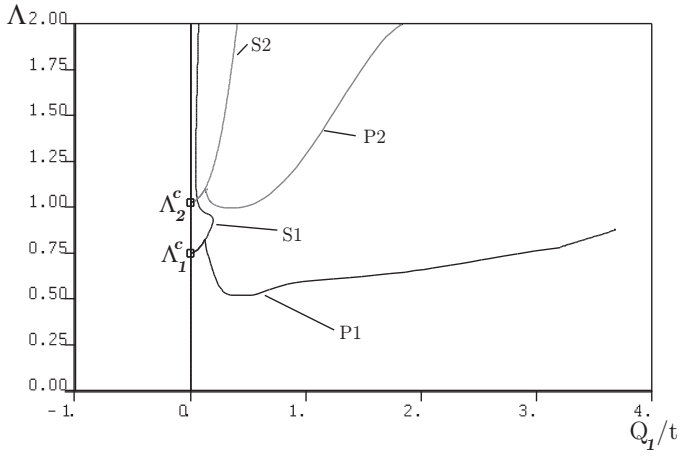

(a)

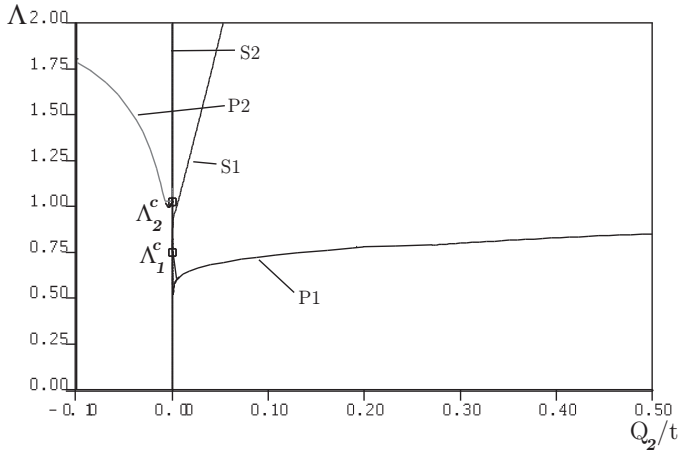

(b)

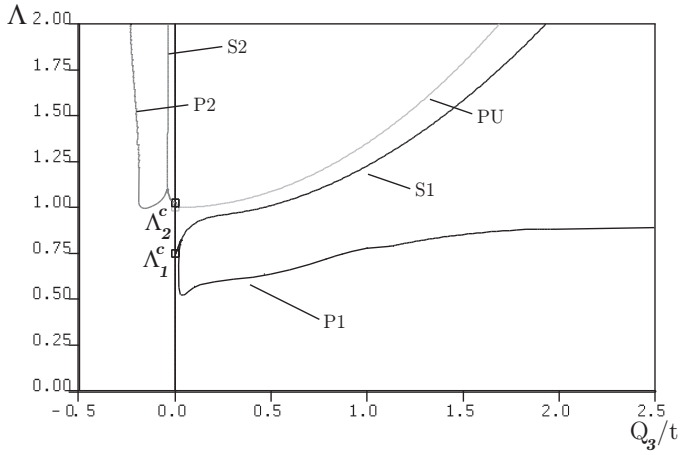

(c)

Figure 7.15: Postbuckling equilibrium paths for global mode: Case 2 (C). Graphs show the normalized axial load Λ versus (a) Q_1/t (upper laminate), (b) Q_2/t (lower laminate) and (c) Q_3/t (intact part).

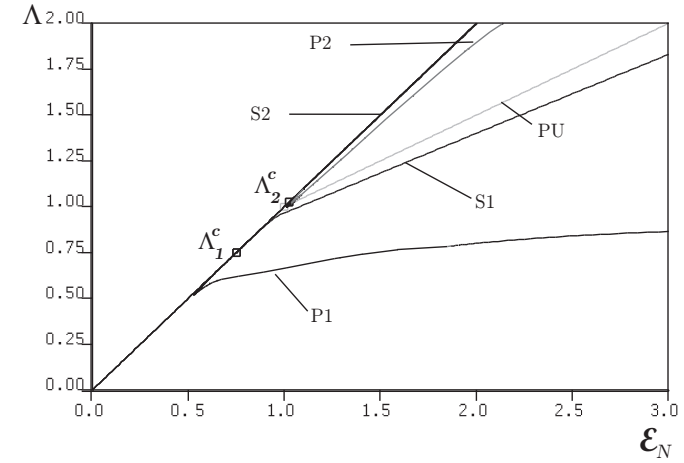

(a)

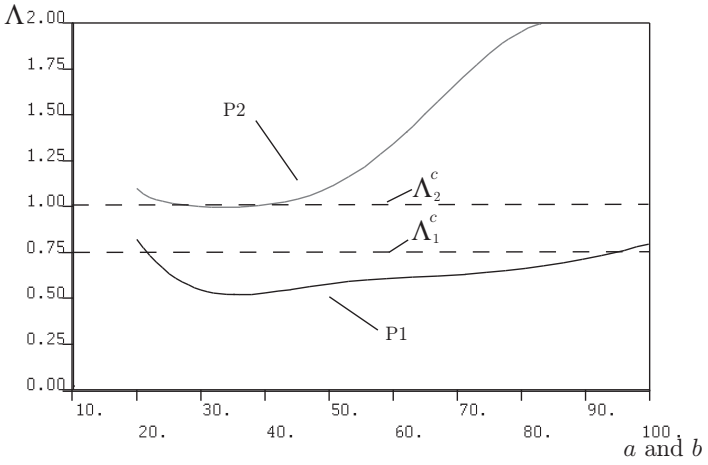

(b)

Figure 7.16: Delamination growth rate: Case 2 (C). Normalized axial load Λ versus (a) normalized end-shortening $\mathcal{E}_N$ and (b) delaminated patch dimensions a and b.

amount of strain energy is released to promote delamination growth. The first critical load is at $\Lambda_1^{\mathrm{C}} = 0.897$, and the load can be increased in the postbuckling range with a slight stiffness reduction compared to the undamaged panel, path "S1".

The second critical load occurs at $\Lambda_2^{\mathrm{C}} = 1.597$ thus higher than 100% and can be increased up to 170.5% until delamination growth occurs. The growth is highly unstable, as seen in path "P2" in Figure 7.18b, until $\Lambda_2^{\mathrm{min}} = 1.093$ is reached. The delamination has then grown to dimensions $a = b = 36$ mm and the system restabilizes, and the load can be increased again with a growing delamination. However, it should be noted here, that the minimum load is close to 100% of an undamaged panel's strength, thus if a panel was designed to 100% strength without allowing for the defect, a dynamic growth would occur if the panel is loaded and a delamination of this size would appear. A through-the-width delamination of similar dimensions, but with a larger relative delamination depth was investigated by Whang & Zhang (2009) and their numerical results also showed an unstable growth behaviour for a delamination at one-third of the overall depth.

7.1.3.5 Summary: Case 2

In the case of a delamination of dimensions $a = b = 20$ mm, the following conclusions can be drawn. The results for case 2 are summarized in Table 7.6. In all cases where growth occurs for the first critical load, the plate will fully delaminate before reaching the capacity of 100% of the undamaged panel. The reserve stiffness in the postbuckling graphs, path "P1" in Figures 7.12a, 7.14a and 7.16a, is subsequently overestimated since the clamped boundary conditions would not be present any more and the two separate laminates that comprise the plated panel would buckle. Hence, compared to the previous case of a delaminated patch where $a = b = 15$ mm, it can be seen that a marginal increase in the initial delamination size leads to a significant reduction in postbuckling capacity and the growth is far more pronounced. However, the growth characteristics, *i.e.* the stability of the growth, when compared with the

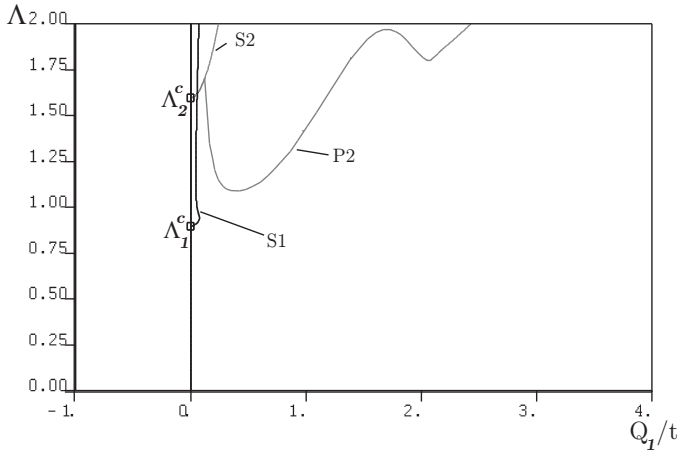

(a)

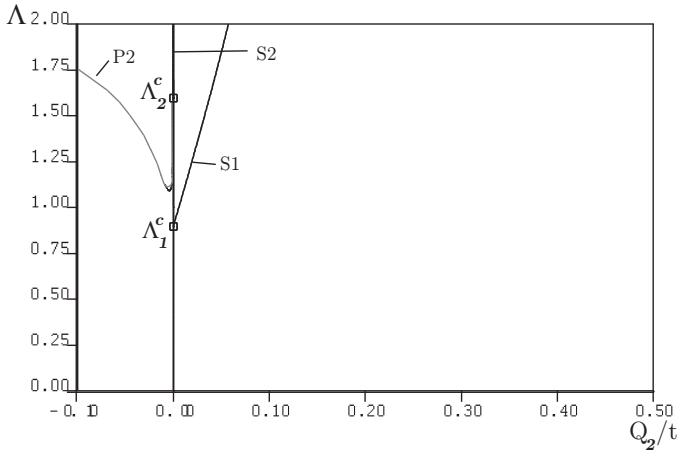

(b)

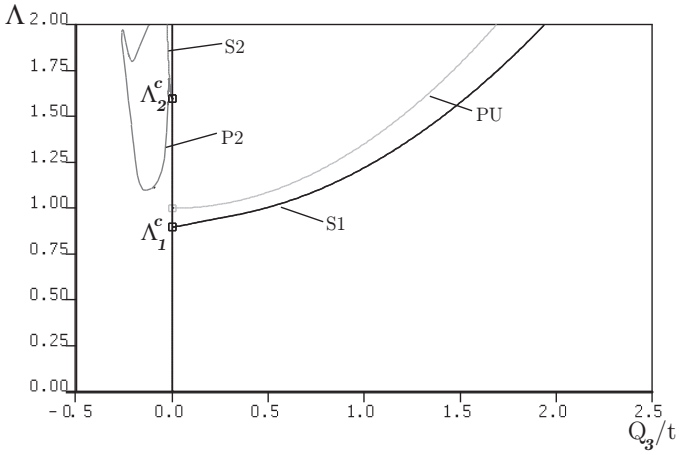

(c)

Figure 7.17: Postbuckling equilibrium paths for global mode: Case 2 (D). Graphs show the normalized axial load Λ versus (a) Q_1/t (upper laminate), (b) Q_2/t (lower laminate) and (c) Q_3/t (intact part). Note the lack of path "P1".

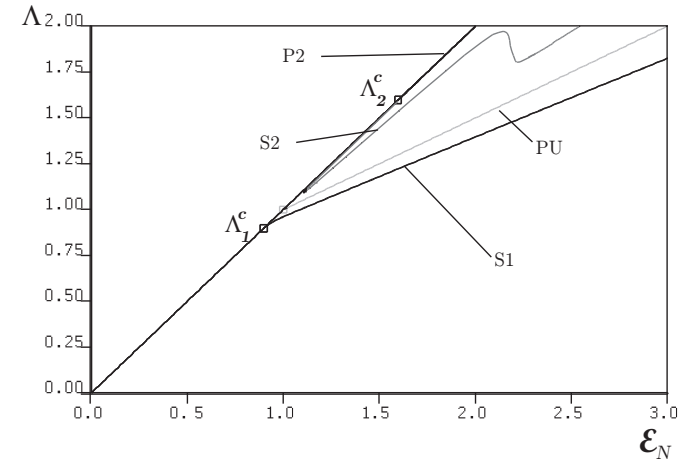

(a)

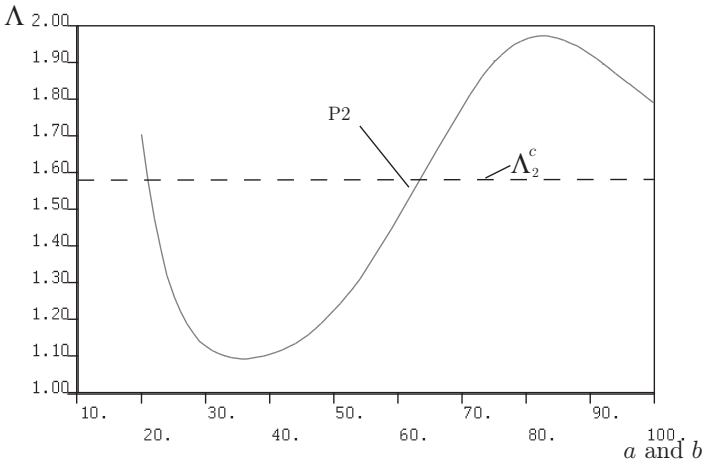

(b)

Figure 7.18: Delamination growth rate: Case 2 (D). Normalized axial load Λ versus (a) normalized end-shortening $\mathcal{E}_N$ and (b) delaminated patch dimensions a and b. Note the lack of path "P1".

previous case, are identical. This means that stable growth occurs from a thin-film delamination and unstable growth from a mixed mode buckling configuration where the minimum load is below the initial critical load. This could potentially be very dangerous if the panel was under monotonic loading conditions since a dynamic snap would occur as described in Figure 7.4.

Case 2	(A)	(B)	(C)	(D)
Λ_1^{C}	0.166	0.475	0.750	0.897
$\Lambda_1^{\mathrm{prop}}$	0.265	0.567	0.820	–
Λ_1^{min}	0.252	0.417	0.520	–
a and b at Λ_1^{min} (mm)	23	30.5	36.5	–
Λ_1^{max}	0.869	0.818	0.791	–
a and b at Λ_1^{max} (mm)	100	100	100	–
growth stationary at Λ_1^{max}?	n/a	n/a	n/a	–
Λ_2^{C}	0.955	0.968	1.026	1.597
$\Lambda_2^{\mathrm{prop}}$	0.979	1.007	1.098	1.705
Λ_2^{min}	0.925	0.965	0.997	1.093
a and b at Λ_2^{min} (mm)	41.5	36.5	34.5	36
Λ_2^{max}	2.063	2.051	2.014	1.802
a and b at Λ_2^{max} (mm)	90	90	85	100
growth stationary at Λ_2^{max}?	no	no	no	n/a

Table 7.6: Results summary: Case 2.

In addition, the growth initiation of case 2 (A) compares well with previous findings by Nilsson *et al.* (1993), hence the model has been validated to a large extent with their experimental and numerical investigations.

The second critical loads for thin delaminations, (A), (B) and (C), are triggered below or around 100% of the capacity of an undamaged panel. All of these cases feature fast and unstable growth. This means that under monotonic loading, a dynamic snap would occur until the system restabilizes. The delamination would

snap to approximately $a = b = 50$ mm for 100% loading in all cases, as seen in Figures 7.12b, 7.14b and 7.16b, which is a significant increase in the defect's size. In the global buckling case (D), the second critical load is well above 100% of an undamaged panel. However, unstable growth occurs again and the lowest load is around $\Lambda = 1$ which means even in this case, a dynamic snap could occur when the panel is loaded up to the full undamaged panel's capacity.

7.1.4 Results and discussion: Case 3

In this section, a selection of the results varying the delamination depth c for case 3, $a = b = 25$ mm, as summarized in Table 7.2, are presented and discussed. Again, these are first detailed with the postbuckling plots for each case and then summarized in §7.1.4.5. However, the load versus laminate displacement Q_i plots are not presented for this delamination size since they do not yield any new results in terms of the findings for local, mixed or global buckling. The relevant plots are the load versus end-shortening and delamination growth figures, which will be presented and discussed.

Four different delamination depths are investigated currently, again in the neighbourhood of the transitional depth c_t, where case (A) features thin-film buckling, (B) and (C) feature mixed mode buckling and (D) features global buckling.

7.1.4.1 Case 3 (A)

The thin-film case for this delamination size contains a delamination at depth $c = 0.05$ as before. The first critical load is triggered at $\Lambda_1^{\mathrm{C}} = 0.107$ and can be increased to $\Lambda_1^{\mathrm{prop}} = 0.169$ until delamination growth occurs. The ratio of $\Lambda_1^{\mathrm{prop}}/\Lambda_1^{\mathrm{C}} = 1.57$ again corresponds well to the values found by Nilsson *et al.* (1993) for a similar delamination configuration. There is then a significant load drop once the delamination propagates which also ties in with the findings for the other thin-

film configurations discussed previously. With increasing load the delamination spreads and the maximum load that can be reached for the first equilibrium path "P1" is now only 51% of an undamaged panel, Figure 7.19b, which represents a significant difference to the configurations discussed above. At this load level, the plate has fully delaminated, *i.e.* $a = b = 100$ mm and the reserve capacity shown in Figure 7.19a is understood to be overestimated for the same reasons as previously discussed.

The second critical load is also triggered below 100% of an undamaged panel's capacity at $\Lambda_2^{\mathrm{C}} = 0.929$ and a fast, unstable growth, shown in path "P2", occurs after propagation is initiated at $\Lambda_2^{\mathrm{prop}} = 0.947$. The system eventually restabilizes, Figure 7.19b, but even for the second postbuckling solution now full delamination occurs below 200% of the load capacity of an undamaged panel.

Again, the stiffness decrease is more pronounced for the first postbuckling solution, see Figure 7.19a, but in both the first and second buckling modes, the system now fully delaminates meaning that for an initial delamination of this size, catastrophic growth is predicted.

7.1.4.2 Case 3 (B)

Case 3 (B) represents the mixed mode buckling case for a delamination of dimensions $a = b = 25$ mm with depth of $c = 0.11$. Again, the displacement characteristics of the upper, lower and intact parts are not significantly different to previously discussed mixed mode configurations and are therefore not presented here.

The first critical load is triggered at $\Lambda_1^{\mathrm{C}} = 0.504$ and can be increased to a value of $\Lambda_1^{\mathrm{prop}} = 0.562$ until delamination propagation occurs. Again, the growth is highly unstable, as in the previously discussed mixed mode cases, and the system restabilizes under monotonic loading at $\Lambda_1^{\mathrm{min}} = 0.338$ where $a = b = 44.5$ mm, Figure 7.20b. This is significantly lower than the initial critical load, and if force-controlled loading was employed, a dynamic snap would again occur. The most important

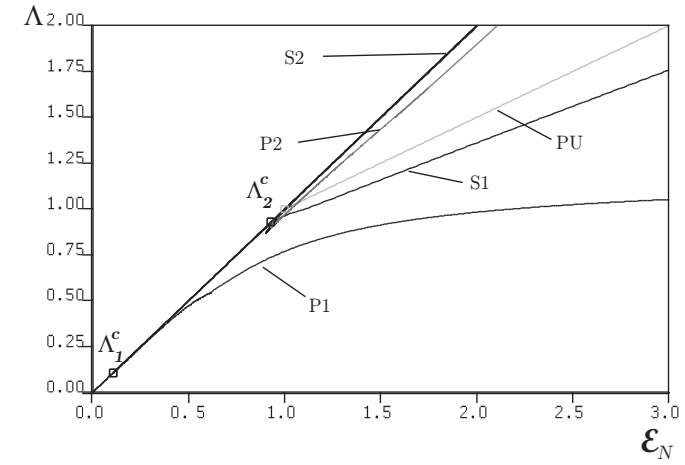

(a)

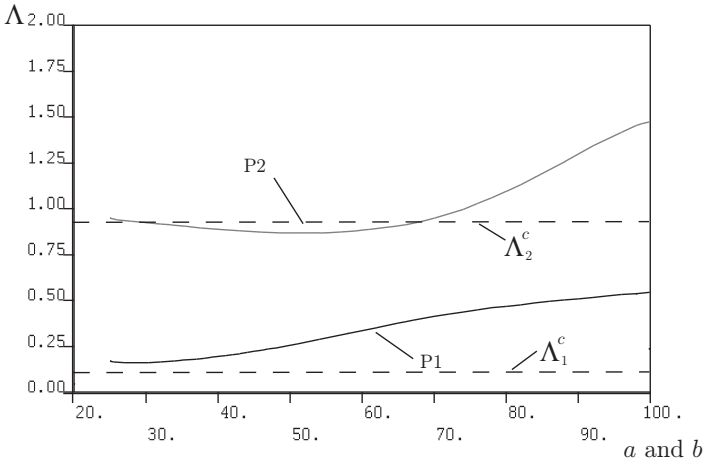

(b)

Figure 7.19: Delamination growth rate, case 3 (A). Normalized axial load Λ versus (a) normalized end-shortening $\mathcal{E}_N$ and (b) delaminated patch dimensions a and b.

aspect to identify currently, is that with growing delamination, the maximum possible load achievable would be 44.9% of the undamaged panel's buckling capacity, *i.e.* lower than the initial critical load. At this load, the panel would have fully delaminated. Hence, a delamination of these dimensions is even more dangerous than the previously discussed, slightly smaller delamination, configurations in case 2 and should be avoided, since not even 50% of the undamaged panel's capacity can be attained.

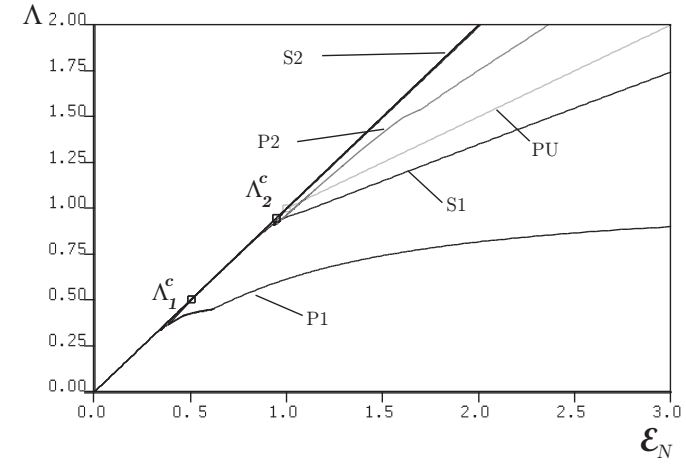

(a)

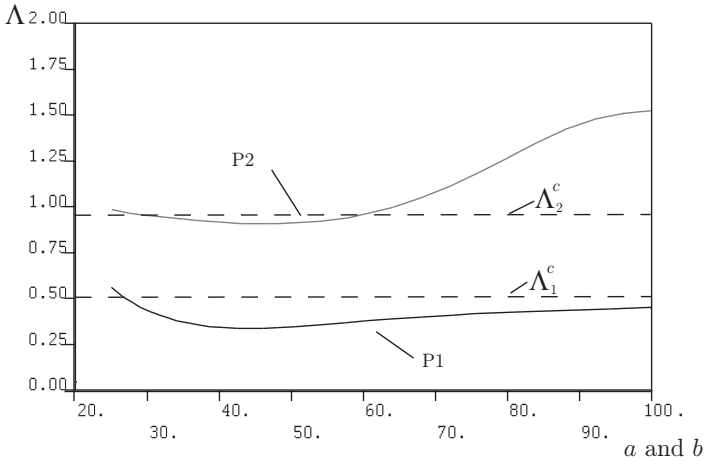

(b)

Figure 7.20: Delamination growth rate: Case 3 (B). Normalized axial load Λ versus (a) normalized end-shortening $\mathcal{E}_N$ and (b) delaminated patch dimensions a and b.

The second critical load occurs at $\Lambda_2^{\mathrm{C}} = 0.948$ and can be increased slightly until propagation occurs. The delamination again grows in a fast and unstable manner,

path "P2" in Figure 7.20b, until the system restabilizes at $\Lambda_2^{\min} = 0.909$. However, the system also fully delaminates under a monotonic loading increase before $\Lambda = 2.0$ is reached. Furthermore, the postbuckling reserve capacity, Figure 7.20a, is overestimated in both, first and second equilibrium cases since $a = b = 100$ mm and hence the assumed boundary conditions in the Rayleigh–Ritz procedure are no longer an accurate representation.

7.1.4.3 Case 3 (C)

Case 3 (C) is another mixed mode that borders on a global mode configuration with a delamination located at $c = 0.15$. As in the previously described case of this characteristic, case 2 (C) in §7.1.3.3, the growth for the first and second critical load is highly unstable and fast once triggered, Figure 7.21b. In the first postbuckling path, full delamination occurs again at a value well below the full capacity of an undamaged panel, at $\Lambda_2^{\max} = 0.427$ which is even lower than for the thinner delaminations of the same size, *i.e.* case 3 (A) and (B). The reserve capacity shown in Figure 7.21a can again be regarded as an overestimation for both postbuckling solutions.

The second critical load is in this case at $\Lambda_2^{\mathrm{C}} = 1.113$ and can be increased marginally until the delamination propagates. Again, a highly unstable and fast growth occurs and the load drops below 100%, *i.e.* depending on the loading scenario this could lead to a dynamic snap as outlined before.

7.1.4.4 Case 3 (D)

The final case contains a delamination patch of dimensions $a = b = 25$ mm at depth $c = 0.20$ and is the global buckling case. Hence, no growth occurs at the first postbuckling solution, Figure 7.22b, but does in the second postbuckling configuration, path "P2". The load at which propagation initiates can again, in the latter case, never be attained, see the relevant values in Table 7.7, and the system fully

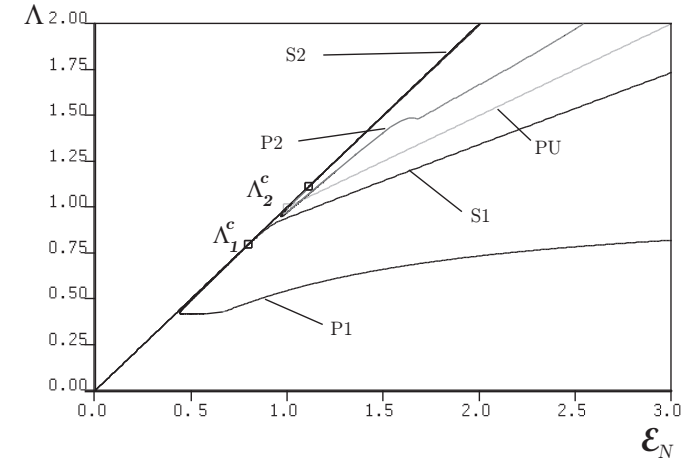

(a)

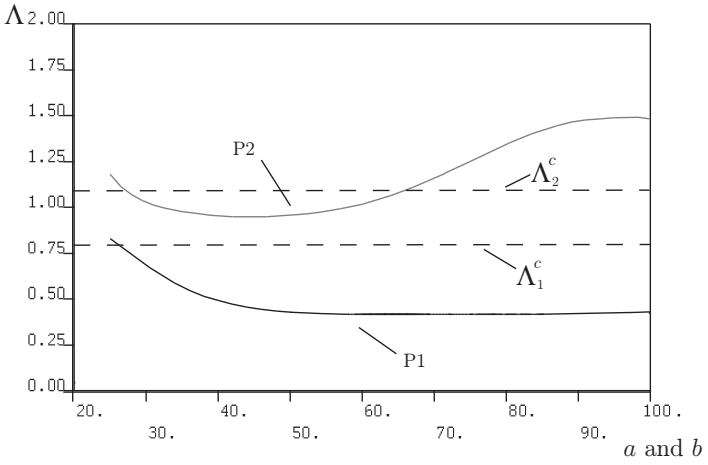

(b)

Figure 7.21: Delamination growth rate: Case 3 (C). Normalized axial load Λ versus (a) normalized end-shortening $\mathcal{E}_N$ and (b) dimensions a and b.

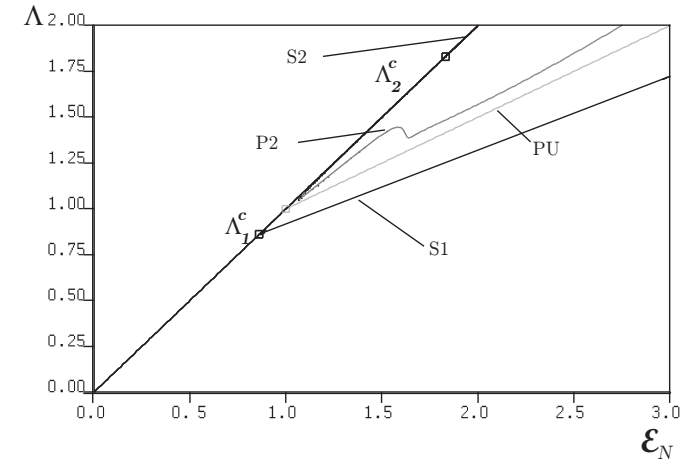

(a)

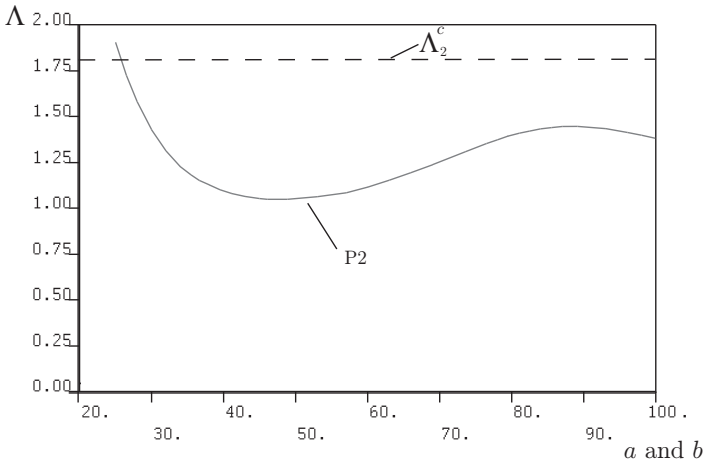

(b)

Figure 7.22: Delamination growth rate: Case 3 (D). Normalized axial load Λ versus (a) normalized end-shortening $\mathcal{E}_N$ and (b) delaminated patch dimensions a and b. Note the lack of path "P1".

delaminates before reaching 200% of an undamaged panel. The reserve stiffnesses that could be taken from the load versus end-shortening graphs in Figure 7.22a are inaccurate as explained above.

Interestingly, the postbuckling behaviour in the opening mode configuration recovers after the minimum load and the load can be increased again. However, at $a = b =$ 88 mm the load begins to drop again with growing delamination, hence a limit point is reached which is below the initial critical load and the load at which delamination growth occurs, see Figure 7.22.

7.1.4.5 Summary: Case 3

The final delamination size investigated and reviewed currently contained a initial delamination patch of dimensions $a = b = 25$ mm. It can be seen that even for a relatively small delamination of these dimensions, the incorporation of the irreversible damage mechanism can lead to global failure of the structural component.

In all cases where delamination propagation occurs in the closing mode configuration, *i.e.* thin-film and mixed mode buckling, the system fully delaminates at low load levels around 50% or less of an undamaged panel. This means that even if a panel was designed only up to that load level, catastrophic consequences could potentially occur due to the presence of the delamination that could have not been predicted without allowing for the growth of the localized defect.

Even for the second postbuckling solution, the opening mode, significant growth occurs at load levels below 100% of an undamaged panel and the stiffness decrease is more pronounced than in previous, smaller delamination configurations. Hence it can be concluded that delaminations of these dimensions should not be allowed to occur since they would lead to structural failure in all cases.

Case 3	(A)	(B)	(C)	(D)
Λ_1^{C}	0.107	0.504	0.790	0.861
$\Lambda_1^{\mathrm{prop}}$	0.169	0.562	0.835	–
Λ_1^{min}	0.162	0.338	0.419	–
a and b at Λ_1^{min} (mm)	37	44.5	62	–
Λ_1^{max}	0.510	0.449	0.427	–
a and b at Λ_1^{max} (mm)	100	100	100	–
growth stationary at Λ_1^{max}?	n/a	n/a	n/a	–
Λ_2^{C}	0.929	0.948	1.113	1.832
$\Lambda_2^{\mathrm{prop}}$	0.947	0.986	1.182	1.906
Λ_2^{min}	0.869	0.909	0.949	1.049
a and b at Λ_2^{min} (mm)	52.5	47	45	48
Λ_2^{max}	1.705	1.518	1.518	1.446
a and b at Λ_2^{max} (mm)	100	100	100	100
growth stationary at Λ_2^{max}?	n/a	n/a	n/a	n/a

Table 7.7: Results summary: Case 3.

7.2 Concluding remarks

In this chapter, parametric investigations were presented that incorporated the delamination propagation model established in Chapter 6. Different delamination sizes and depths were studied, principally in the neighbourhood of the transitional depth c_{t} (Melin & Schön, 2001) where the buckling behaviour changes from local via mixed mode to global buckling. The postbuckling behaviour and growth characteristics were identified and discussed. Moreover, the model was quantitatively compared to existing experimental and numerical results from the literature (Melin & Schön, 2001; Nilsson *et al.*, 1993) for different dimensions and found to be in very good phenomenological agreement.

With the model developed it can be shown that thin-film and mixed mode buckling

lead to delamination growth (Chai *et al.*, 1981; Simitses *et al.*, 1985; Hunt *et al.*, 2004) and potentially due to progressive failure, *i.e.* extensive growth, to premature overall structural instability (Shivakumar & Whitcomb, 1985; Rolfes *et al.*, 2009). Hence, the first conclusion can be established in agreement with Melin & Schön (2001):

(I) The transitional depth c_t is located at between 10–20% of the depth of this panel. Buckling-driven delamination growth only occurs where the pre-existing delaminations are closer to the surface than c_t or precisely located at depth c_t.

Furthermore, it should be noted that force-controlled or dead loading may lead to catastrophic debonding of the laminates (Bottega & Maewal, 1983), as seen particularly in the examples for marginally larger delaminations, *i.e.* in cases 2 and 3, of dimensions $a = b = 20$ mm and 25 mm respectively. In addition, if monotonic loading conditions are employed, dynamic effects such as snap-backs may occur during delamination growth and loading (Bolotin, 1996; Wimmer & Pettermann, 2008). In all cases it can be seen that the load carrying capacity is considerably reduced when delamination propagation is incorporated, as also found by Suemasu *et al.* (2008), and cannot reach the reserve capacity of an undamaged panel in the postbuckling range (Bisagni & Walters, 2008) nor the capacity of the non-propagating cases discussed in Chapter 5. Moreover, in agreement with Chen & Sun (1999) it was shown that the midpoint deflections of the laminates are larger with delamination propagation than without and that the postbuckling behaviour is strongly affected by delamination growth, a feature also found by Sheinman *et al.* (1998).

Since the current design criteria in aircraft construction do not allow for growth to occur (Melin *et al.*, 2002) the structure may not be exhausted to its possible limits due to the low admissible design forces when only the critical buckling loads are established. Hence, it may be desirable to find threshold parameters for a safe design scenario, such as the largest, admissible defect diameter and threshold strain for delamination initiation (Rhead & Butler, 2009), and an attempt to identify

Case	0(A)	0(B)	1(A)	1(B)	1(C)
$\Lambda_1^{\max}$	0.884	0.902	0.874	0.870	0.849
$\Lambda^{\mathrm{C}}_{1,c=0.5}$	0.967	0.967	0.950	0.950	0.950
$\Lambda^{\mathrm{C}}_{1,c=0.5}$ - $\Lambda_1^{\max}$ [%]	8.4	6.6	7.6	8.0	10.1

Table 7.8: Critical loads for $c = 0.5$ and maximum capacity of panel with propagating delamination.

critical parameters will be undertaken herein.

The investigations showed that for the smaller BVIDs, cases 0 and 1 with $a = b =$ 12 mm and 15 mm respectively, delamination growth occurs up to a certain delamination size but is then arrested and overall buckling occurs[2]. However, once the delamination is equal to or larger than $a = b = 20$ mm the growth spreads over the entire panel dimensions, thus a defect of that size should be avoided or repaired when detected. Potential measurements on containing damage within safe boundaries would include a three-dimensional mesh or weave geometry of the laminates and transverse reinforcement such that the delamination could be kept in safe dimensional boundaries, recall Figure 1.2 and the discussion in §1.1.1. This may require more detailed investigations in the mesh geometries employable for the design scenarios in the spirit of Verpoest & Lomov (2009). However, from the current small-scale investigation for a particular panel it can be concluded that a maximum permissible delamination size must be smaller than $a = b = 20$ mm or contained within these boundaries, *i.e.* conclusion (II) reads:

(II) The maximum permissible delamination size for the panel considered in the current study: $a = b \leqslant 20$ mm to avoid complete debonding of the layers due to progressive damage.

If the growth can be contained to these dimensions, it can be observed that the maximum load for these panels is no lower than 10% of the critical load for an

[2]For the actual values please refer to each section in this chapter.

undamaged panel with a delamination at $c = 0.5$ before global buckling occurs, see Table 7.8. A third conclusion reads:

(III) If $a = b \leqslant 20$ mm then the maximum permissible design load is approximately 10% lower than the critical load derived with linearized analysis for a panel of the same delamination configuration, containing a delamination at $c = 0.5$.

Sheinman *et al.* (1998) identified that the length to thickness ratio of the delamination mostly affects the growth. In their assessment, it was found that growth may commence when the ratio of the delamination length to the overall length of the panel is larger than or equal to ratio of the delamination depth to the overall thickness. Defining this using the parameters in the current model yields the next conclusion for the panel investigated:

(IV) $\dfrac{a}{L} \geqslant c \Rightarrow$ delamination growth .

This is true for the current model for the first critical load and the statement is in fact conservative, since in cases 0 (C) and (D); 1 (D); 2 (D) and 3 (E) no propagation occurs, see the summary in Table 7.9.

Furthermore, when defining the so-called slenderness of the sublaminate as $\lambda = a/(ct)$, it can be concluded that growth, after the first critical load is triggered (refer to Table 7.9), only occurs for delaminations which initially also agree with conclusion (IV):

(V) $\lambda = \dfrac{a}{ct} > 80 \Rightarrow$ delamination growth .

The next conclusions that can be established, are that thin-film delamination leads to stable growth and mixed mode buckling to unstable growth in all cases, thus:

(VI) thin-film buckling $\Rightarrow$ stable delamination growth.

Case	a (mm)	a/L	c	$\lambda = a/(ct)$	growth
0(A)	12	0.12	0.05	120	yes
0(B)	12	0.12	0.065	92	yes
0(C)	12	0.12	0.075	80	no
0(D)	12	0.12	0.10	60	no
1(A)	15	0.15	0.03	250	yes
1(B)	15	0.15	0.05	150	yes
1(C)	15	0.15	0.085	88	yes
1(D)	15	0.15	0.12	62	no
1(E)	15	0.15	0.20	37	no
2(A)	20	0.20	0.05	200	yes
2(B)	20	0.20	0.085	117	yes
2(C)	20	0.20	0.11	91	yes
2(D)	20	0.20	0.15	67	no
3(A)	25	0.25	0.05	250	yes
3(B)	25	0.25	0.11	113	yes
3(C)	25	0.25	0.15	83	yes
3(D)	25	0.25	0.20	63	no

Table 7.9: Propagation conclusions summary for the first critical load for all cases of the panel with dimensions $L = B = 100$ mm and $t = 2$ mm.

(VII) mixed mode buckling ⇒ unstable delamination growth.

The drop in the load is, however, dependent on the physical parameters. Whether thin-film or mixed mode buckling occurs can easily be identified via the transitional depth c_t using linear eigenvalue analysis as shown in Chapter 5 §5.2.2 when plotting Λ versus c.

Finally, it should be noted that for the second critical load, for thin-film as well as mixed mode buckling, the load may drop below 100% capacity of an undamaged panel, hence:

(VIII) thin-film and mixed mode buckling ⇒ unstable delamination growth for the second postbuckling path at load levels around or below 100%.

However, this only occurs for delaminations in the current study where $a = b \geqslant 20$ mm which is to be avoided or restricted when applying conclusion (II).

With these conclusions in mind, a panel can be designed to operate safely in service under in-plane loading conditions, assuming that the delamination patch remains the same basic shape; scaling and the generic effects of changing size would of course become important (Bažant & Cedolin, 1991). Obviously, for a specific panel of different materials and geometries similar studies would need to be conducted as presented in this chapter to ascertain the specific values of the size of the delaminated patch $a \times b$ given in conclusion (II) and (III). In the next chapter, this assumption will be loosened and differing shaped delamination patches and their potential effect on the mechanical response will be discussed.

Chapter 8

Postbuckling regime of a unidirectionally propagating delamination

8.1 Introduction

In this part of the current work a pilot study on unidirectionally delamination propagation is presented where a general trend of the behaviour is identified. However, it should be noted that this part of the research has the potential to be considerably expanded in future investigations, particularly in light of enhancing the model's material properties to incorporate orthotropy, as will be discussed in the next chapter.

Unidirectional delamination growth occurs essentially when the delamination propagates predominantly in one direction, *i.e.* either in the same direction as (Figure 8.1a) or transverse (Figure 8.1b) to the load. This type of growth has been observed to occur principally in the direction perpendicular to the loading direction by other researchers (Bottega & Maewal, 1983; Chai & Babcock, 1985; Peck & Springer, 1991; Yin & Jane, 1992a; Nilsson *et al.*, 1993). However, this is not always the case

as investigations by Nilsson *et al.* (2001b) have shown where the growth direction was observed to be linked to the depth of the delamination; shallow delaminations yielded growth perpendicular to the loading direction and deep defects resulted in propagation in the loading direction in this investigation. Different cases will be discussed in the following sections where propagation is permitted to occur in one direction only and the algorithm developed in Chapter 6 is changed accordingly.

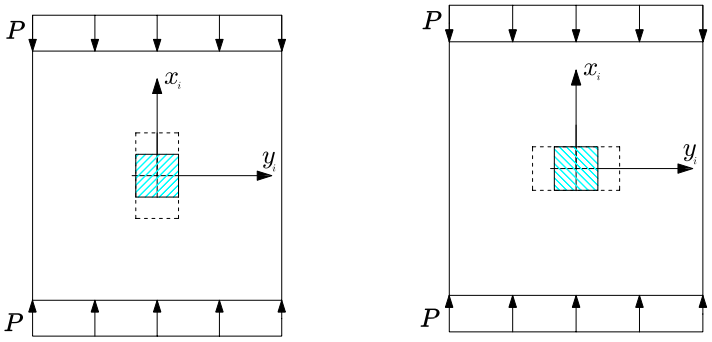

Figure 8.1: Unidirectional delamination propagation originating from an initially square delamination; (a) growth in the longitudinal direction only – x_i-axis and (b) growth in the transverse direction only – y_i-axis.

8.2 Numerical experimentation and results

During the course of this pilot study, different growth scenarios are investigated. Firstly, unidirectional growth is assumed to occur originating from a square delamination as investigated in the previous chapter. Thereafter, propagation is investigated for panels containing a rectangular delamination, either initially wide or long.

8.2.1 Unidirectional delamination propagation originating from an initially square delamination

Having established in the previous chapter that once the pre-existing delamination is marginally larger, delamination growth can cause complete debonding of the interface, an initial defect of square dimensions $a = b = 15$ mm is investigated. Furthermore, these dimensions are consistent with the investigations in the preceding chapter.

In the following sections, the cases summarized in Table 8.1 are presented and discussed for unidirectional delamination propagation originating from an initially square delamination for growth in either the longitudinal direction, *i.e.* in the x_i-direction, Figure 8.1a and §8.2.1.1, or the transverse direction, *i.e.* in the y_i-direction, Figure 8.1b and §8.2.1.2. It should be made clear that this initial study does not say whether non-uniform or uniform growth would occur, but investigates which direction growth would occur if it were to be constrained into one direction.

Case I	(A)	(B)	(C)
c	**0.05**	*0.085*	0.12

Table 8.1: Examples of postbuckling with unidirectional delamination propagation originating from an initially square delamination. Thin-film buckling cases are indicated in **bold**, mixed mode cases in *italics* and global buckling in Roman font

An index for each case indicates the propagation direction, *i.e.* x for growth in the x_i-direction and y for growth in the y_i-direction. The convention for the abbreviations in the graphs are as described in Table 7.3. However the additional cases including unidirectional delamination propagation are as denoted in Table 8.2.

Label	Description
S1	First physical postbuckling path of a damaged panel containing a stationary delamination
S2	Second physical postbuckling path of a damaged panel containing a stationary delamination
P1x	First postbuckling path of a damaged panel containing non-uniformly propagating delamination in the x_i-direction
P2x	Second postbuckling path of a damaged panel containing non-uniformly propagating delamination in the x_i-direction
P1y	First postbuckling path of a damaged panel containing non-uniformly propagating delamination in the y_i-direction
P2y	Second postbuckling path of a damaged panel containing non-uniformly propagating delamination in the y_i-direction

Table 8.2: Abbreviations for the graph labels describing the postbuckling behaviour of a panel containing a unidirectionally propagating delamination.

8.2.1.1 Growth in the longitudinal direction only – x_i-axis

Only the local, case I $(\mathrm{A})_x$, and the mixed buckling mode, case I $(\mathrm{B})_x$, are presented with all postbuckling paths in this chapter since the other case essentially yields the same conclusions regarding the propagation behaviour. For global buckling, case $(\mathrm{C})_x$, only the normalized load versus normalized end-shortening as well as the growth plots are shown in Figure 8.6. Further results can be found in Appendix B in graphical form in Figure B.3 and listed in Table B.1. In the current chapter, only the graphs are shown and a summarizing discussion of growth in the longitudinal and transverse direction can be found in §8.2.2.

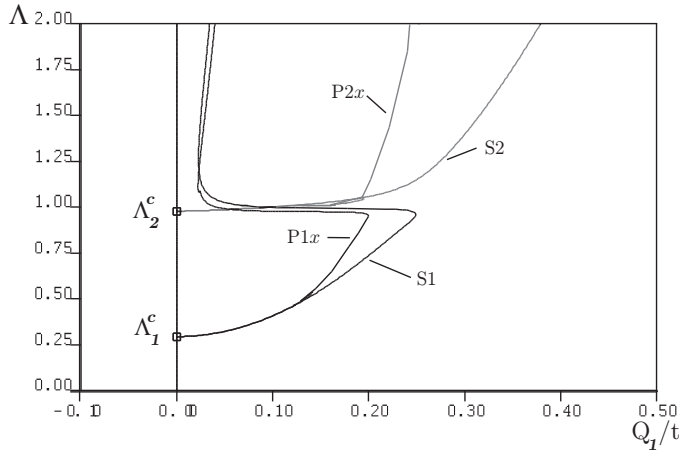

(a)

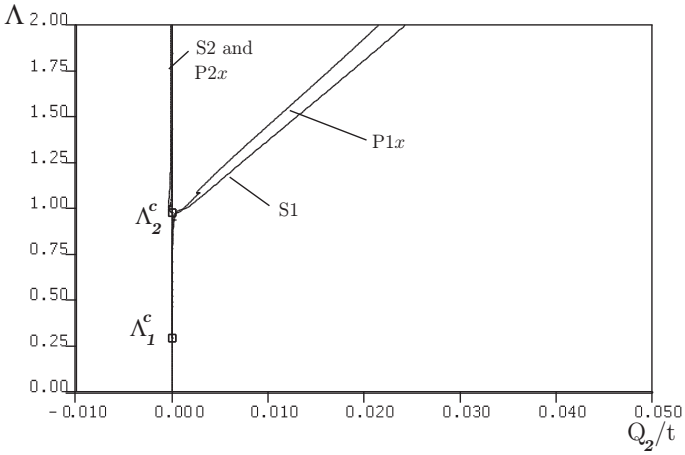

(b)

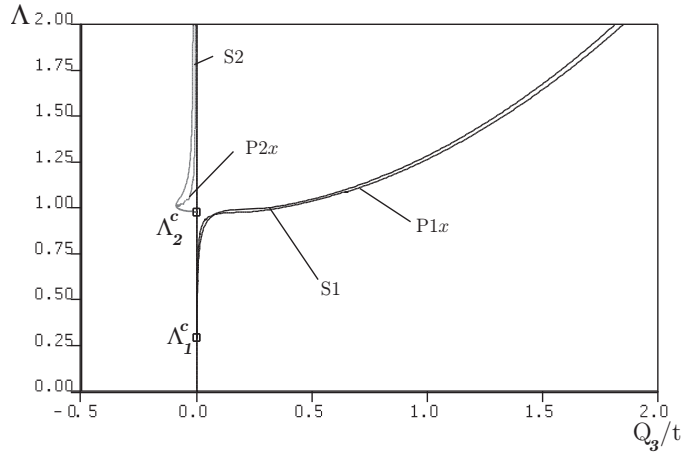

(c)

Figure 8.2: Postbuckling equilibrium paths for the local mode: case I $(\mathrm{A})_x$. Graphs show the normalized axial load Λ versus (a) Q_1/t (upper laminate), (b) Q_2/t (lower laminate) and (c) Q_3/t (intact part).

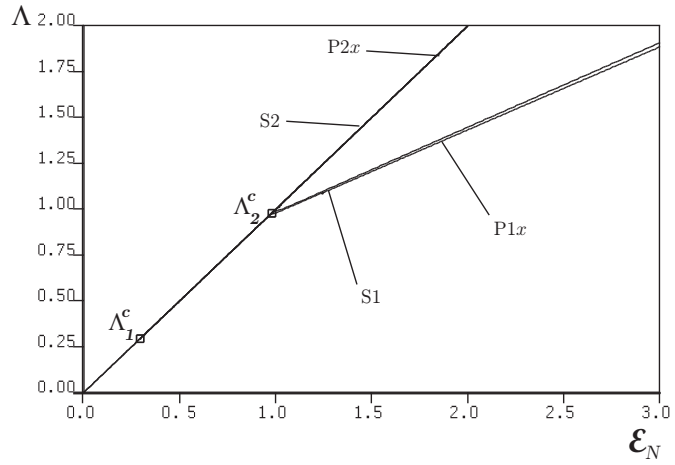

(a)

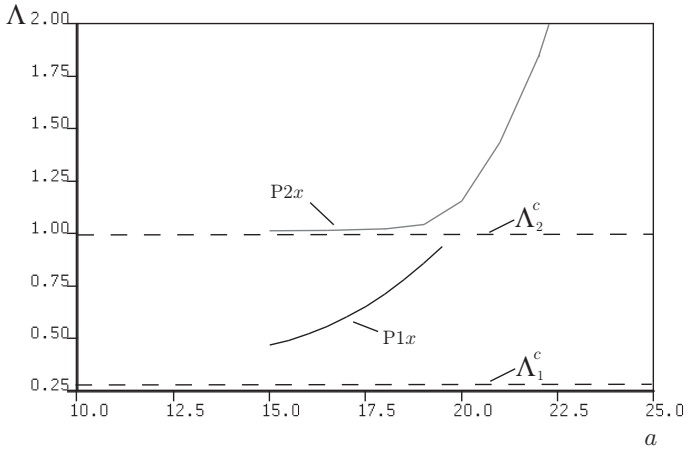

(b)

Figure 8.3: Delamination growth rate: case I $(\mathrm{A})_x$. Normalized axial load Λ versus (a) normalized end-shortening $\mathcal{E}_N$ and (b) delaminated patch dimension a.

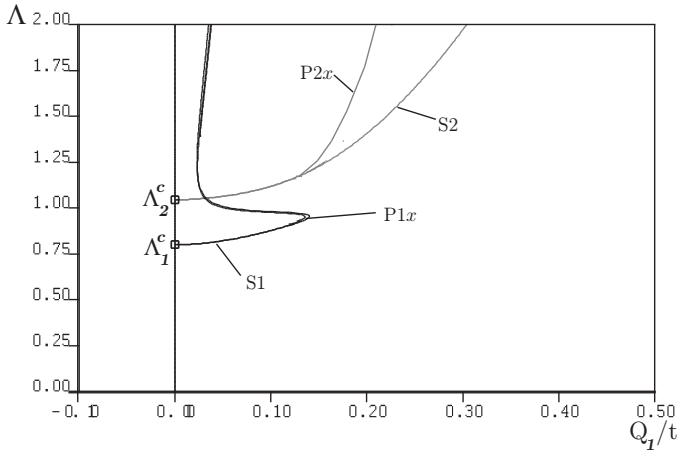

(a)

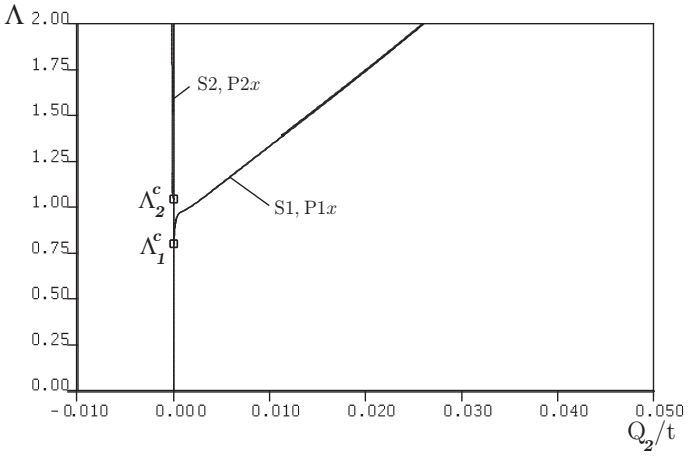

(b)

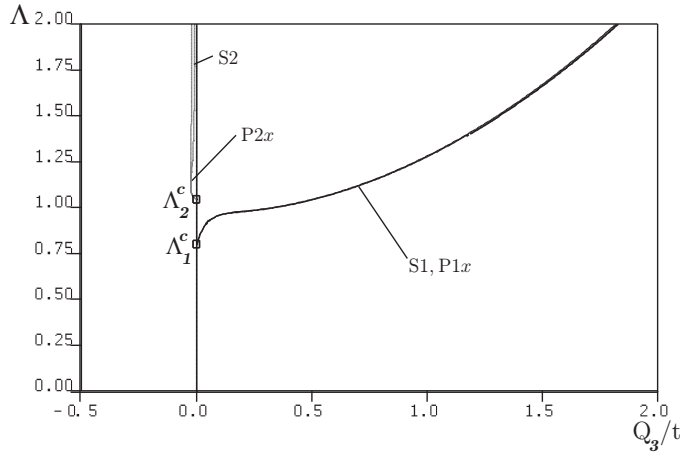

(c)

Figure 8.4: Postbuckling equilibrium paths for the mixed mode: case I $(\mathrm{B})_x$. Graphs show the normalized axial load Λ versus (a) Q_1/t (upper laminate), (b) Q_2/t (lower laminate) and (c) Q_3/t (intact part).

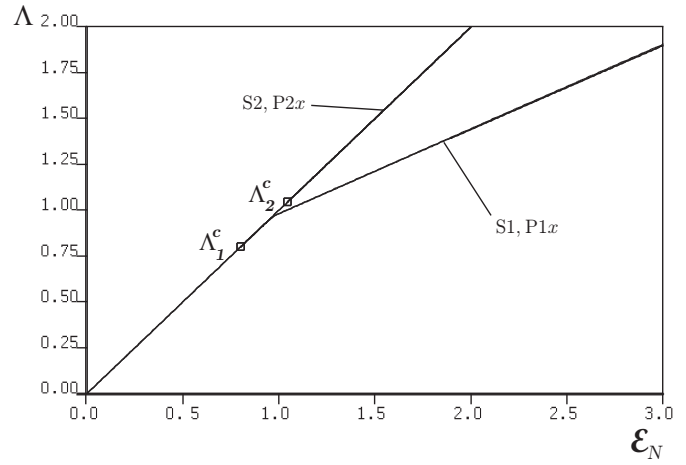

(a)

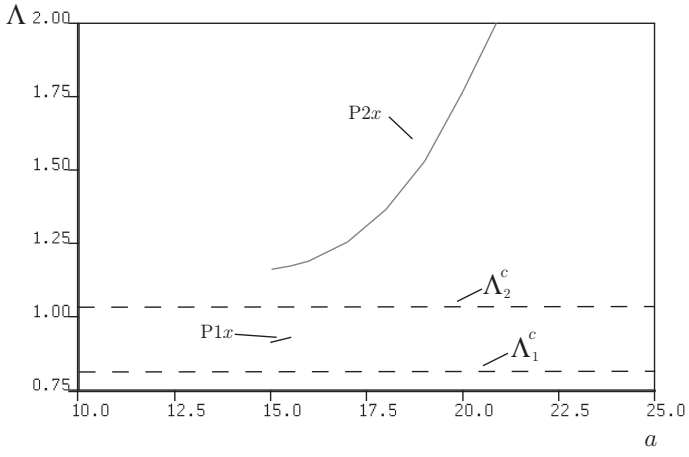

(b)

Figure 8.5: Delamination growth rate: case I $(\mathrm{B})_x$. Normalized axial load Λ versus (a) normalized end-shortening $\mathcal{E}_N$ and (b) delaminated patch dimension a.

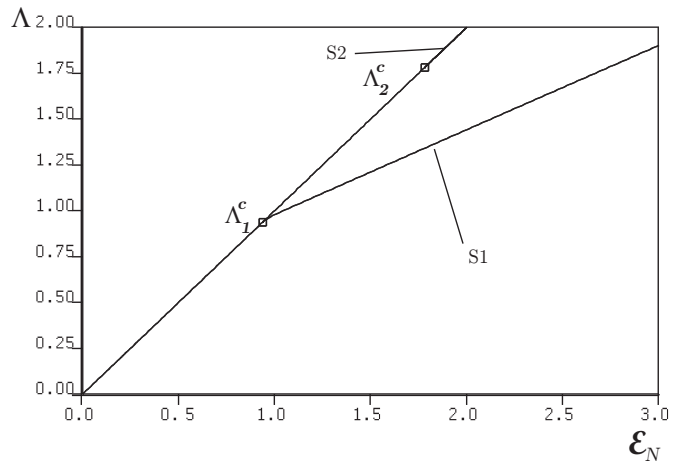

(a)

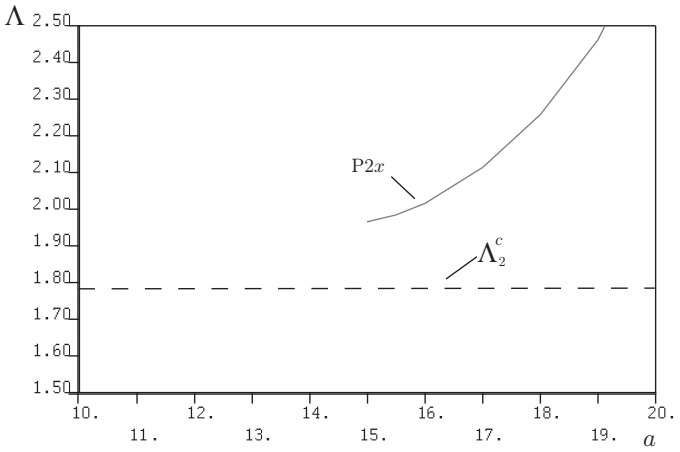

(b)

Figure 8.6: Delamination growth rate: case I $(\mathrm{C})_x$. Normalized axial load Λ versus (a) normalized end-shortening $\mathcal{E}_N$ and (b) delaminated patch dimension a. Note the lack of path "P1x".

8.2.1.2 Growth in the transverse direction only – y_i-axis

Again, only the local mode and mixed buckling mode, case I $(A)_y$ and I $(B)_y$, are presented with all postbuckling paths and further graphs can be found in Appendix B.2.2.2. Case I $(C)_y$, the global mode, is only included herein with the normalized load versus end-shortening graph, Figure 8.11, for completeness.

8.2.2 Remarks

Case I	$(A)_x$	$(A)_y$
Λ_1^{C}	0.295	0.295
Λ_1^{prop}	0.467	0.467
Λ_1^{min}	–	0.457
a or b at Λ_1^{min} (mm)	–	16
Λ_1^{max}	1.087	0.853
a or b at Λ_1^{max} (mm)	22 (a)	22.5 (b)
growth stationary at Λ_1^{max}?	yes	yes
Λ_2^{C}	0.979	0.979
Λ_2^{prop}	1.012	1.012
Λ_2^{min}	1.011	–
a or b at Λ_2^{min} (mm)	15.5 (a)	–
Λ_2^{max}	5.675	2.425
a or b at Λ_2^{max} (mm)	26	27
growth stationary at Λ_2^{max}?	no	no

Table 8.3: Results summary: case I (A). Growth in the longitudinal (x) and transverse (y) direction.

In agreement with previous investigations (Bottega & Maewal, 1983; Chai & Babcock, 1985; Peck & Springer, 1991; Yin & Jane, 1992a; Nilsson *et al.*, 1993) it can be observed that, within the scope of this pilot study, growth occurs predominantly in

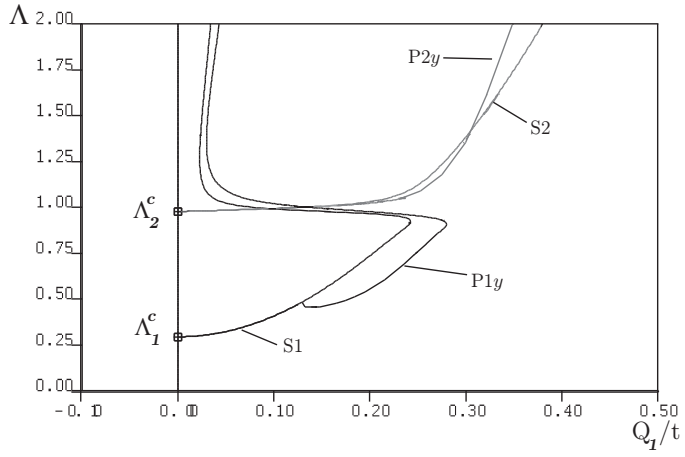

(a)

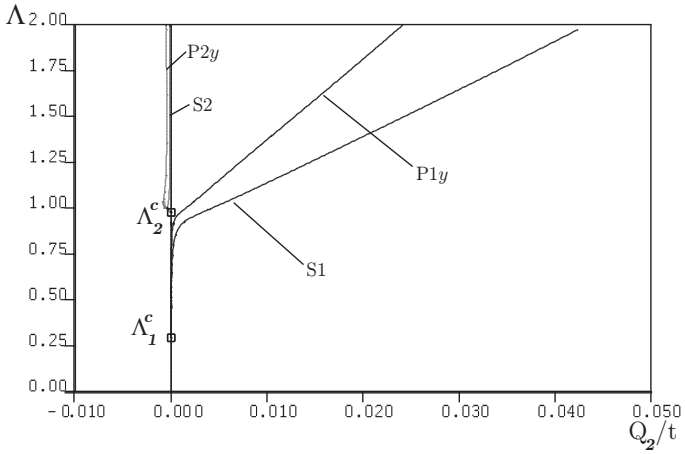

(b)

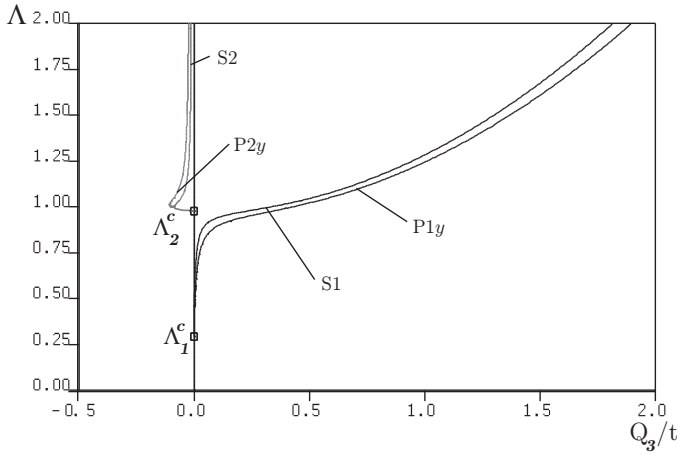

(c)

Figure 8.7: Postbuckling equilibrium paths for local mode: case I $(\mathrm{A})_y$. Graphs show the normalized axial load Λ versus (a) Q_1/t (upper laminate), (b) Q_2/t (lower laminate) and (c) Q_3/t (intact part).

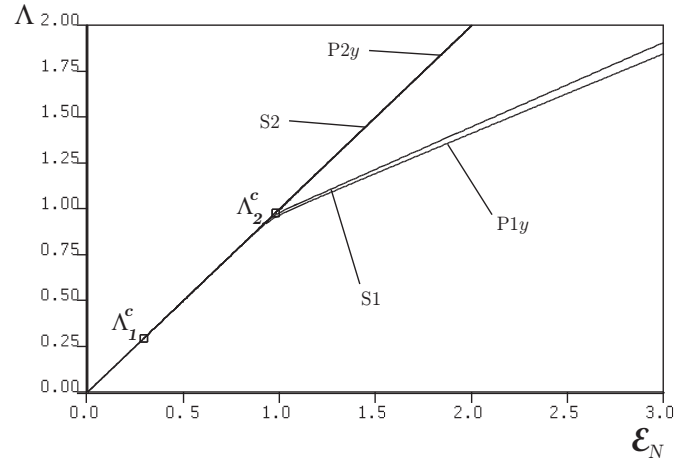

(a)

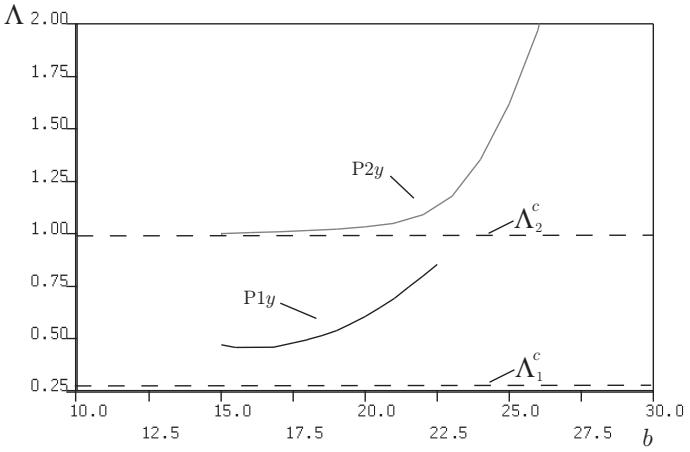

(b)

Figure 8.8: Delamination growth rate: case I $(\mathrm{A})_y$. Normalized axial load Λ versus (a) normalized end-shortening $\mathcal{E}_N$ and (b) delaminated patch dimension b.

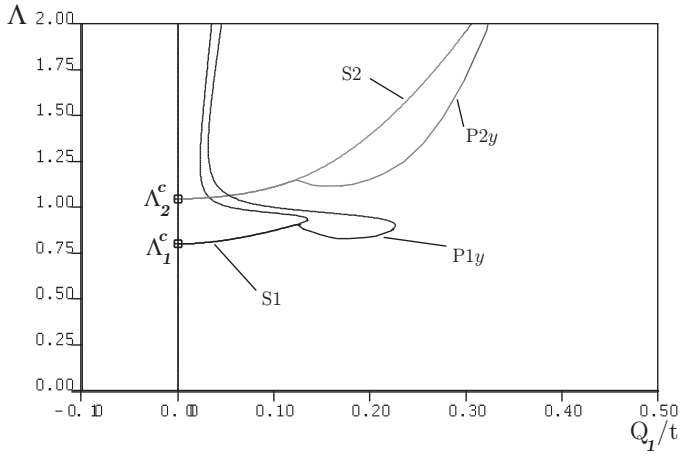

(a)

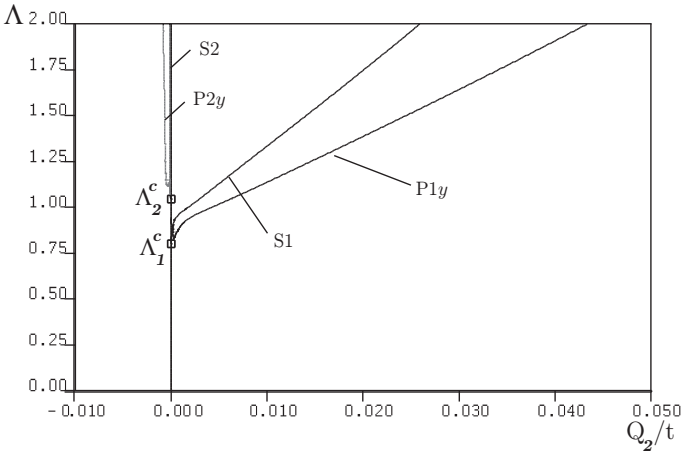

(b)

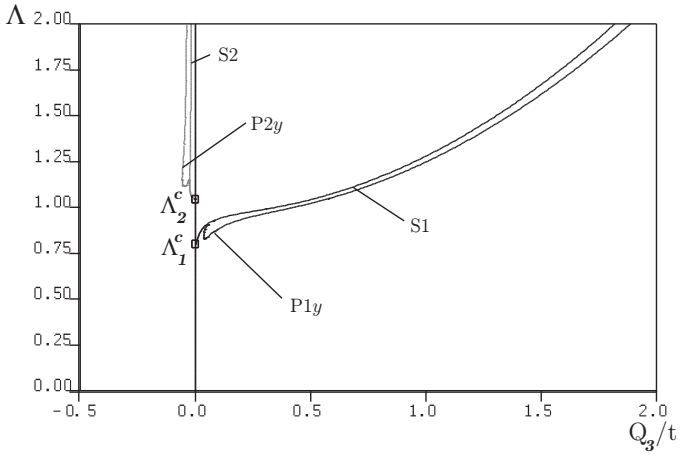

(c)

Figure 8.9: Postbuckling equilibrium paths for mixed mode: case I $(\mathrm{B})_y$. Graphs show the normalized axial load Λ versus (a) Q_1/t (upper laminate), (b) Q_2/t (lower laminate) and (c) Q_3/t (intact part).

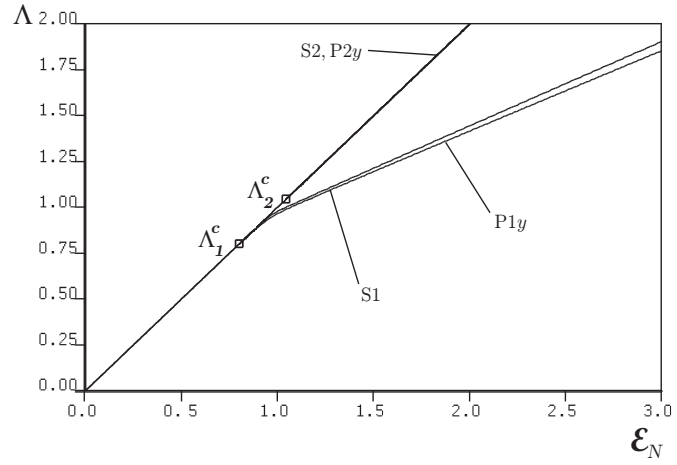

(a)

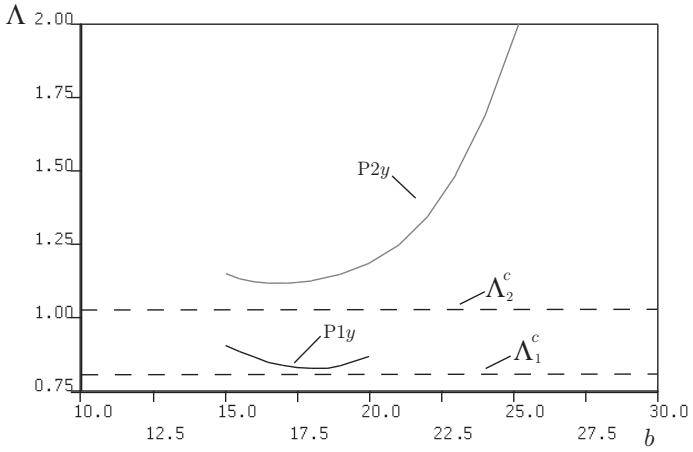

(b)

Figure 8.10: Delamination growth rate: case I $(\mathrm{B})_y$. Normalized axial load Λ versus (a) normalized end-shortening $\mathcal{E}_N$ and (b) delaminated patch dimension b.

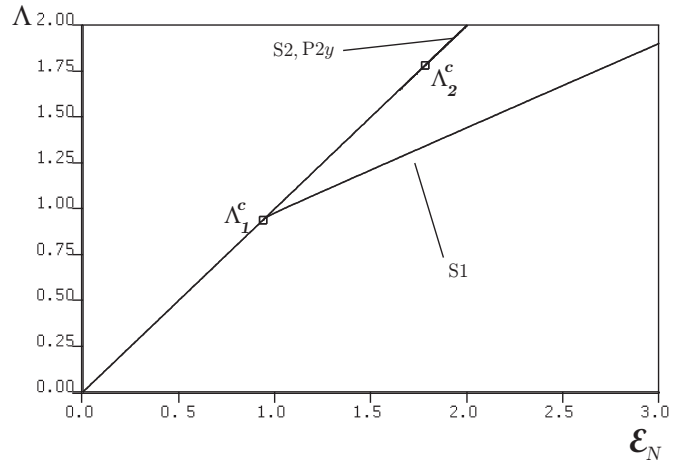

(a)

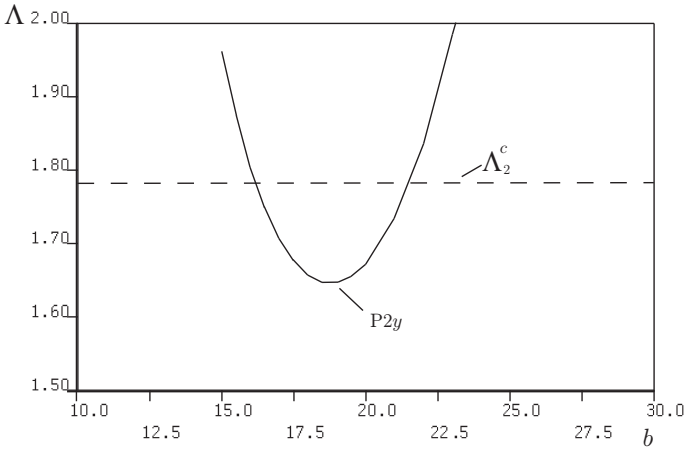

(b)

Figure 8.11: Delamination growth rate: case I $(C)_y$. Normalized axial load Λ versus (a) normalized end-shortening $\mathcal{E}_N$ and (b) delaminated patch dimension b. Note the lack of path "$P1_y$".

the direction transverse to the loading direction for the cases investigated. However, this strongly depends on the fibres in the sublaminate as well as the fibre orientation and subsequently needs to be pursued further when an anisotropic material model is to be allowed for. Nonetheless, the growth behaviour can be observed in the postbuckling graphs when comparing *e.g.* Figure 8.2a and 8.7a for case I $(\mathrm{A})_x$ and $(\mathrm{A})_y$, respectively, since the deflection of the dominant sublaminate buckle (Q_1) is furthermore pronounced when growth occurs in the y-direction. This can also be observed for the other cases investigated, see for example Figures 8.4 and 8.9 for case I $(\mathrm{B})_x$ and $(\mathrm{B})_y$. However, when propagation is permitted in the x-direction only, the sublaminate buckle reduces and less growth occurs. This means the panel would rather propagate in the transverse direction since it requires less energy, if growth was constrained in one direction only. However, when comparing the unidirectionally propagating cases, *e.g.* the local mode case (I) $(\mathrm{A})_x$ and $(\mathrm{A})_y$, Figures 8.2 and 8.7 respectively, with the corresponding uniformly propagating case 1 (B) discussed in Chapter 7 (Figure B.2), it should be noted that growth is most likely to occur uniformly currently. This is because the magnitude of the upper laminate buckle, and subsequently the relative displacement δ between the laminates, is more pronounced and therefore would lead to more excessive growth. This can also be seen in the other cases when comparing non-uniform delamination growth with a uniformly propagating delamination.

Furthermore, as listed in Table 8.3, a barely noticeable load drop is observed for transverse growth for the first postbuckling path including growth, as shown with path "P1x". In addition, the maximum load, $\Lambda_1^{\max}$ is below 100% of an undamaged panel's capacity, whereas this value is shown to be above that threshold for longitudinal propagation. A similar trend is observed for the other cases in Appendix B and furthermore for a delamination of dimensions $a = b = 20$ mm which, however, is not included in this work.

Since deeper delaminations are not investigated within this preliminary assessment, it can not be ascertained whether this configuration may lead to growth in the

longitudinal direction (Nilsson, 2001b).

8.2.3 Unidirectional delamination propagation originating from an initially rectangular delamination

Since it was established in §4.3.1.2, Figure 4.5, that for the current isotropic model, wide delaminations yield lower critical loads than long delaminations, the former is subsequently pursued further to ascertain the effects of non-uniform delamination propagation. Nonetheless, a few cases listed in Table 8.4 are investigated to study the effects of non-uniform growth originating from a long delamination geometry. However, only propagation in the transverse direction is investigated for those cases, since it was ascertained to be more critical in the previous section.

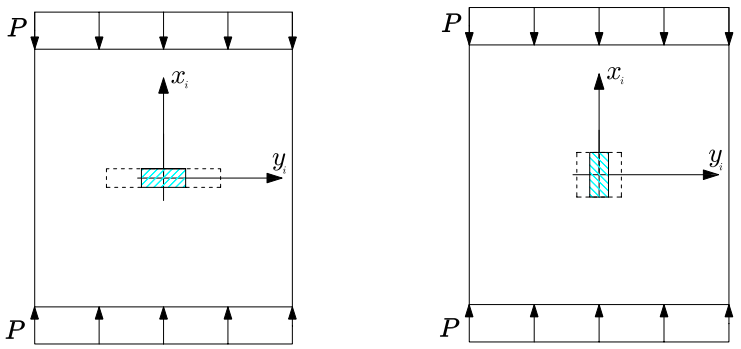

(a) (b)

Figure 8.12: Unidirectional delamination propagation originating from an initially rectangular delamination; initial growth in the transverse direction – y_i-axis – originating from a (a) wide delamination and (b) long delamination.

Although the propagation is initiated in one direction in the beginning, the delamination is eventually of square shape, which is the case when the delamination grows in the longitudinal direction when originating from a wide defect, as in cases II (A), (B) and (C), or vice versa, as in cases III (A) and (B), see Figure 8.12b. Once a square shape is reached and further delamination occurs, both uniform, as illustrated in Figure 7.1 and investigated in Chapter 7, or continuing non-uniform

Case II ($a = 0.10L$, $b = 0.15B$)	(A)	(B)	(C)
c	**0.05**	*0.085*	0.12
Case III ($a = 0.20L$, $b = 0.15B$)	(A)	(B)	–
c	**0.05**	*0.085*	–

Table 8.4: Cases investigated with unidirectional delamination propagation in either the x_i- and y_i-direction originating from an initially wide rectangular delamination—case II—and unidirectional and uniform delamination propagation in the y_i-direction originating from an initially long rectangular delamination—case III. Thin-film buckling cases are indicated in **bold**, mixed mode cases in *italics* and global buckling in Roman font

delamination, *i.e.* either longitudinal or transverse to the loading direction (Figure 8.1a or 8.1b respectively), are investigated to determine the worse case.

To maintain consistency with the previous investigations, the studies are undertaken in the BVID range with one delamination dimension being 15 mm. Investigations into initially smaller rectangular geometries, *i.e.* one dimension being a or $b = 5$ mm or 7.5 mm and various values of parameter c, resulted in no significant delamination propagation and were therefore not pursued further. The geometries discussed herein are listed in Table 8.4 for an initially wide defect of dimensions $a = 0.10L$ and $b = 0.15B$ (case II, see Figure 8.12a) and for a long delamination of size $a = 0.20L$ and $b = 0.15B$ (case III).

As before, the index for each case indicates the propagation direction, *i.e.* x for initial growth in the x_i-direction and y for initial growth in the y_i-direction. Cases where the delamination was of dimensions $a = 0.20L$ and $b < 0.15B$ were investigated but no delamination growth occurred.

8.2.3.1 Initial growth in the longitudinal direction – x_i-axis

Since case II $(A)_x$ is a panel that contains a wide delamination with propagation permitted in the longitudinal direction initially, at a certain load level, where $\Lambda = \Lambda_2^{\text{square}}$, the delamination becomes square, *i.e.* $a = b = 15$ mm. Hence, to cover the worse case, the delamination is studied to continue either propagating in the x_i-direction only, Table B.2, or in the y_i-direction only as well as uniformly in both directions, Table B.3. The same behaviour is exhibited for case II $(B)_x$ but at such a high load level that it is not pursued further.

8.2.3.2 Initial growth in the transverse direction – y_i-axis

Since in §8.2.2, transverse delamination growth was established to be more severe for a delamination of square shape, it is furthermore investigated to originate from an initially rectangular delamination shape. Results are presented herein in tabulated form only in Table 8.5. Since in case III (A) and III (B) the initial delamination is long and growth is initiated in the y_i-direction, the delamination could potentially be of square shape when propagation occurs as discussed previously. However, in accordance with the findings in §8.2.2 it should be noted that propagation in the x_i-direction is not critical once the delamination is of square dimension, as shown in case II (A) (Figure 8.13 and Table B.3). Hence this type of growth is subsequently neglected in the following investigations and only uniform or propagation transverse to the loading direction is pursued further. This is summarized for cases III (A) and III (B) in Tables B.4 and B.5, respectively, in Appendix B. In case III (A) this happens at both the first and second critical load. However, once the delamination is located deeper into the panel—mixed mode buckling, case III (B)—the delamination only reaches square dimensions at the second critical load.

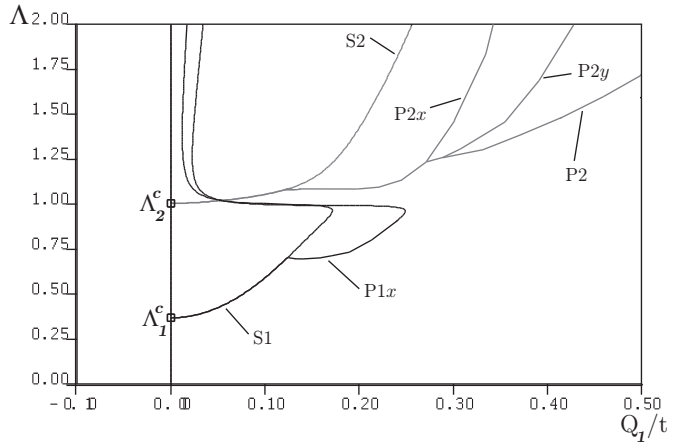

(a)

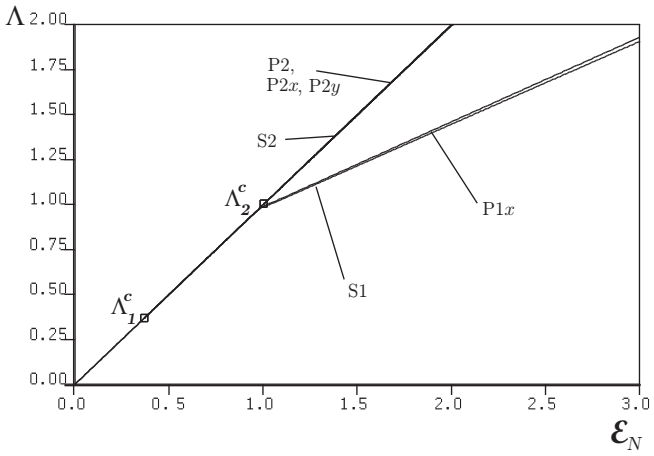

(b)

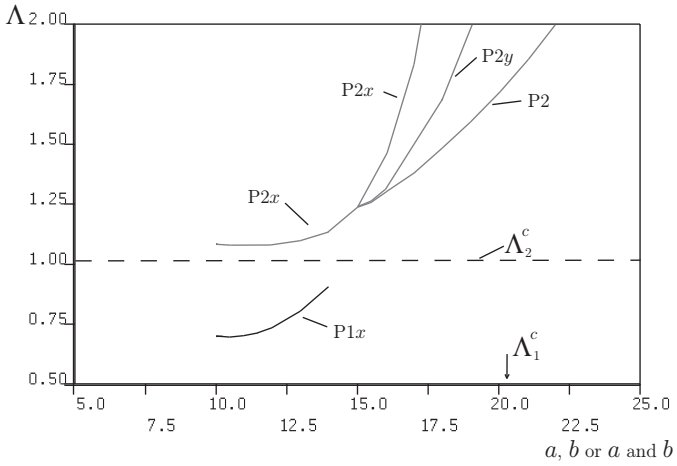

(c)

Figure 8.13: Postbuckling equilibrium paths for local mode: case II (A). Graphs show the normalized axial load Λ versus (a) Q_1/t (upper laminate), (b) normalized end-shortening $\mathcal{E}_N$ and (c) delaminated patch dimension a and/or b.

Case	II $(A)_y$	II $(B)_y$	II $(C)_y$	III $(A)_y$	III $(B)_y$
Λ_1^{C}	0.366	0.868	0.942	0.333	
$\Lambda_1^{\mathrm{prop}}$	0.700	–	–	0.582	0.891
Λ_1^{min}	–	–	–	0.457	–
b at Λ_1^{min} (mm)	–	–	–	19	–
Λ_1^{max}	0.824	–	–	0.882	–
b at Λ_1^{max} (mm)	17	–	–	27.5	–
growth stationary at Λ_1^{max}?	yes	–	–	yes	–
Λ_2^{C}	1.004	1.249	2.318	0.964	1.042
$\Lambda_2^{\mathrm{prop}}$	1.084	1.579	–	0.991	1.259
Λ_2^{min}	–	–	–	0.991	1.068
b at Λ_2^{min} (mm)	–	–	–	15.5	18.5
Λ_2^{max}	2.380	2.295	2.894	2.463	2.700
b at Λ_2^{max} (mm)	20	18.5	17	33	33
growth stationary at Λ_2^{max}?	no	no	no	no	no

Table 8.5: Results summary: growth in the transverse direction only: y-axis originating from a wide (case II) or long (case III) defect.

8.2.4 Remarks

In accordance with the findings in §8.2.2, it should be noted that growth is less likely to occur in the longitudinal direction and more critical in the direction perpendicular to the loading direction for cases of a rectangular defect shape. This is regardless of whether the delamination is long or wide initially. Once the delamination is square, uniform growth is also permitted and it is found that uniform growth yields more critical growth than in one direction only.

8.3 Remarks

This part of the current work was a pilot study only and requires further work as will be discussed in the next chapter. However, with these preliminary studies it can already be observed that if growth was constrained to one direction it is more likely to occur perpendicular to the loading direction, which is in agreement with previous research (Bottega & Maewal, 1983; Chai & Babcock, 1985; Peck & Springer, 1991; Yin & Jane, 1992a; Nilsson *et al.*, 1993). This conclusion reached made because in the postbuckling range it was found that the load dropped and more growth at a lower load level occurred when propagating in the transverse direction. Owing to the more pronounced local buckle of the upper laminate, growth continued further due to the higher local energy stored in the spring in the cohesive zone. This is the case for all configurations investigated, thus only a few cases are presented within this chapter and further results can be found in Appendix B. It should also be stated that once the initially rectangular defect patches become square, it was found that uniform growth was found to govern henceforth.

However, it should be noted that deeper delaminations are not investigated within this preliminary assessment, since they would require a change in the local energy model to incorporate Mode II fracture since sliding is understood to become the governing growth criteria, as will be discussed in the following chapter. Therefore currently it cannot be ascertained whether this configuration may lead to growth in the longitudinal direction as found by Nilsson *et al.* (2001b).

Chapter 9

Conclusions and further work

9.1 Concluding remarks

This thesis has presented an analytical, nonlinear model for an isotropic panel with a pre-existing, embedded delamination that is loaded under in-plane compression. Since composites are increasingly being used in aircraft, as well as other types of structures, it is of utmost importance to simulate and investigate their failure mechanisms (Linde, 2008) to predict their behaviour when damaged. Since delaminations can reduce the load carrying capacity of a component considerably, it is crucial to investigate the behaviour carefully to enable the structural component's safe application. This is because significant strength and stiffness degradation may result from the defect. The stability and integrity of the structural component can be adversely affected by the presence of the delamination and results can be catastrophic (Shivakumar & Whitcomb, 1985; Garg, 1988; Kardomateas & Schmueser, 1988; Short *et al.*, 2001).

The model developed in Chapter 3 primarily builds upon the two-layer strut model presented by Hunt *et al.* (2004) with the underlying assumptions and development of the model being extensively discussed. The model was formulated via minimum

energy principles employing a Rayleigh–Ritz procedure, where initially only linear eigenvalue analysis was employed to obtain the critical loads and corresponding eigenvectors in Chapter 4. However, to exploit fully the potential of the panel, it was crucial to investigate the panel in the postbuckling range, first for a stationary delamination (Chapter 5). Delamination propagation, moreover, can potentially lead to further instabilities of the panel, hence a formulation for the inclusion of growth of the defect in the form of a discrete cohesive zone model was developed in Chapter 6. This type of model was then incorporated into the model and a uniformly propagating delamination was extensively investigated in Chapter 7 for different model parameters. In addition, a pilot study on non-uniform delamination growth was conducted in Chapter 8.

This section summarizes the essential findings from the current work and makes some general concluding remarks. However, a more detailed discussion of the findings can be found at the end of each of the aforementioned chapters.

With the isotropic model developed in Chapter 3, the critical buckling loads for different delamination geometries were obtained using the Rayleigh–Ritz method. Furthermore, the corresponding eigenvectors were identified via linear analysis. Comparisons with the isotropic finite element model described in §3.6, as well as results from the literature, compared well phenomenologically and therefore manifested the underlying assumptions within the model and justified the general formulation. It was also concluded that smaller delaminations only have a marginal influence on the buckling load when linearized analysis was employed and that the critical loads decreased with the size of the delamination. Moreover, a long rectangular delamination was ascertained to be not as critical as a square delamination. However, investigations on wide, pre-existing delaminations resulted in slightly lower critical loads than a square configuration. In accordance with Hunt *et al.* (2004), the critical loads varied with the depth of the delamination c with a rapid reduction in load level observed for both the first and second critical loads once the delamination was located closer to the surface. Furthermore, three distinct eigenvectors were identified

corresponding to the critical loads—namely the *closing* mode for the first critical load, the *opening* mode corresponding to the second critical load and the *reverse closing* mode for the third critical load.

In Chapter 5 the nonlinear system was analysed numerically in the postbuckling range using the powerful continuation software AUTO (Doedel, 2007) which solved the equilibrium equations simultaneously to detect branching points and equilibrium paths. This gave rise to the key information that described the physical behaviour beyond the critical loads, obtained in the previous chapter. The topic of physical and non-physical branches was addressed first, with the latter being subsequently discarded. It was already established that the critical loads decreased when located closer to the surface of the panel; the transitional depth c_{t} was therefore introduced, which is located at approximately 10–20% of the thickness of the panel for smaller delaminations. This depth constituted the boundary between local, *i.e.* excessive sublaminate buckling, and global buckling, where the overall panel buckling dominated. Despite the critical loads being very low for small and thin delaminations, it could be established that the postbuckling stiffness had a high reserve capacity until the overall panel started to buckle. Nonetheless, compared to an undamaged panel, the panels investigated never attained the residual capacity of one-half of the pre-buckling stiffness, which is the case for a fully restrained, simply supported panel without any defect. However, the postbuckling paths of the thinner delaminations followed the path almost asymptotically and results were validated in the postbuckling range by comparison with the finite element model. Moreover, the analytical model was shown to give a safe estimate of the postbuckling behaviour since the derived postbuckling paths from the model were lower than the finite element results, assuming that they were used as a benchmark. Furthermore, it was established that for delaminations of the same dimensions but located closer to the mid-thickness of the panel, overall buckling commenced almost immediately after the critical load. This resulted in the consequence that thereafter it was crucial to incorporate delamination propagation since this could potentially lead to a further reduction of the postbuckling capacity of the panels. This meant that a postbuckling analysis of the

panel without incorporating a growth criterion might overestimate the strength of the structural component, and hence compromise its safe working condition.

Since the elastic buckling and postbuckling behaviour of the delaminated plate model had been established, it was a logical consequence subsequently to incorporate the irreversible damage mechanism of delamination propagation into the model. The model of choice was the discrete cohesive zone model established in Chapter 6 which assumed that a fictitious crack extended to the beginning of the inelastic zone based on the Dugdale–Barenblatt approach (Bažant & Cedolin, 1991; Camanho *et al.*, 2001). The critical strain energy release rate G_{iC}, an inherent property of the material interface, corresponding to the fracture Mode i, which in the current work is assumed to be a pure peeling mode for simplicity, *i.e.* Mode I fracture (Figure 6.2), was linked to the energy released in the cohesive surface. To capture the energy released during the fracture process, a virtual interface layer of zero thickness consisting of springs was positioned between the two laminates in the delaminated patch. An algorithm was developed to incorporate the damage mechanism into the numerical investigations.

Extensive parametric investigations were subsequently undertaken in Chapter 7 for a uniformly propagating delamination focusing on defect dimensions in the barely visible impact damage range, principally in the neighbourhood of the transitional depth c_{t} (Melin & Schön, 2001). Quantitative comparisons of the results were undertaken against existing experimental and numerical results in the literature (Melin & Schön, 2001; Nilsson *et al.*, 1993) as well as finite element results. It was shown, in particular, that thin-film and mixed mode buckling lead to delamination growth (Chai *et al.*, 1981; Simitses *et al.*, 1985; Hunt *et al.*, 2004) and potentially to premature overall structural instability (Shivakumar & Whitcomb, 1985; Rolfes *et al.*, 2009). Current design criteria in aircraft construction do not allow for such growth to occur (Melin *et al.*, 2002), hence a structure may not be exhausted to its possible limits. Therefore, various criteria were suggested and presented for the design of this particular panel to operate safely in service under in-plane loading conditions,

assuming that the delamination patch remained the same basic shape.

In the penultimate chapter, the assumption of uniform delamination growth was loosened and a pilot study on non-uniform delamination growth was conducted. Different shaped delaminations and their effect on the mechanical response were outlined and it was concluded that if propagation was constrained to one direction, it was more likely to occur perpendicular to the loading direction. This was also the case in various other studies by previous researchers (Bottega & Maewal, 1983; Chai & Babcock, 1985; Peck & Springer, 1991; Yin & Jane, 1992a; Nilsson *et al.*, 1993). However, this part of the current work has the potential to be expanded in future investigations as will be, amongst other possible extensions to the current investigations, discussed in the subsequent section.

9.2 Further work

As mentioned above, the work could potentially be extended in the non-uniform growth investigations since so far only preliminary studies have been conducted. A series of parametric studies could therefore be performed to strengthen the conclusions that propagation appears to occur predominantly in the direction transverse to the load. As research by Nilsson *et al.* (2001b) has shown, the growth behaviour is linked to the depth of the delamination, therefore it would be worthwhile to investigate the spread of the defect for delaminations outside the thin-film range.

However, before this could be implemented in the current model, the growth criteria established in Chapter 6 require the incorporation of further fracture modes. Currently, only Mode I fracture is considered to maintain model simplicity. However, it is understood that even in the thin-film configuration and particularly once overall buckling dominates the behaviour, Mode II fracture, *i.e.* the sliding mode (Figure 6.2b), will produce a gain in strain energy that could potentially cause further delamination growth (Pinho, 2005). With the current cohesive zone model, mixed

mode fracture could relatively easily be incorporated (Whitcomb, 1989; Hutchinson & Suo, 1992; Kardomateas, 1993; Davidson, 1995) *e.g.* by introducing a penalization function of the relative sliding of the layers once the defect grows by a certain length; such approaches have borne fruit in the modelling of kink bands (Wadee *et al.*, 2004).

Furthermore, it may be interesting to extend the model such that the onset of the formation of a delamination originating from an undamaged panel is predicted (Wimmer *et al.*, 2009). This could be undertaken by incorporating a strength based criterion as suggested by those researchers. However, as described in §3.3, plane stress is assumed in the current model, hence an incorporation of a strength based criterion cannot easily be accommodated with the current formulations since transverse normal stresses are zero; an alternative approach would be necessary.

In addition to delamination and subsequent propagation, further failure mechanisms might be worthwhile investigating and simulating (Linde, 2008). Since composites are materials of a complex nature, other stiffness and strength reducing defects may occur, such as fibre fracture, transverse and longitudinal matrix fracture and fracture of the fibre–matrix interface (Simitses *et al.*, 1985; Garg, 1988; Whitcomb, 1989; Berthelot, 1999; Nilsson, 2001b; Craven *et al.*, 2010). For example, fibre or matrix fracture could easily be ascertained by determining the stresses in the fibres or matrix due to the buckling of the structure. This stress could then be compared to the ultimate stresses of the constituents of the material and a conclusion can be drawn whether material failure will occur.

Another beneficial development would be to formulate an automation of the growth algorithm described in Chapter 6. This could be achieved by implementing a user-defined subroutine in the software that automatically changes the parameters once the delamination grows. Wadee & Blackmore (2001) employed a modified Heaviside function within AUTO in their investigations on the effects of a delamination on sandwich panels. This function accounts for the changes in the formulations due to the propagation of the defect.

Furthermore, only uniaxially compressive and static loading conditions were investigated within the current model formulations. However, it is understood that fatigue loading may yield further delamination and subsequently a reduction in the reserve strength of the panels (Melin & Schön, 2001; Melin *et al.*, 2002; Butler *et al.*, 2007). Additionally, combined loading such as shear and compression may be of interest in future investigations (Bisagni & Walters, 2008).

In terms of the model geometry and properties, quasi-homogeneous material assumptions were currently considered. However, owing to the complex nature of composite materials, anisotropic material properties (Shivakumar & Whitcomb, 1985) as well as different lay-up angles and orientations (Bottega & Maewal, 1983; Whitcomb, 1989; Kardomateas & Pelegri, 1994; Sekine *et al.*, 2000) may be worthwhile investigating by incorporating different material properties and surface energy parameters. The current model already has the potential to allow for different materials of the sublaminates by introducing the quantity ψ, which accounts for the shift in the neutral axis when using different material properties *c.f.* equation (3.18) (Hunt *et al.*, 2004; Wright, 2006a). However, the introduction of anisotropic material properties would furthermore lead to more complicated formulations in the energy expressions and would therefore infringe with the desired simplicity of the model. Thus, studies so far were only conducted assuming smeared, isotropic material properties resulting in the same Young's Modulus for the sublaminates as well as the intact parts of the panel. Investigations into the behaviour of the panels when changing the interface properties could be easily undertaken by changing the parameters in another study.

Investigations into different shaped delamination geometries could be extended, *e.g.* elliptical or circular delaminations (Bottega & Maewal, 1983; Chai & Babcock, 1985; Craven *et al.*, 2010), as well as allowing for curved panels (Short *et al.*, 2002). However, when formulating the assumptions of the current model, as can be reviewed in §3.3, the model was deliberately developed such that a rectangular defect is allowed for to keep the model as simple as possible for the coordinate system used. In addition, curved panels could be easily adopted by incorporating an

initial imperfection in the formulations of the out-of-plane displacement functions w_i described in §3.4.1. However, this is not deemed to take priority in future investigations since previous research conducted by Bottega *et al.* (1983) concluded that imperfections had no noticeable effect on the delamination process and yielded asymptotic results to the perfect case as would be expected.

The introduction of a penalty function or some form of other criteria to allow for the contact behaviour between the sublaminates once buckling occurs may be worthwhile (Shivakumar & Whitcomb, 1985). This could be simulated by very stiff springs that account for the effect when the laminates would theoretically interpenetrate (Nilsson *et al.*, 1993).

Since the current small scale investigations have been conducted for specific parameters only, *i.e.* plate dimensions and material properties, size effects on the failure loads may be expected (Bažant & Cedolin, 1991; Bažant & Grassl, 2007). Scaling laws have increasingly become an important topic of investigations and the size effect of linear elastic fracture mechanics can be generally defined as:

$$\sigma_{\mathrm{N}} = \frac{\text{constant}}{\sqrt{\mathrm{X}}}\,, \tag{9.1}$$

where σ_{N} is the nominal strength of the structure at failure and X the characteristic dimension of the structure or specimen (Bažant & Cedolin, 1991). Thus size effects may be expected to occur for the plate parameters such as the delamination patch dimensions a and b as well as the depth of the delamination ct. Furthermore, the overall dimensions of the plate L and B and the overall thickness t might influence the results, therefore investigations into scaling laws would be an important aspect of future investigations. Investigations into those effects in sandwich skin delamination has been undertaken by Bažant & Grassl (2007) where it was found that up-scaling of the problem led to a significant reduction in the nominal strength of the structure when imperfections were introduced. Subsequently, size effects would be important to include in future investigations to generalize and extend the findings of the current model. The following works that deal with the problem of scaling laws are, amongst others, to be consulted in detail in future investigations: Bažant & Planas (1998),

Bažant (1991; 2002; 2004), Bažant & Grassl (2007).

Finally, it would clearly be beneficial, if experiments were conducted to investigate and to validate further the buckling and subsequent growth behaviour of the delamination determined with the current model. As mentioned in Chapter 2, previous researchers, to name a few: Peck & Springer (1991), Yin & Jane (1992b), Nilsson *et al.* (1993), Short *et al.* (2001; 2002), Melin *et al.* (2002) have successfully employed experimental methods to study the behaviour of delaminations which, however, require the facilities as well as the funding to conduct these investigations. Problems of detection and visualization of the delamination growth during loading would be of course the main issues after the panels are manufactured to a given standard.

Appendix A

Stress functions

In this part of the Appendix, the derivation of the mixed mode terms $\varphi_{i(\text{mixed})}$ comprising $Q_i Q_3$ in the stress functions shown in Chapter 3, §3.4.2, equations (3.16) and (3.17), is presented, following the procedure developed by Little (1987). These mixed mode terms are required in the stress functions to allow for the mixed effects stemming from interactive buckling of the intact and delaminated parts. The direct strains are based on von Kármán's large deflection theory, for example for ε_x, can be expressed in terms of displacements as (Timoshenko & Goodier, 1987):

$$\varepsilon_x = \frac{\partial u}{\partial x} + \frac{1}{2}\left(\frac{\partial w}{\partial x}\right)^2 . \tag{A.1}$$

With the nature of the superimposed out-of-plane displacement functions w_i, equation (3.5), defined in Chapter 3, this leads to $Q_i Q_3$ terms in the stress function due to the quadratic slope term in equation (A.1); hence, these terms must not be ignored when describing the in-plane behaviour of the plates after buckling.

In the article by Little (1987), the elastic behaviour of a typical rectangular, orthotropic plate which undergoes a deflection that is of the same order as the plate thickness, *i.e.* moderately large but small compared to the overall plate dimensions, is considered, as shown in Figure A.1. The overall dimensions of the plate are lengths a and b with uniform thickness t and a uniform compressive force is applied on the

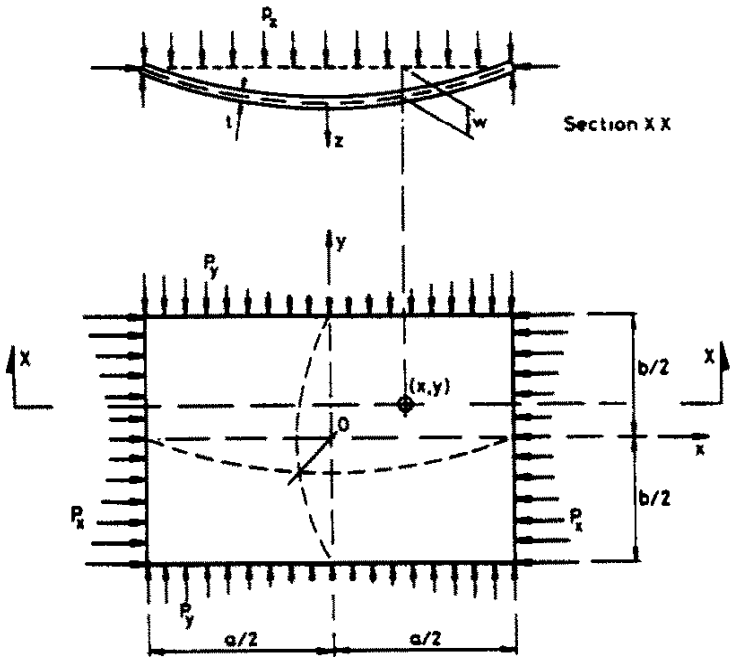

Figure A.1: Plate dimensions, coordinate axes and loading of Little's (1987) model.

edges, namely $P_x(y)$ and $P_y(x)$ as illustrated in the figure. As in the model developed in Chapter 3, plane stress is assumed, however, an imperfection w_0 is furthermore included by Little, which is not accounted for in the current model and is therefore not incorporated in the procedure discussed below. The general, orthotropic case Little considers can be reduced to homogeneous and isotropic material properties, where after equation (8) in Little (1987):

$$E_x = E_y = E; \quad \nu_{xy} = \nu_{yx} = \nu; \quad G = \frac{E}{2(1+\nu)} \tag{A.2}$$

and the $\mathbf{a}$ matrix, which comprises the membrane flexibility coefficients, follows:

$$\mathbf{a} = \frac{1}{t} \begin{pmatrix} \frac{1}{E} & \frac{-\nu}{E} & 0 \\ \frac{-\nu}{E} & \frac{1}{E} & 0 \\ 0 & 0 & \frac{1}{G} \end{pmatrix} .$$

Note that a separate part of the nomenclature at the beginning of this thesis specifi-

cally denotes the abbreviations and notations used within this part of the appendix.

The boundary conditions are restricted in the publication to so-called "Type A" plates only, which means that the longitudinal as well as the transverse edges are held straight in the same manner and the prescribed forces are mean values. To apply the procedure: in one case, the plate is treated as clamped along $x = \pm a/2$ and simply supported (ss) along $y = \pm B/2$, Figure A.2b (Little: Case III), and in the other case the plate is treated as simply supported along the edges $x = \pm L/2$ and clamped along $y = \pm b/2$, Figure A.2a (Little: Case II).

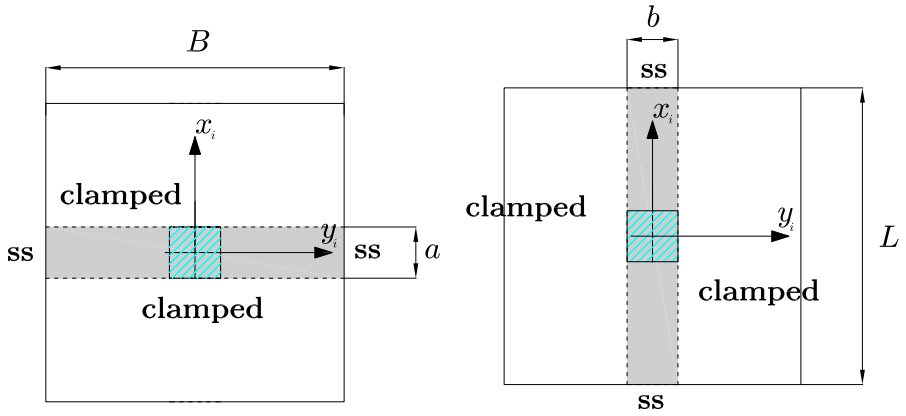

Figure A.2: Cases used to apply the procedure developed by Little (1987); (a) clamped along $x = \pm a/2$ and simply supported along $y = \pm B/2$ and (b) simply supported along the edges $x = \pm L/2$ and clamped along $y = \pm b/2$.

The out-of-plane displacement functions s_i are subsequently described, applying Little's notation in the reference's equation (15), as:

$$s_1 = \frac{Q_i Q_3}{2} \left\{ 1 + \cos\left(\frac{2\pi x_i}{a}\right) \right\} \cos\left(\frac{\pi y_i}{B}\right) \tag{A.3}$$

for the first case (Little: Case III) and

$$s_2 = \frac{Q_i Q_3}{2} \cos\left(\frac{\pi x_i}{L}\right) \left\{ 1 + \cos\left(\frac{2\pi y_i}{b}\right) \right\} \tag{A.4}$$

for the second case (Little: Case II).

The procedure is now discussed below for the first case only to avoid repetition since the other case can be solved in an identical procedure. Thus, for the second case, with $m_i = 2$, $n_j = 1$ and $I_{xi} = 1$ as in Little (1987), the values $M_1 = 4$ and $M_2 = 4$ follow. Table 3 in the publication can then be derived as follows (Table A.1 currently): the factor in equation (26) in the reference can be summarized, using

J	$2p$	$2q$	I
1	4	1	0
2	0	1	-8
3	0	2	-8
4	0	0	0
5	2	1	0
6	4	1	0
7	0	1	0
8	2	2	-8
9	2	0	-8

Table A.1: Values for p, q and I for applying Little's (1987) procedure.

algebraic manipulation and with $\psi_{pq} = 1/4\, I$ and $\mathbf{a}$ from above, to the following expression:

$$\eta_{pq} = \frac{1}{2} I \psi_{pq} \frac{1}{\frac{1}{Et}(p^2 \frac{B}{a} + \frac{a}{B} q^2)^2}\,. \tag{A.5}$$

With the stress function F, omitting the terms stemming from uniform squashing, being defined as

$$F = \sum_{pq} \eta_{pq} \cos\left(\frac{2p\pi x}{a}\right) \cos\left(\frac{2q\pi y}{b}\right) \tag{A.6}$$

the mixed mode terms in φ_i for Little's Case II can be derived, with $b = B$, thus:

$$\varphi_{m1} = -\frac{Q_1 Q_3}{128}\left(\frac{8a^2}{B^2}\cos\frac{2\pi x_1}{a} + \frac{a^2}{2B^2}\cos\frac{4\pi x_1}{a} + \frac{8B^2}{a^2}\cos\frac{2\pi y_1}{B} + \frac{8}{(B/a + a/B)^2}\cos\frac{2\pi x_1}{a}\cos\frac{2\pi y_1}{B}\right) \tag{A.7}$$

and for Case III accordingly:

$$\varphi_{m2} = -\frac{Q_1 Q_3}{128}\left(\frac{b^2}{2L^2}\cos\frac{4\pi y_1}{b} + \frac{8L^2}{b^2}\cos\frac{2\pi x_1}{L} + \frac{8b^2}{L^2}\cos\frac{2\pi y_1}{b} + \frac{8}{(L/b + b/L)^2}\cos\frac{2\pi x_1}{L}\cos\frac{2\pi y_1}{b}\right). \tag{A.8}$$

These are then incorporated into the expressions for the stress functions shown in equations (3.16) and (3.17), where a factor of 1/2 is furthermore employed to avoid accounting for the effects twice, thus:

$$\varphi_{i(\text{mixed})} = \frac{\varphi_{m1} + \varphi_{m2}}{2}\,. \tag{A.9}$$

Appendix B

Further results

B.1 Critical loads

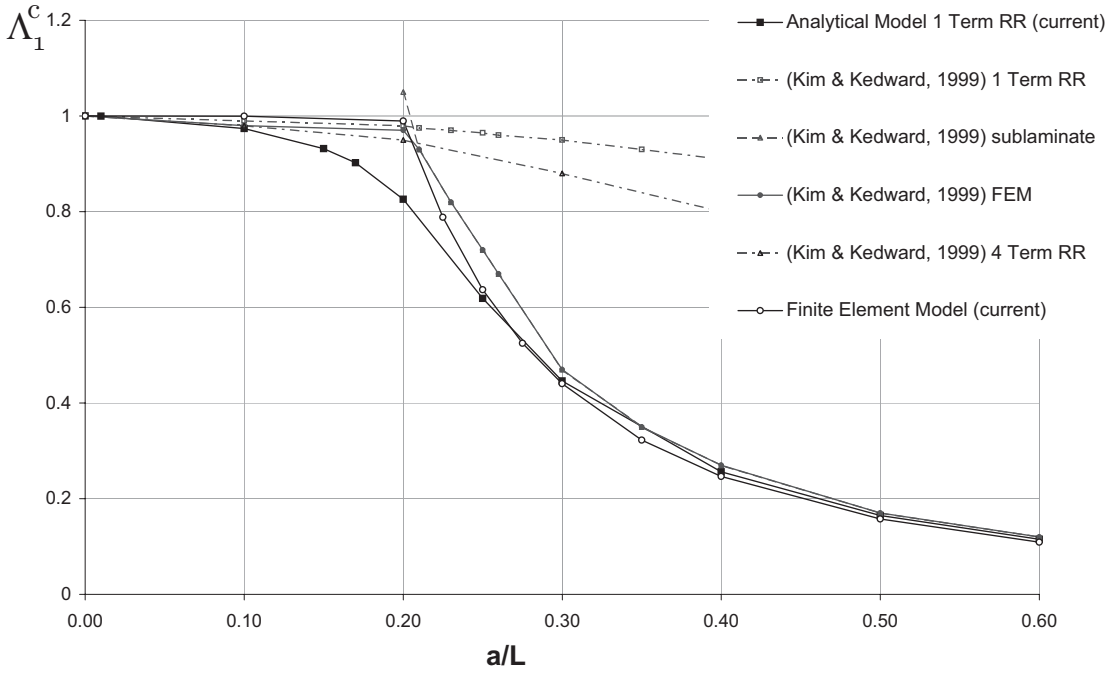

Figure B.1: Normalized critical load Λ_1^C versus delamination size for $c = 0.125$ compared to results obtained with the finite element model from §3.6 and results from the literature (Kim & Kedward, 1999).

Normalized critical loads corresponding to the linearized analysis presented in Chapter 4 are presented in Figure B.1 for a square delamination at relative depth $c = 0.125$.

B.2 Supplementary postbuckling graphs

Supplementary postbuckling graphs corresponding to the discussions on growing defects in Chapters 7 and 8 for uniformly and unidirectional propagating delaminations, respectively, are provided in this part of the Appendix. Note that the results have already been discussed in the main chapters and are presented herein for reference only.

B.2.1 Postbuckling graphs with uniform delamination propagation

Supplementary graphs illustrating the postbuckling behaviour for the mixed mode case 1 (B) containing a uniformly propagating delamination of dimensions $a = b = 15$ mm at depth $c = 0.085$, as discussed in Chapter 7, are presented in Figure B.2. The standard notations defined in Table 7.3 apply.

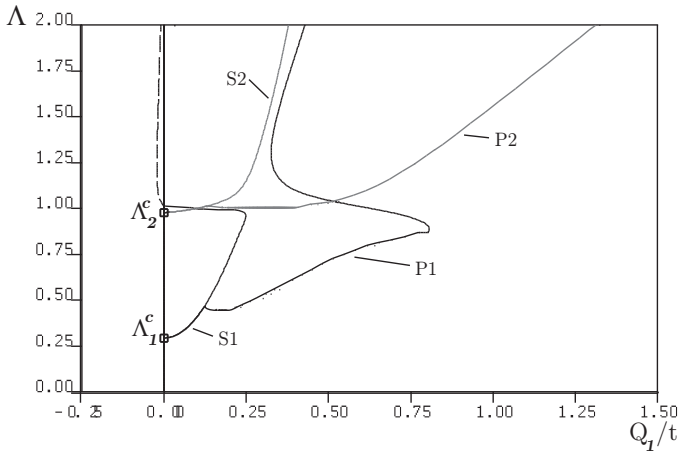

(a)

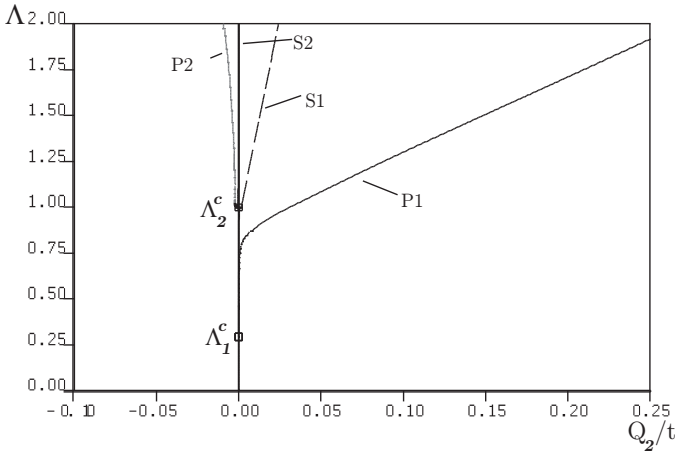

(b)

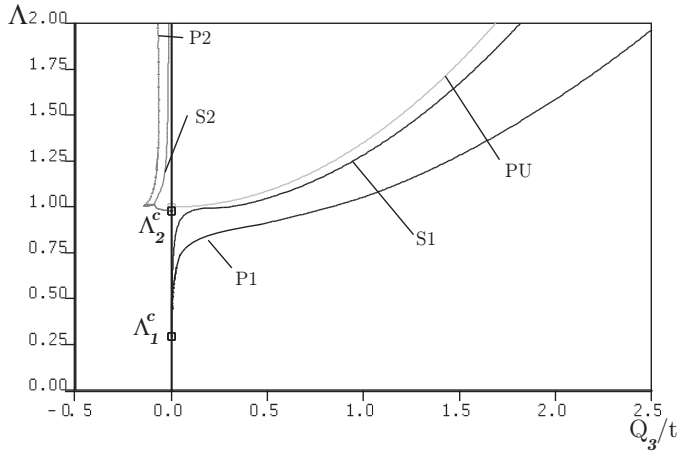

(c)

Figure B.2: Postbuckling equilibrium paths for mixed mode: case 1 (B). Graphs show the normalized axial load Λ versus (a) Q_1/t (upper laminate), (b) Q_2/t (lower laminate) and (c) Q_3/t (intact part).

B.2.2 Postbuckling regime of a unidirectionally propagating delamination

Postbuckling for a unidirectionally propagating delamination was discussed in a pilot study in Chapter 8. Supplementary graphs as well as tabulated values can be found currently. The notation for the graphs remains as summarized in Table 8.2. Initially, unidirectional delamination propagation is presented originating from a square defect of dimensions $a = b = 15$ mm, but further results for growing delaminations originating from a wide or long delamination are presented subsequently.

B.2.2.1 Growth in the longitudinal direction only originating from a square delamination

Figure B.3 shows the buckling behaviour of the global mode case for growth in the longitudinal direction originating from a square delamination.

B.2.2.2 Growth in the transverse direction only – originating from a square delamination

Figure B.4 shows the buckling behaviour of the global mode case for growth in the transverse direction originating from a square delamination.

B.2.2.3 Comparison for growth originating from a square delamination

Table B.1 compares the values found during the pilot study discussed in Chapter 8 for unidirectional growth originating from a square panel for the mixed mode—case I (B)—and global—case (C)—buckling.

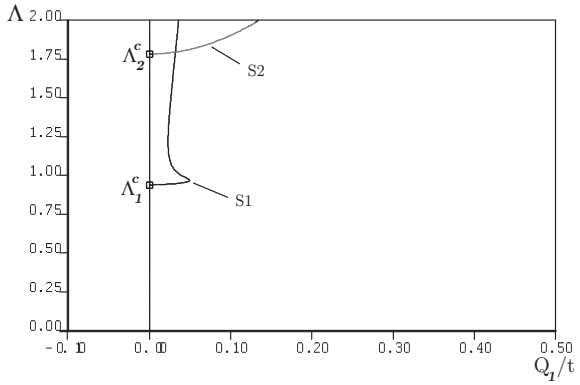

(a)

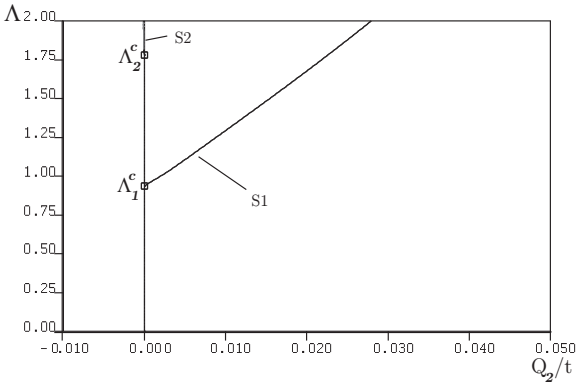

(b)

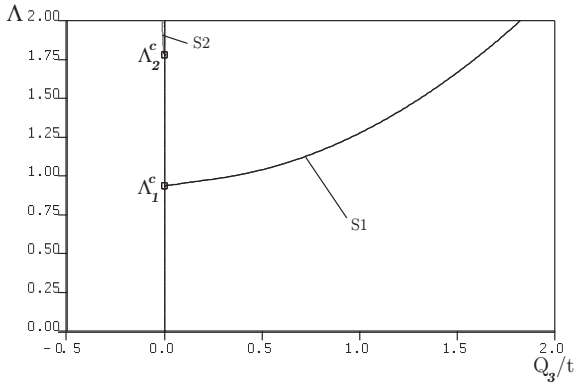

(c)

Figure B.3: Postbuckling equilibrium paths for global mode: case I $(\mathrm{C})_x$. Graphs show the normalized axial load Λ versus (a) Q_1/t (upper laminate), (b) Q_2/t (lower laminate) and (c) Q_3/t (intact part). Note the lack of path "P1x".

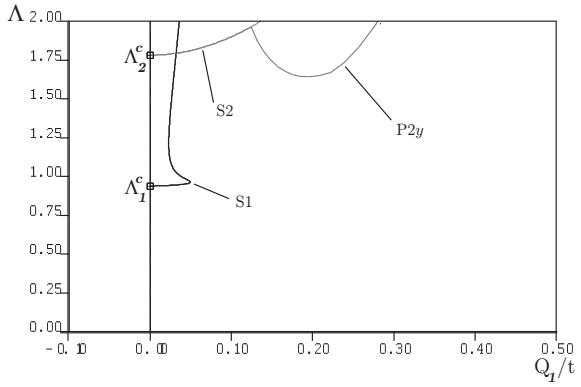

(a)

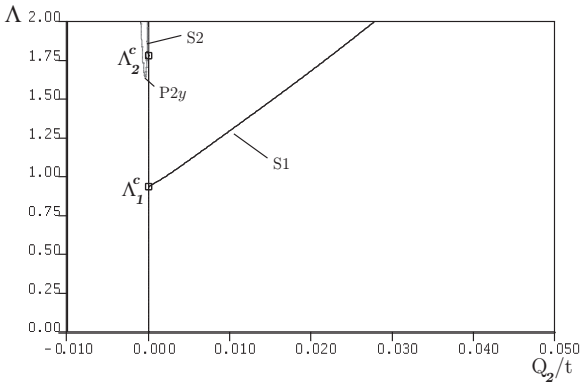

(b)

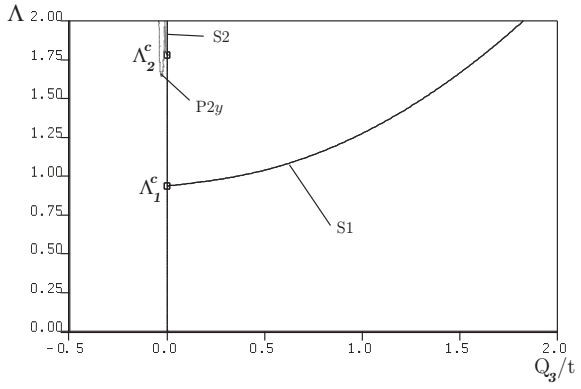

(c)

Figure B.4: Postbuckling equilibrium paths for global mode: case I $(\mathrm{C})_y$. Graphs show the normalized axial load Λ versus (a) Q_1/t (upper laminate), (b) Q_2/t (lower laminate) and (c) Q_3/t (intact part). Note the lack of path "P1y".

Case I	$(\mathrm{B})_x$	$(\mathrm{B})_y$	$(\mathrm{C})_x$	$(\mathrm{C})_y$
Λ_1^{C}	0.801	0.801	0.932	0.932
$\Lambda_1^{\mathrm{prop}}$	0.915	0.915	–	–
Λ_1^{min}	–	0.829	–	–
a or b at Λ_1^{min} (mm)	–	18	–	–
Λ_1^{max}	1.39	0.881	–	–
a or b at Λ_1^{max} (mm)	16.5 (a)	21 (b)	–	–
growth stationary at Λ_1^{max}?	yes	yes	–	–
Λ_2^{C}	1.045	1.045	1.783	1.783
$\Lambda_2^{\mathrm{prop}}$	1.162	1.162	1.965	1.965
Λ_2^{min}	–	1.118	–	1.647
a or b at Λ_2^{min} (mm)	–	17	–	19
Λ_2^{max}	2.546	2.317	2.740	2.189
a or b at Λ_2^{max} (mm)	22 (a)	26 (b)	20 (a)	24 (b)
growth stationary at Λ_2^{max}?	no	no	no	no

Table B.1: Results summary: case I (B) and (C). Growth in the longitudinal – x- and transverse – y-direction.

B.2.3 Unidirectional delamination propagation originating from an initially rectangular delamination

Unidirectional delamination propagation results originating from a rectangular delamination are presented in tabulated form; they relate to the discussion presented in §8.2.3.

B.2.3.1 Initial growth in the longitudinal direction – x_i-axis

Table B.2 corresponds to case II ($a = 0.10L$, $b = 0.15B$), an initially wide defect propagating in the x-direction only, whereas Table B.3 presents this particular case in detail for growth in the x- and y-direction as well as uniform growth once the

defect is square, as described in the main part of the thesis.

Case II	$(A)_x$	$(B)_x$	$(C)_x$
Λ_1^{C}	0.366	0.868	0.942
$\Lambda_1^{\mathrm{prop}}$	0.700	–	–
Λ_1^{min}	0.696	–	–
a at Λ_1^{min} (mm)	10.5	–	–
Λ_1^{max}	0.906	–	–
a at Λ_1^{max} (mm)	15	–	–
growth stationary at Λ_1^{max}?	yes	–	–
Λ_2^{C}	1.004	1.249	2.318
$\Lambda_2^{\mathrm{prop}}$	1.084	1.579	2.698
Λ_2^{min}	1.080	1.489	2.411
a at Λ_2^{min} (mm)	11	12	12.5
Λ_2^{max}	2.371	2.432	3.337
a at Λ_2^{max} (mm)	18	17	17
growth stationary at Λ_2^{max}?	no	no	no

Table B.2: Results summary: growth in the longitudinal direction only – x-axis originating from a wide (case II) defect.

Case II	$(A)_x$	$(A)_y$	(A) uniform
$\Lambda_2^{\mathrm{square}}$	1.237	1.237	1.237
a and b at $\Lambda_2^{\mathrm{square}}$ (mm)	15	15	15
Λ_2^{max}	2.371	2.410	2.154
a and/or b at Λ_2^{max} (mm)	18 (a)	20 (b)	23 (a and b)
growth stationary at Λ_2^{max}?	no	no	no

Table B.3: Results summary extended: case II (A).

B.2.3.2 Initial growth in the transverse direction – y_i-axis

Growth in the transverse direction is now considered for case II (a wide delamination) and III (a long delamination of dimensions $a = 0.20L$, $b = 0.15B$), and the results are presented in Table 8.5. Tables B.4 and B.5 present cases III (A) and (B), respectively, in detail for uniform propagation once the defect is square.

Case III	$(A)_y$	(A) uniform
$\Lambda_1^{\text{square}}$	0.462	0.462
a and b at $\Lambda_1^{\text{square}}$ (mm)	20	20
$\Lambda_1^{\max}$	0.882	0.870
a and/or b at $\Lambda_1^{\max}$ (mm)	27.5 (b)	38 (a and b)
growth stationary at $\Lambda_1^{\max}$?	yes	yes
$\Lambda_2^{\text{square}}$	1.006	1.006
a and b at $\Lambda_2^{\text{square}}$ (mm)	20	20
$\Lambda_2^{\text{min, unif}}$	n/a	1.006
a and b at $\Lambda_2^{\max}$ (mm)	n/a	22 (a and b)
$\Lambda_2^{\max}$	2.462	2.087
a and/or b at $\Lambda_2^{\max}$ (mm)	33 (b)	51 (a and b)
growth stationary at $\Lambda_2^{\max}$?	no	no

Table B.4: Results summary extended: case III (A).

Case III	$(B)_y$	(B) uniform
$\Lambda_2^{\text{square}}$	1.074	1.074
a and b at $\Lambda_2^{\text{square}}$ (mm)	20	20
$\Lambda_2^{\text{min, unif}}$	n/a	1.073
a and b at $\Lambda_2^{\max}$ (mm)	n/a	21 (a and b)
$\Lambda_2^{\max}$	2.700	2.088
a and/or b at $\Lambda_2^{\max}$ (mm)	33 (b)	49 (a and b)
growth stationary at $\Lambda_2^{\max}$?	no	no

Table B.5: Results summary extended: case III (B).

References

ABAQUS. 2006. *Abaqus/standard: User's manual version 6.6.* Pawtucket, USA: Hibbitt, Karlsson & Sorensen, Inc.

Alfano, G., & Crisfield, M. A. 2001. Finite element interface models for the delamination analysis of laminated composites: Mechanical and computational issues. *International Journal for Numerical Methods in Engineering*, **50**(7), 1701–1736.

Allix, O., Lévêque, D., & Perret, L. 1998. Identification and forecast of delamination in composite laminates by an interlaminar interface model. *Composites Science and Technology*, **58**(5), 671–678.

Balzani, C., & Wagner, W. 2008. An interface element for the simulation of delamination in unidirectional fiber-reinforced composite laminates. *Engineering Fracture Mechanics*, **75**(9), 2597–2615.

Bažant, Z. P., & Cedolin, L. 1991. *Stability of structures: Elastic, inelastic, fracture and damage theories.* New York, USA: Oxford University Press.

Bažant, Z. P., & Grassl, P. 2007. Size effect of cohesive delamination fracture triggered by sandwich skin wrinkling. *Journal of Applied Mechanics - Transactions of the ASME*, **74**(6), 1134–1141.

Bažant, Z. P. 2002. *Scaling of structural strength.* London, UK: Hermes Penton Science.

Bažant, Z. P. 2004. Scaling theory for quasibrittle structural failure. *Proceedings*

of the National Academy of Sciences of the United States of America, **101**(37), 13400–13407.

Bažant, Z. P. and Planas, J. 1998. *Fracture and size effect in concrete and other quasibrittle materials*. Boca Raton, FL, USA: CRC Press.

BBC. 2009a. *Boeing 787 dreamliner completes its first flight*. http://news.bbc.co.-uk/1/hi/8413466.stm. Online; accessed 02 February 2010.

BBC. 2009b. *Fresh delay for boeing dreamliner*. http://news.bbc.co.uk/1/hi/-business/8115147.stm. Online; accessed 25 June 2009.

Belytschko, T., Liu, W. K., & Moran, B. 2000. *Nonlinear finite elements for continua and structures*. Chichester, UK: Wiley.

Benzerga, D., Haddi, A., Seddak, A., & Lavie, A. 2008. A mixed-mode damage model for delamination growth applied to a new woven composite. *Computational Materials Science*, **41**(4), 515–521.

Berthelot, J.-M. 1999. *Composite materials: Mechanical behavior and structural analysis*. New York, USA: Springer.

Bisagni, C., & Walters, C. 2008. Experimental investigation of the damage propagation in composite specimens under biaxial loading composite structures. *Composite Structures*, **85**(4), 293–310.

Boeing. 2009. http://www.boeing.com/commercial/787family/. Online; accessed 01 July 2009.

Bolotin, V. V. 1996. Delaminations in composite structures: Its origin, buckling, growth and stability. *Composites Part B-Engineering*, **27**(2), 129–145.

Bolotin, V. V. 2001. Mechanics of delaminations in laminate composite structures. *Mechanics of Composite Materials*, **37**(5–6), 367–380.

Bottega, W. J., & Maewal, A. 1983. Delamination buckling and growth in laminates. *Journal of Applied Mechanics - Transactions of the ASME*, **50**(1), 184–189.

Budiansky, B. (ed). 1976. *Buckling of structures*. IUTAM Symposium, Cambridge, USA, 1974. Berlin, Germany: Springer.

Bulson, P. S. 1969. *The stability of flat plates*. New York, USA: American Elsevier.

Butler, R., Almond, D. P., Hunt, G. W., Hu, B., & Gathercole, N. 2007. Compressive fatigue limit of impact damaged composite laminates. *Composites Part A-Applied Science and Manufacturing*, **38**(4), 1211–1215.

Camanho, P. P., Dávila, C. G., & Ambur, D. R. 2001. *Numerical simulation of delamination growth in composite materials*. Tech. rept. NASA/TP-2001-211041. Nasa Langley Research Center.

Camanho, P. P., Dávila, C. G., & De Moura, M. F. 2003. Numerical simulation of mixed-mode progressive delamination in composite materials. *Journal of Composite Materials*, **37**(16), 1415–1438.

Cappello, F., & Tumino, D. 2006. Numerical analysis of composite plates with multiple delaminations subjected to uniaxial buckling load. *Composites Science and Technology*, **66**(2), 264–272.

Chai, H., & Babcock, C. D. 1985. Two-dimensional modelling of compressive failure in delaminated laminates. *Journal of Composite Materials*, **19**, 67–98.

Chai, H., Babcock, C. D., & Knauss, W. G. 1981. One dimensional modelling of failure in laminated plates by delamination buckling. *International Journal of Solids and Structures*, **17**(11), 1069–1083.

Chen, H., & Yu, W. B. 2006. Postbuckling and mode jumping analysis of composite laminates using an asymptotically correct, geometrically non-linear theory. *International Journal of Non-Linear Mechanics*, **41**(10), 1143–1160.

Chen, H. R., & Sun, X. N. 1999. Residual compressive strength of laminated plates with delamination. *Composite Structures*, **47**, 711–717.

Chen, J., Crisfield, M. A., Kinloch, A. J., Busso, E. P., Matthews, F. L., & Qiu, Y. 1999. Predicting progressive delamination of composite material specimens via interface elements. *Mechanics of Composite Materials and Structures*, **6**(4), 301–317.

Chilver, A. H. 1967. Coupled modes of elastic buckling. *Journal of the Mechanics and Physics of Solids*, **15**(1), 15–28.

Craven, R., Iannucci, L., & Olsson, L. 2010. Delamination buckling: A finite element study with realistic delamination shapes, multiple delaminations and fibre fracture cracks. *Composites Part A: Applied Science and Manufacturing*, **In Press, Accepted Manuscript**.

Croll, J. G., & Walker, A. C. 1972. *Elements of structural stability.* New York, USA: Wiley.

Cutler, J. 1999. *Understanding aircraft structures.* 3rd edn. Oxford; Malden, MA, USA: Blackwell Science.

Davidson, B. 1995. 3-dimensional analysis of center-delaminated unidirectional and multidirectional single-leg bending specimens. *Composites Science and Technology*, **54**(4), 385–394.

Davidson, B. D. 1991. Delamination buckling – theory and experiment. *Journal of Composite Materials*, **25**(10), 1351–1378.

de Boor, C., & Schwartz, B. 1973. Collocation of gaussian points. *SIAM Journal on Numerical Analysis*, **10**(4), 582–606.

Doedel, E. J. 1984. The computer–aided bifurcation analysis of predator–prey models. *Journal of Mathematical Biology*, **20**, 1–14.

Doedel, E. J. 1997. Nonlinear numerics. *Journal of the Franklin Institute*, **334B**(5–6), 1049–1073.

Doedel, E. J. 2007. *Auto-07p: Continuation and bifurcation software for ordinary differential equations.* Available from http://indy.cs.concordia.ca/auto/.

Elices, M., Guinea, G. V., Gomez, J., & Planas, J. 2002. The cohesive zone model: advantages, limitations and challenges. *Engineering Fracture Mechanics*, **69**(2), 137–163.

Everall, P. R. 1999. *Mode jumping and quasi-periodicity in nonlinear elastic structures.* Ph.D. thesis, University of Bath.

Everall, P. R. 2000. Mode jumping in the buckling of struts and plates: a comparative study. *International Journal of Non-Linear Mechanics*, **35**(6), 1067–1079.

Everall, P. R., & Hunt, G. W. 1999. Arnold tongue predictions of secondary buckling in thin elastic plates. *Journal of the Mechanics and Physics of Solids*, **47**(10), 2187–2206.

Falzon, B. G., & Aliabadi, M. H. 2008. *Buckling and postbuckling structures: Experimental, analytical and numerical studies.* London, UK: Imperial College Press.

Frostig, Y. 1992. Behavior of delaminated sandwich beam with transversely flexible core – high order theory. *Composite Structures*, **20**(1), 1–16.

Garg, A. C. 1988. Delamination – a damage mode in composite structures. *Engineering Fracture Mechanics*, **29**(5), 557–584.

Gaudenzi, P. 1997. On delamination buckling of composite laminates under compressive loading. *Composite Structures*, **39**(1–2), 21–30.

Gaudenzi, P., Perugini, P., & Riccio, A. 2001. Post-buckling behavior of composite panels in the presence of unstable delaminations. *Composite Structures*, **51**(3), 301–309.

Griffith, A. A. 1921. The phenomena of rupture and flow in solids. *Philosophical Transactions of the Royal Society of London Series A*, **221**, 163–198.

Heck, A. 1996. *Introduction to maple.* 2nd edn. New York, USA: Springer.

Hunt, G. W. 1986. Hidden (a)symmetries of elastic and plastic bifurcation. *Applied Mechanics Review*, **39**(8), 1165–1186.

Hunt, G. W. 1989. Bifurcations of structural components. *Proceedings of the Institution of Civil Engineers Part 2 – Research and Theory*, **87**, 443–467.

Hunt, G. W. 2006. Buckling in space and time. *Nonlinear Dynamics*, **43**(1–2), 29–46.

Hunt, G. W., & Wadee, M. A. 1998. Localization and mode interaction in sandwich structures. *Proceedings of the Royal Society Series A*, **454**(1972), 1197–1216.

Hunt, G. W., Williams, K. A. J., & Cowell, R. G. 1986. Hidden symmetry concepts in the elastic buckling of axially-loaded cylinders. *International Journal of Solids and Structures*, **22**(12), 1501–1515.

Hunt, G. W., Da Silva, L. S., & Manzocchi, G. M. E. 1988. Interactive buckling in sandwich structures. *Proceedings of the Royal Society Series A*, **417**(1852), 155–177.

Hunt, G. W., Hu, B., Butler, R., Almond, D. P., & Wright, J. E. 2004. Nonlinear modeling of delaminated struts. *AIAA Journal*, **42**(11), 2364–2372.

Hutchinson, J. W., & Koiter, W. T. 1970. Postbuckling theory. *Applied Mechanics Review*, **23**, 1353–1366.

Hutchinson, J. W., & Suo, Z. 1992. Mixed-mode cracking in layered materials. *Advances in Applied Mechanics*, **29**, 63–191. J. W. Hutchinson and T. Y. Wu, Eds.

Hutchinson, J. W., He, M. Y., & Evans, A. G. 2000. The influence of imperfections on the nucleation and propagation of buckling driven delaminations. *Journal of the Mechanics and Physics of Solids*, **48**(4), 709–734.

Hwang, S., & Huang, S. 2005. Postbuckling behavior of composite laminates with two delaminations under uniaxial compression. *Composite Structures*, **68**(2), 157–165.

Hwang, S.-F., & Liu, G.-H. 2001. Buckling behavior of composite laminates with multiple delaminations under uniaxial compression. *Composite Structures*, **53**(2), 235–243.

Jensen, H. M., & Sheinman, I. 2002. Numerical analysis of buckling-driven delamination. *International Journal of Solids and Structures*, **39**(13–14), 3373–3386.

Johns, K. C., & Chilver, A. H. 1971. Multiple path generation at coincident branching points. *International Journal of Mechanical Sciences*, **13**(11), 899–910.

Johnson, W. S. 1985. *Delamination and debonding of materials: a symposium sponsored by ASTM Committees D-30 on High Modulus Fibers and their Composites and E-24 on Fracture Testing*. Philadelphia, PA, USA: ASTM.

Kachanov, L. M. 1988. *Delamination buckling of composite materials*. Dordrecht, The Netherlands: Kluwer Academic Publishers.

Kardomateas, G. A. 1993. The initial postbuckling and growth-behavior of internal delaminations in composite plates. *Journal of Applied Mechanics - Transactions of the ASME*, **60**(4), 903–910.

Kardomateas, G. A., & Pelegri, A. A. 1994. The stability of delamination growth in compressively loaded composite plates. *International Journal of Fracture*, **65**(3), 261–276.

Kardomateas, G. A., & Schmueser, D. W. 1988. Buckling and postbuckling of delaminated composites under compressive loads including transverse-shear effects. *AIAA Journal*, **26**(3), 337–343.

Kim, H., & Kedward, K. T. 1999. A method for modeling the local and global buckling of delaminated composite plates. *Composite Structures*, **44**(1), 43–53.

Kim, H. J., & Hong, C. S. 1997. Buckling and postbuckling behavior of composite laminates with a delamination. *Composites Science and Technology*, **57**(5), 557–564.

Koiter, W. T. 1945. *On the stability of elastic equilibrium.* Ph.D. thesis, Technische Hogeschool Delft (Technological University Delft), Delft, The Netherlands. English translation issued as NASA *Tech Trans*, **F10**, 833, 1967.

Koiter, W. T., & Pignataro, M. 1976a. An alternative approach to the interaction between local and overall buckling in stiffened panels. *In:* (Budiansky, 1976).

Koiter, W. T., & Pignataro, M. 1976b. *A general theory for the interaction between local and overall buckling of stiffened panels.* Tech. rept. WTHD 83. Delft University of Technology, Delft, The Netherlands.

Kouchakzadeh, M. A., & Sekine, H. 2000. Compressive buckling analysis of rectangular composite laminates containing multiple delaminations. *Composite Structures*, **50**(3), 249–255.

Li, D., Tang, G., Zhou, J., & Lei, Y. 2005. Buckling analysis of a plate with built-in rectangular delamination by strip distributed transfer function method. *Acta Mechanica*, **176**(3–4), 231–243.

Linde, P. 2008. Overview of test prediction and damage simulation of composite aircraft structures. *In: Proceedings of the 2nd International Conference on Buckling and Postbuckling Behaviour of Composite Laminated Shell Structures.* on conference CD.

Little, G. H. 1987. Efficient large deflection analysis of rectangular orthotropic plates by direct energy minimisation. *Computers & Structures*, **26**(5).

Lord, G. J., Champneys, A. R., & Hunt, G. W. 1997. Computation of localized post buckling in long axially compressed cylindrical shells. *Philosophical Transactions of the Royal Society of London Series A*, **355**(1732), 2137–2150.

Marsh, G. 2007. Airbus takes on Boeing with reinforced plastic A350 XWB. *Reinforced Plastics*, **51**(11), 26–29.

Megson, T. H. G. 1999. *Aircraft structures for engineering students.* 3rd edn. London, UK: Wiley.

Mei, H., Huang, R., Chung, J. Y., Stafford, C. M., & Yu, H.-H. 2007. Buckling modes of elastic thin films on elastic substrates. *Applied Physics Letters*, **90**(15), 151902.

Melin, L., & Schön, J. 2001. Buckling behaviour and delamination growth in impacted composite specimens under fatigue load: an experimental study. *Composites Science and Technology*, **61**(13), 1841–1852.

Melin, L., Schön, J., & Nyman, T. 2002. Fatigue testing and buckling characteristics of impacted composite specimens. *International Journal of Fatigue*, **24**(2–4), 263–272.

Mi, Y., Crisfield, M. A., Davies, G. A. O., & Hellweg, H. B. 1998. Progressive delamination using interface elements. *Journal of Composite Materials*, **32**(14), 1246–1272.

Mitrevski, T., Marshall, I. H., Thomson, R., Jones, R., & Whittingham, R. 2006. The influence of impactor shape on the damage to composite laminates. *Composite Structures*, **76**(1–2), 116–122.

Nilsson, K. F. 2001a. Delamination buckling and growth for delaminations at different depths in a slender composite panel. *International Journal of Solids and Structures*, **38**(17), 3039–3071.

Nilsson, K. F. 2001b. On transition of delamination growth behaviour for compression loaded composite panels. *International Journal of Solids and Structures*, **38**(46–47), 8407–8440.

Nilsson, K. F., & Stårakers, B. 1992. On interface crack-growth in composite plates. *Journal of Applied Mechanics - Transactions of the ASME*, **59**(3), 530–538.

Nilsson, K. F., Thesken, J. C., Sindelar, P., Giannakopoulos, A. E., & Stårakers, B. 1993. A theoretical and experimental investigation of buckling induced delamination growth. *Journal of the Mechanics and Physics of Solids*, **41**(4), 749–782.

Nyhoff, L. R., & Leestma, S. 1997. *Fortran 90 for engineers and scientists*. Upper Saddle River, N.J., USA: Prentice Hall.

Orifici, A., Thomson, R. S., Degenhardt, R., Bisagni, C., & Bayandor, J. 2007. Development of a finite-element analysis methodology for the propagation of delaminations in composite structures. *Mechanics of Composite Materials*, **43**(1), 9–28.

Orifici, A., Herszberg, I., & Thomson, R. S. 2008. Review of methodologies for composite material modelling incorporating failure. *Composite Structures*, **86**(1–3), 194–210.

Østergaard, R. C. 2008. Buckling driven debonding in sandwich columns. *International Journal of Solids and Structures*, **45**, 1264–1282.

Peck, S. O., & Springer, G. S. 1991. The behavior of delaminations in composite plates – analytical and experimental results. *Journal of Composite Materials*, **25**(7), 907–929.

Pinho, S. T. 2005. *Modelling failure of laminated composites using physically-based failure models*. Ph.D. thesis, Imperial College of Science, Technology and Medicine.

Rhead, A. T., & Butler, R. 2009. Compressive static strength model for impact damaged laminates. *Composites Science and Technology*, **69**(14), 2301–2307.

Rhead, A. T., Butler, R., & Hunt, G. W. 2008. Post-buckled propagation model for compressive fatigue of impact damaged laminates. *International Journal of Solids and Structures*, **45**(16), 4349–4361.

Riks, E. 1972. The application of Newton's method to the problem of elastic stability. *Transactions of the ASME - Journal of Applied Mechanics*, **39**(4), 1060–1065.

Rolfes, R., Vogler, M., & Kriegesmann, B. 2009. Novel trends in failure analysis of composite structures. *Pages 139–140 of: Proceedings of ICCES'09*.

Roorda, J. 1965. The buckling behaviour of imperfect structural systems. *Journal of the Mechanics and Physics of Solids*, **13**, 267–280.

Russell, R. D., & Christiansen, J. 1978. Adaptive mesh selection strategies for solving boundary value problems. *SIAM Journal on Numerical Analysis*, **15**(1), 59–80.

Rybicki, E., & Kanninen, M. 1977. Finite-element calculation of stress intensity factors by a modified crack closure integral. *Engineering Fracture Mechanics*, **9**(4), 931–938.

Saito, D., & Wadee, M. A. 2009. Numerical studies of interactive buckling in pre-stressed steel stayed columns. *Engineering Structures*, **31**(2), 432–443.

Sekine, H., Hu, N., & Kouchakzadeh, M. A. 2000. Buckling analysis of elliptically delaminated composite laminates with consideration of partial closure of delamination. *Journal of Composite Materials*, **34**(7), 551–574.

Sewell, M. J. 1970. On the branching of equilibrium paths. *Proceedings of the Royal Society Series A*, **315**, 490–518.

Seydel, R. 1994. *Practical bifurcation and stability analysis*. Interdisciplinary Applied Mathematics, vol. 5. New York, USA: Springer.

Seydel, R. 1997. Nonlinear computation. *Journal of the Franklin Institute*, **334B**(5–6), 1015–1047.

Sheinman, I., Kardomateas, G. A., & Pelegri, A. A. 1998. Delamination growth during pre- and post-buckling phases of delaminated composite laminates. *International Journal of Solids and Structures*, **35**(1–2), 19–31.

Shivakumar, K., Tan, P., & Newman, J. 1988. A virtual crack-closure technique for calculating stress intensity factors for cracked 3-dimensional bodies. *International Journal of Fracture*, **36**(3), R43–R50.

Shivakumar, K. N., & Whitcomb, J. D. 1985. Buckling of a sublaminate in a quasi-isotropic composite laminate. *Journal of Composite Materials*, **19**(1), 2–18.

Short, G. J., Guild, F. J., & Pavier, M. J. 2001. The effect of delamination geometry on the compressive failure of composite laminates. *Composites Science and Technology*, **61**(14), 2075–2086.

Short, G. J., Guild, F. J., & Pavier, M. J. 2002. Delaminations in flat and curved composite laminates subjected to compressive load. *Composite Structures*, **58**(2), 249–258.

Simitses, G. J., Sallam, S., & Yin, W. L. 1985. Effect of delamination of axially loaded homogeneous laminated plates. *AIAA Journal*, **23**(9), 1437–1444.

Somers, M., Weller, T., & Abramovich, H. 1991. Influence of predetermined delaminations on buckling and postbuckling behavior of composite sandwich beams. *Composite Structures*, **17**(4), 295–329.

Suemasu, H., Sasaki, W., Ishikawa, T., & Aoki, Y. 2008. A numerical study on compressive behavior of composite plates with multiple circular delaminations considering delamination propagation. *Composites Science and Technology*, **68**(12), 2562–2567.

Sun, C., & Jin, Z. H. 2006. Modeling of composite fracture using cohesive zone and bridging models. *Composites Science and Technology*, **66**(10), 1297–1302.

Supple, W. J. 1967. Coupled branching configurations in the elastic buckling of symmetrical structural systems. *International Journal of Mechanical Sciences*, **9**, 97–112.

Szilard, R. 1974. *Theory and analysis of plates: classical and numerical methods*. Englewood Cliffs, NJ, USA: Prentice Hall.

Szodruch, J. 2008. Future aircraft technologies – The European strategic research agenda. *In: Proceedings of the 2nd International Conference on Buckling and Postbuckling Behaviour of Composite Laminated Shell Structures*. on conference CD.

Tafreshi, A.and Oswald, T. 2003. Global buckling behaviour and local damage propagation in composite plates with embedded delaminations. *International Journal of Pressure Vessels and Piping*, **80**(1), 9–20.

The Design Council. 1989. *Design with advanced composite materials*. New York, USA: Springer. edited by Leslie N. Phillips.

Thompson, J. M. T., & Hunt, G. W. 1973. *A general theory of elastic stability*. London, UK: John Wiley and Sons.

Thompson, J. M. T., & Hunt, G. W. 1984. *Elastic instability phenomena*. London, UK: John Wiley and Sons.

Thompson, J. M. T., & Supple, W. J. 1973. Erosion of optimum designs by compound branching phenomena. *Journal of the Mechanics and Physics of Solids*, **21**, 135–144.

Timoshenko, S., & Gere, J. M. 1961. *Theory of elastic stability*. 2nd edn. New York, USA: McGraw-Hill.

Timoshenko, S., & Goodier, J. N. 1987. *Theory of elasticity*. 3rd edn. New York, USA: McGraw-Hill.

Timoshenko, S., & Woinowsky-Krieger, S. 1959. *Theory of plates and shells*. 2nd edn. New York, USA: McGraw-Hill.

Tsutsui, H., Kawamata, A., Sanda, T., & Takeda, N. 2004. Impact damage detection system using small-diameter optical-fiber sensors embedded in CFRP laminate structures. *Advanced Composite Materials*, **13**(1), 43–55.

Turon, A., Dávila, C. G., Camanho, P. P., & Costa, J. 2007. An engineering solution for mesh size effects in the simulation of delamination using cohesive zone models. *Engineering Fracture Mechanics*, **74**(10), 1665–1682.

USA Today. 2009. *Yet another 787 delay puts Boeing's credibility at risk*. http://www.usatoday.com/travel/flights/2009-06-23-boeing-787-delay--affects-credibility_N.htm. Online; accessed 25 June 2009.

Verpoest, I., & Lomov, S. V. 2009. Simulation of damage in textile composites: model development and experimental validation. *Pages 480–480 of: Proceedings of ICCES'09.*

Wadee, M. A. 1998. *Localized buckling in sandwich structures.* Ph.D. thesis, University of Bath.

Wadee, M. A. 2002. Localized buckling in sandwich struts with pre-existing delaminations and geometrical imperfections. *Journal of the Mechanics and Physics of Solids*, **50**(8), 1767–1787.

Wadee, M. A. 2007. Nonlinear mathematics in structural engineering. *Mathematics Today*, **43**(3), 104–108.

Wadee, M. A., & Blackmore, A. 2001. Delamination from localized instabilities in compression sandwich panels. *Journal of the Mechanics and Physics of Solids*, **49**(6), 1281–1299.

Wadee, M. A., Hunt, G. W., & Peletier, M. A. 2004. Kink band instability in layered structures. *Journal of the Mechanics and Physics of Solids*, **52**(5), 1071–1091.

Wadee, M. A., Yiatros, S., & Theofanous, M. 2010. Comparative studies of localized buckling in sandwich struts with different core bending models. *International Journal of Non-Linear Mechanics*, **45**(2), 111–120.

Wang, S., & Zhang, Y. 2009. Buckling, post-buckling and delamination propagation in debonded composite laminates part 2: Numerical applications. *Composite Structures*, **88**(1), 131–146.

Whitcomb, J. D. 1989. Three-dimensional analysis of a postbuckled embedded delamination. *Journal of Composite Materials*, **23**(9), 862–889.

Wilkins, D. J., Eiserman, J. R., Camin, R. A., Margolis, W. S., & Benson, R. A. 1982. Characterizing delamination growth in graphite-epoxy. *Damage in Composite Materials*, 168–183.

Williams, D. G., & Aalami, B. 1979. *Thin plate design for in-plane loading*. New York, USA: Wiley.

Wimmer, G., & Pettermann, H. E. 2008. A semi-analytical model for the simulation of delamination in laminated composites. *Composites Science and Technology*, **68**(12), 2332–2339.

Wimmer, G., Schuecker, C., & Pettermann, H. E. 2009. Numerical simulation of delamination in laminated composite components - a combination of a strength criterion and fracture mechanics. *Composites Part B: Engineering*, **40**(2), 158–165.

Wright, J. 2006a. Compound bifurcations in the buckling of a delaminated composite strut. *Nonlinear Dynamics*, **43**(1–2), 59–72.

Wright, J. E. 2006b. *Compound bifurcations in delamination buckling*. Ph.D. thesis, University of Bath.

Xie, D., & Biggers, S. B. 2006. Progressive crack growth analysis using interface element based on the virtual crack closure technique. *Finite Elements in Analysis and Design*, **42**(11), 977–984.

Xie, D., & Waas, A. M. 2006. Discrete cohesive zone model for mixed-mode fracture using finite element analysis. *Engineering Fracture Mechanics*, **73**(13), 1783–1796.

Xie, D., Salvi, A. G., Sun, C., Waas, A. M., & Caliskan, A. 2006. Discrete cohesive zone model to simulate static fracture in 2d triaxially braided carbon fiber composites. *Journal of Composite Materials*, **40**(22), 2025–2046.

Yin, W.-L., & Jane, K. C. 1992a. Refined buckling and postbuckling analysis of two-dimensional delaminations - i. analysis and validation. *International Journal of Solids and Structures*, **29**(5), 591–610.

Yin, W.-L., & Jane, K. C. 1992b. Refined buckling and postbuckling analysis of two-dimensional delaminations - ii. results for anisotropic laminates and conclusion. *International Journal of Solids and Structures*, **29**(5), 611–639.

Yu, H. 2003. Delamination of thin film strips. *Thin Solid Films*, **423**(1), 54–63.

Zienkiewicz, O. C., Taylor, R. L., & Zhu, J. Z. 2005. *The finite element method – its basis and fundamentals*. 6th edn. Elsevier. Online version available at: http://knovel.com/web/portal/browse/display? _EXT _KNOVEL _DISPLAY _bookid=1886.